Ekaterina Kim

Experimental and numerical studies related to the coupled behavior of ice mass and steel structures during accidental collisions

Doctoral Thesis

Submitted for partial fulfillment of requirements for the degree of

Philosophiae doctor

Trondheim, March 2014

Department of Marine Technology
Faculty of Engineering Science and Technology
Norwegian University of Science and Technology

NTNU

ISBN 978-82-326-0192-9 (printed version)

ISBN 978-82-326-0193-6 (electronic version)

ISSN 1503-8181

Theses at NTNU; 2014:135

Printed in Norway by Skipnes Kommunikasjon AS, Trondheim

Explorers, entrepreneurs and engineers!
In the name of Arctic adventures, let us all unite!

Abstract

More and more people are attracted to go North. To design a fixed or a floating structure for Arctic conditions, to set operational limits or to specify certain safety requirements, one must rely on limited knowledge, data and experience. Several marine incidents have shown that absolute safety does not exist, including the holing and sinking of the cruise ship *Explorer* in 2007 and the holing of the tanker *Nordvik* in 2013. The concept of structural analysis in which the structure is allowed to deform inelastically due to rare and extreme actions (e.g., a collision with an ice mass) is of crucial importance in engineering. In the literature, this concept is often referred to as Accidental Limit State (ALS) design. With the ALS approach, adequate precautions against scenarios outside of ice class requirements can be established for both ships and offshore structures. Understanding ice behavior and structural performance during collisions allows us to develop predictive tools that form the core of design.

Although the topic of ice-mass collisions with structures is not new, the present study is one of a few to address the experimental aspects of ice-structure collisions in which the impacted structure undergoes irreversible deformation together with ice crushing. Inelastic behavior of ice and of steel panels has been studied in experimental tests and numerical simulations. This study is a continuation of research performed in the Department of Marine Technology at the Norwegian University of Science and Technology and is a component of a larger research project on the prediction of loads exerted by various types of ice (including icebergs) on floating structures.

This study provides an overview of existing methods for the analysis of ALS due to ice actions, including different ice failure/yield criteria that might be considered for ALS. It was acknowledged that ice behavior under rapid compressive loading is not fully understood and that there is a complete lack of direct, full-scale field measurements of ice forces on structures that deform plastically under ice actions. These facts served as motivation for carrying out three main types of experiments:

1. Small-scale indentation tests on confined and unconfined laboratory-grown freshwater granular and columnar S2 ice at temperatures of –10°C and –40°C. In these tests, the events that are observed in full- and medium-scale tests were reproduced with remarkable similarity.
2. Drop tests of ice blocks onto stiffened steel panels.
3. Laboratory impact tests of ice blocks onto stiffened panels in water. The tests were conducted at a scale approaching full-scale ice impact using laboratory-grown freshwater ice blocks and panels of varying rigidity.

The first set of tests served as a basis for validation of a constitutive ice model. The parameters of the model were measured in experiments that are independent of the tests

used to validate the accuracy of the ice model. To assess whether the model is applicable for describing ice crushing, the energy absorption from numerical simulations was compared with that found experimentally. This comparison showed that the model is, in fact, able to capture the energy absorption during ice crushing.

The results of the second and third sets of experiments were also used for validation of the ice model. The study indicated that both the plastic methods of analysis and numerical simulations could be used to assess damage to the structure due to ice actions. A comparison of the structural damages from laboratory tests and numerical simulations showed that the numerical simulations slightly overestimate the maximum damage, and the difference between the estimates increases for the tests conducted in water.

To improve the ice model, several modifications have been suggested and include the generalized version of a strain-based, pressure-dependent (or triaxiality-dependent) failure criterion, and a combination of a nonlinear finite element method and smooth particle hydrodynamics for modeling of the ice fragmentation and contact-pressure patterns. An interpretation of the model parameters was also suggested. An advantage of the ice model is that it is rather simple and does not require sophisticated tests for validation of the material parameters.

Preface

This thesis is submitted to the Norwegian University of Science and Technology (NTNU) for partial fulfillment of requirements for the degree of philosophiae doctor. This study was carried out primarily at the Department of Marine Technology, NTNU in Trondheim, Norway under the supervision of Prof. Jørgen Amdahl and Prof. Sveinung Løset. A portion of the studies (11 weeks) took place at the Thayer School of Engineering at Dartmouth, Hanover, USA under the supervision of Prof. Erland M. Schulson. The experimental studies presented in this thesis were supported by the Research Council of Norway through NTNU's Centre for Sustainable Arctic Marine and Coastal Technology (SAMCoT, Work Package 4), by the National Science Foundation of the United States through grants EAR-0911071 and EAR-071019 and by the European Community's Seventh Framework Programme through a grant to the budget of Integrating Activity HYDRALAB IV, Contract no. 261520 (FP7).

Acknowledgements

One day Jørgen Amdahl said to me when I asked what motivates him to wake up every morning: "I go to work and it works".

THANK YOU

Jørgen Amdahl and Sveinung Løset
(I must have done something right in my academic journey to deserve you as the guardians of this study)

Erland M. Schulson and Knut V. Høyland
(It was more than just collaboration, a jointly written manuscript or a discussion)

Karl N. Shkhinek
(You have done so many things for me, you helped me to gain strength and balance so I could start crawling toward the ice science)

Kaj A. Riska, Mauri Määttänen, Robert E. Gagnon, Ian J. Jordaan, Odd M. Faltinsen, Sören Ehlers, Marilena Greco, Narayana Golding, Martin Storheim, Rüdiger U.F. von Bock und Polach, Kari Kolari, Per Olav Moslet, Olga Shipilova and Ann-Johanne Bjørgen
(This thesis has benefited from your knowledge and expertise)

My husband Gurvinder
(More important than knowledge, you are always there for me)

My wonderful parents Elena, Alexander, Manjit Kaur and Jasbir Singh
(I was constantly surrounded with your love, care and support)

The one who is going to read this thesis
(I am connected to you)

Last but not least, I am grateful to all of my dear friends and colleagues at NTNU and elsewhere, in particular Sergiy B. Sukhorukov, Arun M. Kamath, Anton Kulyakthin, Wenjun Lu, Raed Lubbad, Fachri Panusunan Nasution, Maria Azucena Gutierrez Gonzalez, Marat Kashafutdinov, Sergey A. Kulyakhtin, Johan Wåhlin, Ivan Metrikin, Andrei Tsarau, Wolfgang Kampel, Zhenhui Liu, Ole-Christian Ekeberg, Torodd Skjerve Nord and Anna Pustogvar. All of you shared with me the memory, the fun, the moments…

Contents

ABSTRACT V

PREFACE VII

ACKNOWLEDGEMENTS IX

CONTENTS XI

NOMENCLATURE XV

ABBREVIATIONS XXIII

CHAPTER 1 1

INTRODUCTION 1

1.1 Background 1
1.2 Knowledge gaps and research needs 5
1.3 Objectives 5
1.4 Research design 6
1.5 Thesis organization 8

CHAPTER 2 11

STATE-OF-THE-ART KNOWLEDGE 11

2.1 How should rare ice actions be dealt with in design? 11
2.1.1 Methods and considerations in ALS design – a review 14
2.1.2 Summary 26
2.2 How should ice behavior during a collision be dealt with? 26
2.2.1 Review of failure and yield criteria 29
2.2.2 Applicability of failure and yield criteria 31
2.2.3 Evaluation of failure and yield criteria 33
2.2.4 Summary 36
2.3 What next? 37

CHAPTER 3 39

EXPERIMENTAL STUDIES 39

3.1 Small-scale indentation experiments 39
3.1.1 Experimental method 40
3.1.2 Results and analyses 45
3.1.3 Discussion of results 58

3.1.4 Summary 75
3.2 Angle-of-repose study on crushed ice particles 75
3.2.1 Experimental apparatus 76
3.2.2 Results and discussion 78
3.2.3 Summary 81
3.3 Drop tests of ice blocks on stiffened panels 82
3.3.1 Experimental apparatus 82
3.3.2 Results 89
3.3.3 Analysis and discussion 93
3.3.4 Discussion of uncertainties and limitations 100
3.3.5 Summary 104
3.4 Accidental collisions between an ice block and a floating structure 104
3.4.1 Experimental methodology 105
3.4.2 Data analysis and discussion 122
3.4.3 Summary 148
3.5 Concluding remarks 149

CHAPTER 4 151

NUMERICAL STUDIES 151
4.1 Design material model of ice 151
4.1.1 Model description 151
4.1.2 Model evaluation 155
4.1.3 Combined SPH and FEM 168
4.1.4 Engineering-scale model validation 172
4.2 Application example 175
4.3 Concluding remarks 178

CHAPTER 5 181

CONCLUSIONS AND SUGGESTIONS FOR FUTURE WORK 181
5.1 Conclusions 182
5.2 Summary of original contributions 183
5.3 Recommendations for future work 184

REFERENCES 187

APPENDIX 205
A. Analytical model of indentation 207
B. Yield surface. Parametric study 211
C. Estimation of ice pressure during impact 215
D. Nonlinear-finite element analysis. Uncertainty of ice material parameters ... 217

E. Crystallography of impacted ice..... 219

Nomenclature

SECTION 2.1

A	contact area
C, ex	coefficients
p	ice crushing pressure
t	time
x, y	spatial coordinates

SECTION 2.2

Indicial notation is used where necessary. Indices repeated twice in a term are summed (Einstein summation convention). For example

$$\boldsymbol{\sigma} \cdot \mathbf{A} \cdot \boldsymbol{\sigma} = \boldsymbol{\sigma}^T \mathbf{A} \boldsymbol{\sigma} = \sum_{i,j=1}^{6} A_{ij}\sigma_i\sigma_j = A_{ij}\sigma_i\sigma_j \,,$$

where first order tensors (column matrices) are denoted by lowercase boldface letters, such as $\boldsymbol{\sigma}$; a second-order tensor (a square matrix) is denoted by upper case boldface letters, such as $\mathbf{A}$. The transpose of a matrix is denoted by a superscript T. The components of $\boldsymbol{\sigma}$ and $\mathbf{A}$ are explicitly specified as σ_i and A_{ij}.

a, b, c	material parameters
A, B, C, D	material parameters
a_1, c_1, b_1	material parameters
F_{11}, G_{1111}	material parameters
G_{1122}, G_{1212}	material parameters
F_{ij}	components of a strength tensor $\mathbf{F}$
I_1	first invariant of a stress tensor
J_2	second invariant of the deviatoric stress tensor
p	hydrostatic pressure
P^*	ice melting pressure
q	equivalent stress
R_4	shear strength
R_t and R_c	uniaxial tensile and compressive strengths, respectively
T	temperature
T^*	yield stress in biaxial tension
Y, $\overline{\alpha}$, $\overline{\beta}$	material parameters

λ, P_c, q_{max}	material parameters
σ_1, σ_2, σ_3	principal stresses
σ_i, σ_j	components of a stress tensor rearranged into a six-component vector
σ_{ij}	components of a stress tensor
τ_i	octahedral shear stress

SECTION 3.1

A	contact area
A_c	design contact area
A_n	projected contact area
C, x	empirical coefficients
d	grain size
d_{ice}	ice grain diameter
d_{indr}	indenter diameter
d_{pen}	penetration depth
d_{smpl}	sample size (ice thickness)
$d_{smplwidth}$	width of ice sample
e	coefficient of restitution
E	Young's modulus
$E(u)$	energy
$F(u)$	force
F_A	corresponding factor for ice reinforced area in question
F_{max}	maximum load in Y direction
F_{max}^Z, F_{max}^X	maximum lateral forces in Z and X direction, respectively
h	depth of an impact crater
H	drop height
h_0, D_0	depth and diameter of an ice crater, respectively
m	projectile mass
N	number of measurements
$\bar{p}$, σ_p	mean value and standard deviation of indentation pressure
p	pressure
P	weight of a dropped object
p_f^a, p_f^b	failure pressures
$p_i(u_i)$	contact pressure at penetration depth u_i
R	confinement
r	radius of indenter
R^2	goodness-of-fit parameter; values closer to 1 indicate a better fit
t	time

T_i	ice temperature
$u_{\max}$	maximum penetration
v	indentation speed
ε	energy absorption capacity of ice during crushing
ρ	ice density
σ_1, σ_3	major and minor principal stress, respectively
σ_{ice}	nominal strength of ice

SECTION 3.2

d	particle size
d_{av}	average particle size
F_c	cohesive force between particles
F_n	external normal force
F_{tot}	total cohesive force
i, j	time-dependent coefficients
T	temperature
t	time

SECTION 3.3

A	contact area
c	empirical coefficient
E_{bc}	energy dissipated through flexibility of wooden supports
E_{cr}	energy dissipated within an ice block
E_{kin}	kinetic energy of an ice block before impact
$E_{platedef}$	energy dissipated in a steel structure
E_{rot}	energy dissipation due to rotation of an ice block
F	impact force
F_{bc}	peak force at wooden supports
G_s	energy required to create a new crack surface of unit area
l_i	vertical dimension of an ice block
m_i	mass of an ice block
p	contact pressure
p_{film}	measured pressure
r_{is}	radius of an ice particle
t	time
t_f	frame thickness

t_p	plate thickness
t_s	stiffener thickness
u	ice crushing distance
u_{bc}	vertical displacement of an impacted panel
V_{cr_total}	total crushed volume
v_i	initial velocity of ice
V_{is}	volume of an ice particle
σ	ice crushing strength

SECTION 3.4

a, a_1, c	distances in "Stiffener model"
a_0, a_1, a_2	material parameters of ice
A_i	hydrodynamic added mass of ice (surge motion)
A_s	hydrodynamic added mass of a structure (sway motion)
a_s	peak sway acceleration
B	Timco's empirical coefficient
b, b_1, b_2	widths of load patches
C, x	empirical constants
C_d	drag coefficient
E_{imp}	energy at impact
E_s, E_i	Young's modulus of steel and ice, respectively
F	impact load
F^D	towing force
G_i	total energy loss during ice crushing
G_s	kinetic energy difference
h	stiffener height
h_p	plastic hardening modulus
IW	internal work
K, n	strength and strain indexes, respectively in Alsos's material model for steel
L	frame spacing
m_i	ice mass
M_p	plastic bending moment
M_s	mass of a structure
p	pressure
p_c	critical pressure
Q_p	shear force
R_i	radius of a spherical ice mass

R_x, R_y, R_z	radii of gyration about x, y and z axes
s	stiffener spacing
s_{el}	characteristic element size
t_f	frame thickness
t_{impact}	impact duration
t_p	plate thickness
t_s	stiffener thickness
u	crushing distance
v	towing speed
v_c	common velocity
v_R	rolling linear speed
v_s	velocity of a structure
X_G, Y_G, Z_G	coordinates of the vertical center of gravity
Y	non-uniformity factor
$\dot{\varepsilon}$	strain rate
ε_0	initial ice failure-strain
ε_{plat}	yield plateau strain
ζ	vertical distance between the center of gravity and a collision point
θ, θ_1, θ_2	rotation angles of a beam
ν_s, ν_i	Poisson's ratio of steel and ice, respectively
ρ	density of water
ρ_s, ρ_i	density of steel and ice, respectively
σ_c	compressive strength of ice under uniaxial loading
σ_y	yield stress
σ_{Yd}	dynamic yield stress
$\dot{\omega}_x$	roll rate

SECTIONS 4.1–4.3

Tensor notation is used.

A	contact area
a_0, a_1, a_2	material parameters
c, s_1, γ	parameters of the Mie-Grüneisen equation of state in LS-DYNA
$\mathbf{C}e$	elastic stress-strain tensor
$\mathbf{e}$	deviatoric component of $\boldsymbol{\varepsilon}$
E	Young's modulus of ice
G	shear modulus of ice
J_2	second invariant of $\mathbf{s}$

K	bulk ice modulus
k	number of iterations
l_c	characteristic element length
m, n, b, c	empirical coefficients in the equation of energy absorption capacity of ice
n_1, n_2, n_3, n_4	material parameters
p	hydrostatic pressure
$p\mathbf{1}$	hydrostatic component of $\boldsymbol{\sigma}$
p_2	largest root of f(p, J_2)=0
$p_{cut\ off}$	material parameter
r	radius of an ice block
$\mathbf{s}$	deviatoric component of $\boldsymbol{\sigma}$
t	time
α^*	attack angle
α, β	ratios between principal stresses
$\boldsymbol{\varepsilon}$	strain tensor
ε_0, M, N	dimensionless material parameters
$\boldsymbol{\varepsilon}^{el}$, $\boldsymbol{\varepsilon}^{pl}$	elastic and plastic components of $\boldsymbol{\varepsilon}$
ε_f	failure strain
$\varepsilon_m\mathbf{1}$	hydrostatic component of $\boldsymbol{\varepsilon}$
$\varepsilon^p{}_{eq}$	equivalent plastic strain
μ	dynamic viscosity coefficient
μ_s	static friction coefficient in LS-DYNA
ν	Poisson's ratio of ice
$\boldsymbol{\sigma}$	Cauchy stress tensor
σ^*	degree of stress triaxiality
σ_c, σ_t	uniaxial compressive and tensile strengths, respectively
$\boldsymbol{\sigma}_j$	Cauchy stress tensor at time j
τ	shear strength

APPENDIX A

F	force
R	radius of indenter
s	arc length
u	penetration distance
$y(x)$	shape function
Γ	splitting energy per unit area
ε	specific energy absorption

λ	scale factor (assuming the ratio of all corresponding linear dimensions in a model and prototype are equal).
μ	coefficient of static friction
ρ	density
σ and σ_c	normal pressure (stress)
τ	friction force per unit area due to sliding
Ψ	energy

Superscripts p and m denote prototype and model, respectively.

APPENDIX B

Components of a stress tensor $\boldsymbol{\sigma}$ are arranged into a 3×3 matrix which is replaced by a six-component vector σ_i. Indicial notation is used.

A_i and A_{ij}	interactive strength terms, components of strength tensors $\mathbf{A}^*$ and $\mathbf{A}$
a_0, a_1, a_2	material constants
J_2	second invariant of the deviatoric stress tensor
p	hydrostatic pressure
p^*	ice melting pressure
T	temperature
σ_c	uniaxial compressive strength
σ_t	uniaxial tensile strength
τ	shear strength

APPENDIX C

A	contact area (projected area)
C, x	empirical constants
p	average pressure over the contact area
r_i	radius of an ice block
u	crushing distance

APPENDIX D

E_i	elasticity modulus of ice
J_2	second invariant of the deviatoric stress tensor
p	hydrostatic pressure

p_c	cutoff pressure
R_i	radius of ice sphere
R^2	goodness-of-fit parameter
ε_0	initial failure strain
ε_{eff}^{p}	effective plastic strain

Abbreviations

AL	Abnormal Level
ALIE	Abnormal-Level Ice Event
ALS	Accidental Limit State
AMSA	Arctic Marine Shipping Assessment
AOR	Angle of Repose
BC	Before Christ
CCGS	Canadian Coast Guard Ship
CPU	Central Processing Unit
CSA	Canadian Standards Association
DEM	Discrete Element Method
DMU	Dynamic Motion Unit
DNV	Det Norske Veritas
EL	Extreme Level
ELIE	Extreme-Level Ice Event
ESA	European Space Agency
FE	Finite Element
FEM	Finite Element Method
FLS	Fatigue Limit State
FPF	Fuji Prescale Film
FPSO	Floating Production, Storage and Offloading
FS	Failure Surface
GD	Global Displacement
HPZ	High Pressure Zone
HSV	High Speed Video
ISO	International Organization for Standardization
LC	Load Cell
MATS	Multiaxial Testing System
NRC	National Research Council
NTNU	Norwegian University of Science and Technology
PCL	Progressive Collapse
PMMA	Polymethyl Methacrylate
PS	Pressure Sensor
RAM	Random Access Memory
RMS	Royal Mail Steamer (Ship)
RP	Recommended Practice
SEA	Specific Energy Absorption

SLS	Serviceability Limit State
SPH	Smooth Particle Hydrodynamics
S4R	Four-node shell element with reduced integration
ULS	Ultimate Limit State
USA	United States of America
YS	Yield Surface
1GS, 2GS and 3GS	First-Generation Criteria, Second-Generation Criteria and Third-Generation Criteria, respectively

Chapter 1

Introduction

> "In 1580, about the time that John Davis was seeking a way to the Pacific from the east, the Russians in Europe began their march to the same objective from the opposite direction."
>
> L.H. Neatby, 1958
> "In Quest of the Northwest Passage"

This thesis is a noteworthy adventure story of an indefatigable fellow's attempt to advance human knowledge on the coupled behavior of an ice mass and a structure during accidental collisions through experimental and numerical studies at different scales. This story tells of ice and steel structures, intriguing observations, brave theories and great ice-structure impacts (and indentations).

1.1 BACKGROUND

Recent developments in the Arctic regions and climatic changes have led to increased offshore activities and marine transportations in the North. "Never before have so many vessels taken the Arctic shortcut between Europe and Asia, and never before has so much cargo been transported along the route", writes Barents Observer in 2012 (Pettersen, 2012). What have we learnt from this long history of exploration and exploitation of the North?

There was a time when marine transport in the North was driven by man's will to explore a region that was described by Herodotus, 4.28 as "so exceedingly severe in climate, that for eight months of the year there is frost so hard as to be intolerable; and during these if you pour out water you will not be able to make mud, but only if you kindle a fire can you make it; and the sea is frozen…". Among the first explorers of the North were Pytheas of Massalia (4th century BC); Gardar Svavarsson, Floke Vilgerdsson and Ohthere of Hålogaland (9th century); and Eirik Thorvaldsson, Eirik Haraldsson and Harald Eiriksson Gråfell (10th century) (Magidovich and Magidovich, 1982; Cunliffe, 2002; Johannessen et al., 2007 and AMSA, 2009).

From the late 14th century onwards, the term Arctic (from the Greek word *arktos*) was used to define the region of the North (Online Etymology Dictionary, 2013). By the 16th century, most educated Western Europeans accepted the viewpoint expressed by Ancient Greeks that the earth was spherical. However, virtually everyone believed

that the world was restricted to the temperate regions of Europe, Asia and North Africa. As Small (2007) stated, "in ancient Greek geography, the north was regarded as a liminal region; a frame for the rest of the continent…" This frame exhibited the following primary features: (i) an outer circumambient Ocean; (ii) an extensive band of uninhabitable frozen wetlands and (iii) an inner region of extreme climate that bordered on the known world. One of the ancient descriptions of the northern seas that dates back to the 4th century BC is given by Strabo, 2.4.1:

> Those parts where neither earth still existed by itself, nor sea nor air, but a mixture of these things like a marine lung [*πλεύμονι θαλαττίῳ,* most likely referring to sludge ice and drifting ice floes, or to the thick sea fog] in which the earth and the sea and all things are suspended and this lung is, as it were, a fetter of everything, and is neither passable nor navigable (Cunliffe, 2002 and Small, 2007).

Currently, the Arctic is understood to be the northern part of the Earth, the area encompassed by the Arctic Circle at latitude 66° 33'N. "Ice" is mostly understood to be frozen water. Planetary scientists use the term "ice" to refer to solid hydrates of the most basic elements: oxygen, carbon and nitrogen and combinations of these elements. Ices are found in numerous locations in the universe and are considered to be some of the most abundant materials of the cosmos (Fundamentals of Planetary Materials, 2013). In this thesis, the word "ice" refers to frozen water in the Ih form, i.e., hexagonal ice.

Throughout the centuries in the Northern regions, efforts have been directed toward obtaining a better understanding of ice behavior and the development of engineering solutions to prevent damage to structures. These efforts have mainly been driven by economic interests, including searches for food and suppliers (e.g., searches for new transport corridors and trading contacts, the extension of navigational seasons, river and flood control and the exploration and exploitation of hydrocarbons and minerals). There have been many notable Arctic voyages from the late 15th century until recently, including the planting of a flag on the seabed below the North Pole in 2007. Figure 1 is an artist's rendering of a "battle" for territory and resources in the High North.

By the 19th century, there was an unprecedented increase in interest in the Arctic regions. Canada, the United States, Russia and Norway extended their economic activities to areas with low temperatures, darkness and ice. Wooden hulls were replaced by steel hull structures, and sails were replaced by steam engines. Ashton (1986) has noted that ice engineering originated as a discipline in the 19th century in response to the demand for engineering solutions to control the ice. In those days, little was known about the nature of different ice features or about the actions of these features on engineering structures. On April 15th, 1912, the RMS "Titanic" hit an iceberg and sank, causing 1513 persons to lose their lives (Zubov, 1963). Korzhavin (2002) has given examples of structural damage caused by ice. These examples include the following: (i)

the destruction of old spillway crib dams on the Mushingum River, Ohio from ice passage in 1852; (ii) repeated damage to the Columbia crib dam in Pennsylvania in 1857, 1865, 1873 and 1875; (iii) the destruction of the bridge across the Swatora-Creek River in 1910; (iv) damage to the crib pier of the docks in Siberia during the Spring of 1948; and (v) the damage to the bridge support in a river in China in 1955. Between 1619 and 2004, approximately 670 incidents of ships striking icebergs, growlers and bergy bits occurred (Hill, 2005), including the disaster of 1830 described by Neatby (1958) when pack ice had crushed an entire convoy of whalers against the shore ice and grounded 19 ships to matchwood. In 1986, one century later, ice actions on the Molikpaq platform put the bottom-founded caisson structure at severe risk (Jefferies and Wright, 1988). Not long ago, on the Northern Sea Route, an ice floe breached off one of the port-side ballast tanks of the tanker Nordvik loaded with diesel fuel.

Figure 1: Political cartoon by Kevin Kallaugher (reproduced from "The Economist", 18 August 2007).

From the 19th century until the present, ice has continued to be a subject of engineering interest. It is difficult, or perhaps impossible, to say either when ice science began or who pioneered the development of ice research. There was a period over which research on ice was driven by the development of ice-going ships and icebreakers. For example, Runeberg (1889) has described different ice formations that are hazardous to ships and estimated the ice-breaking capacity of steam-ships using analytical approximations. Ice observations and studies have also been conducted during exploratory expeditions; see, e.g., Pettersson (1883), Makarov (1901), Nansen (1905).

There was a period over which studies on the mechanical properties of ice were motivated by the construction of ice-crossings, aerodromes (Zubov, 1963), bridges and dams.

From approximately 1960 through the 1980s, the major developments in ice engineering were primarily motivated by exploratory drilling for oil and gas in the Canadian Arctic and along the Coast of Alaska. When oil prices crashed in the mid-1980s (Gately et al., 1986), interest in Arctic development plummeted. In the late 1990s and early 2000s, global demand for hydrocarbons, the development of improved drilling technologies (and production techniques) and debates on climate change produced a new spike in Arctic research.

Over the past five decades, scientists and engineers have maintained a continuous interest in understanding the local and global ice loads arising from ice-structure interactions. Arctic shipping scenarios (e.g., ECON, 2007 and Smith and Stephenson, 2013) forecast the opening of new shipping lines and an increase in marine transportation in the North. The cumulative knowledge and expertise on ice and its effect on engineering structures can be found in books by Zubov (1963), Pounder (1965), Hobbs (1974), Michel (1978), Ashton (1986), Cammaert and Muggeridge (1988), Sanderson (1988), Smirnov (1996), Petrenko and Whitworth (1999), Wadhams (2000), Korzhavin (2002), Leppäranta (2005), Vershinin et al. (2005), Løset et al. (2006), Gudmestad et al. (2007), Vershinin et al. (2008), Schulson and Duval (2009), Eicken et al. (2009), Weeks (2010) and Palmer and Croasdale (2013). The field of ice research is dynamic and rapidly evolving. I apologize to those authors whose work I have overlooked.

One of the fundamental problems still encountered in ice engineering is the determination of ice actions and the corresponding action effects on ships (i.e., shuttle tankers, cruise ships and offshore supply vessels) and offshore structures (i.e., stationary installations and FPSO units) from different types of ice features (i.e., ice ridges, glacial ice masses, isolated ice floes). Ice engineering has not been developed to the point where design standards can be firmly established from analytical considerations. The European Space Agency website (ESA, 2013) stated that "ice information is required by a wide spectrum of users operating at high latitudes. These include fishing activities in areas such as the Barents Sea and waters around Svalbard, and merchant vessels on-route through ice-infested regions in the Baltic or the Canadian, Alaskan and European Arctic…" The analysis of ice-structure interaction has been hampered by the complex ice behavior, the presence of waves and the complex geometry of bodies in contact. "No single constitutive model currently in use is able to represent the response of ice in any practical situation", stated Vinogradov in 1987. Recent progress in fracture mechanics, high performance computing, modern instrumentation methods and techniques have supplied new momentum to the development of this field.

1.2 Knowledge gaps and research needs

The fundamental problems in ice engineering in the 21st century can be broken down into several research questions ranging from theoretical to practical in nature. Some examples are given below.

(a) What are the mechanisms that occur during ice-structure interactions?
(b) How do different mechanisms contribute to global (and local) ice loads on structures (ships, offshore and hydraulic structures, bridges, etc.)?
(c) How can ice loads at different scales be estimated?
(d) How to design a structure against various ice actions?
(e) For specified environmental conditions, how should a cost-effective design be performed?

This list is by no means complete.

1.3 Objectives

The primary objective of this doctoral study is to advance the understanding of rare, extreme ice loads on structures (including the structural response to ice loads) by addressing the coupled behavior of an ice mass and a structure during an accidental collision (i.e., an impact event). A more detailed description of the "accidental collision" concept and the term "coupled behavior" is provided in the next chapter.

The secondary objectives of this thesis are as follows:

(a) To specifically address the behavior and modeling of ice during an impact event and increase the understanding of the physical processes that occur during an ice-structure impact. In particular, the aim is to establish test methods and obtain experimental data for ice under high strain rate conditions (10^{-3} –10 s^{-1}) and in multiaxial stress states.

(b) To evaluate existing empirical, analytical, phenomenological and analogical models (or constitutive theories of ice) that are available in the literature.

(c) To improve, further develop and verify the material model for ice of glacial origin under a rapidly applied stress. In particular, such development should be based on existing models and further validation (or calibration) of the model should be manageable. Ice fracture has to be taken into consideration. It is necessary to understand how state-of-the-art fracture modeling techniques (e.g., the element deletion technique; the cohesive element

technique for dynamic crack propagation and the SPH/FEM coupling technique) could be put to the most use.

(d) To advance our knowledge on the importance of accounting for ice-structure interactions in the damage assessment of structures under rare and extreme ice actions.

1.4 Research design

This study is a follow-up to a previous study on iceberg collisions with ship-shaped structures that was conducted in the Department of Marine Technology. In the current work, the focus was on the further development of a finite element model formulated by Liu (2011) to simulate iceberg-structure collision scenarios and predict ship hull damage. It was highly desirable to obtain full-scale data to test theories and to validate the numerical model; however, the accuracy of the experiments had to be balanced against the total cost. In this study, a multi-disciplinary approach consisting of experimental research was used in conjunction with information obtained from knowledge in numerical modeling. We performed experiments both at Dartmouth's Ice Research Laboratory, USA and at the Aalto Ice Basin, Finland to study ice behavior under rapidly applied stresses at small scales and the coupled behavior of ice masses and a floating structure during collision at medium scales, respectively.

To characterize the behavior of ice under multiaxial stress states, small-scale laboratory indentation experiments were performed on freshwater granular and columnar S2 ice. The primary focus was placed on freshwater granular ice because its behavior resembles ice of glacial origin (i.e., icebergs, bergy bits, growlers). The mechanical behavior of sea ice and freshwater columnar ice was beyond the scope of this work.

An extensive literature review of methods available for the design against rare, extreme (abnormal) ice actions and a review (and evaluation) of the ice failure/yield criteria are presented in the next chapter. The literature review revealed that little scientific attention has been paid to the problems in which both the ice and the structure undergo severe deformations during ice-structure collision events. The available full-scale data have been mostly obtained from experiments in which the impacted structure remained intact during the tests. Most experimental ice loads are measured on flat or convex contact surfaces. If the structure was allowed to deform, the contact surface would no longer be flat. The structure may become concave and encompass the ice. It is uncertain whether such experimental data should be used for scenarios in which the structure may be damaged by ice actions.

A series of laboratory tests was performed at the Norwegian University of Science and Technology, Norway and the Aalto University of Technology, Finland. The aim

was to obtain data to develop and verify existing analytical models for analysis of full-scale collisions between ice-masses and steel structures, and to build expertize in modelling accidental collisions under laboratory conditions.

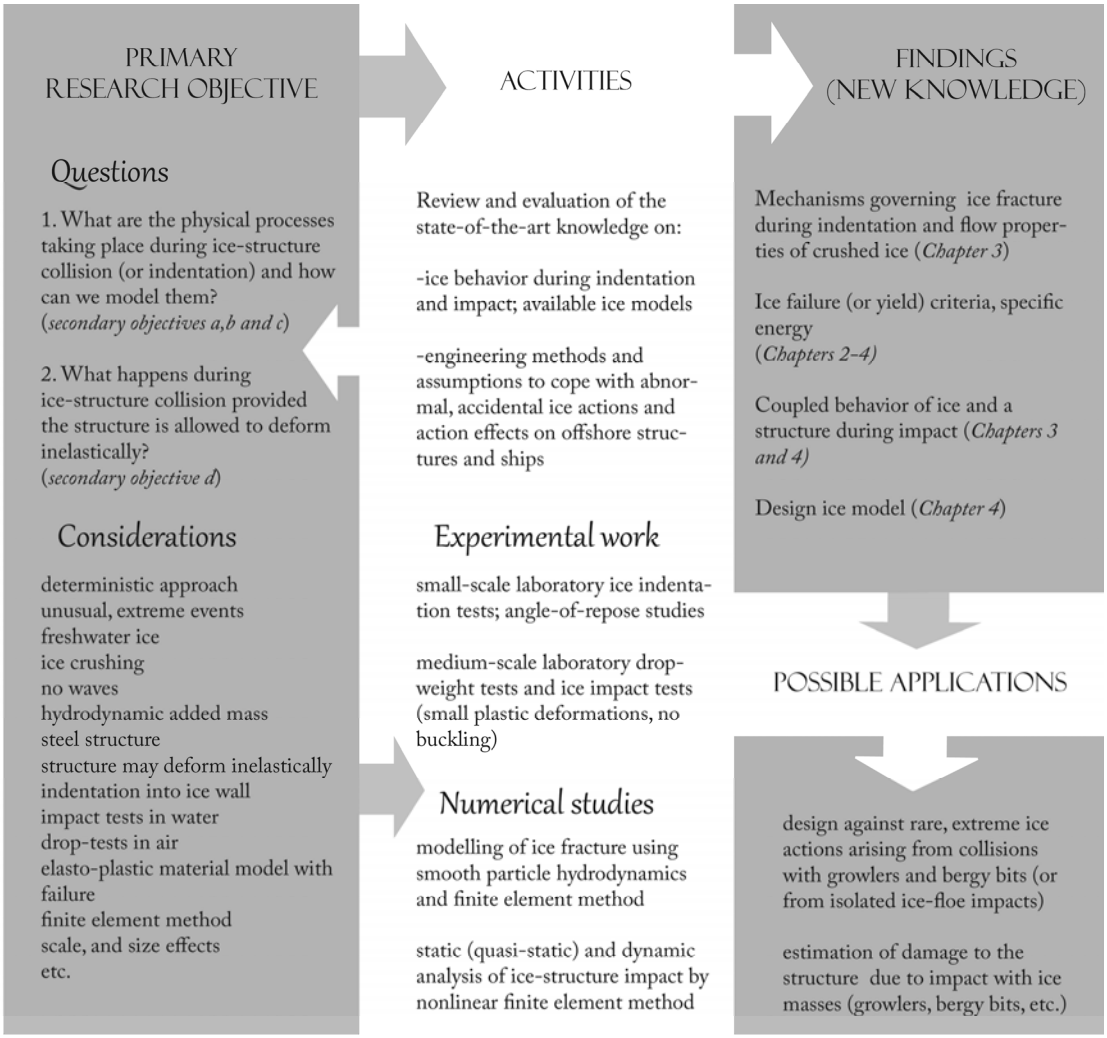

Figure 2: Structure of the research process.

A finite element model developed by Liu (2011) was used to predict structural deformations following an ice impact. Good agreement was obtained between the model predictions and the experimental data; however, the numerical model suffered from shortcomings such as an unrealistic representation of the contact area throughout the collision and the manageability of the ice material properties, in particular the ice failure criteria. Experience shows that the choice of input parameters is transparent if a constitutive model is based on ice physics. It was decided to re-examine the experimental data obtained for freshwater and iceberg ice at different scales. The intention was to determine whether the specific energy absorption during the ice crushing process could be considered as scale-independent. If the specific energy of ice

is scale-independent, it may be used as a criterion for the validation (or verification) of numerical models.

In this study, medium-scale experiments of ice-structure collisions and numerical simulations were limited to cases involving isolated ice floes, growlers and bergy bits, for which ice crushing is the principal failure mechanism. Aspects of high-energy collisions between a structure and large or medium icebergs are not addressed in this thesis.

Figure 2 shows the connections between the research objectives, including the questions addressed, the research activities and the major findings. Figure 3 is a schematic in which the different activities within the doctoral study are connected to each other.

1.5 Thesis organization

This monograph is organized into five separate, yet interrelated chapters. *Chapter 1* (the present chapter) provides a brief historical description of the origins of ice engineering, and the research objectives and motivation for this study. In *Chapter 2*, an introduction to rare and extreme ice loads is presented, including an overview of the existing methods for prediction of ice actions and the corresponding action effects on ships and offshore structures, with a suitable emphasis on state-of-the-art ice material models. In Chapter 2, the fundamental concepts needed to understand the subsequent material in the thesis are explained. *Chapter 3* describes experimental procedures and presents the results of experiments carried out in the United States, Norway and Finland at two different scales. The experiments were designed to simulate ice/structure behavior under fast compressive loading during indentation and impact. The types of experiments are summarized below.

(a) Small-scale indentation tests were conducted on confined and unconfined laboratory-grown freshwater granular and columnar S2 ice at temperatures of –10°C and –40°C, in which events observed at full and medium scales were reproduced with remarkable accuracy.
(b) An angle-of-repose (AOR) study was performed on crushed ice particles of different sizes to better understand the behavior of powdered ice extruded during indentation.
(c) Drop tests were performed in air, in which an ice block was dropped onto a stiffened panel.
(d) Laboratory-scale ice mass/stiffened panel impact tests were carried out in water on structures of varying rigidity with ice masses at a scale approaching full-scale ice impact.

In Chapter 3, the uncertainties and limitations of the experimental results are also discussed. *Chapter 4* is dedicated to numerical studies. The contents of this chapter are

original and have not been published elsewhere. The chapter describes the nonlinear finite element analysis of ice collisions with a rigid plate and steel flexible plates. In this chapter, a new scheme for modeling ice fracture is introduced that could be used in engineering applications, such as the analysis of collisions between ice-masses (e.g., small glacial ice masses) and a ship-side structure.

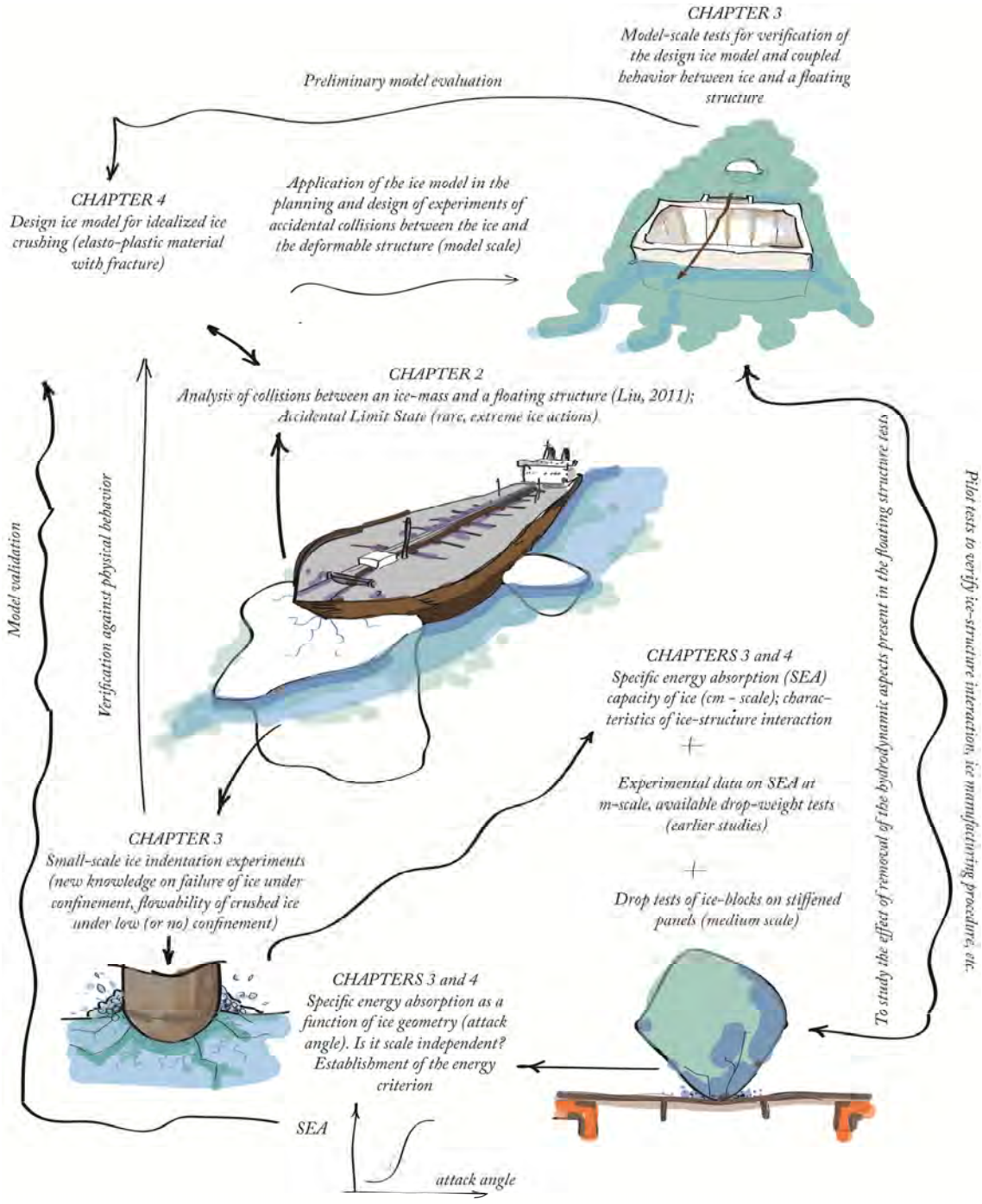

Figure 3: Diagram showing the objective-related activities of the doctoral study, including the connections between these activities.

The numerical simulations in Chapter 4 are carried out as explicit analyses in the finite element code LS-DYNA. In *Chapter 5*, the doctoral study is summarized, final conclusions are drawn and suggestions are presented for future research.

.

Chapter 2

State-of-the-art knowledge

> Idea is like a toothbrush... "Everyone wants a toothbrush, everyone needs one, everyone has one, but no one wants to use anyone else's"
>
> D. Ariely, 2011
> "The Upside of Irrationality"

This chapter provides an overview of state-of-the-art knowledge on ice actions that arise from collisions with rare and extreme ice-masses. A review of state-of-the-art ice models that can be used for iceberg impact simulations is also presented. Section 2.1 delivers a review of existing methods for predicting structural damage due to collisions between ice masses and ships (or offshore structures). Section 2.2 evaluates the existing ice failure/yield criteria with respect to the physical plausibility of the material constants and manageability of their calibration.

In this chapter, an explanation of the fundamental concepts, needed to understand the subsequent material in the thesis, is included. The terms "rare, extreme ice actions" or "abnormal, accidental ice actions" are used to define the external loads exerted by ice on a structure once in 10000 years.

2.1 How should rare ice actions be dealt with in design?

In structural design, design checks are often referenced to a *limit state*. In this context, the "limit state" is a condition of a structure (or a structural member) beyond which the structure (or a structural member) no longer fulfils the relevant design criteria and is considered to be unsafe. The limit state is an important concept in evaluating hazards that originate from external loads exerted on the structure. Limit states are usually classified into four categories: the *ultimate limit state* (ULS), the *serviceability limit state* (SLS), the *fatigue limit state* (FLS) and the *accidental limit state* (ALS) or the progressive collapse limit (PCL). The ULS corresponds to conditions that terminate future use of the structure. The SLS corresponds to conditions that pose restrictions on normal use and occupancy of the structure. The FLS corresponds to the reduction of the ultimate strength of the structure (or a structural member) due to repetitive loads. The ALS (or PCL) typically corresponds to a progressive collapse of the structure when subjected to unusual, extreme action effects. Moan (2009) has noted that the requirements for dealing with a progressive structural collapse emerged in the early 1970s following the partial progressive collapse of Ronan Point Apartment Tower in London on May 16,

1968, which was caused by a gas explosion. Further information on the history of the ALS concept has been compiled by Moan (2009). The design guidance document DNV-RP-C204 states that "the overall goal for the design of the structure against accidental loads is to prevent an incident to develop into an accident disproportional to the original cause". In ALS design, two conditions are usually considered in the order given below.

a. The *ALS condition*, which corresponds to the structure during the accidental event: the ability of the structure to resist accidental (abnormal) events is investigated, and the structure may be damaged because of an accidental event.
b. The *post-ALS* (or damaged) *condition*: the structural resistance to overturning or progressive collapse is analyzed in the damaged condition under exposure to environmental actions with a certain return period.

The report of the 18th International Ships and Offshore Structures Congress (ISSC) expert committee on Arctic technology (Fricke and Bronsart, 2012) provides an overview of the design guidance and rules for ships and offshore structures operating in the Arctic. The rules and regulations for ice-going ships have been in existence longer than those for Arctic structures. After numerous years of experience, questionable models and assumptions for assessment of ice actions and the effects of these actions on ships have been compensated for via various adjustment factors. Kujala and Ehlers (2013) have noted that all current ice class rules accept some amount of plastic deformations as the design limit states; however, this amount is not clearly defined. In some cases, ship rules are adjusted based on the amount of ice damage versus the cost of reinforcement, see, e.g., Riska and Kämäräinen (2011).

Expertize in designing offshore structures for the Arctic and Northern regions is limited to a few "one-of-a-kind" structures. The use of ship rules (or design methodologies) in the design of non-ship-shaped structures is non-trivial. The new international standard ISO 19906 "Petroleum and natural gas industries – Arctic offshore structures" uses the limit state design methodology. Note that there are significant uncertainties in the characterization of ice parameters (i.e., the geometry of the ice feature and the ice physics), which are independent of the design approach (ULS, SLS, FLS or ALS). *In this study, the focus was placed on the ALS condition.*

It is important to emphasize the difference between the ULS and ALS approaches. In the ULS approach, design verification is based on elastic response or limited plastic deformations of the structure, whereas severe nonlinear behavior of the structural components (large deformations) is addressed in the ALS approach. The difference between the ALS and ULS approaches is illustrated in Figure 4 for an ice-structure collision.

For structures operating in ice-infested waters, the ALS may be triggered by rare, abnormal ice actions, such as from loads arising from collision with icebergs (or multiyear ice ridges, bergy bits, growlers and thick isolated floes of rafted ice) and corresponding to a 10000-year event.

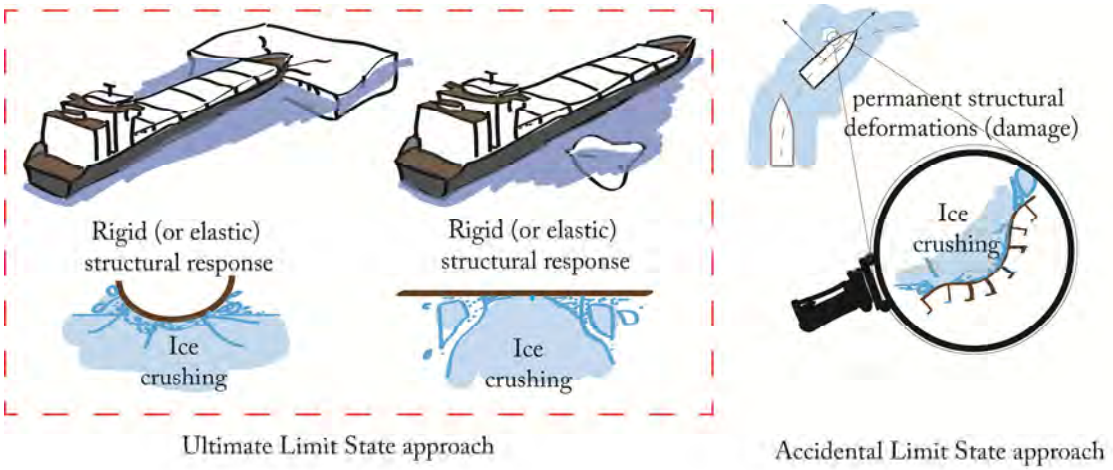

Figure 4: Difference between ULS and ALS approaches for an ice-structure collision scenario.

Three design principles may be applied to enable structures to resist unusual, extreme ice actions from collisions with ice-masses: *strength design*, *ductile design* and *shared energy design* (see Figure 5). One may draw an analogy between Figure 5 and Figure A.3-1 in NORSOK N-004 (2004).

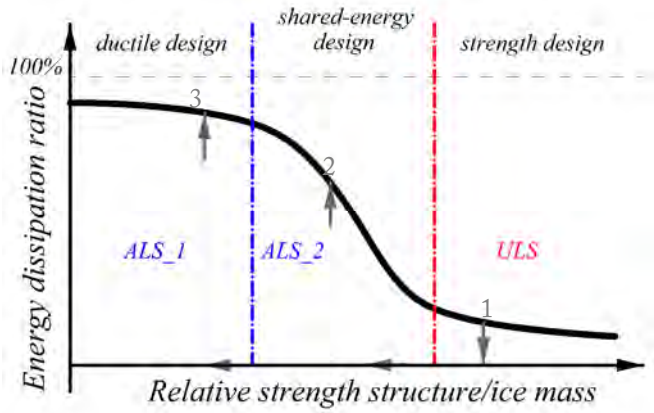

Figure 5: Characterization of design principles depending on the distribution of energy dissipation in the ice mass and the structure.

Strength design assumes that the ice will dissipate most of the collision energy and that the structure will undergo small plastic deformations. This assumption is virtually identical to the ULS considerations and leads to overly conservative and costly designs in most cases for a 10000-year event.

Ductile design assumes that all of the collision energy is dissipated by the structure. Structures properly designed according to ULS principles (actions with a return period

of 100 years) exhibit relative strength similar to the lower bound for strength design as indicated in Figure 5 by the dashed red vertical line (the farthest right dashed line). When structures are subjected to actions with a return period of 10000 years, the larger ice strength will move the design point to smaller values on the *x*-axis and may cause the structure to respond according to ductile design principles (i.e., the structure dissipates most of energy, as indicated by the ALS_1 label). If the collision energy is dissipated with moderate damage to the structure (e.g., no penetration of cargo tanks or buoyancy compartments essential for hydrostatic stability) and satisfactory residual strength, the ALS acceptance criteria may be satisfied. In this type of design, the shape of the ice feature is a consideration because it is easy to select an ice shape that does not comply with the ALS acceptance criteria.

Shared energy design implies that both the ice and the structure undergo significant deformations and dissipate energy. At any instant, the weaker structure (or ice) will deform. In practice, the actual relative strength of ice with return periods of 10000 years and 100 years causes sheared-energy design to be a likely response mode for ice collisions, as indicated by the ALS_2 label. This design is the most demanding of the three design types because the response of both the ice and the structure are considered.

To demonstrate the relevance of the design principles in Figure 5, consider the following example. The structure designed according to ULS principles must be classified in the strength domain (see label "1" in Figure 5). The ice strength corresponding to ALS increases and may push the relative strength between the structure and the ice feature into the ALS_2 region (see label "2" in Figure 5). Additionally, the structural strength may be reduced because a growler may strike areas outside the ice-reinforced region. The additional reduction of strength moves the relative strength value further left into the ALS_1 region (see label "3" in Figure 5).

Independent of the design principle, the major uncertainties result from the characterization of the ice properties and the assumptions made for the local and global ice shape.

2.1.1 Methods and considerations in ALS design – a review

The review presented in this section is limited to the methods for analysis of ALS due to ice actions only. I have attempted to generalize the available data for analysis of ALS due to ice actions. The aim was to review existing deterministic methods that utilize the limit energy approach (i.e., the kinetic energy of the ice feature/structure limits the ice action). The review did not address design criteria or how a representative abnormal ice

event should be chosen. Studies on the design of ice platforms (ice islands) were omitted.

All the methods may be divided into three main categories: *analytical methods*, *numerical methods* and *empirical methods*.

ALS in ISO 19906

ISO 19906 Arctic Offshore Structures is the most recently published standard. For structures in Arctic and cold regions, ISO 19906 requires a design based on both Extreme-Level (EL) and Abnormal-Level events (AL), which include ice actions arising from Extreme-Level Ice Events (ELIE) and Abnormal-Level Ice Events (ALIE). Climate change considerations are recommended. ISO 19906 refers to ALS as abnormal (accidental) limit state and requires structures to be designed for adequate reserve capacity and energy dissipation capability to achieve ALS. The ALS design condition for ice should consider ALIE. Local and global actions must be considered. Icebergs and ice island impact-events, with annual probability of occurrence between 10^{-5} and 10^{-3} with high consequences, are recommended for consideration as ALIE to ensure adequate reliability of the structure.

Non-linear methods may be used for the analysis of ALS. For ALS, some structural damage is allowed. Provisions in ISO 19906 state that components are allowed to behave inelastically (i.e., design resistance may be exceeded) if there is sufficient ductility and if the overall structural design is robust and provides alternative load paths to distribute and resist the action effects and dissipate the energy. The design is based on a combination of static reserve strength, ductility and energy dissipation to resist ALIE conditions. Damaged stability calculations must include the effect of ice accumulation. The expected effects of icing must also be considered in ALIE analysis. Action combinations for each environmental action must be derived by considering each EL and AL representative value of the action in turn, as the principal action. Principal AL actions arising from large icebergs or isolated ice features must be accompanied by companion EL actions such as actions from wind, wind-driven currents, tidal and background currents, waves and swells.

Confirmation that the ice failure process is modelled correctly should also be performed in any model test programme. Local ice actions must also be based on relevant full-scale measurements or established theoretical methods. In ISO 19906, the list of relevant limit energy full-scale global ice data is provided. As mentioned in ISO 19906, most of the relevant field data were obtained from experiments with relatively small ice features (hundreds to several thousand tons). The data were obtained from experiments in which the impacted structure remained intact during the tests. The majority of experimental data are measured for flat or convex contact surfaces. It is

difficult to use these data for ALS scenarios in which the structure may be damaged due to ice actions.

For example, the accidental situations for floating structures must be addressed in accordance with the provisions in ISO 19904-1 in which accidental actions from ice are not considered.

Depending on the assumptions made for analysis of ALS, the results may depend on the shape, orientation and profiles of the iceberg. No clear recommendations regarding the choice of iceberg shapes are provided in ISO 19906. However, the design contact area must be based on the local structural configuration; the size and location of the local contact areas must be selected to ensure that the most critical cases are addressed.

ALS in the literature

The literature review showed that the assumptions of analytical methods for the ALS due to ice actions can be classified into eight basic categories: methodology, scenario, contact geometry, action effect, limit-energy approach, problem size, analysis of structural deformations, ice action (see Figure 6). The figure addresses only methods that can be used to investigate the ability of the structure to resist accidental (abnormal) ice events. In the literature, deterministic methods received more attention than probabilistic approaches. For example, Fuglem et al. (1991 and 1999) presented a probabilistic method for estimating global iceberg collision loads for offshore structures. Fuglem et al. (1991) analyzed spherical icebergs impacting a vertical column, and eccentricity was not considered. The maximum force during a collision was determined using a two-step procedure. First, the maximum penetration and contact area were estimated based on the average ice-crushing pressure. Second, the contact area from step one was multiplied by the peak pressure chosen randomly from a distribution derived from medium-scale indentation tests.

Jordaan et al. (1993) proposed a probabilistic method based on the maximum pressure of a given event (or the event-maximum method) to model local ice pressures.

Taylor et al. (2010) focused on the estimation of local ice pressures from ship-ice interaction data. The authors described a methodology that can be used to estimate local ice pressures corresponding to a given exceedance probability. The authors provided also expressions to account for the effects of exposure, the frequency of ice impacts, the interaction duration and the position of the panel on the structure.

Assumptions of the action effect

When designing a structure, assumptions made for the analysis of ALS (Figure 6) should be consistent with the likely consequences of the accidental event (ALIE) considered. According to Nessim et al. (1984), for a floating structure these consequences could include the following:

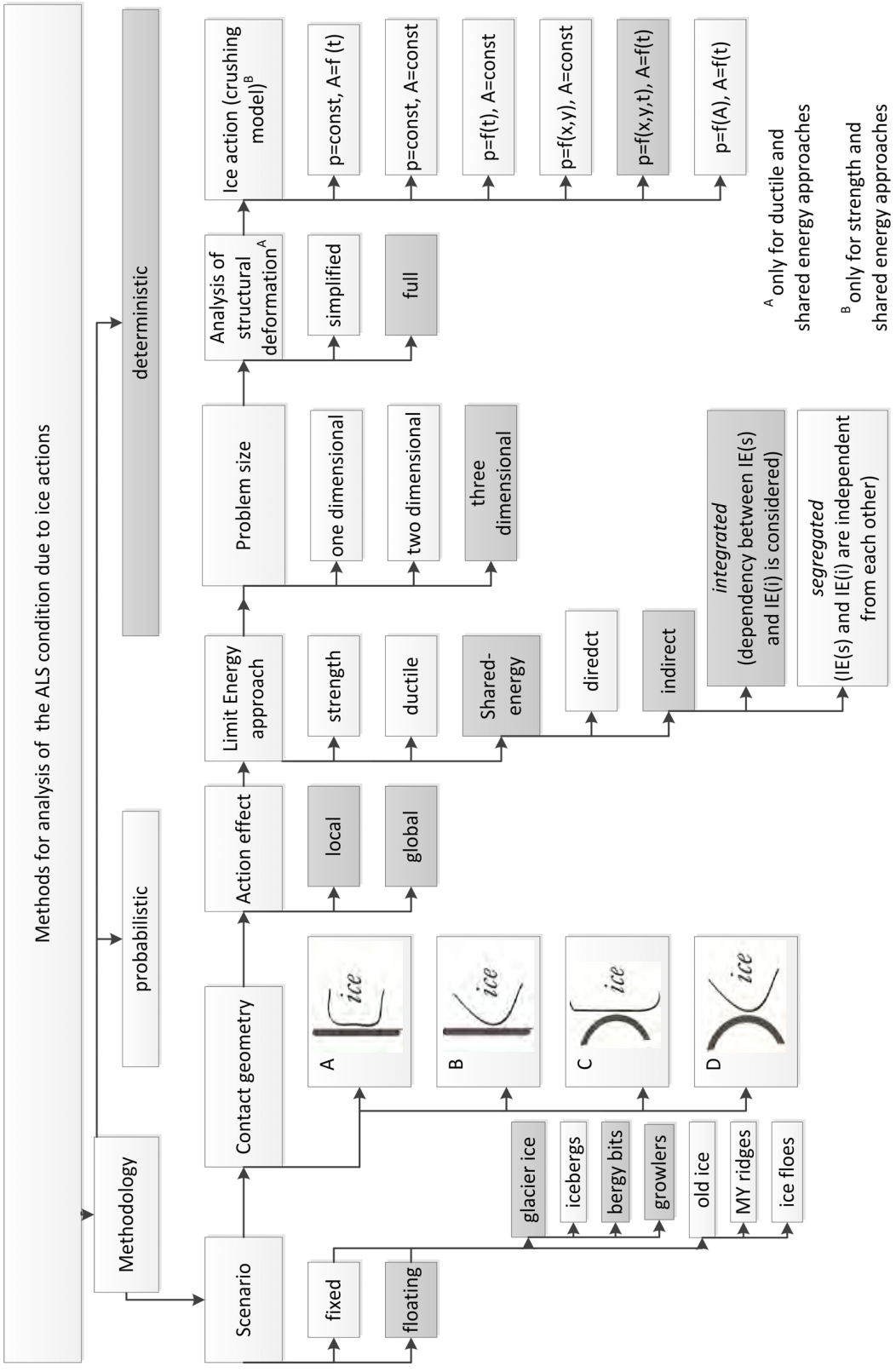

Figure 6: The major parameters and assumptions affecting the analysis of the ALS condition due to abnormal ice actions; the approaches and assumptions behind the coupled analysis of ship/ice collision proposed by Liu (2011) are highlighted in grey.

(i) significant deformation of the mooring system, offset of the structure from the target position and damage to the marine risers as a result;
(ii) local damage, including progressive collapse;
(iii) loss of stability caused by breakage of the mooring lines (or flooded compartments).

Depending on the level of ice actions, the ALS analysis may be divided into methods focusing on (i) the global processes of interaction (i.e., studying ice/structure motions and stability; see Daley (1984), Grace (2011)) and (ii) local processes, for example, calculating the total collision force and stress distribution along the hull; see, e.g., methods used by Swamidas et al. (1983), Aldwinckle and Lewis (1984) and Liu (2011).

Assumptions of the contact geometry

Four typical contact geometries may be distinguished. In Figure 7, various ice/structure interaction scenarios are presented. The scenarios correspond to the different contact geometries listed in Figure 6.

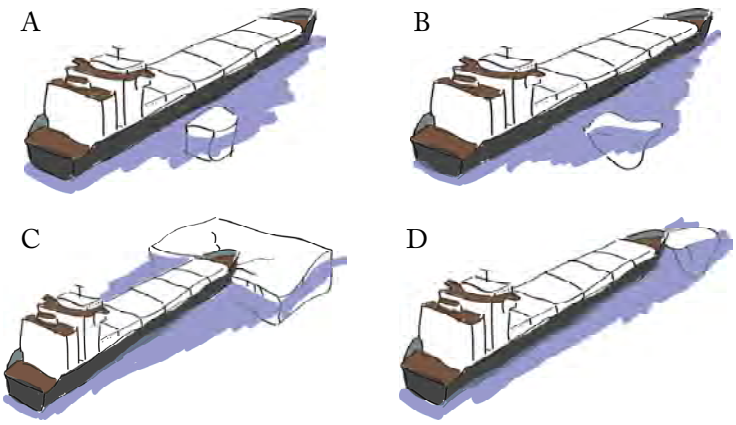

Figure 7: Ice collision scenarios corresponding to the different contact geometries in Figure 6.

A: Contact between two initially flat surfaces. For example, this type of contact occurs during collision between a floating (or fixed) offshore structure and a tabular ice feature.

B: Contact between an initially flat surface (structure) and an initially convex ice surface, such as a bergy bit (or growler) colliding with the side of the ship. Note that ice features are considered that are sufficiently large to represent a threat to a vessel or an offshore structure and that are sufficiently small to escape detection and management system.

C: Contact between an initially convex surface (structure) and an initially flat ice surface, such as a collision between a large tabular iceberg and one of the legs of an offshore platform or a head-on ship collision with a massive ice floe. The width of the

structure is small compared with the size of the iceberg. In Aldwinckle and Lewis (1984), a head-on collision with an ice wall was considered.

D: Contact between two initially convex surfaces, including collisions between structures and ice masses of similar size (e.g., the diameter of the structure is similar to the ice feature).

Assumptions of iceberg shape

Examples of ice shapes used for ALS are shown in Figure 8 and Figure 9.

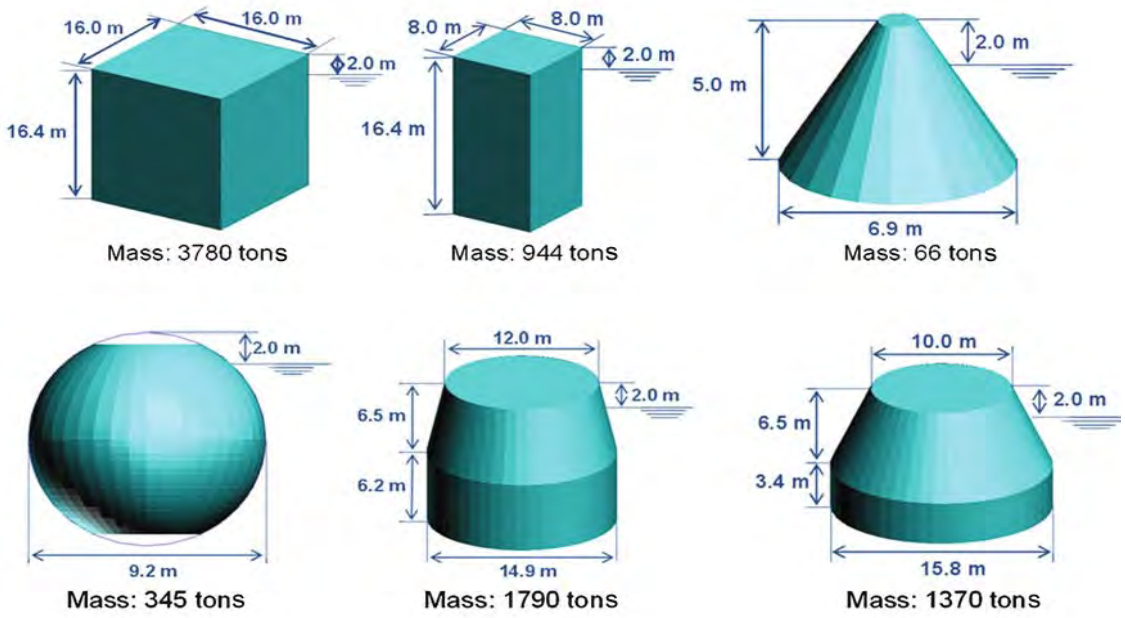

Figure 8: Example of iceberg shapes for ALS analysis (from Han et al., (2008)).

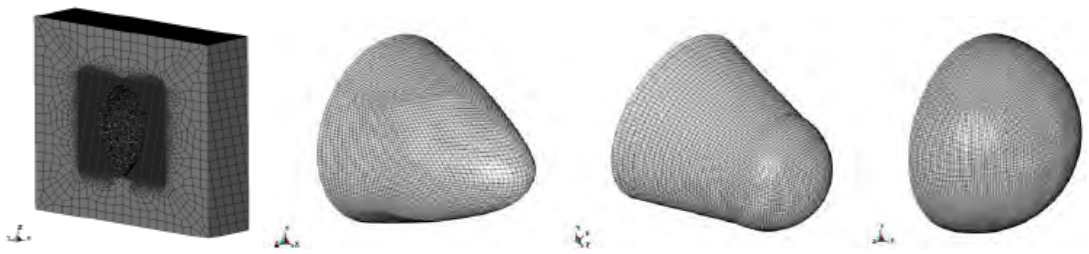

Figure 9: Example of iceberg shapes used in shared energy ALS analysis by Liu (2011).

Nesterov (2010) performed nonlinear analyses of structural deformations for a collision between a cylindrical ice feature (H=6 m, R=25 m with the mass of 10603 tons) and a ship on circulation. The ice action was characterized as pressure of 23.3 MPa uniformly distributed over an area 1.26 m wide and 2.79 m high. For detailed description of the collision scenario see Nesterov (2010).

A spherical iceberg was considered by Brown and Daley (1999). In Tangborn et al. (1998), an iceberg was modelled as a solid cube. Mravak et al. (2009) and Gagnon (2007) used prismatic ice shapes with rounded edges while Lee and Nguyen (2011) used a cubic ice mass. Gagnon and Wang (2012) used a "block type" ice mass with a spherical protrusion, as shown in Figure 10.

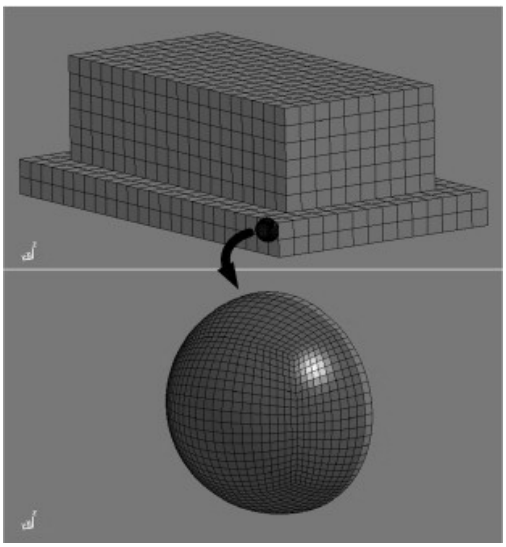

Figure 10: Global and local ice shape used by Gagnon and Wang (2012).

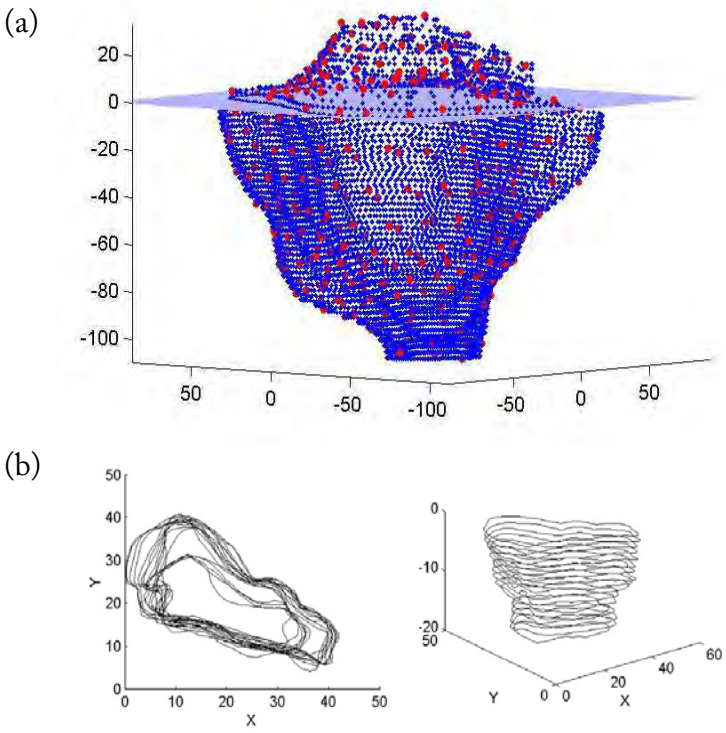

Figure 11: Measured iceberg and bergy bit shapes: (a) iceberg from McKenna (2004) and (b) below-water contours of the bergy bit in Ralph et al. (2008).

For comparison, the realistic iceberg and bergy bit shapes based on actual measurements are shown in Figure 11a and Figure 11b, respectively.

Assumptions of energy dissipation

Depending on the assumption of the distribution of the energy during the accidental event, three basic methods might be distinguished: strength approach, ductile approach and shared energy approach, as discussed earlier (see pp. 13–14).

The studies by Popov et al. (1967), Korzhavin (2002), Matskevitch (1997a, 1997b) and Daley (1999) may be considered as the *strength approach*. Popov et al. (1967) considered inelastic of ship/ice floe impacts. The ice floe was considered to be circular at the water plane and elastic deformations of the ship side and the ice were neglected.

Matskevitch (1997a and 1997b) studied eccentric iceberg impacts and derived a model to calculate the forces on a rigid structure. Force-penetration curves for ice are needed to perform calculations. Korzhavin (2002) proposed a method to calculate load on supports of bridges and hydraulic engineering structures due to ice floe impacts. The method neglects the possibility of plastic structural deformations.

Noble et al. (1979) developed a mathematical model which simulates interaction between selected portions of the ship hull and ice features. The ship was considered to be a solid body (6DOF), and the ice floe was assumed to be circular and comparable with the ship in size. For the ice floe, only surge and sway motions were considered. The model consisted of two parts including a "motion model" and an "impact load model". The calculation of impact load was based on the model presented by Popov (1967). The ice-crushing strength (in pure-crushing failure mode) was held constant over the entire contact area and throughout the collision.

Matsushi et al. (1984) proposed a finite-element based method considering elastic bending and shearing deflections of a hull girder with rigid body motions of the ship. The authors considered head-on, inelastic collisions between the ship and the ice floe (circular disc). Only the ice-crushing failure mode was assumed without considering plastic deformation of the ship.

The approach of Cammaert and Tsinker (1981) and Greshunov (1986) related kinetic energy dissipation to the progressive crushing of ice. Deformations of the structure were neglected by the authors.

Jebaraj et al. (1988) used a finite-element procedure to study the load on hull of a ship during an impact with ice floes. The ship hull was considered to be a rigid indenter impacting the ice. The flexibility of shell plating of the hull in direct contact with the ice was considered using empirical coefficients. The ice failure was modelled using the Tsai-Wu criterion.

Aldwinckle and Lewis (1984) utilized a *ductile approach*. A head-on collision was considered in which the iceberg was modelled as a rigid vertical wall. A ductile approach

was also presented in a study by Suh et al. (2008) in which the icebergs had conical, spherical and cubical shapes and were modelled as rigid bodies.

Laughlin (1970) performed a pioneering study on the plastic collapse of plates under ice loads. An idealized mathematical model of a pinnacle of ice being forced against the plating was used as the assumed loading mechanism. A four sided pyramid of ice was considered. The ice crushing pressure was considered constant throughout the loading process, and contact area continually increased with the applied force. Laughlin (1970) established a solution of large plate-deflections and determined the failure load.

A study by EPOA (1971) is an example of a *shared-energy approach*. The purpose of the study was to determine the maximum size of a growler that may be allowed to strike the hull of the drillship without causing damage. Spherical and ellipsoidal shapes of the ice floe (or growler) were assumed for these calculations. Impact at right angles to the ship side was assumed. The energy dissipated within the ice and due to deflection of the ship hull was considered.

Cammaert et al. (1983) described the development of three dimensional iceberg/structure interaction models incorporating plastic deformation of the iceberg, elastic/plastic deformation of the structure, platform excursions and flexibility of the mooring system but did not include an example calculation.

Wang et al. (2008) developed a global, nonlinear, finite-element model for analysis of ship/ice floe collisions. The hull structure was considered to be a deformable body (elastic-plastic constitutive model), and the ice material was modelled as a crushable body, including failure criterion.

For sheared-energy approach, the question is whether the ice response is independent from that of the structure or whether the response of the ice is a function of the response of the structure and vice versa. One can distinguish between two types of analysis: coupled and uncoupled. *Coupled* (or integrated in Figure 6) *analysis* implies that the weaker structure (or ice) deforms at any instant. In coupled analysis, the ice response is coupled to the response of the structure. In *uncoupled* (or segregated in Figure 6) analysis, the response of the ice is decoupled from the response of the structure.

For example, Swamidas et al. (1983) used an uncoupled approach in which the available kinetic energy is absorbed by the ice and by the structure. A portion of the kinetic energy absorbed by the ice was calculated assuming the structure was rigid and vice versa. The authors described the mechanism of interaction as follows: “when a bergy bit collides with a moored semisubmersible, part of its kinetic energy is absorbed by rigid body rotation (in pitch and roll only) of the semisubmersible, and elastic/plastic deformation of the impacted and other parts of the semisubmersible. Another part is dissipated by rigid body rotation (pitch and roll only) of the bergy bit and local crushing

and splitting of the bergy bit, and the rest by the linear/nonlinear deformation of cables."

Kitami et al. (1984) and Nawata et al. (1984) evaluated bergy bit collision with a semisubmersible drilling unit. The relationships between load and deflection of the bergy bit were derived using indentation tests. The load-deflection relationship of the structure was computed from the results of simplified elasto-plastic analysis. The equations of motions were limited to the water plane. A tabular iceberg was considered. The crushing strength of the bergy bit was assumed to be constant over the area throughout the impact.

Kierkegaard (1993) studied ship collisions with icebergs and compared collision strength from head-on scenario with expected ice strength. The collision strength was calculated assuming right-angled head-on collision against a rigid object (an iceberg), and the expected ice strength was derived using the pressure-area relationship proposed by Sanderson (1988).

The numerical model of Foschi et al. (1996) considers the energy dissipation through local structural collapse using an assumed relationship between the applied force and the additional iceberg penetration due to structural damage.

Daley and Kim (2010) considered the work done during plastic deformations of the structure and during crushing of ice. They assume a conversion of the kinetic energy into the deformation energy of the structure and the deformation energy of ice. The deformation energies of the structure and ice were found by integrating the force over the structural deformations and ice deformations, respectively. To estimate the structural indentation energy, the elastic response was ignored, and a finite-element model was used to establish the simplified relationship. The model evaluates the absorbed energy and permanent deformation of the structure with an elastic-plastic response including linear strain-hardening. The ice load was described as a point load. For the calculation of the ice-crushing energy, the force-indentation relationship was derived using a "process" pressure-area relationship.

In addition, the aforementioned design principles may be utilized via a *direct* or *indirect approach*. In the *direct approach*, the structural deformations and motions are derived using a fluid-structure-interaction (FSI) technique (see Lee and Nguyen (2011), Lobanov (2011) and Gagnon and Wang (2012)). The *indirect approach* implies that a portion of the kinetic energy is dissipated through the relative motions of the ice and the structure (external mechanics), and that the remainder of the energy is dissipated through ice/structure deformations (internal mechanics). The external and internal mechanics are connected through the demand value of the energy dissipation.

Koehler and Jorgensen (1985) divided the problem into two parts: the simulation of the local damage process and the simulation of the motions of the ship and ice feature during the collision.

Liu (2011) performed studies based on the indirect, coupled (integrated) analysis of an iceberg collision with a floating structure. First, the energy to be dissipated as strain energy in the ice and the structure is determined using external mechanics considerations. Second, a non-linear, finite-element analysis of the ice/structure interaction is performed assuming the constitutive behavior of the ice and the steel material. The internal mechanics is coupled with the external mechanics via the demand for energy dissipation. During the integrated analysis, the structural resistance depends on the physical and mechanical properties of the ice and the ship. The energy dissipation capacity of the structure is a function of the energy dissipation capacity of the ice.

Assumptions of problem size

The Popov et al. (1967) collision model considers that a central collision problem may be reduced to a one-dimensional problem viewed in the direction of the impact. In the reviewed literature, different one- two- and three-dimensional problems are considered. For example, Daley (1984) considered a head-on impact between a ship and a large ice floe. A two dimensional problem was formulated (surge, heave and pitch motions were considered). The problem formulation also includes three vertical-bending modes of the vessel.

Assumptions of structural deformation

Two approaches can be used to assess structural deformations during and after an abnormal ice event: *simplified* and *direct* approaches. In the simplified approach, the structural deformations are calculated using plastic methods of analysis (e.g., see Kitami et al. (1984), Arockiasamy et al. (1984) and Koehler and Jorgensen (1985)). In the direct approach, the constitutive behavior of the material is derived from standardized testing procedures and used in the calculation of structural deformations (e.g., see Liu (2011) and Lee and Nguyen (2012)).

Assumptions of the ice crushing model

In the methods that allow energy dissipation due to ice deformation, compression (crushing) failure is commonly assumed. Several different ice-crushing models can be found in the literature. The models can be categorized according to the assumption of ice pressure (crushing strength) variation during the impact.

1. $p=const$; $A=f(t)$. The ice-crushing strength (or the effective crushing pressure) is constant over the contact area throughout the collision event. The contact area changes according to the local iceberg and structure shapes at contact. Noble et al. (1979) and Korzhavin (2002) considered the impact with a rounded/angular-edge ice floe and structural profile, respectively. They assumed the ice-crushing strength to be constant over the area throughout the impact.

2. $p=const$; $A=const$. The pressure is constant over the contact area, which is also considered to be constant. This assumption was widely used in the early 1980s for type C contact geometry (see Figure 7).

3. $p=f(x,y)$; $A=const$. The pressure is non-uniform over the contact area, while the contact area is constant throughout the interaction (e.g., see the method in ISO 19906 section A.8.2.5.5 local ice pressure combinations).

4. $p=f(t)$; $A=const$. The pressure is uniformly distributed over the area and varies in time, while the contact area remains constant (e.g., see the local model for static analysis of Wang et al. (2008); Nesterov (2010) and Daley and Kim (2010)). In Daley and Kim (2010), the pressure was replaced by a point load.

5. $p=f(x,y,t)$; $A=f(t)$. The ice contact pressure is a spatial and temporal function, and the contact area varies with time. In the literature, the pressure evolution with time $p=f(t)$ is often referred to as a "process'" pressure-area relationship, and a pressure distribution $p=f(x,y)$ is referred to as a "spatial" pressure-area relationship. Few studies have considered the process and spatial pressure variations during collisions. The studies are based on non-linear, finite-element methods (e.g., see Liu (2011), Gagnon (2007) and Lee and Nguyen (2011)). Quinton et al. (2012) developed and used numerical algorithms to allow pressure changing in both space and time to be applied to a structure. Only limited full-scale experimental data are available in which the pressure variation is measured with good spatial resolution.

6. $p=f(A)$; $A=f(t)$. This is the most commonly used assumption. The pressure is constant over the area but decreases with increasing contact area. The contact area varies throughout the collision depending on the local shape of ice and structure at contact. Matskevitch (1997a) used linear pressure-area dependency and extended the study to a non-linear relationship (Matskevitch, 1997b). For example, the pressure-area dependency in the form of $p=CA^{ex}$ (C and ex are coefficients) is accepted for the local ultimate limit-state design in ISO 19906 (2010).

Appolonov et al. (2011) studied different design models to describe ice failure by local crushing. The considered models include: (i) a hydrodynamic model of solid-body impact against ice or Kurdumov-Kheisin model, (ii) an empirical model based on the pressure-area relationship and (iii) the dynamic ice failure model. Detailed description of these models and the underlying assumptions are presented in Appolonov et al. (2011).

In addition to the methods and assumptions discussed previously, several studies have addressed hydrodynamic aspects of iceberg/structure interaction. For example, McTaggart (1989) studied various hydrodynamic aspects of iceberg collisions with a large structure and incorporated the finding into a probabilistic model for assessing iceberg collision events.

2.1.2 Summary

The literature review revealed that although ALS is one of the critical limit states (i.e., its violation can directly result in loss of human life, environmental damage and loss of the structure) more attention has been paid to ULS conditions. There is lack of full-scale field measurements of ice forces on structures that deform plastically under extreme ice loads.

The global ice shape is usually chosen arbitrary or is based on the worst-case scenario or statistical measurements. In the methods that allow energy dissipation due to ice deformation, compression (crushing) failure is commonly assumed. The selected ice shapes are mostly simple, axisymmetric geometrical forms, while realistic iceberg and bergy bit shapes are non-convex and have local ice protrusions.

While earlier studies used semi-analytical approaches, numerical algorithms are now being developed for iceberg/structure interaction problems. Non-linear, finite-element methods are widely used for the collision scenario between marine structures and ice features, and continuum models for the ice material are developed.

Numerical approximations of fractures (especially for ice) and contact forces together with a finite-element meshing technique are critical for local analysis of ALS. Experience with state-of-the-art numerical algorithms available for modelling ice fracture is not sufficient for the shared-energy approach. Additional testing procedures should be developed to validate of the particular material models. Aspects of continuum modelling are considered in the next section.

2.2 How should ice behavior during a collision be dealt with?

In 1883, Otto Pettersson wrote: "It has long been a subject of discussion, whether the ice is a brittle or plastic substance." After 130 years, do we have an answer to this question?

It is commonly assumed that the ice pressure exerted on a structure depends on the ice failure mode, i.e., creep, radial/circumferential cracking, buckling, spalling, crushing. A detailed description of ice failure modes has been provided by Sanderson (1988) and Løset et al. (2006). At small scales, ice undergoes various micromechanical processes, in particular micro-cracking, phase change (melting), solid-state recrystallization, grain boundary sliding, sintering (sub-sintering), fragmentation, etc., depending on the degree of confinement. Extensive descriptions of ice behavior under various loading conditions have been provided by Michel (1978) and Schulson and Duval (2009). During an ice-structure interaction, intense stress conditions are created in both the ice and the structure. The ice may undergo different failure modes depending on the

boundary conditions imposed by the geometry and size of the ice feature, the geometry and flexibility of the structure at the contact zone, the presence of wind, waves and currents, etc. Moreover, factors such as the ice temperature, porosity, salinity, ice microstructure (i.e., grain size, shape and orientation) and distribution of internal flaws and stresses contribute to the behavior of ice. There is a rising awareness of the importance of the contribution of small-scale processes to the failure modes that are observed at full-scale. For rare, extreme ice actions, this study is limited to collisions between an ice-mass and a structure. The only ice features considered are those that are sufficiently large to represent a threat to an offshore structure (or a vessel) and those that are sufficiently small to escape detection and ice management systems. An example of such an event is a vessel collision with a bergy bit (or growler). Probable ice responses are listed below.

(a) The ice rebounds with little crushing: this behavior would be observed for an ice mass that is sufficiently small relative to the vessel size.
(b) The ice undergoes crushing, and an inelastic collision can be assumed.
(c) The ice splits, for example, in a high velocity collision where the ice mass already contained initial, predefined cracks well before collision.

Continuing the Liu (2011) work, I studied the ice crushing process caused by fast compressive loading. The processes governing ice crushing are not well understood. Fracture evolution in ice has rarely been directly observed in standard field tests (e.g., Frederking et al., 1990; Sodhi, 2001 and Kheisin and Cherepanov, 1970). Only the external appearance of the ice failure process can be observed in these tests because of the opacity of the ice. In addition, the presence of snow may affect the observations. Studies of microstructural changes can only be performed after completion of the test. With the development of tactile pressure sensors, pressure sensitive films and pressure-sensing mechano-optical technology, including high-speed imaging systems, ice contact pressure can be recorded with an effective unit sensing area ranging from 0.1 mm^2 (FUJIFILM) to approximately 1.8 cm × 1.8 cm (Gagnon, 2008a). This development has resulted in semi-empirical formulations for *process-* and *spatial* pressure-area relationships (see, for example, Frederking, 1998; Frederking, 1999; Daley, 2007 and Gudimelta et al., 2012), non-simultaneous ice failure (Sodhi, 1998), the formation of *high pressure zones* (HPZs) during ice crushing (Varsta, 1983 and Jordaan, 2001), etc.
Here the *process pressure-area relationship* refers to the process of structure (ship, indenter) penetration into an ice feature. The *spatial pressure-area relation* refers to the spatial distribution of pressure at an instant in time.

Ice behavior under a compressive stress field is rather complex: see Tuhkuri (1996), for example. This behavior includes the development of HPZs that accompany the formation of the damage layer in the contact zone, including recrystallization, micro-

cracking, rapid ejection of crushed ice, spalling, splitting events and pressure melting (Gagnon and Mølgaard, 1991); the generation of heat and the production of physical effects such as melting (Gagnon, 1994); and the pressure sintering of crushed ice (Singh and Jordaan, 1996). Golding et al. (2010) and Schulson (2002) have provided strong evidence that the failure mode depends on the geometrical and loading conditions. Depending on the degree of confinement (i.e., the ratio between the minor and major principal stresses), either Coulombic faults (at low confinement) or plastic faults accompanied by dynamic *recrystallization* (at high confinement) are formed in freshwater ice that is rapidly loaded under triaxial compression. Here *recrystallization* refers to a solid-state process in which a new grain structure is created in a deformed material via the formation and migration of high angle grain boundaries driven by the stored energy of deformation (Doherty et al., 1998 and Schulson, 2013). A good description of the ice crushing process is provided by Kuutti et al. (2013) in the chapter "Ice indentation failure".

The aforementioned considerations show that it is extremely difficult to include all aspects of ice behavior in a single model. For example, Carney et al. (2006) wrote: "Ice should be regarded as a class of materials rather than a single, specific material with well-defined properties." Different models for specific ice behavior are used depending on the requirements at hand. For example, the following models have been implemented in commercial finite element codes: Carney et al. (2006), Kolari (2007), Sand (2008), Gürtner (2009), Liu et al. (2011), Hilding et al. (2011), Gagnon (2011), Lu et al. (2012), Moore et al. (2013), Kuutti et al. (2013), etc. Although some of these models have supposedly been "validated" and are based on physical processes, many of these theories suffer from uncertainties associated with the process of estimating the input parameters to the model.

In Section 2.2.1, the focus was placed on the constitutive behavior of ice prior to fracture, in particular, on yield- and failure envelopes that can be used for iceberg impact simulations when local ice crushing is the dominant process. I tried specifically to address issues related to the necessity for calibration and the uncertainties associated with fitting failure criteria to laboratory strength tests, in particular how well various functions can model the uniaxial strength of ice. The question of whether yield (or failure) functions could be used to model ice and its inherent inhomogeneity and the role of ice fracture were outside the scope of this study. Kuutti et al. (2013) reported that classical continuum models are not suitable for simulations of continuous ice-structure interactions without modifications and identified three fundamental requirements for the simulation of the ice-structure interaction process:

(a) modeling the onset of failure, propagation and the orientation of the failure;

(b) modeling material fragmentation (i.e., new free surfaces must be created in the model); and
(c) modeling the interaction among the fractured fragments, the structure and the intact ice.

2.2.1 Review of failure and yield criteria

The literature often describes a semi-empirical failure surface. This surface may be treated as a yield surface (see e.g., Liu et al., 2011). Some yield and failure criteria that have been suggested in the past for ice are now only of historical interest. These proposed yield functions were found to conflict with later experiments in predicting the influence of hydrostatic stress and possible phase changes due to high hydrostatic pressure and temperature. The circumstances of ice yield/failure surfaces are thus unsatisfactory. To investigate this situation, I have made an overview of these past developments.

Figure 12 summarizes past studies focusing on yield/failure surfaces that were used intensively in ice research. These past developments can be divided into four major groups or generations. Many of the strength criteria are well known, so references are only listed for the lesser-known works.

The *first-generation criteria* (1GC) in Figure 12 are represented by the simple yield/failure surfaces of Tresca and von Mises for isotropic materials and the Hill criterion for anisotropic materials. In 1GC, the yield strength of ice (failure stress) is not influenced by hydrostatic pressure, i.e., there is no difference between the tensile and compressive yield strengths. To describe yield/failure stress in an isotropic material, only one material property is needed. According to Schulson and Duval (2009), the ductile strengths of plastic, isotropic granular ice and orthotropic columnar ice are governed by the von Mises and Hill criteria, respectively.

The *second-generation criteria* (2GC) are modifications of the 1GC forms and incorporate a linear dependence on hydrostatic stress. For a fully isotropic material, the Hoffman criterion reduces to the Drucker-Prager form. Here, to describe the yield/failure strength of an isotropic material, two material properties are required. According to Fish and Zaretsky (1997), the Drucker-Prager yield criterion is valid for ice under low hydrostatic pressure (p<<49 MPa for ice at –11°C and a strain rate of 0.005 s^{-1}).

The *third-generation criteria* (3GC) are represented by the generalization of the von Mises criterion by Yang (1980) and the elliptical failure surface of Tsai and Wu (1971). 3GC have quadratic stress terms. These criteria can describe materials that show finite hydrostatic stress. Here, three material properties must be provided to describe yield/failure strength.

The Christensen (1997) criterion is less known in ice science. This criterion lies on the boundary between 2GC and 3GC. It is a two-parameter yield/failure criterion developed for isotropic materials. Expressed in terms of uniaxial strength values and principal stresses (σ_1, σ_2 and σ_3), the Christensen yield criterion is written as:

$$f(\sigma) = \left(\frac{1}{R_t} - \frac{1}{R_c}\right)(\sigma_1 + \sigma_2 + \sigma_3) + \frac{1}{R_t}\frac{1}{R_c}\left(\frac{1}{2}((\sigma_1 - \sigma_2)^2 + (\sigma_2 - \sigma_3)^2 + (\sigma_3 - \sigma_1)^2)\right) - 1, \qquad (1)$$

where R_t and R_c are the uniaxial tensile and compressive strengths, respectively. It will be shown that the Christensen criterion can be used to describe the ductile strength of multiyear ice.

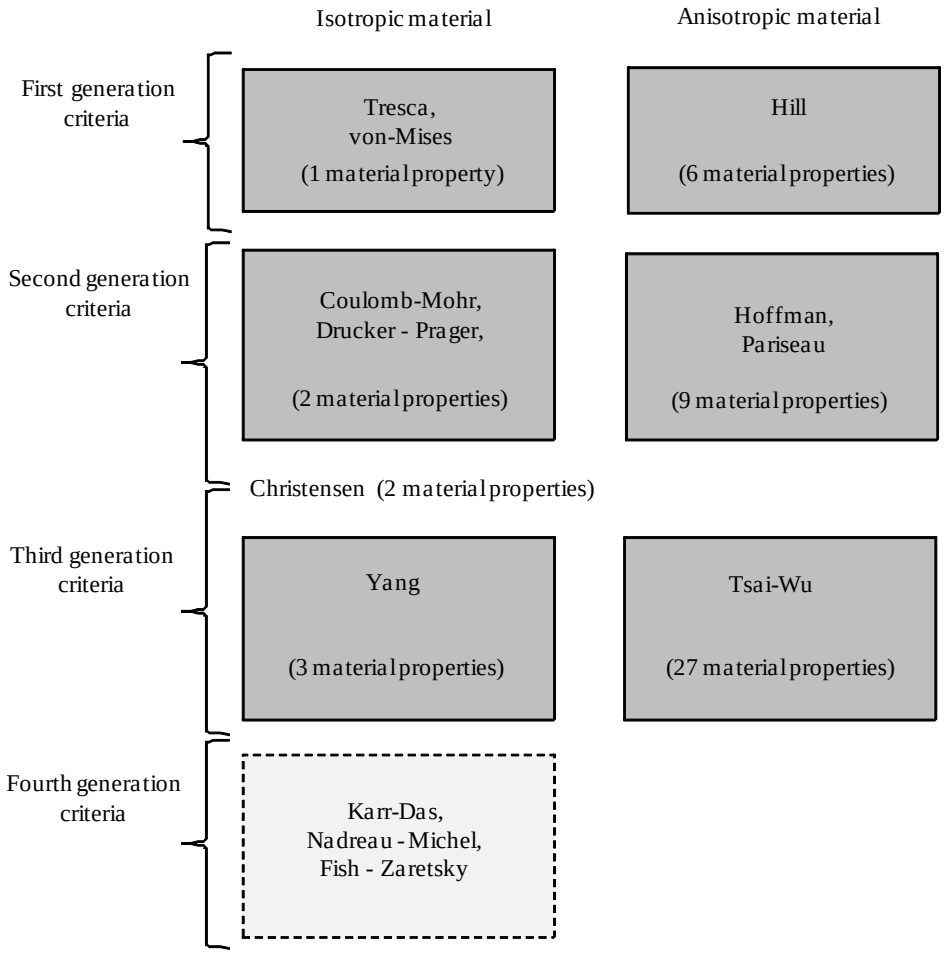

Figure 12: A schematic generalization of the ice yield/failure criteria.

The *fourth-generation criteria* (4GC) are a combination of the 1GC and 3GC forms (Karr and Das, 1983), resulting in teardrop curves having cubic or higher stress terms (Nadreau and Michel, 1986; Fish and Zaretsky, 1997). These criteria can also describe materials that show finite hydrostatic stress. The advantages of using 4GC for the

problems of ice impact will be discussed later. Three or more material properties are needed for such criteria.

Gagnon (2011) suggested a numerical model for ice crushing that could be used in an ice-structure impact scenario. The ice model is phenomenological and represented by a plasticity-based foam model. Gagnon (2011) noted that some model parameters (e.g., yield stress versus volumetric strain curves) do not realistically represent ice properties. Therefore, discussion regarding the physical plausibility of the material constants and manageability of their calibration is not relevant here, and Gagnon's model was omitted from further consideration.

2.2.2 Applicability of failure and yield criteria

This section focuses only on the yield/failure criteria that can potentially be used in the ALS design procedure. In numerical simulations of iceberg impacts, it is common to consider ice as a polycrystalline mass and treat it as a fully isotropic material. In the present work, only fully isotropic forms of the strength criteria were evaluated. Accordingly, the yield/failure surface was expressed in terms of stress invariants.

Experimental studies of freshwater ice by Jones (1978), multiyear ice by Riska and Frederking (1987) and iceberg ice by Gagnon and Gammon (1995a) showed that ice strength has a nonlinear dependence on hydrostatic pressure. The uniaxial strength of freshwater ice in tension is 2–10 times smaller than in compression (recalculated from data in Ashton, 1986). In addition, Mellor (1980) suggested that phase changes due to hydrostatic pressure should also be taken into account. Therefore, the 3GC or 4GC criteria are the most suitable for our analysis.

The expressions in Table 1 have been used by a number of researchers (Reinicke and Remer, 1978; Riska and Frederking, 1987; Liukkonen and Kivimaa, 1991; Kierkegaard, 1993; Horrigmoe et al., 1994; Løset and Kvamsdal, 1994; Liu et al., 2011) to describe ice behavior (including polycrystalline ice, multiyear ice and iceberg ice) in different situations. It can be shown that criteria № 2–4 in Table 1 are mathematically the same as № 1. Hence, the expressions in № 1–4 can be seen as an isotropic case of the Tsai-Wu surface (Riska and Frederking, 1987; Liu et al., 2011), as a three-parameter function (Reinicke and Remer, 1978), or as a generalization of the von Mises criterion proposed by Yang (1980).

Table 1. Third generation criteria for ice.

№	Yield/failure criterion	Description
1	$f(\sigma_{ij}) = aJ_2 + bI_1 + cI_1^2 - 1$	This criterion was used by Reinicke and Remer (1978). I_1 is the first invariant of stress tensor, J_2 is the second invariant of the deviatoric stress tensor, a, b, c

		describe the material properties. Reinicke and Remer (1978) used the experimental data in Jones (1978) to determine the coefficients of the yield function.
2	$f(\sigma_{ij}) = F_{11}I_1 + \frac{1}{3}(G_{1111} + 2G_{1122})I_1^2 + 4G_{1212}J_2 - 1$ $G_{1212} = \frac{1}{2}(G_{1111} - G_{1122})$	This criterion was used by Riska and Frederking (1987). F_{11}, G_{1111}, G_{1122} and G_{1212} are material constants derived from uniaxial, biaxial and triaxial tests.
3	$f(\sigma_{ij}) = a_1 I_1 + F_{ij}\sigma_i\sigma_j - 1$ $a_1 = \frac{1}{R_c} - \frac{1}{R_t}$ $F_{11} = F_{22} = F_{33} = \frac{1}{R_c}\frac{1}{R_t}$ $F_{44} = F_{55} = F_{66} = \frac{1}{R_4^2}$ $F_{12} = F_{13} = F_{23} = 2\left(\frac{1}{R_c}\frac{1}{R_t} - \frac{2}{R_4^2}\right)$	This criterion was proposed by Vershinin et al. (2005) for ice with a randomly oriented crystal structure and for strain rates greater than 10^{-3} s^{-1}. R_4 is the shear strength of ice. The strength terms a_1 and F_{ii} are determined directly from the uniaxial strengths of ice. The remaining parameter $F_{12}=F_{13}=F_{14}$ is the interactive strength term, which must be determined experimentally using combined stress tests. Vershinin et al. (2005) suggested that the interactive term can be specified as a function of the ice strengths, eliminating the need for complex combined stress testing.
4	$f(q,p) = \left(\frac{q}{q_{\max}}\right)^2 + \left(\frac{p-\lambda}{P_c}\right)^2 - 1$ $q = \sqrt{3J_2}$ $p = I_1/3$	The semi-empirical failure criterion was suggested by Derradji-Aouat (2003) for iceberg and freshwater ice, where the stress state $\sigma_2=\sigma_3$. q is the equivalent stress, p is the hydrostatic pressure, and λ, P_c and $q_{\max}$ are parameters of the failure envelope. For freshwater ice and iceberg ice, the parameters were derived from triaxial experiments (with uniform confinement) by Derradji-Aouat (2003).

Table 2. Fourth generation criteria for ice.

№	Yield/failure Criterion	Description
1	$\begin{cases} f(\sigma_{ij}) = 2J_2 + \bar{\alpha}(I_1 + \bar{\beta})^2 - Y^2 \ \ for\ I_1 > -\bar{\beta} \\ f(\sigma_{ij}) = 2J_2 - Y^2 \ \ for\ I_1 \le -\bar{\beta} \end{cases}$	Modified von Mises criterion proposed by Karr and Das (1983) combining the surfaces of von Mises and Yang. $\bar{\alpha}$, $\bar{\beta}$, Y are material constants. The constant $\bar{\beta}$ reflects the level of hydrostatic pressure. The modified Drucker-Prager criterion can be obtained by replacing the Yang surface with the Drucker-Prager function (Karr and Das, 1983). The criterion

		suggested by Schulson and Duval (2009) can be seen as an improved version of the criterion in Karr and Das (1983).
2	$f(\sigma_{ij}) = AI_1^3 + BI_1^2 + CI_1 + DJ_2 - 1$ *or* $f(\sigma_{ij}) = \frac{\tan\theta}{\sqrt{P^* - T^*}}(P^* - \frac{I_1}{3})\sqrt{\frac{I_1}{3} - T^*\sqrt{3}} - \sqrt{J_2}$	Based on the experiments of Jones (1982), Nadreau and Michel (1986) proposed a yield surface for polycrystalline isotropic ice. Kormann and Brown (1990) proposed the modified yield surface. The constants A, B, C and D are dependent on ice-melting pressure (P^*), the yield stress in biaxial tension (T^*) and the function $\tan\theta$ given in Nadreau and Michel (1986).
3	$\tau_i(p,T) = (c_1 + b_1 p) - (c_1 + b_1 P^*)\left(\frac{p}{P^*}\right)^2$ $\tau_i = \sqrt{J_2}$	Fish and Zaretsky (1997) developed a temperature model that describes ice strength in a multiaxial stress state over a wide spectrum of negative temperatures. τ_i is the octahedral shear stress. The ice cohesion, $c_1(T)$, internal friction angle, $b_1(T)$, and $P^*(T)$ are functions of temperature T. The model has been verified by Fish and Zaretsky (1997) using test data on the strength of iceberg ice and laboratory-made polycrystalline freshwater ice under triaxial compression ($\sigma_2=\sigma_3$) at strain rates ranging between 10^{-3} and 10^{-5} s^{-1} over the temperature range between –1°C and –40°C.

i,j=1,2,...6

The 4GC criteria for ice are given in Table 2. Although application of these criteria to problems of accidental ice actions was not found in the literature, we believe that some of the criteria listed in Table 2 can be implemented in ALS design.

2.2.3 Evaluation of failure and yield criteria

A single requirement was used to evaluate the failure functions: *any three-dimensional failure surface must satisfy a one-dimensional loading condition*. This implies that if $\sigma_2=\sigma_3=0$ and $\sigma_1>0$ ($\sigma_1<0$), then $\sigma_1=R_c(R_t)$. This verification was performed for 3GC № 1, 2, and 4 in Table 1 and for 4GC № 3 in Table 2. Table 3 summarizes the results of the calculations that performed using the different material parameters available in the literature. In addition, the ice-melting pressure (the ice strength under hydrostatic compression) is given for each set of ice parameters.

Based on Table 3, the failure curve suggested by Derradji-Aouat (2003) for iceberg ice and the failure surface with ice strength parameters in Fish and Zaretsky (1997) significantly overestimates the tensile strength of ice in the case of one-dimensional loading conditions. For ice at a given temperature, one can estimate the magnitude of the ice-melting pressure as $P^* = -T/0.074$, where T is the ice temperature (°C) (Fish and Zaretsky, 1997; Schulson and Duval, 2009). Barrette and Jordaan (2003) determined that at a temperature of −10°C, ice will be at melting point if it is exposed to a pressure of approximately 110 MPa. Therefore, the values of P^* in Table 3 for cases № 1, 2 and 4 are too low. The remaining results given in Table 3 seem to be physically plausible, and it can be argued that the failure criteria (including material parameters) given in Riska and Frederking (1987) (for a strain rate of 0.002 s^{-1}), Kierkegaard (1993) and Liukkonen and Kivimaa (1991) satisfy the one-dimensional loading case requirement but underestimate the ice-melting pressure. In turn, the failure criterion (including material parameters) suggested by Derradji-Aouat (2003) for ice at −10°C and strain rates >10^{-3} s^{-1} correctly predicts the magnitude of the ice-melting pressure but fails to predict the correct tensile strength. The criterion from Fish and Zaretsky (1997) has a similar behavior.

Table 3. Ice properties that satisfy 3GC (1, 2 and 4) and 4GC (3): R_c (compressive strength), R_t (tensile strength), P^* (ice-melting pressure).

№	Authors	R_c, MPa	R_t, MPa	P^*, MPa
1	Riska and Frederking (1987)[1], −2°C (−10°C)	4.4 (8.1)	0.9 (0.9)	7 (11)
2	Kierkegaard[2] (1993)	9.0	0.8	53
3	Derradji-Aouat[2,3] (2003), −10°C	9.3	7.3	100
4	Liukkonen and Kivimaa[4] (1991)	8.8	0.9	9
5	Fish and Zaretsky (1997)[5], −11°C	14.5	12.9	148.65

[1]for a strain rate of 0.002 s^{-1}; [2]via Liu et al. (2011); [3]for strain rates >10^{-3} s^{-1}; [4]via Kierkegaard (1993); [5]for a strain rate of 0.005 s^{-1}

Next, let's compare the failure surface for ice (including material parameters) suggested by Riska and Frederking (1987) and the Christensen failure criterion (Equation (1)) for ductile isotropic materials. The condition of equivalence for those envelopes (i.e., the surfaces are the same when expressed in terms of principal values) can be derived as follows:

$$F_{11} = \left(\frac{1}{R_t} - \frac{1}{R_c} \right) \tag{2}$$

$$\frac{2}{3}(G_{1111} - G_{1122}) = \frac{1}{R_t}\frac{1}{R_c} \tag{3}$$

$$G_{1111} = -2G_{1122} \tag{4}$$

After examination of the parameters G_{1111} and G_{1122} in Riska and Frederking (1987) for different strain rates and temperatures, it was found that the condition expressed by Equation (2) is fulfilled for the triaxial tests with multiyear ice at a strain rate of 0.0002 s^{-1}. Therefore, it is possible to use Equations (3) and (4) to obtain values of R_c and R_t by solving a system of equations.

R_c=2.7 MPa and R_t=0.3 MPa for multiyear ice at (−2°C)
R_c=3.8 MPa and R_t=0.9 MPa for multiyear ice at (−10°C)

Riska and Frederking (1987) reported the results of experiments on uniaxial compression of ice. For ice at a strain rate of 0.0002 s^{-1}, R_c is approximately 2.5 MPa (−2°C) and R_c is approximately 3.85 MPa (−10°C). The value of R_t=0.9 MPa is in a good agreement with that of Petrovic (2003), whereas R_t=0.3 MPa seems to be low in comparison with the data reported by Gold (1977), Ashton (1986) and Petrovic (2003). Schulson and Duval (2009) reported values of R_t=0.2–0.3 MPa at −2.5°C for saltwater ice. For second-year and multiyear sea ice, Timco and Weeks (2010) gave the values of R_t =0.5–1.5 MPa. Petrovic (2003) notes that the compressive strength of ice increases with decreasing temperature and that ice tensile strength is relatively insensitive to temperature variation. According to Schulson and Duval (2009), the strength increases slightly with decreasing temperature for freshwater ice. Saltwater ice exhibits greater thermal sensitivity (Weeks, 1962 via Schulson and Duval, 2009). Taking into account that the values in Riska and Frederking (1987) correspond to multiyear ice (with a salinity close to zero), it was concluded that the values of R_c and R_t (retrieved using failure function no. 2 from Table 1 and the Christensen failure function as an equivalent curve) are physically plausible and in good agreement with the observed experimental values and trends.

As the criteria in Table 1 are mathematically equivalent, it is possible to compare the ice parameters used in the scenario of the penetration of a structure into a large multi-year ice feature used by Riska and Frederking (1987) and the yield-surface parameters used by Liu et al. (2011) to study bergy bit–ship collisions with those in criterion no. 3. This comparison can give physical meaning to the coefficients in 3GC № 1, 2 and 4 in Table 1. For ice at −10°C and a strain rate of 0.002 s^{-1}, the parameters used in Riska and Frederking (1987) correspond to the parameters in criterion no. 3:

$$\begin{cases} \dfrac{1}{R_c}-\dfrac{1}{R_t}=F_{11}=0.988\ \text{MPa}^{-1} \\ \dfrac{1}{R_c}\dfrac{1}{R_t}=0.137\ \text{MPa}^{-2} \\ 2\left(\dfrac{1}{R_c}\dfrac{1}{R_t}-\dfrac{2}{R_4^{\,2}}\right)=-0.024\ \text{MPa}^{-2} \end{cases} \Rightarrow \begin{cases} R_c=8.1\ \text{MPa} \\ R_t=0.9\ \text{MPa} \\ R_4=3.7\ \text{MPa} \end{cases} \Rightarrow$$

The obtained values of R_c, R_t and R_4 are in good agreement with data in Ashton (1986) and with data in Timco and Weeks (2010).

For iceberg ice at −11°C and strain rates greater than 0.001 s^{-1}, comparing the data in Liu et al. (2011) with the strength parameters in criterion no. 3 from Table 1 reveals that R_c=9.2 MPa, R_t=7.2 MPa and R_4=9.6 MPa. For iceberg ice (at a strain rate of approximately 10^{-3} s^{-1} and a temperature of 8.0°C), Lachance and Michel (1987) reported a maximum value of R_c of approximately 10 MPa. Cammaert and Muggeridge (1988) summarized that R_t of glacial ice and old sea ice is usually 1.0 MPa or less. Experimental data for R_4 (iceberg ice) were not found; therefore, the values given in Ashton (1986) for freshwater ice may serve as a reference. In this case, the values of the shear and tensile strengths are significantly overestimated, whereas the value of R_c=9.2 MPa agrees well with Lachance and Michel (1987). The difference between the calculated and experimental values for R_t and R_4 could be because the assumed interactive term in criterion № 3 (Table 1) is not exactly correct for iceberg ice.

Due to these shortcomings, the problem of assessing proper values for the coefficients of yield/failure criteria for ice masses mentioned by Løset and Kvamsdal (1994) still exists.

2.2.4 Summary

Several yield (and failure) criteria were assessed in Sections 2.2.1 and 2.2.2 above. The main findings are presented in Table 4, in which compliance with the uniaxial strength of ice is considered a minimum requirement for determining whether the failure (or yield) models are physically plausible.

A form of the Tsai-Wu failure envelope as found in Riska and Frederking (1987), Kierkegaard (1993), Liu et al. (2011), Liukkonen and Kivimaa (1991), Derradji-Aouat (2003) (3GC №4), Vershinin et al. (2005) and Løset and Kvamsdal (1994) can be split in two groups based on the values of the constants: Group I includes those models which assume a relatively low value for the hydrostatic compressive strength (Riska and Frederking, 1987; Kierkegaard, 1993, Liukkonen and Kivimaa, 1991 and Løset and Kvamsdal, 1994). Group II includes those criteria that assume relatively high values for ice tensile strength (Liu et al., 2011 and Derradji-Aouat, 2003 (3GC №4)). The criterion proposed by Schulson and Duval (2009) seems promising, but more data are needed (e.g., ice under high hydrostatic pressure) for the determination of parameters for this criterion.

Figure 13 illustrates the Schulson-Duval's failure surface in I_1–$J_2^{1/2}$ space. Under high hydrostatic pressure, the surface may narrow to a point on the I_1 axis. The failure surface may contract or expand depending on the strain rate and temperature, as described by Schulson and Duval (2009).

Table 4. Ice failure (or yield) functions.

Reference	Physical plausibility
Riska and Frederking (1987)	Good
Kierkegaard (1993) via Liu et al. (2011)	Good
Liukkonen and Kivimaa (1991) via Kierkegaard (1993)	Good
Derradji-Aouat (2003)[4]	nonconservative[1]
Fish and Zaretsky (1997)	nonconservative[1]/ conservative[2]
Karr and Das (1983) and Schulson and Duval (2009)	promising[3]
Vershinin et al. (2005)	good[3]

[1]problems encountered when tension predominates; [2]problems encountered for predominant compression; [3]uncertain, because of the limited experimental data provided in the reviewed literature; [4]only semi-empirical failure criterion in $q = (3J_2)^{0.5}$ and $p = I_1/3$ axes is considered.

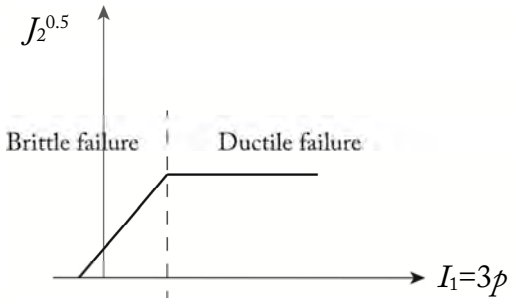

Figure 13: Schematic sketch of the ice failure surface.

It was also shown in Section 2.2.3 that the Christensen's failure criterion (Christensen, 1997) agreed well with triaxial sets of experiments by Riska and Frederking (1987) for multiyear ice under a strain rate of approximately $2 \cdot 10^{-4}$ s^{-1}.

2.3 WHAT NEXT?

The literature review presented in Sections 2.1 and 2.2 was used to narrow down knowledge gaps in the research field. In the analysis of accidental collisions with ice masses (i.e., collision events resulting in significant structural deformations), *limited full-scale data are available to verify the methodologies (theories) based on the coupled behavior of ice and a structure.* The term "coupled behavior" refers to the relationship between the ice response and the structure.

In addition, *the mechanisms underlying ice behavior during fast compressive loading (intense stress conditions) are not yet fully understood, in particular the mechanisms governing ice behavior after its ultimate failure.* Thus, failure criteria for the ice-crushing failure mode are not well established, and current theories are often not physically reasonable. There are also deficiencies in the numerical techniques that are used to model the ice fracture process (i.e., ice fragmentation). For example, Liu (2011) simulated ice crushing during a collision using the element erosion technique in which elements that have reached a certain strain level are removed. Liu (2011) demonstrated that the

element erosion technique could be used to simulate ice crushing events and graphically visualize the actual crushing process. Gürtner (2009), Hilding et al. (2011), Lu et al. (2012) and Kuutti et al. (2013) approximated ice fracture (in a continuous crushing mode) using a cohesive element methodology in which the cohesive elements were used to model potential fracture planes in ice. There are at least two obstacles that limit the use of the last technique in full-scale simulations: (a) the time inefficiency of the computations and (b) the difficulty associated with finding appropriate meshes that coincide with the cracking pattern.

The knowledge gaps defined above have motivated the following research questions, which are addressed in the next two chapters.

Q1: What physical processes occur during an ice-structure collision (indentation) and how can these processes be modeled?
Q2: What processes occur when a structure is allowed to deform plastically during an ice-structure collision?

Chapter 3

Experimental studies

> "Never stop because you are afraid - you are never so likely to be wrong"
>
> Norwegian explorer Fridtjof Nansen (1861-1930)

This chapter describes experimental procedure, presents and discusses the results of experiments carried out at two different scales: centimeter-scale experiments, O[cm] (Sections 3.1 and 3.2) and meter-scale experiments, O[m] (Sections 3.3 and 3.4). The centimeter-scale experiments were designed to simulate ice behavior under fast compressive loading during indentation and impact. In the meter-scale experiments, we attempted to "mimic" an ice-structure interaction during a collision event.

The indentation tests and angle-of-repose studies described in Sections 3.1 and 3.2 were performed in collaboration with Dr. Narayana Golding who helped to perform the tests and took part in the interpretation/discussion of the results. The work was supervised by Prof. Erland M. Schulson at the Thayer School of Engineering at Dartmouth, Hanover, USA. Professor Carl E. Renshaw took part in the discussion of the experimental results. The work presented in the subsection entitled "Energy absorption capacity of ice during crushing" was performed in collaboration with Prof. Knut V. Høyland who provided experience in the domain of ice fracture mechanics and scale and size effects related to ice properties. The experiments discussed in Sections 3.3 and 3.4 were performed in a model ice basin located at Aalto University in Espoo, Finland in collaboration with Rüdiger Ulrich Franz von Bock und Polach and Martin Storheim who provided valuable assistance during planning and execution of the tests and also provided constructive comments that helped to improve the work.

3.1 Small-scale indentation experiments

Understanding of ice-structure collisions (see the research question Q1 in Section 2.3) requires knowledge of failure processes under both high and low confinement. The physical processes involved in the interaction of ice masses with ships, offshore and coastal structures have been focus of many investigations, e.g., Dempsey et al. (2001), Gagnon (2008a), Gagnon (2008b), Johnston et al. (1998), Jordaan and Timco (1988), Li et al. (2004), Masterson and Frederking (1993), Sanderson (1988), Sodhi (2001) and Timco (2011). These studies include: full-scale data (ship trials, ice structure impacts/interactions including ice-bridge pier interactions); medium-scale indentation

tests (e.g., Hobson's Choice tests, Pond Inlet tests and small-scale laboratory experiments (e.g., Barnes and Tabor, 1966; Barrette et al., 2003; Browne et al., 2013; El-Tahan et al., 1988; Gagnon, 1994; Garcia et al., 1985; Grape and Schulson, 1992; Mackey et al., 2007; Tuhkuri, 1994; Wells et al., 2011). Full-scale experiments have traditionally been considered to be a reliable source of information on forces and pressures. Experiments at medium scales are used to obtain information on the characteristics of HPZs, i.e., the development of HPZs and the interaction between different HPZs. It has been argued (Gagnon, 1999; Barrette et al., 2002; Wells et al., 2011 and Browne et al., 2013) that studying ice mechanics during small-scale indentations may shed insight on full-scale processes and advance our understanding of ice behavior during ice-structure interactions/collisions.

This section provides insight into the mechanisms governing failure of ice beneath a spherically shaped indenter. Observations of fracture in freshwater ice during small-scale indentations are compared to the observations made by Gagnon (1999), Gagnon and Bugden (2007), Gagnon (2008b) for the case of an ice wedge impacting a flat rigid surface at a medium-scale. Similarities and differences are highlighted; in particular, the possibility of ice melting and solid-state recrystallization is discussed.

3.1.1 Experimental method

The primary objective of this portion of the studies was to investigate the mechanisms of ice failure under a compressive stress field. An experimental apparatus simulating ice conditions in the field (including high-speed video recordings and detailed examinations of the ice microstructure) was used to address the research question Q1.

The experiments were conducted using the multiaxial testing system (MATS) in the Ice Research Laboratory at Thayer School of Engineering. The main feature of MATS is the ability to apply uniform compressive loads in all three principal directions to a rectangular prismatic specimen. The indentation tests were performed on cubic specimens of freshwater granular and S2 columnar ice at two different temperatures, –10˚C (27 tests) and –40˚C (2 tests).

Sample preparation

In order to prepare the specimens, blocks of bubble-free, freshwater columnar S2 ice (with column diameter ranging between 2 – 10 mm) were crushed using a commercial ice crusher. The crushed ice was sieved to obtain grains in the range 1–2.4 mm. Bubble-free columnar S1 ice was used to prepare larger grains, in the range of 2–4 mm and 4–6 mm. (*S2 ice possesses a crystallographic growth texture in which c-axes are randomly oriented in a plane that is perpendicular to the growth direction; i.e., the horizontal plane. S1 ice has c-axes parallel to the growth direction*).

The granular ice was grown in a cold room using a mixture of crushed ice and deionized, deaerated water. The mixture was held in a 160 × 160 × 260 mm aluminum mold under radial freezing for approximately 14 h. This procedure was similar to that described in Golding et al. (2010). The only difference was that the mould was not held under vacuum prior to flooding with water. This simplified procedure resulted in granular specimens that were similar to those produced using the procedure in Golding et al. (2010). One to two days prior to testing, the ice was machined into cubes approximately 146 mm on edge using a horizontal mill, ensuring parallelism of opposing sides. The edge of 146 mm is the largest allowable size by the experimental setup. The finished ice specimens were semitransparent and free from cracks; residual gas was visible along grains interface. At –10˚C the measured density was 911±7 kg m^{-3}, implying porosity of 0.82±0.01 %. The columnar S2 ice was grown in an insulated tank to affect unidirectional freezing, as described by Smith and Schulson (1993). Samples of freshwater columnar S2 ice were of the same size as granular ice specimens. The density of S2 ice samples was 917.8±2.2 kg m^{-3} at –10˚C, porosity of 0.120±0.002%.

Testing setup and instrumentation

All indentation tests were performed using the MATS. The test setup is shown in Figure 14. The indenter was attached to the upper vertical actuator of the MATS. The ice sample was placed and carefully centered on the test platform. By slowly moving the vertical actuators, the indenter was brought into contact with the specimen. For all tests (except EK1-2, EK1-3 and EK1-4), at this point the applied vertical load was approximately 0.02 – 0.05 kN. At this step no visible ice damage was detected. The tests were performed on both unconfined and confined specimens. In the confined tests the ice was prevented from moving horizontally using aluminum extenders (140 × 140 × 20 mm^3) attached to the X and Z loading platens; see Figure 14a. Figure 14b is a photograph of the experimental apparatus.

In all tests a constant displacement rate was applied in the Y direction to the two opposing actuators operating in tandem. The displacements in the horizontal directions were kept at zero. Shear stresses created during this setup procedure and acting on the vertical edges of the ice specimen were considered to be small (<< 0.1 MPa) and appear to exert little influence on either the fracture mode or peak stress. Boundary conditions are an important factor when considering ice deformed in a brittle manner (Weiss and Schulson, 1995) and this experimental setup was an attempt to simulate ice behavior during a realistic situation (see the ULS illustration in Figure 4, for example).

In unconfined tests EK1-2, EK1-3 and EK1-4, the ice sample from EK1-1 was used and the testing procedure was slightly different from that described above. After the test EK1-1, photographs of the damaged sample were taken and the indenter was brought

to its initial position, corresponding to the beginning of the test. The test EK1-2 was performed on the same ice sample by indenting into the same indent and subsequent returning of the indenter to its initial position. Tests EK1-3 and EK1-4 were performed by indention into the indent that was left from the test EK1-2 and EK1-3, respectively. The aforementioned unconfined tests were conducted as pilot tests in order to check overall system performance.

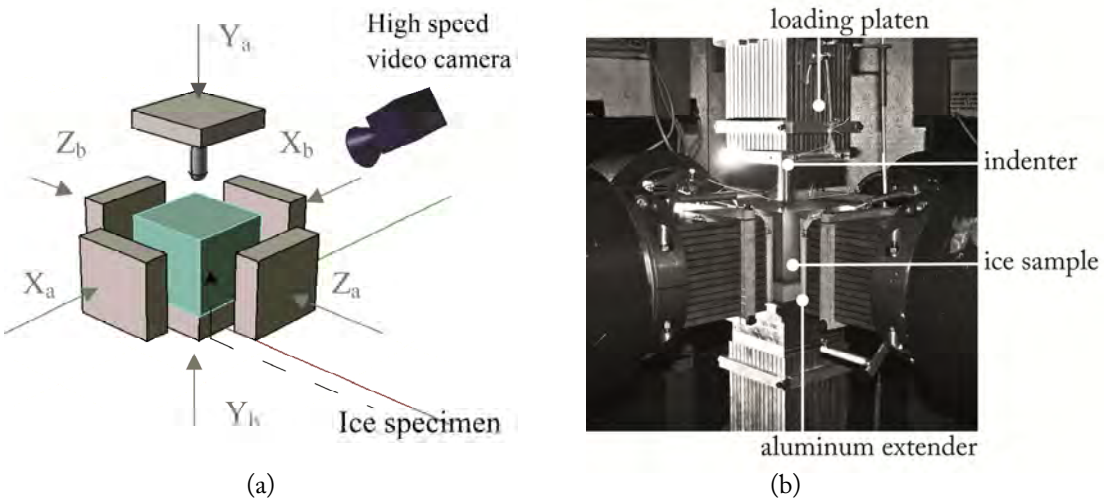

Figure 14: (a) Schematic and (b) photograph of the experimental apparatus and the loading geometry; X, Y and Z denote the directions of the moving actuators.

All tests were controlled and recorded using MATS. During a test, the total load and displacement of actuators in each of the six directions were recorded by the MATS. In each test, the data acquisition rate was varied between 40 to 2000 Hz, depending on the length of the tests and system limitations. A 90 kN load cell was found to be sensitive enough to record load variations. For the tests EK20 – EK23 the video recording system consisted of a Photron FASTCAM APX – RX high-speed camera. The frame rate for all tests was set to 1500 fps with resolution of 1024 × 512 pixels. The chosen frame rate was large enough to find a correlation between a single indentation event and the load signal. The video records were manually synchronized with the data acquisition system (the quality of achieved synchronization is approximately 0.2 s). Each impacted specimen was photographed immediately after each test. In order to prevent sintering of powdered ice with the crater created during indentation, the ejected material was carefully brushed away and the ice samples were stored at –10°C prior the examination of microstructure. The detailed altered ice microstructure was obtained by examining thin sections from all of the indented ice specimens. Examining the thin sections provided additional information on the ice microstructure at the end of the indentation process. The thin sections were photographed through cross-polarized filters.

Test parameters

A total of 29 tests (including pilot tests and tests with S2 columnar ice) were performed using different indentation depths, indenter speeds, radius of the indenter and ice temperatures. The parameters of each test are summarized in Table 5. In the tests two semi-spherical indenters were used with diameters of 25.4 mm and 10 mm made from highly polished stainless steel 304. The choice of indenter shape was based on a discussion provided in Fischer-Cripps (2000). In laboratory indentation tests of ice plates made from freshwater S2 ice, Michel and Toussaint (1977) used a rectangular indenter. Grape and Schulson (1992) used a flat indenter in indentation tests of columnar ice. In small-scale laboratory experiments on the indentation failure of polycrystalline ice, Barrette et al. (2003) and Wells et al. (2011) used a spherical indenter. In reviewing experimental data, it was found that in indentation experiments, dating back to 1980-90s, flat punches were used mainly. Resent work (Barrette et al., 2003; Mackey et al., 2007; Wells et al., 2011) used spherical indenters. We believe that with a spherical cap an expansion of the contact area during indentation is a better representation of a practical situation; e.g., of an interaction of a ship-shaped structure with thick rafted ice, multiyear ice or icebergs. Furthermore, in Johnson (1985), for rigid-perfectly-plastic solids, minimum dimensions of the indented block are recommended to insure that the indentation is not influenced by the size of the block. Accordingly, for curved indenters the minimum width of the block should be at least $6.4r - 17.4r$ and the minimum depth is $3.4r - 8.8r$, where r is radius of the indenter. For a cubic block 146 mm on edge, this consideration would suggest a radius of indenter of about 15 mm (30 mm diameter). An additional concern was to have a sufficient number of grains at the ice-indenter interface. Michel and Toussaint (1977) suggested that the indenter width should be more than 7 grain diameters to avoid a "size effect". Taking the aforementioned points into account, we concluded that an indenter of 25.4 mm in diameter has a size small enough in relation with the block size and has a size big enough to create an indent that is large enough to be examined microstructurally.

Once the indenter fully enters the ice, it spans at least 7 grains with sizes in range 1–2.36 mm and 2–4 mm. Indentation was performed at different displacement rates ranging between $5.08 \cdot 10^{-2}$ mm/s and 5.08 mm/s; see Table 5. The majority of the experiments were performed at 5.08 mm/s. The higher rates used in the present experiments correspond to the brittle-like regime in the ice. The lower rates were chosen to study ice behavior within the ductile regime.

Examination of microstructure

To detail the altered ice microstructure within the indentation zone, thin sections were examined from all indented ice specimens.

Table 5. Summary of experimental conditions and results.

Test no.	Grain size d (mm)	Temperature T_i (°)	Radius of indenter r (mm)	Maximum penetration u_{max} (mm)	Speed v (mm s^{-1})	Sampling rate (Hz)	Maximum load F_{max} (kN)	Displacement at F_{max} (mm)	Lateral confinement of ice	Large-scale fracture before the maximum penetration	Cracks running to the edges	Failure pressure $p_f{}^a$ ($p_f{}^b$)	Effective pressure $\bar{p}$ (σ_p) (Mpa)
Experimental conditions							*Results*						
EK1-1	4 to 6	-10	12.7	1.0	5.08	2000	2.74	0.2	No	No (B)	No	-(145)	- (-)
EK1-2	4 to 6	-10	12.7	2.0	5.08	2000	3.87	2.0	No	No (B)	No	-(-)	- (-)
EK1-3	4 to 6	-10	12.7	5.1	5.08	2000	5.00	4.3	No	No (B)	No	-(-)	- (-)
EK1-4	4 to 6	-10	12.7	7.1	5.08	2000	7.17	6.9	No	Yes (B)	Yes	-(-)	- (-)
EK3	4 to 6	-10	12.7	12.7	5.08	2000	No data	No data	No	No data	Yes	No data	- (-)
EK4	1 to 2.4	-10	12.7	12.7	5.08	2000	No data	No data	No	No data	Yes	No data	- (-)
EK5	1 to 2.4	-10	12.7	12.7	5.08	2000	6.61	5.2	No	Yes (B)	Yes	20.2 (116)	- (-)
EK6	1 to 2.4	-10	12.7	12.7	5.08	2000	5.65	3.9	No	Yes (B)	Yes	21.3 (164)	- (-)
EK7	1 to 2.4	-10	12.7	12.7	5.08	2000	9.47	11.9	Yes	No (B)	Yes	21.3 (119)	- (-)
EK8	1 to 2.4	-10	12.7	12.7	5.08	2000	10.78	11.9	Yes	No (B)	Yes	17.4 (124)	- (-)
EK9	1 to 2.4	-10	12.7	1.0	5.08	2000	1.74	0.2	Yes	No (B)	No	-(105)	- (-)
EK10	1 to 2.4	-10	12.7	5.1	5.08	2000	5.48	3.0	Yes	No (B)	No	-(31.2)	- (-)
EK11	1 to 2.4	-10	12.7	7.6	5.08	2000	8.13	4.8	Yes	No (B)	Yes	24.5 (115)	- (-)
EK12	1 to 2.4	-10	12.7	1.0	0.0508	500	3.52	1.0	Yes	No (D)	No	**(**)	- (-)
EK13	2 to 4	-10	12.7	12.7	2.8	1000	6.56	12.7	Yes	No (B)	No	-(53.9)	- (-)
EK14	1 to 2.4	-10	12.7	12.7	0.508	400	13.30	11.4	Yes	No (D)	Yes	28.8 (**)	- (-)
EK15	1 to 2.4	-10	12.7	12.7	0.0508	40	9.56	12.5	Yes	No (D)	Yes	21.8 (**)	- (-)
EK16	2 to 4	-10	12.7	20.0	5.08	2000	8.39	10.4	Yes	No (B)	Yes	20.9 (131)	9.5 (3)
EK17	1 to 2.4	-10	5.0	1.0	5.08	2000	1.35	0.7	Yes	No (B)	No	-(240)	- (-)
EK18	1 to 2.4	-10	5.0	5.1	5.08	2000	2.09	5.0	Yes	No (B)	No	-(42.0)	- (-)
EK19	1 to 2.4	-10	5.0	15.0	5.08	2000	3.26	10.2	Yes	No (B)	No	-(46.1)	22.7 (7.0)
EK20	4 to 6	-10	12.7	20.0	5.08	2000	No data	No data	Yes	No data	Yes	No data	No data
EK21	1 to 2.4	-10	12.7	20.0	5.08	2000	No data	No data	Yes	No data	Yes	No data	No data
EK22	S2 (across col.)	-10	12.7	5.1	5.08	2000	3.48	3.3	Yes	No (B)	Yes	- (88.3)	- (-)
EK23	1 to 2.4	-10	12.7	20.0	5.08	2000	10.60	14.5	Yes	No (B)	Yes	19.5 (112)	12.8 (3)
EK24	S2 (across col.)	-10	12.7	5.1	5.08	2000	3.65	4.6	Yes	No (B)	No	- (40.7)	- (-)
EK25	S2 (along col.)	-10	12.7	5.1	5.08	2000	6.52	4.9	Yes	No (D)	Yes	* (**)	- (-)
EK26	1 to 2.4	-40	12.7	1.0	5.08	2000	2.87	0.9	Yes	No (B)	No	- (190)	- (-)
EK27	1 to 2.4	-40	12.7	1.0	5.08	2000	2.17	0.8	Yes	No (B)	No	- (99.0)	- (-)

* load is transmitted in horizontal direction at t=0.

** there is no pronounced peak in the registered load signal

B, D - brittle or ductile dominating behavior

For each specimen, thick sections (approximately 1 cm) were cut perpendicular to the indented surface using a band saw. They were cut as close to the center of the indentation zone as possible. The sawed surfaces were gently melted from both sides to a thin section slide (approximately 1 mm). In order to melt the thin section to a desired thickness, the ice was bonded to a piece of glass, and then melted by using a wetted glass plate. The entire procedure was performed in a cold-room held at –10°C. Thin sections were photographed through cross-polarized filters.

Comparison of thin sections taken from the undamaged virgin ice with those sampled from the indentation zone showed that no cracks or changes in microstructure were introduced by the sectioning procedure described.

3.1.2 Results and analyses

Figure 15 shows an example of a force vs. displacement curve that was registered during the confined experiments at loading rates above 2.8 mm/s.

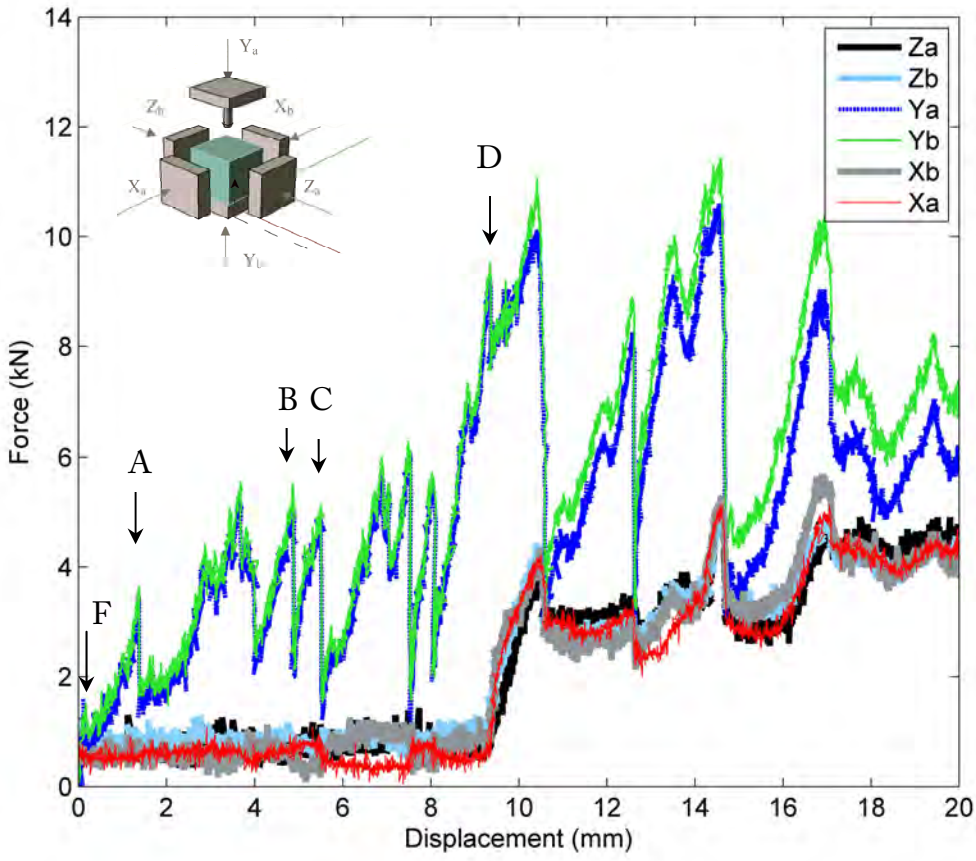

Figure 15: Force vs. vertical displacement registered in *X*-, *Y*- and *Z*-directions during a confined test using an indenter of radius 12.7 mm at a speed of 5.08 mm/s and a temperature of –10°C.

The registered load signals shown in Figure 15 are typical of those tests made under confinement at higher indentation rates and larger penetration depths. In most of the tests there is an agreement between the load traces recorded in the direction X_a (Z_a) and X_b (Z_b).

Figure 16 shows consecutive images taken by the HSV camera of the freshwater granular ice under confinement. The images "a–d" correspond to the spalling events A–D that are shown in Figure 15. Note that HSV could only be used to analyze the external appearance of the indentation process. In addition, observation of crack propagation in ice was limited by the chosen frame rate (1500 fps). Examining the HSV recordings in conjunction with the force-time history enabled us to relate some of the physical processes to the total load.

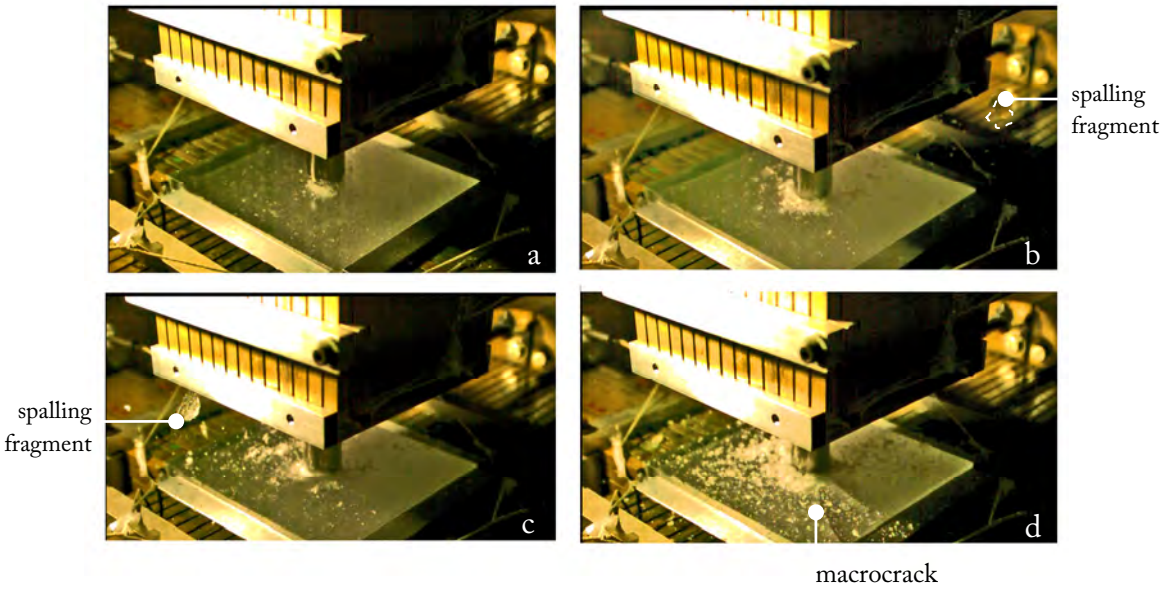

Figure 16: Frames extracted from high-speed video recording of the test shown in Figure 15. Fast ejection of crushed ice resulted in load-drop in *Y* direction. Development of the radial crack running to the edge contributed to the load-drop in *Y* direction and subsequent load-rise in *X*, *Z* direction.

The abrupt load-drops are a result of spalling events, when ejected ice fragments are expelled from the indentation zone and cracks radiated away from the indentation zone. The average indentation pressure was roughly estimated as force divided by the projected contact area, A_n, and is a function of the vertical displacement of the indenter. Projected area was calculated as $A_n = \pi u(2r-u)$, where u is the vertical displacement of the indenter. An example of calculated curves of pressure (average indentation pressure) vs. displacement (curve 2) and registered load vs. displacement (curve 1) is shown in Figure 17.

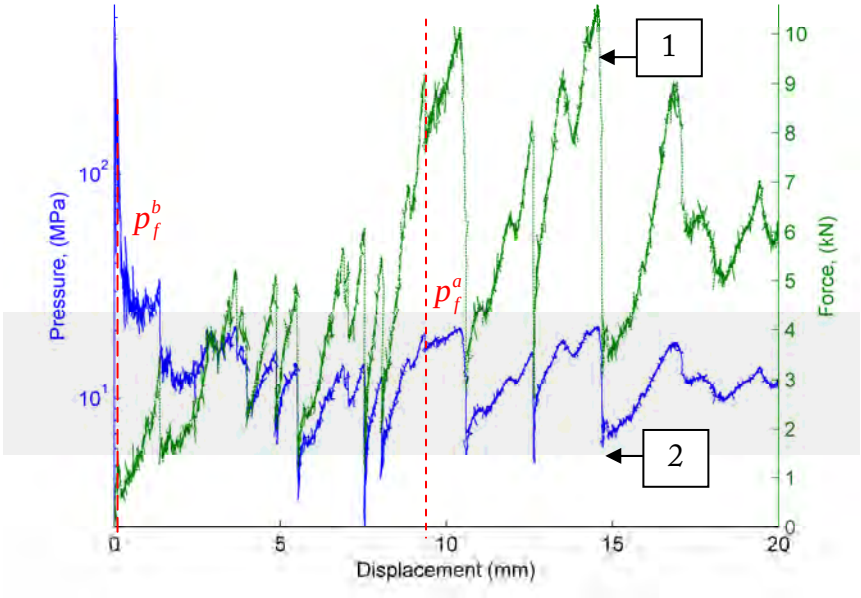

Figure 17: Registered force versus displacement (curve 1) and calculated effective pressure versus displacement (curve 2) for the confined test EK23 shown in Figure 15.

The maximum pressure occurred at the beginning of each experiment and decreased with increasing contact area. As at the beginning of the test, the pressure is highly localized. One may argue that pressure at the beginning of each test could be as high as the theoretical ice strength that is roughly approximated by $0.1E$ (Parameswaran and Jones, 1975 and Renshaw and Schulson, 2007), where E is Young's modulus. As may be seen from Figure 17, the maximum load registered during the tests does not correspond to the maximum pressure. Hence, the question arises: how to define failure pressure for the case of confined tests? In this study, under failure pressure two definitions will be considered, as follow:

A. Failure pressure, p_f^a, is the average pressure corresponding to the moment of expansion of ice in either of X or Z direction due to a macro-cracking event. In Figure 15 this moment is shown; see label "D".
B. Failure pressure, p_f^b, is the average pressure corresponding to the first pronounced peak taken from the vertical load vs. displacement curve (Figure 15; see label "F").

Both values of failure pressure for all tests are reported in Table 5.
Mean value, $\overline{p}$, and standard deviation, σ_p, of the indentation pressures that correspond to a constant contact area during the test are also reported in Table 5. $\overline{p}$ and σ_p were calculated as:

$$\overline{p} = \frac{1}{N}\sum_{i=1}^{N} p_i(u_i) \tag{5}$$

and

$$\sigma_p = \sqrt{\frac{1}{N-1}\sum_{i=1}^{N}\left(p_i(u_i) - \overline{p}\right)^2} \tag{6}$$

where N is a total number of measurements, p_i is the contact pressure at the penetration depth, u_i, (for the indenter r =12.7 mm, 12.7≤ u_i ≤ 20 mm and for the indenter r =5 mm, 5≤ u_i≤ 15 mm).

Each test was reviewed individually. The characteristic results of the individual experiments are described below.

Effect of indentation speed

The failure behavior was found to be rate dependent (similar to Wells et al. (2011)). Figure 18 shows representative force vs. displacement curves registered during the confined experiments performed with maximum displacement of 12.7 mm at different indentation speeds.

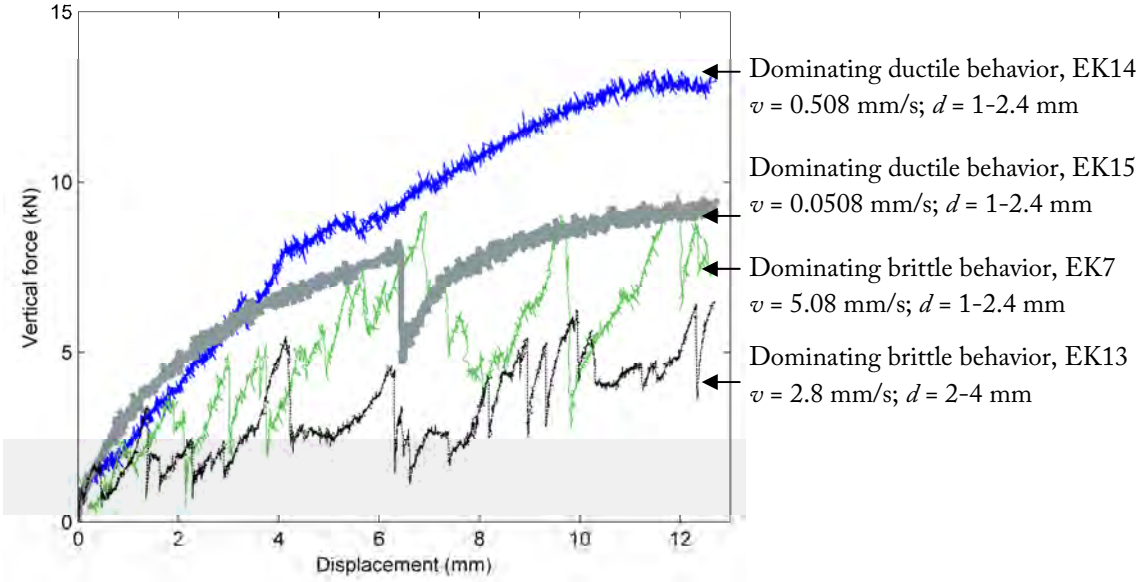

Figure 18: Force versus displacement registered at −10°C and at different indentation speeds, v, for the indenter r =12.7 mm; d is the grain size.

Ductile behavior dominated for the slow indentation speeds (0.0508 and 0.508 mm/s) and was characterized by smooth variations in the recorded force, by extrusion of powdered ice (crushing) and by little (or no) spalling. In this regime the vertical force rose in time. An example of this type of behavior is shown in Figure 18. At higher rates, brittle-like behavior was registered with an abrupt decrease in ice force and a production

of large spalls and crushing; see Figure 18. Remarkably, as observed also Wells et al. (2011), the extent of the ductile regime decreases with increase of indentation rate. At high rates (>2.8 mm/s) brittle-like behavior dominates throughout the entire indentation. The appearance of the indented surface at different indentation rates is shown in Figure 19.

The effect of the indentation speed may be summarized as the following:

(i) Strong effect of the indentation speed on characteristic behavior of ice, i.e., ice appears to fail in the dominating brittle regime at higher indentation rates.

(ii) Weak effect of the indentation speed on ice failure pressure, i.e., lower indentation rates lead to slightly higher values of ice failure pressure p_f^a; see Table 5.

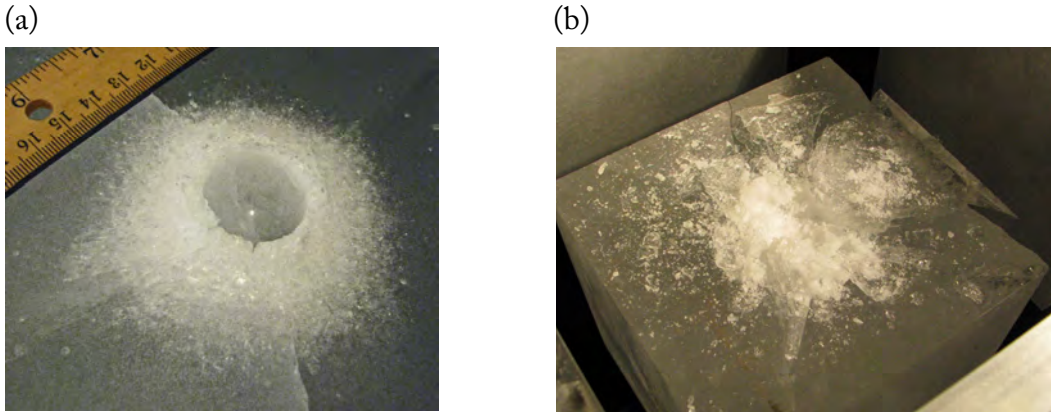

Figure 19: Photographs of the indented surface of confined ice at –10°C: (a) after u_{max} =12.7 mm with indenter speed v =0.0508 mm/s (test EK15); (b) after u_{max} =20 mm with indenter speed v =5.08 mm/s (test EK20).

Effect of confinement

Figure 20a shows typical force versus displacement curves registered during confined and unconfined experiments at the indentation rate of v=5.08 mm/s with maximum displacement of 12.7 mm.

At penetration depths of 12.7 mm, the failure was dominated by the development of large radial cracks. During the unconfined tests, the ice failed by splitting, and the load could no longer be maintained. During the confined tests, global failure of ice was suppressed due to the aluminum plates preventing ice movement in the lateral directions. In this case, radial cracks developed, but the force continued to vary in a cyclic crushing/ejecting manner.

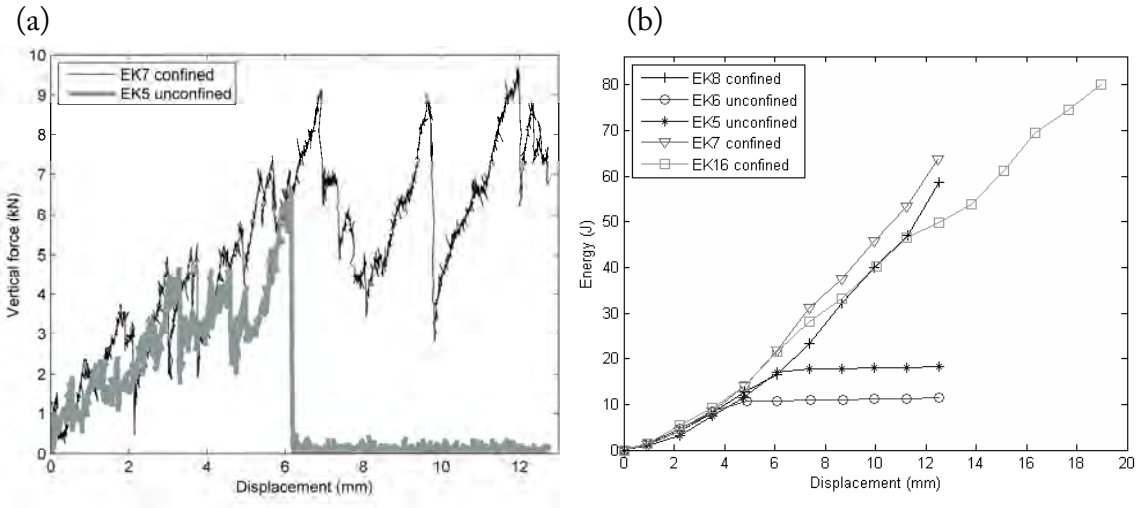

Figure 20: Effect of confinement for tests at −10°C with an indenter speed of 5.08 mm/s. (a) Force versus displacement curve registered during tests with and without confinement. (b) Total energy, required to penetrate the ice versus displacement.

To understand further the difference in the behavior of unconfined and confined ice, it is reasonable to look at the energy involved in the ice indentation process; see Figure 20b. Energy $E(u)$ plotted in Figure 20b for unconfined and confined tests was calculated using force-displacement records as:

$$E(u) = \int_0^u F(u)du \tag{7}$$

where $F(u)$ is a force-displacement record.

The calculated value of $E(u=u_0)$ is the energy involved in the whole process of ice indentation to a depth u_0 and represents the energy absorption capacity of ice.

The forces registered in the lateral directions (X and Z) were always lower than the forces registered in the direction of indentation (Y – direction). For each confined test, maximum values of the lateral forces normalized to the maximum force in Y– direction (F_{max}) are plotted in Figure 21. From Figure 21 it can be seen that partly fractured ice is capable of transmitting the forces in lateral directions in a symmetric bilateral manner $F^x_{max} \approx F^z_{max}$. This suggests that the ice fracture is symmetric about the Y loading axis.

The effect of confinement may be summarized as follows:

(i) There is a strong effect of confinement on the energy absorption capacity of ice. Confined ice, where global failure by splitting is suppressed by the boundary conditions, can absorb more energy; see Figure 20b.

(ii) There is a weak effect of confinement on the failure pressure, p_f^a (Table 5). There are almost no differences between failure pressures for unconfined ice (p_f^a=20–21 MPa) and for displacement limited confined ice (p_f^a=17–21 MPa).

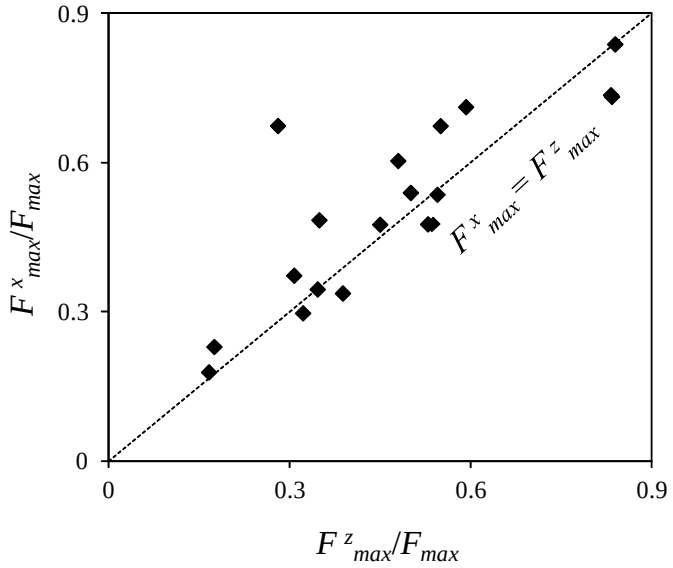

Figure 21: Normalized values of the maximum lateral forces in X and Z directions, i.e., F^x_{max} and F^z_{max}, respectively, registered during the indentation tests under confinement. The dashed line corresponds to the situation of $F^x_{max} = F^z_{max}$.

Effect of penetration depth

For the indenters r=12.7 mm and r=5 mm and for penetrations less than the radius of the indenter, the maximum indentation load increases with increasing penetration depth (see Table 5, Figure 15 and Figure 18). Conversely, the pressure that corresponds to the maximum indentation decreases with increasing penetration depth. For the smaller indenter, radial cracks running to the edge were not been observed even at 15 mm penetration depth at v=5.08 mm/s, while for the larger indenter these edge cracks appear after a penetration of approximately 7 mm. In summary, there is a strong effect of the penetration depth on the maximum load and pressure.

Effect of indenter size

At the same penetration depth, the area of contact in the case of a smaller indenter is less than that for the bigger indenter. Also, for the small indenter the area of contact increases with penetration slower than that for the larger indenter.

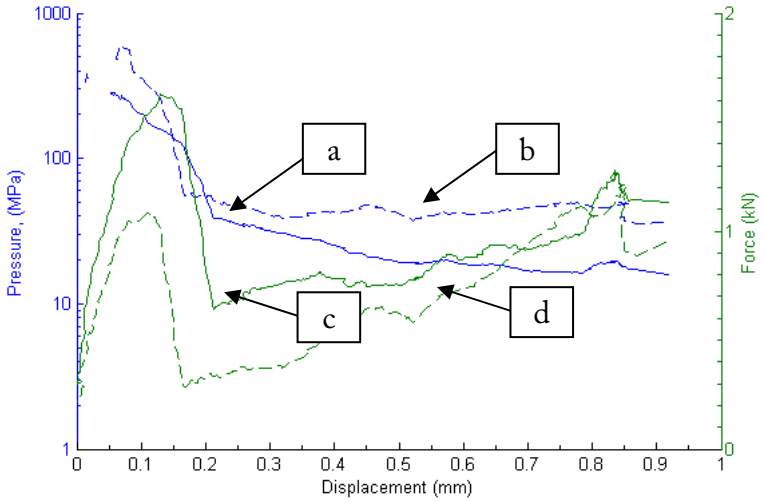

Figure 22: Force vs. displacement (c, d curves) and decadic logarithm of calculated pressure versus displacement (a, b curves) for confined tests EK9 and EK17 with different indenters at –10°C. Solid lines represent tests with indenter of r=12.7 mm; dashed lines – with indenter r=5 mm.

For different indenters and for a penetration depth of 1 mm, curves of force vs. displacement and pressure vs. displacement (smoothed) are shown in Figure 22 for v=5.08 mm/s.

From Figure 22 it can be seen that the peak vertical force for the larger indenter is slightly larger than that for the smaller indenter. The pressure, corresponding to the peak force, is larger for smaller indenter. For penetration depths ≤1 mm, the indentation pressure for smaller indenter is sometimes lower and sometimes higher than that for the larger indenter and depends on the test run. The variations for small depth could reflect the number of grains in the contact area or an error introduced in calculating the contact area.

Visual inspection of indented samples revealed that the appearance of the damage zone at 1 mm and 5 mm penetration for the larger indenter was almost indistinguishable (apart from the size of the indent) from that for the smaller indenter. It can be characterized by a transparent zone in the middle, surrounded by ejected, highly pulverized ice. Since for smaller indenter (i) no radial cracks ran to the edges of the ice sample after a 15 mm penetration depth and (ii) lateral Z, X loads were constant (approximately 0.5 kN) during the indentation process, it might be concluded that for the smaller indenter, there were not any effects of lateral confinement on the ice failure process.

Therefore, the effect of the indenter size can be summarized as follows:

(i) There is a strong effect of indenter size on the vertical load; i.e., the smaller indenter results in lower forces.

(ii) There is a weak effect on the ice behavior and on the average pressure during indentation; i.e., both small and large indenters result in similar ice failure behavior (crushing, spalling, etc.) and have relatively close values of indentation pressure.

Evolution of damage

It was found that the damage zone, localized in front of the indenter, is marked by dynamic recrystallization and microcraking (Figure 23). For the indenter of r =12.7 mm moving at a velocity of 5.08 mm/s into confined ice, recrystallized grains were found at 1 mm penetration depth. The recrystallized grains are always small (approximately 0.5–0.2 mm); see Figure 23a. The recrystallized grains were observed at full indent width. Microcracks intensify around the indentation zone; see Figure 23b.

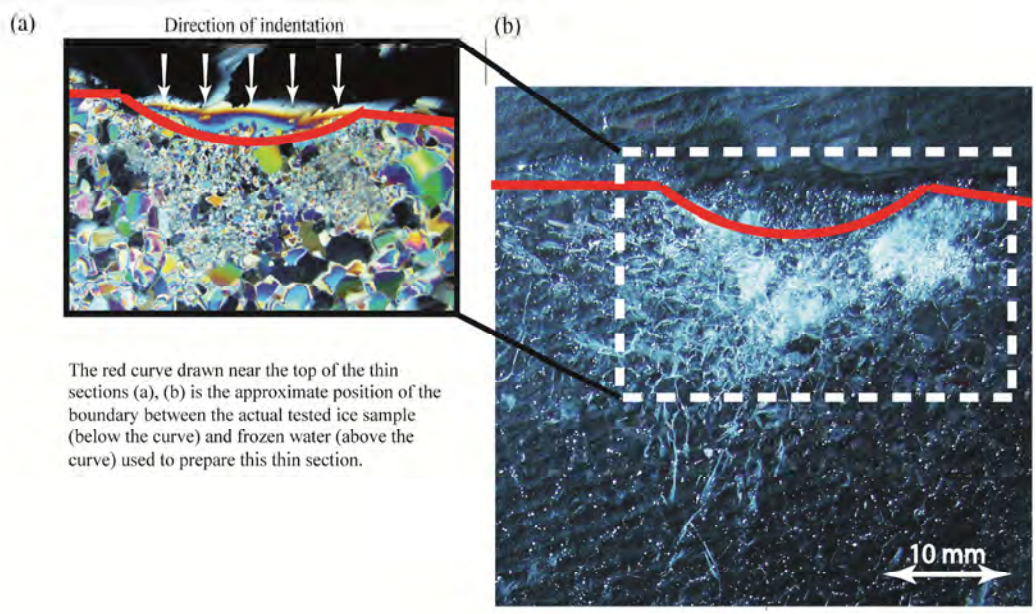

Figure 23: Photographs of the damage zone in confined ice at –10°C after an indentation of 12.7 mm at v=5.08 mm/s using punch of r=12.7 mm (test EK7): (a) – appearance of the damage zone under cross-polarized light; (b) – damage zone under ordinary light. In the damage zone, an aggregate of small recrystallized grains scatters light strongly and appears white, while the surrounding ice remains relatively transparent. The short, whitish lines are arrangements of microcracks.

With an increase of the penetration depth, the damage zone expands downwards and in both lateral directions. It was observed that after the indentation the surface of the contact zone was glossy. This glossy appearance of the contact zone might be evidence for the occurrence of local melting at the ice-indenter interface. The underlying possible mechanisms are melting due to frictional heating, intrinsic premelting and, less likely,

pressure melting, as discussed by Timco and Frederking (1995), Gagnon (2008b), Li and Somorjai (2007).

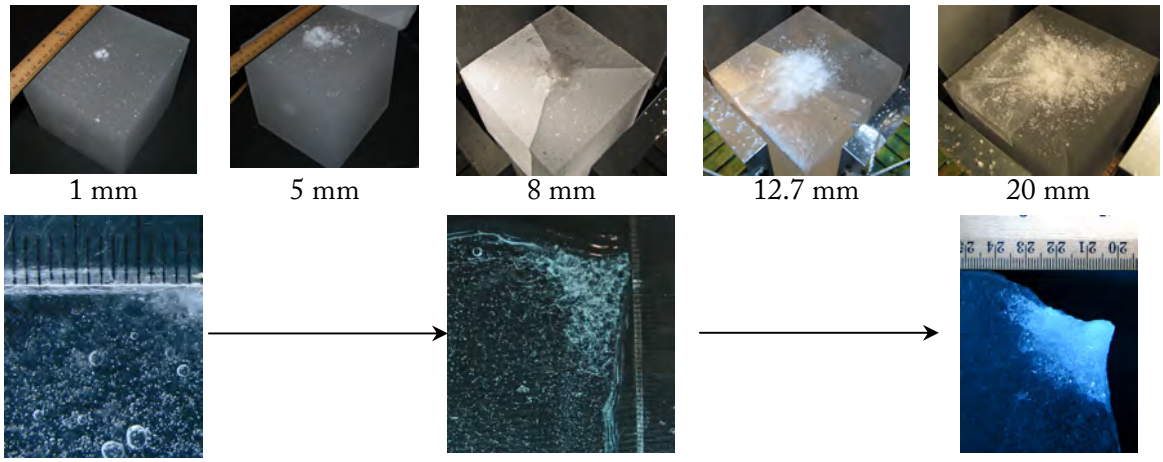

Figure 24: Evolution of damage of the confined ice at –10°C and v=5.08 mm/s. The upper images are photographs of the ice sample immediately after the test and correspond to different penetration depths. Lower images are fragments of vertical thin sections from the indentation zone of the image above.

Figure 24 shows development of damage in confined ice at –10°C and v=5.08 mm/s for the indenter of radius r=12.7 mm. It can be seen that the formation of radial cracks starts at penetration depth between 5 mm and 8 mm. As radial cracks formed, confined ice does not fail by splitting (the case with unconfined ice), but rather continues to deform. At this moment the load registered in the lateral directions starts to build up (Figure 15, point D) and load registered in the vertical direction does not increase further but becomes rather cyclic in nature.

Figure 25 shows vertical thin sections of the damage zone in S2 columnar freshwater ice together with the force vs. displacement curves. Wing cracks in Figure 25c are evidence of brittle compressive failure under low/moderate levels of confinement and are similar to those observed by Grape and Schulson (1992) during indentation of S2 ice with a flat indenter. Since we performed very few experiments on columnar grained ice, further discussion will be mainly focused on the results for the granular ice. Nevertheless, it is interesting to note that for the same penetration depth of 5 mm the entire column recrystallizes during indentation along the columns (Figure 25a), while during indentation across the columns only a few grains recrystallize. This is a manifestation of the fact that loading at some angle to the basal plane results in less recrystallization in comparison with loading along the basal plane.

For the purpose of comparison, Figure E1 in Appendix E presents a vertical thin section of freshwater columnar S2 ice impacted by a free-fall spherical projectile.

Effect of temperature

Figure 26 shows photographs of the ice surface of confined ice immediately after a 1 mm indentation at –10°C (on the left) and –40°C (on the right) using the larger (r=12.7 mm) indenter. Ice at –40°C seems to be more brittle than ice at –10°C, and few spalls were observed. Amount of powdered ice produced during two tests above seems to vary (slightly more at –10°C) as well as the size of the broken fragments (finer pieces at –40°C).

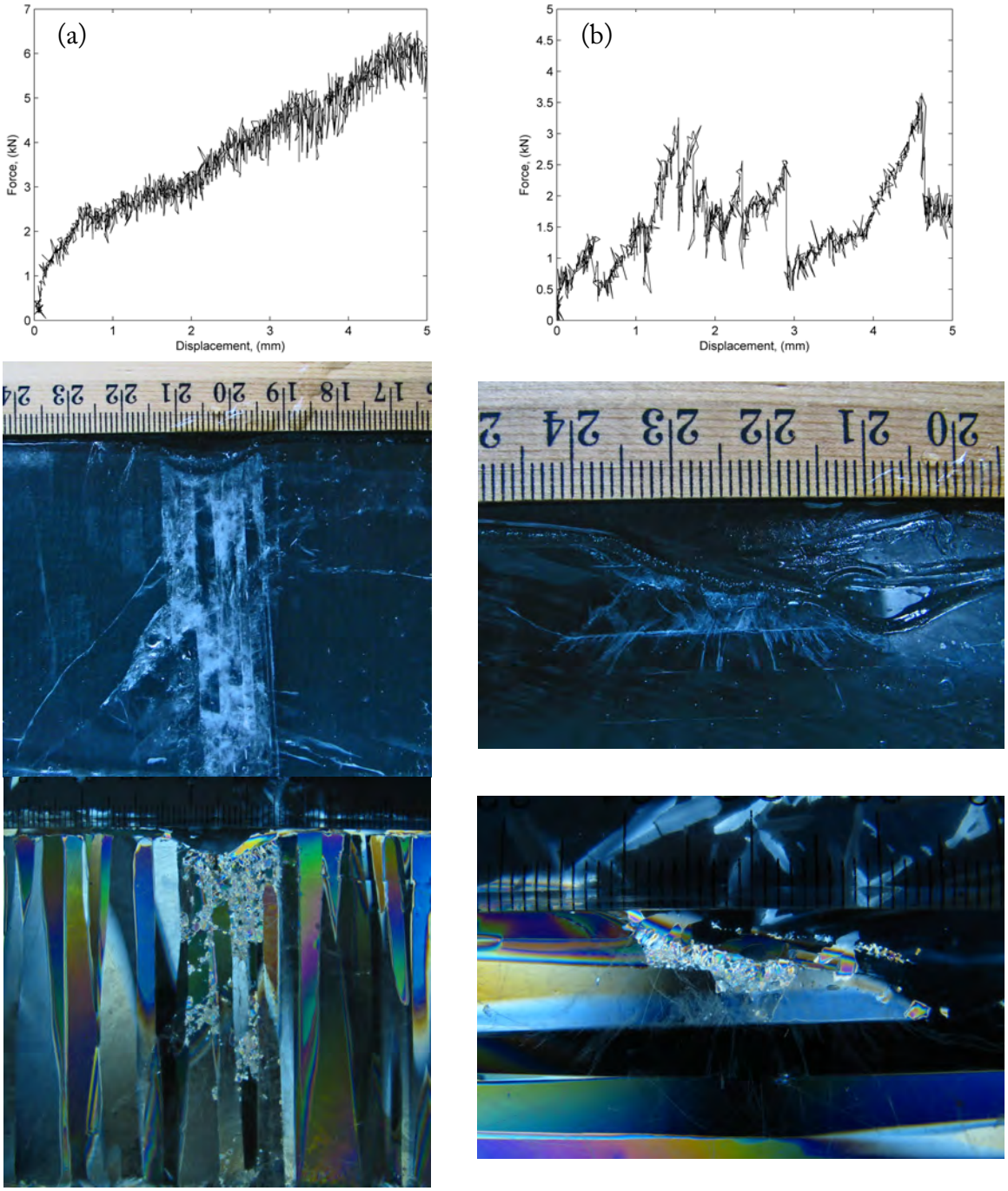

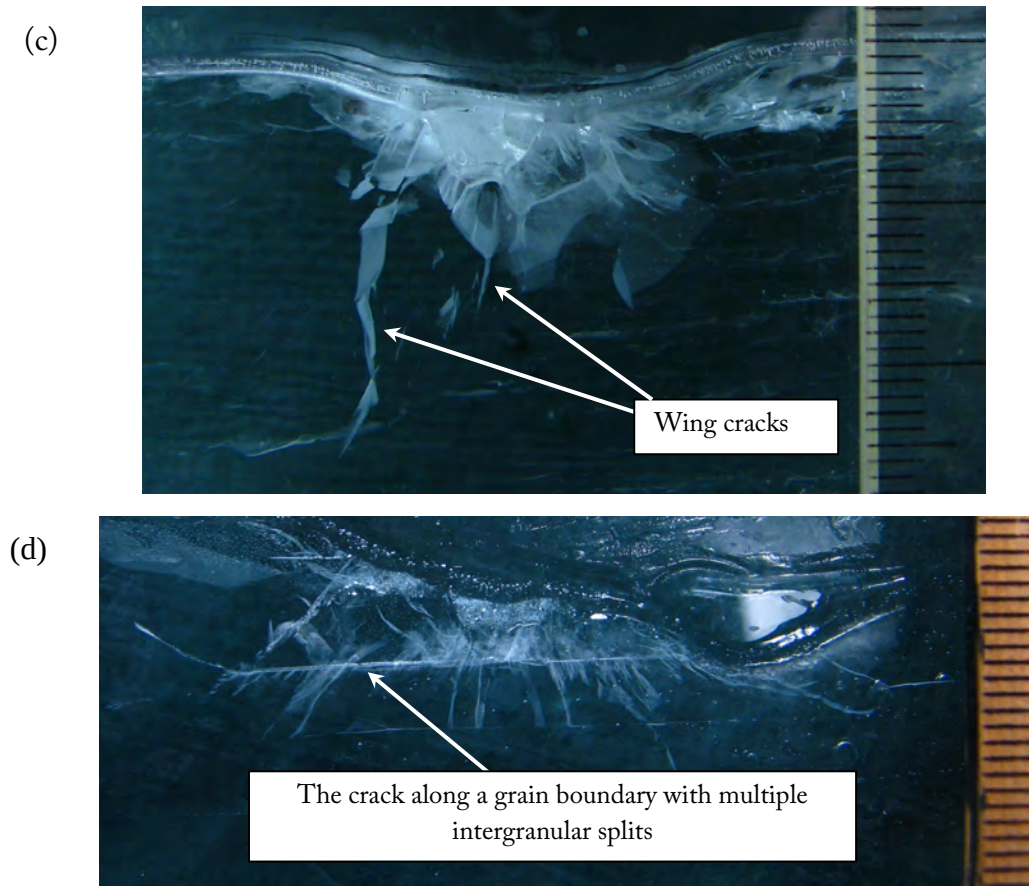

Figure 25: Photographs of the vertical section of the indentation zone in confined S2 columnar ice at – 10°C and corresponding load signal, for v=5.08 mm/s. (a) Indentation along the columns (test EK25); (b) indentation across the columns (test EK24); (c) and (d) magnified photographs of the mutually perpendicular vertical thin sections of damaged zone, indentation across the columns. Tick marks are spaced at 1 mm intervals.

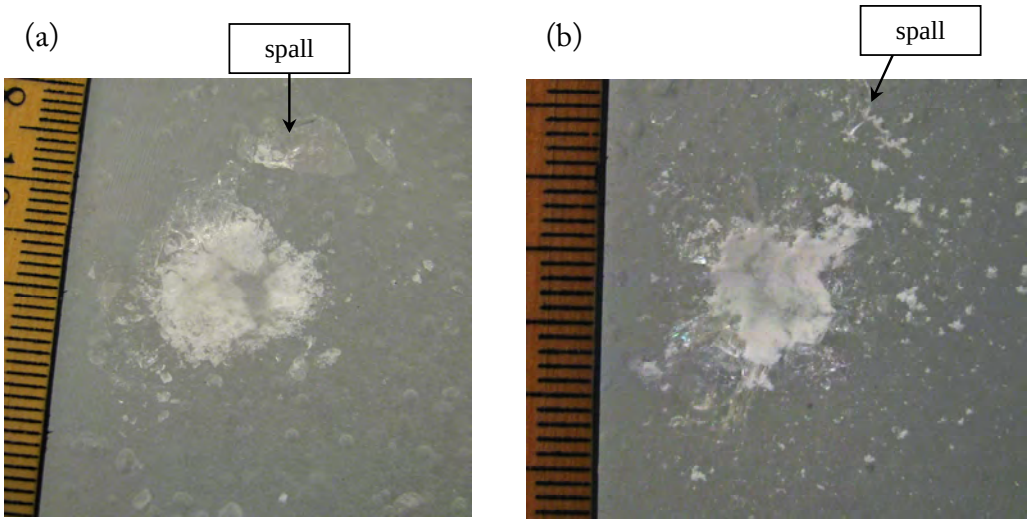

Figure 26: Appearance of the ice surface after 1 mm indentation at v=5.08 mm/s at –10°C, test EK9 (a) and at –40°C, test EK26 (b). Tick marks are spaced at 1 mm intervals.

A zone of intact ice (transparent spot in the middle of the indent) can be seen as relatively small compared with the overall appearance of the indent. The indent is surrounded by crushed and damaged ice. From corresponding vertical thin sections (Figure 27), it can be seen that the damage zone is localized in a semicircular region under the indenter and consists of recrystallized grains and microcracks.

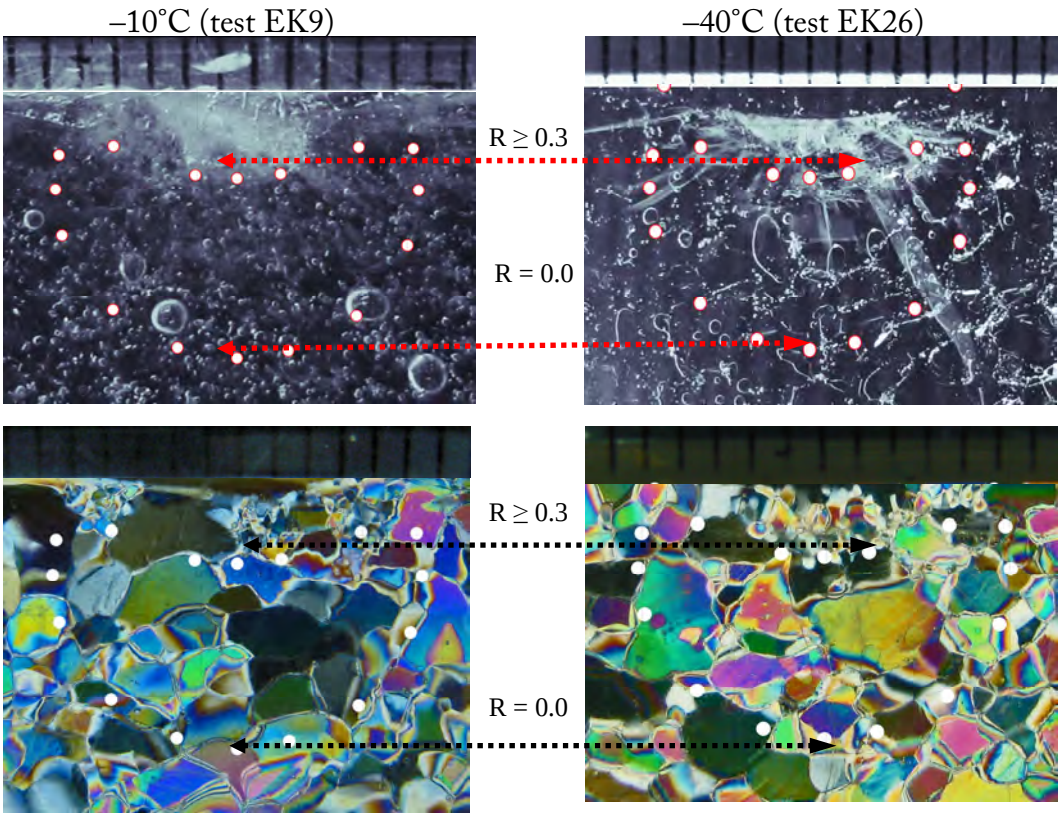

Figure 27: Vertical thin sections from the center of the indentation zone; white circles are superimposed on the original photograph showing the different levels of confinement *R*, which is defined as the ratio between the minor and the major principal stresses; tick marks are spaced at 1-mm intervals; indentation at a speed of 5.08 mm/s with a 12.7-mm indenter.

In Figure 28 force versus time and displacement versus time, corresponding to the indentation zone in Figure 27, are shown. It can be seen that there is almost no difference between the recorded load signal at –10°C and at –40°C. The total energy involved in the ice indentation process was estimated using Equation (7) for penetration depth of 1 mm. At –10°C the energy is 0.65 J (in the test EK9) and at –40°C it is 0.86 J and 0.71 J (in tests EK26 and EK27, respectively).

Hence, there is a weak effect of temperature on the peak load and ice failure behavior. However, there are more microcracking events at –40°C than at –10°C (Figure 27). This is a curious result. Colder ice is generally stronger than warmer ice when loaded

under multiaxial confinement (Schulson and Duval, 2009). On the other hand, we are considering a penetration depth of 1 mm to be a local failure process. On a more speculative note, we believe that at this penetration depth, the failure process is associated with the fracture toughness, which, in turn, varies little with temperature (see Schulson and Duval (2009)).

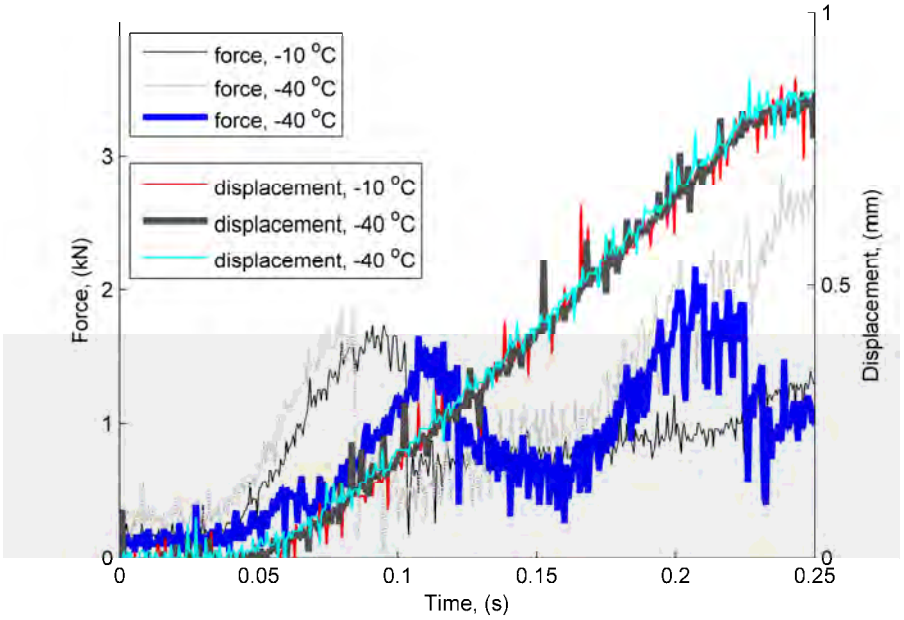

Figure 28: Force versus time and displacement versus time registered during the indentation into the ice at –10˚C and –40˚C, v=5.08 mm/s.

3.1.3 Discussion of results

Analyzing the visual observations together with the force history and the microstructural changes in the ice showed a cyclical ice response upon indentation that is described below.

Once the ice indentation process has started, the material under the indenter is no longer homogeneous. The ice began to deform in the vicinity of the contact zone. The ice was driven downwards and outwards in a hemispherical direction. Recrystallization and microcracking occurred almost immediately after indentation began (Figure 27). A layer of damaged ice was formed under the contact surface, and the crushing process began. In the high confinement zone, crack development was suppressed, and the damaged microstructure tried to rearrange into a new stress-free microstructure. The reported photographs of highly recrystallized grains just below the indenter (Figure 23a, Figure 25a, b and Figure 27) are a manifestation of this process. The material was expected to soften during the recrystallization process (see Burg et al., 1986). From Figure 25a, it can be seen that recrystallization along the columns dominated. On moving away from indenter to the zone of low and moderate confinement, the material

exhibits predominantly microcracking. Ice fragmentation was primarily dominated by local shear and tensile forces. The crushing process was accompanied by ice spalling and the ejection of ice fragments. The crushed (ejected) ice and localized spalls usually seen on the photographs (e.g., Figure 26) and on the video recordings (Figure 16) are the result of localized fracture events. Significant pile-up of ejecta appeared around the indenter. As the indentation process occurred, powdered ice moved in the vertical direction (opposite to the indenter direction of motion) and in both lateral directions (away from the indenter interface). The pile-up process was more pronounced at the lower indentation rates (i.e., within the regime of ductile behavior). During the pile-up process at the higher indentation rates, a part of the piled-up ice was removed from the indenter interface by frequently occurring spalling events.

As the indentation process proceeds further, the zone under the indenter (e.g., depicted in Figure 23) does not solely consist of recrystallized grains and bulk ice with microcracks (as it seems from thin sections). The crushed and consequently sintered ice could also appear as recrystallized grains under cross-polarized light.

After some volume of ice spalled out, the next cycle began. This cycle differed from the first cycle quantitatively rather than qualitatively because the ice in the indentation zone had a history from the previous cycles.

The load-displacement curves in Figure 15 reflect the complexity of the processes that were activated. The size of the spall appeared to be directly proportional to the magnitude of the spall induced load-drop.

An example of the ice fragments created during indentation is shown in Figure 29. The semicircular shape of the ice fragments in Figure 29 suggests that a ring crack formed from the fracture in the polycrystalline ice under spherical indentation. The cross-sectional view of the crack system around the spherical indentation (Figure 30a) was similar to that described by Hagan and Swain (1978) for brittle materials and is shown in Figure 30b.

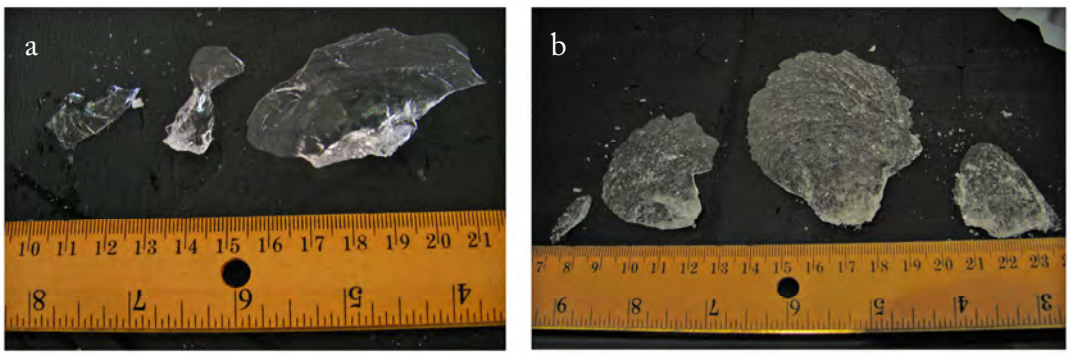

Figure 29: Photographs of ice fragments created during (a) indentation into columnar ice (i.e., indentation along the columns) at a speed of 5.08 mm/s and at a temperature of –10°C and (b) indentation into granular ice at a speed of 2.8 mm/s and at a temperature of –10°C.

The observations of ice failure and the micro-structural changes in the ice in the laboratory agreed well with those observed at large scales; see, e.g., Gagnon (1999) and Jordaan (2001). However, discrepancies were found between earlier observations and this study. For example, Gagnon (1999), Gagnon and Bugden (2007) and Gagnon (2008b) recorded and observed liquid water production during the crushing of laboratory-grown freshwater ice and iceberg ice.

Gagnon and Bugden (2007) performed experiments in which ice wedges were crushed against a flat rigid surface. The authors reported that a thin viscous layer formed at the contact zone. Using HSV recordings, the authors were able to observe wet crushed ice even at an ambient temperature of –10°C.

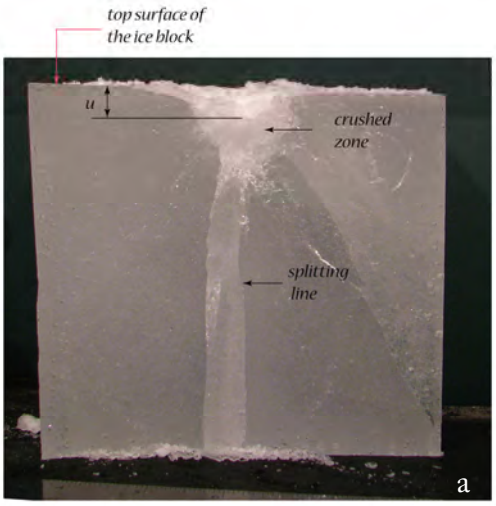

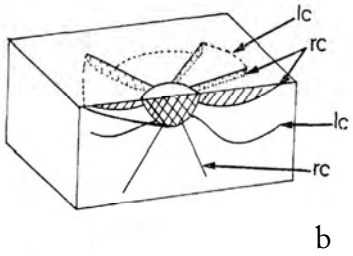

"rc" denotes the radial crack confined to the specimen surface; "lc" denotes the lateral crack (or the ring crack); the oval-hatched zone in the middle marks the extent of the deformed zone.

Figure 30: (a) Cross-sectional view of crack system around spherical indentation in polycrystalline freshwater ice at –10°C at a speed of 5.08 mm/s, where "*u*" denotes the penetration distance; (b) schematic of lateral and radial cracks around small-diameter indenters in brittle materials such as limestone, quartzite, granite, PMMA, hardened steel, soda-lime, calcium alumino-silicate, calcium aluminate glasses and soda-lime glass (source: Hagan and Swain, 1978).

In our experiments, the presence (or absence) of water could not be confirmed because of the experimental apparatus. Even if ice melted beneath the indenter and the melt was pushed out of the indentation zone, the melt would have appeared as tiny ice crystals (ejecta) in the HSV recordings. Other evidence for the presence of water would have been ice fragments (ejecta) with a smooth round shape. However, it was impossible to confirm the presence of liquid water at the ice-indenter interface from the photographs of ice fragments produced during the tests. However, the surface of the contact zone was glossy after indentation. This glossy appearance of the contact zone could indicate local melting at the ice indenter interface. Possible underlying mechanisms were melting from frictional heating, intrinsic premelting and pressure melting, which was a less likely mechanism.

Coulombic and plastic faults

The load registered during experiments synchronized with high-speed video recordings and ice microstructure obtained after the tests are evidence of the brittle and ductile fracture of ice. In the present study, ice showed characteristics of both ductile and brittle fracture (Figure 18). Here, under brittle fracture it is understood that material breaks without previous plastic deformation (i.e., without dislocation movement), and ductile fracture is associated with dislocation movement. To further our understanding of ice behavior during the indentation tests, a contact mechanics model was used to estimate the stress field beneath the indenter at the beginning of the experiments. The stress distribution under the indenter was estimated using an analytical solution given by Fisher-Cripps (2000).

At small penetration depths ($u<<r$), one might assume the validity of the Hertzian stress field. At 1 mm indentation depth, the confinement R ($R=\sigma_3/\sigma_1$, where σ_3 is least principal stress and σ_1 is highest principal stress) was estimated using the Hertzian solution for a case of hemispherical indenter and Poisson's ratio of 0.3 (Golding et al., 2011). The theoretical calculations, (R=0.3 and R=0), superimposed on the actual damage zone, are shown in Figure 27 for high-speed indentation and in Figure 31 for lower indentation speeds.

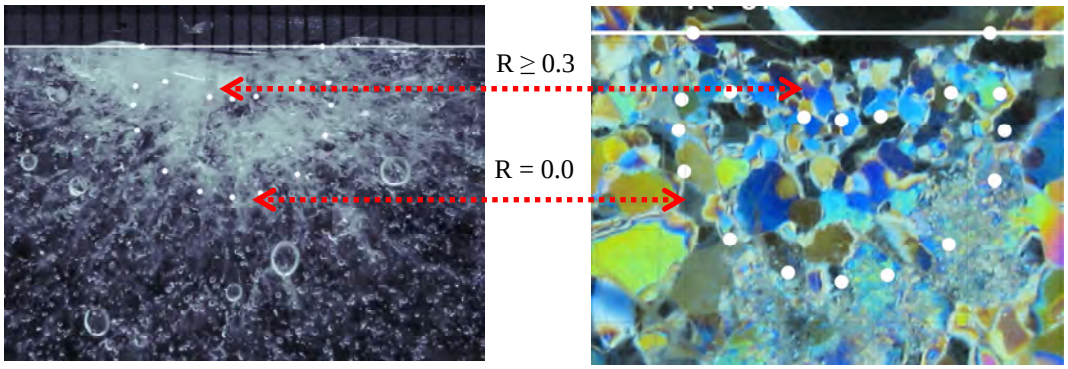

Figure 31: Damage zone after a 1-mm indentation with an indenter speed of 0.0508 mm/s (for an indenter radius of 12.7 mm and at a temperature –10°C, in the ductile-dominated regime); tick marks are spaced at 1-mm intervals.

From Figure 27 and Figure 31, it can be seen that the white (nontransparent) area beneath the indenter consists of recrystallized grains. For the indentation in the brittle dominated regime (indenter speed v=5.08 mm/s), the calculations show that the recrystallized region lies within the inner contact zone where confinement exceeds a threshold level of 0.3 and resembles a zone of plastic faulting, described in Golding et al. (2010). A zone, with levels of confinement R<0.3, is the zone of Coulombic faults. The term "*Coulombic faults*" means that frictional sliding is a component of the failure

process. Plastic faults occur when the hydrostatic component of stress tensor is large enough to suppress frictional sliding. The transition from a region of Coulombic to a region of plastic faulting corresponds to the levels of confinement in agreement with Golding et al. (2010). For the ductile dominated regime, the recrystallized region expands to the greater depths; see Figure 31. It should be noted, that, unlike the case in Golding et al. (2010), we did not observe clear faults within the ice beneath the indenter.

There are two possible reasons for this:

(i) since minor principal stresses were roughly equal, there was no clearly defined intermediate plane for the fault to follow, so it was difficult to perfectly capture the fault in a thin section;

(ii) owing to spalling events, the state of confinement within the ice may have been continuously changing, such that there was not enough deformation applied at a given confinement to cause faulting.

Nevertheless, the transition from a region comprising recrystallized grains (region of plastic faulting) and a region comprising microcracks (region of Coulombic faulting) is very evident in the results.

The theory of contact mechanics (Fischer-Cripps, 2000) suggests that the stress trajectories move as the radius of contact increases. Therefore it is reasonable to expect changes in the recrystallized region with increasing penetration depth. For the larger indentation depths, the elasticity theory, used in the present study, is no longer valid and different approach is needed for estimation of the confinement levels under the indenter. Besides, strength of extruded ice may provide an additional degree of confinement for the undamaged ice.

Comparison with earlier works at different scales

Pressure-area data at the time of peak vertical load registered by the MATS load cell are plotted in Figure 32. It is interesting to compare pressure area relationship at small-scale (single HPZ) to that at larger scales. Table 6 compares the pressure-area relationship obtained from the present study (i.e., at small scales) with that obtained at larger scales.

The experimental data showed consistent behavior of the indentation pressure (both the "process" pressure and the pressure corresponded to the maximum force). The indentation pressure decreased with increasing contact area. This result was in agreement with those reported by Barnes and Tabor (1966), Masterson and Frederking (1993), Masterson et al. (2007) and Sanderson (1988). In Figure 32, a power-type curve $p=CA^x$, where C=0.10 and x=−0.64 are fitted to the data using Matlab. R^2 is the square of the correlation between the response values and the predicted response values.

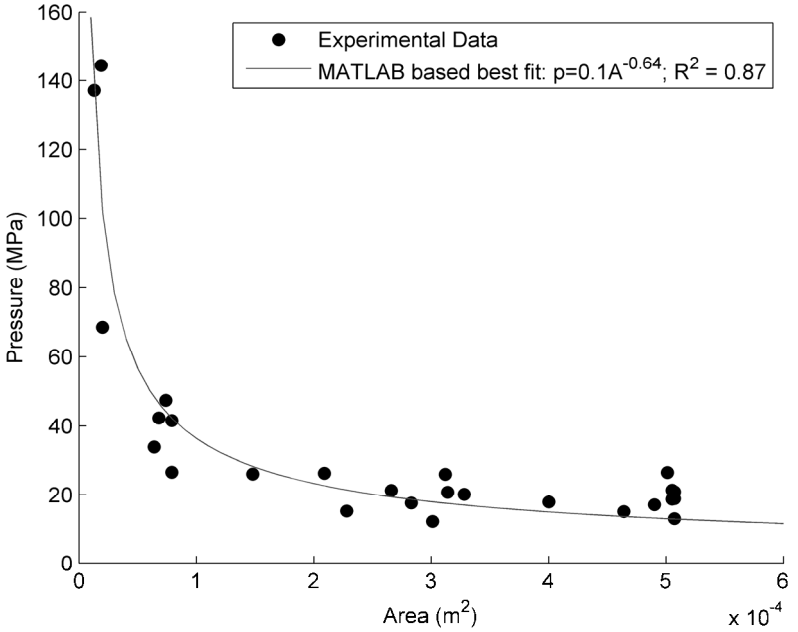

Figure 32: Average pressure versus contact area.

Referring to Table 6, it can be argued that the p=0.10$A^{-0.64}$ relationship obtained in this study is related to the behavior of a single high pressure zone.

Table 6. Comparison of results from the present study with those from previous studies.

Data source	Range of loaded areas	PA relationship, p [MPa], A [m^2]
Present study	<5·10^{-4} m^2	p = 0.1$A^{-0.64}$
Terry Fox glacial ice pressure-area curve (Ritch et al., 2008)	0.12 – 2.4 m^2	p = 3.5$A^{-0.56}$
Louis S. St-Laurent North Pole Trip (Ritch et al., 2008)	0.7 – 22 m^2	p = 6$A^{-0.4}$
Molipaq design (Masterson et al., 2007)	≈0.1 – 10 m^2	p = 5.1$A^{-0.4}$
2 STD curve for combined data in (Masterson and Frederking, 1993)	≤19 m^2	p = 8.1$A^{-0.572}$
Average + 3 STD curve derived by (Masterson et al., 2007)	≈0.1 – 10 m^2	p = 7.4$A^{-0.7}$
DNV (2011) Rules for classification of ships for vessels for Arctic and ice breaking service	≤1 m^2	p^* =5.8$A_c^{-0.5}$

*Estimate of design local ice pressure acting on a design contact area A_c (F_A=1.0 and σ_{ice}=10 MPa, which is defined following DNV Rules for Classification of Ships (2011)).

If this is true, then at high indentation rates, for larger loaded areas, one could expect the existence of several HPZ's with no mutual interaction between them (non-simultaneous contact described in Dempsey et al. (2001)). Therefore, it is reasonable to

use the principle of superposition to describe the pressure-area relationship at larger scales:

$$p_{full\ scale} = \sum_{1}^{number\ of\ HPZ's} p_{small\ scale} = \sum_{1}^{number\ of\ HPZ's} 0.10A^{-0.64} \tag{8}$$

where the number of HPZ's depends on the loaded area and the spatial density of HPZ's. To illustrate the physical plausibility of this thinking, one may consider the following example. The number of HPZ's in full scale is approximately 1 per m^2 (Jordaan, 2001). Considering a 90 m wide structure and 1 m thick ice, we could expect to have in total around 90 HPZ's. Substituting this number of HPZ's into Equation (8) and assuming that HPZ's account for the majority of the load we get:

$$p_{full\ scale} = \sum_{1}^{90} 0.10A^{-0.64} = 9.0A^{-0.64} \tag{9}$$

For comparison, in ISO 19906 (2010) $p=7.4A^{-0.7}$. $p_{full\ scale}$ could be viewed as an upper limit estimation, since, in reality, there will be a mutual temporal and spatial interaction between single HPZ's, effects of confinement, indentation geometry effects etc. However, this simple example indicates that our findings are physically plausible and in agreement with full-scale observations.

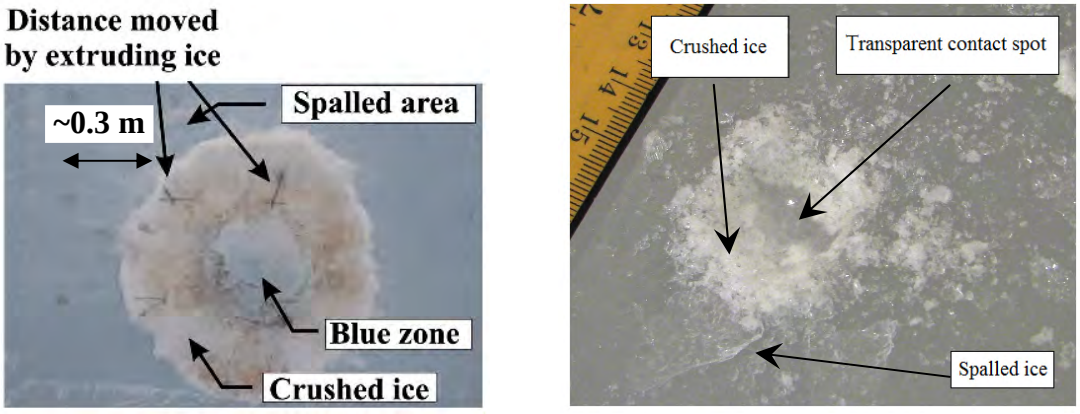

(a) (b)

Figure 33: Appearance of indented surface (a) following medium-scale tests (from Jordaan, 2001) and (b) following small-scale tests for a 5-mm penetration at a displacement rate of 5.08 mm/s and –10°C.

The results of this work are probably more relevant to the problem "indentation into an ice wall". This type of indentation was discussed in Sodhi (2001). During this type of ice-structure interaction, the aspect ratio (defined as the structure width divided by the ice thickness) is close to 1.0 and ice is ejected in all radial directions within the contact area. Examples of such interactions are during the impact of an ice mass (iceberg,

multiyear ice floe) against structures (a ship or a platform) or during accidental collisions of ice masses with structures (see Figure 7c).

For aspect ratios close to 1.0, the appearance of the ice surface after indentation at the medium scale and the small scale is shown in Figure 33a and Figure 33b, respectively. Figure 33a refers to the Hobson's choice 1989 multiyear ice indentation tests and is taken from Jordaan (2001). Figure 33b refers to the indentation tests on granular freshwater ice in the present study.

Despite differences in scales and experimental setup, in both medium- and small-scale indentation experiments it is possible to find similar patterns of ice failure behavior; e.g., visible presence of spalls, transparent ice (blue zone) in the middle of the indentation zone, crushed and extruded ice.

The results of the present study were compared with those from medium- and small-scale indentation tests and are shown as a pressure-area log-log plot in Figure 34.

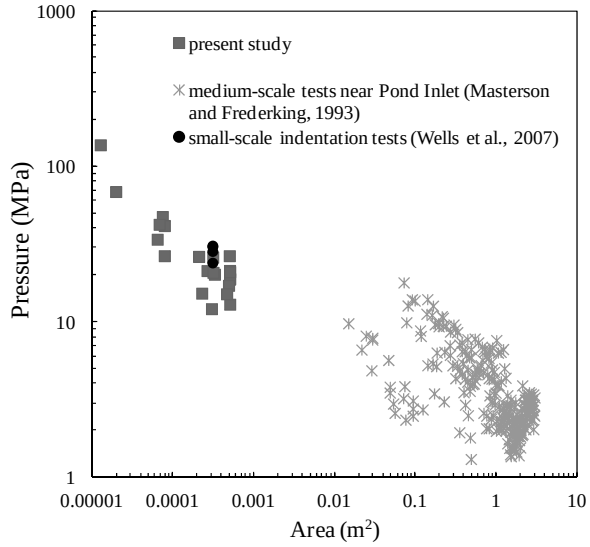

Figure 34: Comparison of present results with earlier works. Log-log plot of pressure versus contact area.

The source of pressure-area information at the medium-scale was taken from Pond Inlet indentation experiments reported in Masterson and Frederking (1993) (for the indenters with 0.1–3.0 m^2 contact area at full penetration). As source of pressure versus area information at the small-scale MTS load-cell and piezoelectric load cell records in Wells et al. (2007) were used, where the pressures were calculated as the maximum force divided by the projected contact area. One may argue that a small-scale ice indentation experiment with confinement, to some extent, echoes a small-scale in-situ testing of ice, like the tests with a borehole jack. Hence, it seems reasonable to compare

our results with those from borehole jack tests (e. g., multiyear ice tests in Johnston et al. (2003). Results of a comparison are shown in Figure 35.

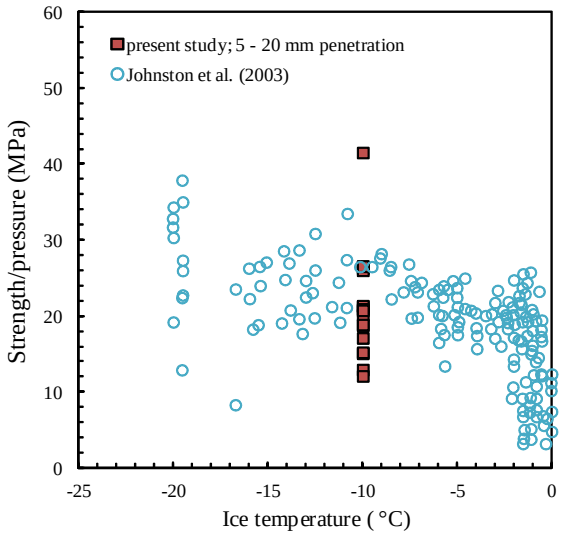

Figure 35: Comparison with ice strength records from borehole jack experiments. Plot of ice strength (pressure) vsersus temperature.

From Figure 33–Figure 35 it can be seen, that the observed behavior of confined ice and forces (pressure), registered during indentation in the laboratory at small scale, is close to those observed (or registered) earlier in small/medium-scale, laboratory/in-situ experiments and at full-scale.

Energy absorption capacity of ice during crushing

In this section, the major focus was placed on *the energy absorbed per unit mass of crushed material* or the so-called specific energy absorption (SEA). Several important parameters might affect the SEA, i.e., type of ice, temperature, microstructure (grain size and shape, grain interlocking, etc.), ice failure mode, geometry of the ice feature, rate of deformation, etc., including the loading and boundary conditions. If we postulate that *the specific energy absorption during the local ice crushing process is a physical characteristic of an ice-structure interaction*, then the SEA is a scale-independent parameter for certain boundary conditions (including the geometry and the size of the ice specimen and the indenter) and the temperature. To verify this hypothesis, experimental data at different scales were re-examined. The experimental data include the following:

– Small-scale laboratory indentation tests on freshwater granular and freshwater columnar S2 ice (this study);

- Drop-weight impact experiments on lake ice presented by Kheisin and Cherepanov (1970), Likhomanov and Kheisin (1971), Kheisin and Likhomanov (1973) and Likhomanov et al. (1998);
- Small-scale laboratory drop-weight tests on freshwater granular ice carried out by Garcia et al. (1985);
- Drop impact tests on freshwater columnar S2 and S1 ice conducted by Timco and Frederking (1990);
- Drop-weight impact experiments on iceberg ice reported by Gagnon and Gammon (1997).

Small-scale experimental data (Garcia et al. (1985) and this study) were compared to medium-scale data (Kheisin and Likhomanov, 1973; Timco and Frederking, 1990 and Gagnon and Gammon, 1997).

A *scale effect* was defined as follows: *A scale effect is operational if the size of a problem changes to such an extent that another physical phenomenon starts to govern the problem* (Langhaar, 1951).

Let us assume that the SEA of freshwater ice is generally a function of geometry, size and ice temperature (Equation (10)):

$$\varepsilon = f(geometry, size, T_i) \tag{10}$$

For our geometrically defined problem (circular indenter), we address four independent different lengths: ice grain diameter (d_{ice}), indenter diameter (d_{indr}), sample size (d_{smpl}) and penetration depth (d_{pen}). This situation defines three independent (six in total) dimensionless ratios, and thus, the specific energy becomes a function of these ratios and ice temperature:

$$\varepsilon = f\left(\frac{d_{indr}}{d_{ice}}, \frac{d_{smpl}}{d_{indr}}, \frac{d_{pen}}{d_{ice}}, \frac{d_{smpl}}{d_{pen}}, \frac{d_{indr}}{d_{pen}}, \frac{d_{smpl}}{d_{ice}}, T_i\right) \tag{11}$$

The ratio $d_{smpl}/d_{ice} \leq 1.0$ corresponds to experiments with single crystals. All tests considered in this section had the ratio $d_{smpl}/d_{ice} >> 1.0$ and the ratio $d_{indr}/d_{pen} > 1.0$, except for the tests in Garcia et al. (1985), in which the penetration depth was larger than the indenter diameter.

Table 7 provides values for the dimensionless ratios from the different experiments.

Table 7. Dimensionless ratios.

Authors	d_{indr}/d_{ice}	d_{smpl}/d_{indr}	d_{pen}/d_{ice}	d_{smpl}/d_{pen}
This study	6–11	6	0.3–5	11–146
Gagnon and Gammon (1997)	47–76	0.6	0.7–5	9–40
Garcia et al. (1985)	2–4	48	0.1–21	9–610
Kheisin and Likhomanov (1973)	23–286	0.7–1.2	0.1–20	10–233
Timco and Frederking (1990)	67–200	0.9–1.8	1–18	10–90

Drop tests by Kheisin and Likhomanov

During the period 1967–1969, drop-tests were conducted on the freshwater ice of Lake Ladoga; for a detailed description of the experimental setup, please refer to Likhomanov and Kheisin (1971). In these experiments, two hemispherical weights of 300 kg and 156 kg with a radius of curvature of 28.6 cm were dropped onto the flat and free-from-snow surface of the lake ice. The accelerations of the weights and the size of ice damage zone were registered for each test and a total of 200 experiments were conducted. The texture and structure of the ice before and after the drop tests are reported in Kheisin and Cherepanov (1970). After impact, the authors observed fine-grained ice (randomly oriented grains with sizes of 0.01–0.2 mm) arranged in a thin layer (0–2 cm) close to the surface, with cracks located below this layer and flakes near the perimeter of indentation. In Kheisin and Likhomanov (1973), the specific energy was defined as the energy per unit mass of crushed ice, i.e., the energy required to turn solid ice into crushed (pulverized) material. In Kheisin and Likhomanov (1973), the SEA was calculated as follows:

$$\varepsilon = \frac{PH(1-e^2)}{\rho(\pi/8)(h_0 D_0^2)} \tag{12}$$

where P is the weight of the dropped object, H is the drop height, e is the coefficient of restitution found experimentally for each test, ρ is the average ice density (900 kg/m^3) and h_o and D_o are the depth and the diameter of the ice crater, respectively. For lake ice, Kheisin and Likhomanov (1973) found that average value of the SEA was dependent on the ice structure and temperature and varied between $0.3 \cdot 10^4$ J/kg and $1.4 \cdot 10^4$ J/kg for spring and winter ice, respectively. Kheisin and Likhomanov (1973) observed that the specific energy was a decreasing function of the drop height. The specific energy was larger for smaller drop heights (<10 cm) or for smaller sizes of the imprints left by the projectiles. Kheisin and Likhomanov (1973) also noted that the specific energy of the mechanical crushing of ice is a stable characteristic for drop heights greater than 10

cm and corresponds to a velocity of impact ≥1.4 m/s. According to Kheisin and Likhomanov (1973), the specific energy absorption during material fragmentation is a physical characteristic of the dynamic strength of the material.

Considering the values in Table 7, one can argue that the decreasing trend of SEA as a function of the drop height (or the depth of imprint) can perhaps be explained by the case in which the penetration depth was too small compared with the grain size of the ice. Additionally, the decrease of the SEA with the increasing penetration depth might be due to values of d_{smpl}/d_{indr} that were slightly less than that recommended by Johnson (1985). To avoid scale effects, the following conditions should be met: $d_{pen}/d_{ice} \geq Limit_1$ and $d_{smpl}/d_{indr} \geq Limit_2$. Johnson (1985) recommends $Limit_2$=1.7–4.4. Unfortunately, from the data presented in Kheisin and Cherepanov (1970), Likhomanov and Kheisin (1971), Kheisin and Likhomanov (1973) and Likhomanov et al. (1998), it was impossible to derive the value of $Limit_1$. The SEA as a function of the penetration depth (or the maximum crater depth) is not provided in the published literature.

Drop-weight tests by Garcia et al.

Garcia et al. (1985) conducted a series of drop-weight impact tests. The ice was fine-grained and polycrystalline with grain sizes in the range of <1.7 mm and 1.7–3.4 mm and with a mean density of 905 kg/m^3. Two flat-ended steel indenters with diameters of 6.3 mm and 11.1 mm were used in drop-weight tests conducted at a temperature of –5°C. The rims of the indenters were machined to a small radius. Despite this precaution, the indenter was not a perfect spherically shaped object, but we still considered the results for comparison purposes. The ice specimens were cylinders 165 mm in diameter and 305 mm long and were confined by a metal ring. Garcia et al. (1985) noted that the experimental setup "mimics" the penetration into semi-infinite ice. The specific energy was calculated as the impact energy divided by the measured crater volume. The presented data do not support the concept of constant specific energy. The specific energy appears to be constant for the mid-range results (10 MJ/m^3) and appears to decrease as the crater volume increases. Taking into account the ice density of 905 kg/m^3, the recalculated specific energy is approximately $1.1 \cdot 10^4$ J/kg (at –5°C). This result is rather similar to the SEA value of $1.4 \cdot 10^4$ J/kg for winter ice reported in Kheisin and Likhomanov (1973).

The increase of SEA for lower penetration depths may have occurred because d_{indr}/d_{ice} and d_{pen}/d_{ice} were too small (see Table 7). Michel and Toussaint (1977) suggested that the indenter width should be greater than seven grain-diameters (d_{indr}/d_{ice}>7.0) to avoid a "scale effect". However, for the larger penetration depths (d_{indr}/d_{pen}<1.0), the geometry of the problem was changed. In addition, the diameter of the ice sample might be too small compared with the penetration depth.

Impact tests by Gagnon and Gammon

Gagnon and Gammon (1997) conducted impact tests on iceberg ice from Labrador using a smooth, spherically shaped projectile with a radius of curvature of 22.9 cm. The impacted mass varied between 155 kg and 510 kg. The ice specimens had a cylindrical shape, with a diameter of 68.5 cm and a thickness of 25.7 cm. The specimens were radially confined using a 3.8-cm-thick aluminum ring; for detailed information, please refer to Gagnon and Gammon (1997). The mean grain diameter of the ice was 6.03–9.69 mm. A total of 40 impact tests were conducted, and the temperature of ice specimens varied from –0.5°C to –14.5°C. Gagnon and Gammon (1997) observed that after the impact, the ice crater was underlain first by a region of finely crushed ice with a thickness that was notably thin to several millimeters in area, and subsequently by a pattern of tensile cracks radiating into the bulk of the specimen. The degree of tensile cracking was proportional to the impact energy. In Gagnon and Gammon (1997), the specific energy was estimated in MPa and defined as the ratio of the energy imparted to the ice divided by the measured crater volume. The volume of the crater was determined using two different data sources: (i) direct measurements of the crater depth at the conclusion of the test and (ii) registered accelerations of the projectile. Gagnon and Gammon (1997) found that the specific energy at the instant of peak force and at the conclusion of the test decreased with increasing temperature. Additionally, the specific energy was observed as a decreasing function of the crater volume and ice penetration.

We believe that a size effect exists in the data of Gagnon and Gammon (1997). In their experiments, the sample size (both width and the thickness) was too small compared with the size of the indenter and the penetration depths. Johnson (1985) recommends minimum dimensions of the indented block for rigid-perfectly-plastic solids to ensure that the indentation is not influenced by the size of the block, i.e., for a curved indenter $d_{smpl}/d_{indr} \geq 1.7–4.4$ and $d_{smplwidth}/d_{indr} \geq 3.2–8.7$.

This study

Only the tests on confined ice were considered (see Table 5). Using force-displacement records for each penetration distance u, the specific energy absorption ε was calculated as follows:

$$\varepsilon = \frac{\int_0^{u(t)} F(u)du}{\rho(\pi/3)u^2(3r-u)} \tag{13}$$

where $F(u)$ is the force registered by the load cell, u is the penetration distance, ρ is the ice density, and r is the radius of the indenter. An example of the calculation is given in Figure 36 for Test EK7 (parameters for this test can be found in Table 5).

From Figure 36d, it can be observed that at a certain penetration depth, the SEA approaches a steady-state value of approximately $1.7 \cdot 10^4$ J/kg. This value is remarkably close to the value reported by Kheisin and Likhomanov (1973) for winter ice. The high SEA values at the beginning of indentation are likely due to the effect of fewer grains, i.e., the ice crushing process was governed by the behavior of a single crystal. For small penetration depths (d_{pen}/d_{ice} <5.0), the ice crushing was governed to a greater extent by the behavior of single crystals (shape and size, grain interlocking, etc.) The specific energy was more or less constant for d_{pen}/d_{ice} > 5.0.

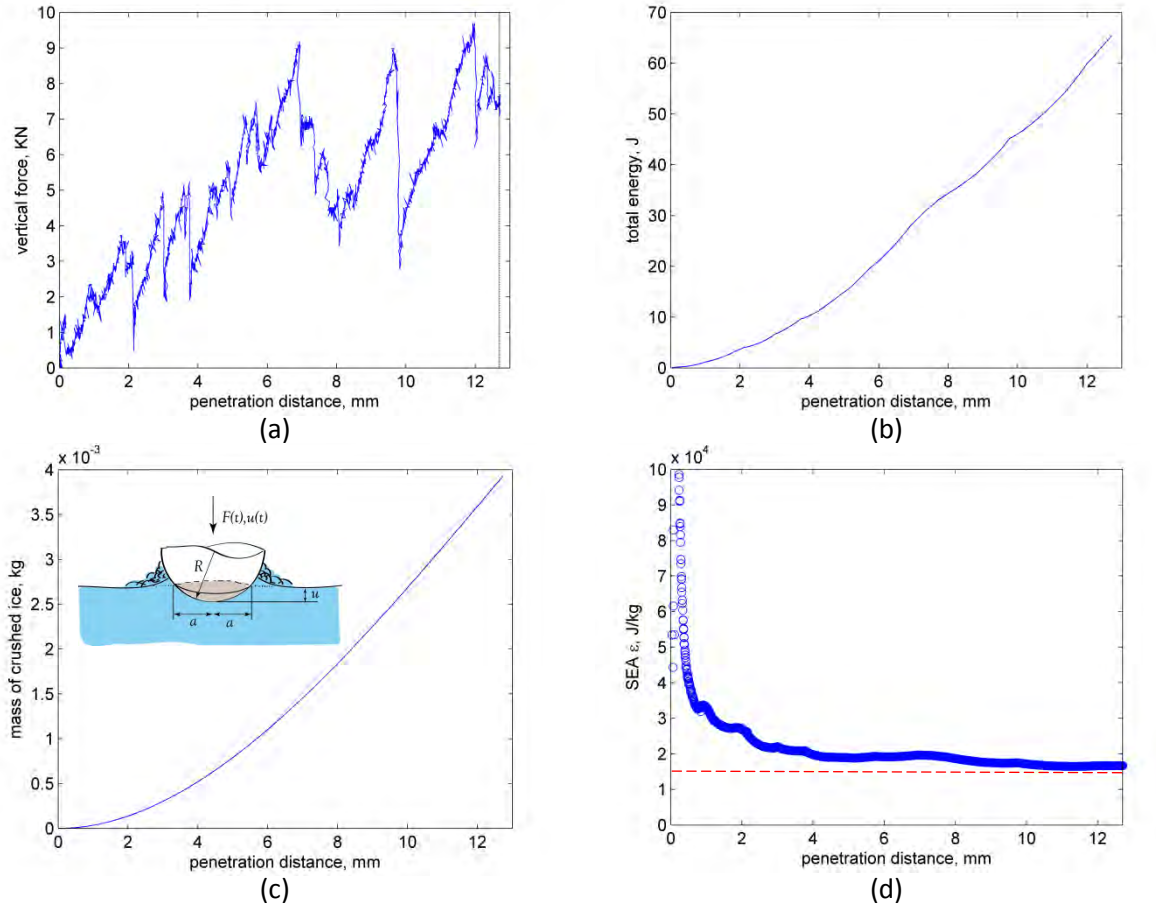

Figure 36: Determination of the specific energy for the EK7 test (ice at –10°C): (a) history of the load record during the indentation test; (b) total energy computed by integrating the force applied to the indenter over the penetration distance specified by the penetration curve; (c) the calculated mass of the crushed ice for each penetration distance, corresponds to the volume of the spherical cap with the base radius found from the penetration distance; (d) the SEA as a function of the penetration distance.

Drop tests by Frederking and Timco

Drop impact tests on laboratory-grown freshwater columnar S2 and S1 ice were performed using a spherically shaped projectile of 100 mm radius in the 21 m long, 7 m wide and 1.2 m deep ice tank located at the National Research Council (NRC) in

Ottawa. The projectile masses were approximately 36 kg and 64 kg. Timco and Frederking (1990) provide descriptions of the experimental setup and the results of the tests. A total of 45 impact tests were performed at an ambient temperature of –12°C, and the ice thickness for tests was between 17.8 cm and 36.8 cm.

The grain size varied from approximately 1 mm at the top of the sheet to approximately 3 mm at the bottom (Timco and Frederking, 1982). The crystallography of the impacted ice was presented in Jones and Sinha (1990). The authors observed a heavily damaged zone immediately below the indenter, including radial cracks and many intra-granular micro-cracks, which formed throughout the ice below the indenter. The crater volume was observed as an increasing function of the impact energy determined from the potential energy of the projectile before each drop. In this study, the SEA was calculated as follows:

$$\varepsilon = \frac{0.5mv^2}{\rho(\pi/3)h^2(3r-h)} \tag{14}$$

where m is the projectile mass, v is the projectile speed at impact, and h is the depth of the impact crater. The values of m, v and h are reported in Timco and Frederking (1990), and r is the radius of the spherical portion of the projectile (r=100 mm). The ice density ρ=900 kg/m^3.

To compare the results of this study with those in Garcia et al. (1985) and Gagnon and Gammon (1997), it was necessary to redefine the calculation of the specific energy. The specific energy reported in Gagnon and Gammon (1997) was divided by the ice density (900 kg/m^3), which resulted in the specific energy defined as energy absorbed per unit mass of crushed material (J/kg). The results of the comparisons between different scales are summarized in Figure 37.

Figure 37 shows that results of Timco and Frederking (1990) are slightly size-dependent and their ratio of the sample thickness to indenter diameter approached the limit of Johnson (1985) of d_{smpl}/d_{indr}=0.9–1.8<1.7–4.4. For the smaller penetration depths the effect of d_{pen}/d_{ice} is evident in Figure 37.

From the data of Gagnon and Gammon (1997) and Garcia et al. (1985), it appears that the specific energy is a decreasing function of the crater volume. However, the data in Kheisin and Likhomanov (1973), the NRC tests by Timco and Frederking (1990) and this study indicate that the specific energy is a scale-independent characteristic. A possible explanation for these contradicting data sets is the fact that "to realistically capture the mechanisms of localized zones in quasi-brittle materials, material microstructures have to be taken into account" (Skarżyński and Tejchman, 2012).

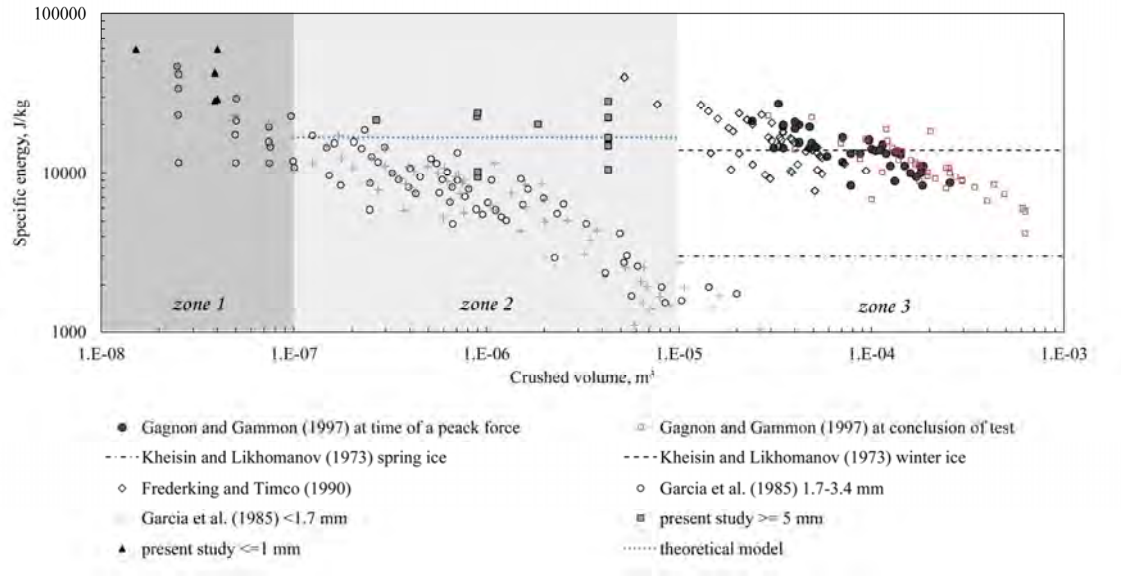

Figure 37: Comparison of specific energies determined from experiments at different scales with provisional zoning. *Zone 1* corresponds to a penetration depth of a few millimeters, which is on the order of a single grain (the forces governing the failure process at this scale could be different from those in Zones 2 and 3); *Zone 2* corresponds to indentation for a penetration depth larger than 5 mm for the tests in Table 5, which are referred to as small-scale tests; *Zone 3* corresponds to the scale of the experiments conducted by Kheisin and Likhomanov (1973), Timco and Frederking (1990) and Gagnon and Gammon (1997), which is referred to as a medium scale; a theoretical model was adopted from Jones and Rule (2000) and is given in Appendix A.

The size of the tested ice specimen should be chosen such that homogenized properties become independent of the micro-structural changes and boundary conditions. However, in selected tests, the experimental setup provided ice confinement and simulated an infinite extent of ice around the specimen; the size effect was still present in the data (see, e.g., Garcia et al. (1985) and Gagnon and Gammon (1997)). The dimensions of the indented block (width and the thickness), the size of the indenter and the maximum penetration depth should be chosen to ensure that the indentation is not influenced by the size of the block. Additionally, there should be a sufficient number of grains at the ice-indenter interface to avoid the d_{indr}/d_{ice} effect. With respect to the tests in this study, a possible d_{pen}/d_{ice} effect for the value of specific energy is shown in Figure 37 (see Zone 1). In our indentation tests, it was observed that as the splitting crack reaches the external edges of the ice specimen, the load begins to accumulate in the confining plates (i.e., the confining plates take on a portion of the vertical load). The cracks that radiate away from the impacted surface and reach the edge of the confining ring can be observed in certain pictures reported by Garcia et al. (1985). Hence, for greater penetration depths, the confining ring and the limited thickness of ice sample influenced the reported values in Garcia et al. (1985) and

Gagnon and Gammon (1997). Additionally, for smaller penetration depths, the results presented in Kheisin and Likhomanov (1973), Garcia et al. (1985), Timco and Frederking (1990), Gagnon and Gammon (1997) and this study do not fully represent the behavior of polycrystalline ice and likely governed to a greater extent by the behavior of individual crystals. Based on the above considerations, the following dimensionless ratios are recommended to minimize the possible scale- and size-effects on the SEA:

$$\frac{d_{indr}}{d_{ice}} \geq 7.0;\ \frac{d_{smpl}}{d_{indr}} \geq 1.7;\ \frac{d_{pen}}{d_{ice}} \geq 5.0;\ \frac{d_{smpl}}{d_{pen}} \geq 10 \tag{15}$$

One may argue that the SEA is a parameter of the ice/indenter system. An SEA measure is useful because it remains constant over a certain range of system sizes (Equation (15)) and hence may be introduced in the physical laws. Outside of this range, the SEA shows dependency on system size and expresses multi-scale character.

To summarize, the specific energy of the ice crushing process is independent of the interaction scenario because similar energies were obtained from both the drop-weight tests and the indentation tests. The SEA depends on the geometry, the size and the ice temperature. As long as the grain size is sufficiently small relative to the penetration depth and the indenter diameter, and the sample size (the width and the thickness) is sufficiently large relative to the indenter diameter and the penetration depth, the specific energy is scale-independent at least for the scales considered. We recommend that the SEA be used as an additional validation criterion for numerical models in problems with significant energy dissipation in ice crushing. An example of how the SEA criterion can be used will be given in Chapter 4 (Section 4.1.4).

Uncertainties of results

As already noted, the present experimental results (including observations) mirror some recent studies on ice indentation, e.g., (Barrette et al., 2003; Gagnon, 2008b; Golding et al., 2010; Jordaan, 2001; Wells et al., 2011). However, it is necessary to discuss some uncertainties of our experimental results.

One uncertainty is related to the interpretation of the thin sections from the indentation zone. The new grains that formed at the boundaries of the columns (case of indentation into columnar grained ice) or grains, deep into the block, could potentially have formed from freezing melt water in the long cracks upon thinning the section by warming. If a thin section exists where freezing of water in cracks has occurred, the recrystallized grains would be observed in other regions of the indentation zone where many cracks have developed. For example, in Figure 25b and Figure 25d the cracks also ran along the grain boundaries and made multiple splits. Despite this, the recrystallized

region lies within the inner contact zone. Besides, as calculations show in this zone, for granular ice, the confinement exceeds a threshold level, in agreement with Golding et al. (2010).

Another uncertainty is related to the calculations of the contact area. In the present study, in order to calculate the indentation pressure, the values of the projected area were used (see Section 3.1.2). The actual contact area might be different from the projected area and, for example, ice during ductile deformation may have larger contact areas. Besides, ice pile-up during indentation might have an influence on the actual contact area, and subsequently, on the reported pressure values. At small penetration depths, the projected and surface areas are almost the same, but the difference between these two areas increases with increasing penetration depth. On the other hand, we are considering very small areas, of the order of centimeters, and it is difficult to believe that the additional information on the actual contact area will alter the trends and overall conclusions reached in this work.

The SEA provides a measure of the energy absorption capacity of ice during the crushing process but does not describe the resistance with respect to other processes, i.e., buckling, splitting, vibrations. The SEA discussed in the section above does not take into account the flexibility of the indenting structure and is limited to spherically shaped indenters and initially flat ice surface.

3.1.4 Summary

This work has presented results from small-scale indentation experiments, with emphasis on micromechanical processes underlying the indentation pressure as a function of indentation speed, penetration depth, size of the indenter, confinement of ice and temperature. The relevance of the recorded load signal and calculated indentation pressure to those at larger scales has been demonstrated. Developed earlier by Golding et al. (2010) the theory of Coulombic-to-plastic transition has been verified for the problem of indentation into granular ice for conditions of Hertzian contact. In addition to measured data this work provides details of ice failure mode and micromechanical changes. It is also addresses the energy absorption capacity of ice during crushing.

3.2 ANGLE-OF-REPOSE STUDY ON CRUSHED ICE PARTICLES

In general, crushed (or pulverized) ice has greater mobility than the parent ice. The behavior of crushed ice depends on the local confining stress. The behavior of crushed ice under confinement has been described by Singh and Jordaan (1999). In order to understand behavior of powdered ice extruded during small-scale indentation tests

(Section 3.1), a series of angle of repose (AOR) experiments were performed on ice particles of different sizes. The experiments presented in this section attempt to characterize the flow properties of crushed ice in the absence of confinement.

In addition to the traditional well established engineering approaches, such as extrusion tests by Sayed and Frederking (1992) and Singh et al. (1995), triaxial tests by Singh and Jordaan (1996) and ice fragmentation studies by Tuhkuri (1994), this AOR study is the first systematic approach used in the ice indentation problem. This characterization method for powdered ice was chosen based on the studies by Serré (2011) and Wouters and Geldart (1996). Wouters and Geldart (1996) mentioned that AOR is a useful property for characterizing the flow of powders and Serré (2011) performed "pile tests" to measure the angle of repose of ice rubble.

3.2.1 Experimental apparatus

Angle-of-repose (AOR) experiments were performed on ice particles with different sizes ranging between 0.85 and 19 mm (see Figure 38) at temperatures of –10°C, –20°C and –40°C. In this study, the AOR was defined as the angle formed between the horizontal plane and a slope line extending along the face of an ice-heap formed by Step 1: pouring material into a cylindrical bucket with inner diameter of 100 mm and by Step 2: lifting the bucket vertically allowing material to form a heap onto the horizontal surface.

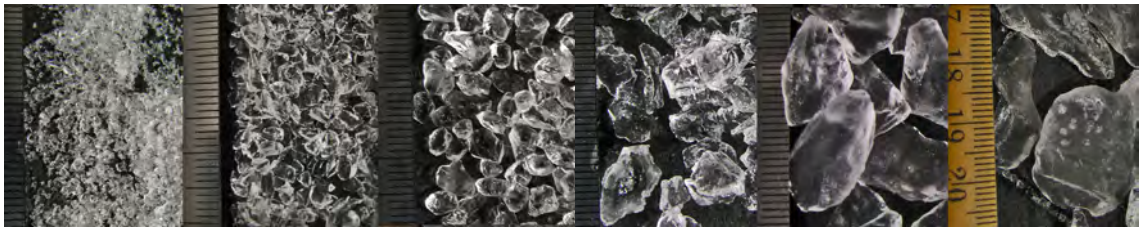

Figure 38: Photographs of ice particles used in the AOR experiments. Tick marks are spaced at 1 mm intervals.

The time lapse between Steps 1 and 2 was varied during the tests (between approximately 0 and 10 min). To investigate the effect of bottom friction in Step 2, an ice sheet and a mild steel plate were used as a horizontal surface. A schematic of the basic test apparatus is shown in Figure 39. The test parameters are given in Table 8.

Two or three photographs were taken during each AOR test. The AOR was estimated from digital photographs using a Java program (i.e., plot digitizer) with an average measurement error (uncertainty) of approximately 2°. The averaged AOR values are reported in Table 8.

Table 8. Summary of AOR experiments.

Test no.	Temperature T °C	Particle size d (mm)	Average particle size d_{av} (mm)	Volume of specimen (cc)	Time lapse b/w pouring and lifting t (s)	Horizontal surface	AOR (deg)
6	-10	6.0-4	5.0	200	~ 2	ice sheet	24
7	-10	6.0-4	5.0	425	~ 2	ice sheet	20
8	-10	6.0-4	5.0	150	~ 2	ice sheet	20
9	-10	1-0.85	0.93	225	~ 2	ice sheet	90 v
14	-10	4.0-2.4	3.2	150	~ 2	ice sheet	21
15	-10	4.0-2.4	3.2	475	~ 2	ice sheet	10
16	-10	4.0-2.4	3.2	150	~ 2	ice sheet	19
17	-10	4.0-2.4	3.2	150	~ 2	ice sheet	21
18	-10	2.4-1	1.7	150	~ 2	ice sheet	36
19	-10	2.4-1	1.7	150	~ 2	ice sheet	25
20	-10	2.4-1	1.7	150	~ 2	ice sheet	25
21	-40	2.4-1	1.7	150	~ 2	ice sheet	27
22	-40	2.4-1	1.7	150	~ 2	ice sheet	27
23	-40	2.4-1	1.7	150	~ 2	ice sheet	25
24	-40	6.0-4	5.0	200	~ 2	ice sheet	24
25	-40	6.0-4	5.0	200	~ 2	ice sheet	17
26	-40	6.0-4	5.0	200	~ 2	ice sheet	22
27	-40	1-0.85	0.93	200	~ 2	ice sheet	90 v
28	-40	19 -16	18	~ 500	~ 2	ice sheet	12
29	-20	2.4-1 packed	1.7	475	~ 2	ice sheet	26
30	-20	2.4-1	1.7	475	~ 2	ice sheet	23
31	-20	2.4-1 packed	1.7	475	~ 2	ice sheet	25
32	-20	2.4-1 packed	1.7	475	90	ice sheet	22
33	-20	1-0.85	0.93	350	~ 2	ice sheet	90 v
34	-20	1-0.85 packed	0.93	450	~ 2	ice sheet	90 v
35	-20	1-0.85	0.93	225	~ 2	ice sheet	33
36	-20	6.0-4	5.0	375	~ 2	ice sheet	12
37	-20	6.0-4	5.0	375	~ 3	ice sheet	16
38	-20	6.0-4	5.0	375	~ 0.5	ice sheet	10
39	-20	6.0-4	5.0	150	~ 2	ice sheet	16
40	-20	4.0-2.4	3.2	350	~ 2	ice sheet	8
41	-20	4.0-2.4	3.2	350	~ 2	ice sheet	18
42	-20	4.0-2.4	3.2	200	~ 2	ice sheet	16
43	-10	6.0-4	5.0	200	~ 2	steel plate	10
44	-10	6.0-4	5.0	200	~ 2	steel plate	14
45	-10	6.0-4	5.0	200	~ 2	steel plate	17
46	-10	2.4-1	1.7	200	~ 2	steel plate	21
47	-10	2.4-1	1.7	200	~ 2	steel plate	24
48	-10	2.4-1	1.7	200	~ 2	steel plate	24
49	-10	2.4-1	1.7	200	~ 0.5	steel plate	16
50	-10	2.4-1	1.7	200	~ 0.5	steel plate	13
51	-10	4.0-2.4	3.2	200	~ 2	steel plate	12
52	-10	4.0-2.4	3.2	200	120	steel plate	17
53	-10	4.0-2.4	3.2	200	120	steel plate	18
54	-10	4.0-2.4	3.2	200	~ 0.5	steel plate	17
55	-10	4.0-2.4	3.2	200	150	steel plate	17
55-1	-10	1-0.85	0.93	250	~ 2	steel plate	90 v
56	-10	1-0.85	0.93	250	~ 0	steel plate	37
57	-10	1-0.85	0.93	250	~ 0	steel plate	36
58	-10	1-0.85	0.93	250	~0.5	steel plate	90 v
59	-10	1-0.85	0.93	250	~ 2	steel plate	90 v
60	-10	1-0.85	0.93	250	~ 2	steel plate	90 v
61	-10	1-0.85	0.93	250	~ 2	steel plate	90 v
62	-10	1-0.85	0.93	250	~ 2	steel plate	90 v
63	-10	1-0.85	0.93	250	~ 0	steel plate	45
64	-10	19 -16	18	no data	600	steel plate	10
65	-10	19 -16	18	no data	~ 2	steel plate	0
66	-10	19 -16 (wetted)	18	no data	~ 2	steel plate	9
67	-10	12.5-8.00	10	375	~ 2	steel plate	7
68	-10	12.5-8.00	10	375	~ 2	steel plate	15
69	-10	12.5-8.00	10	375	~ 2	steel plate	11
70	-10	12.5-8.00	10	375	300	steel plate	15
71	-10	12.5-8.00	10	375	~ 2	steel plate	13
72	-10	12.5-8.00	10	375	~ 2	steel plate	8
73	-10	12.5-8.00	10	375	~ 2	ice sheet	16
74	-10	12.5-8.00	10	375	~ 2	ice sheet	8
75	-10	12.5-8.00	10	375	~ 2	ice sheet	9

v -Visual estimation from the photographs

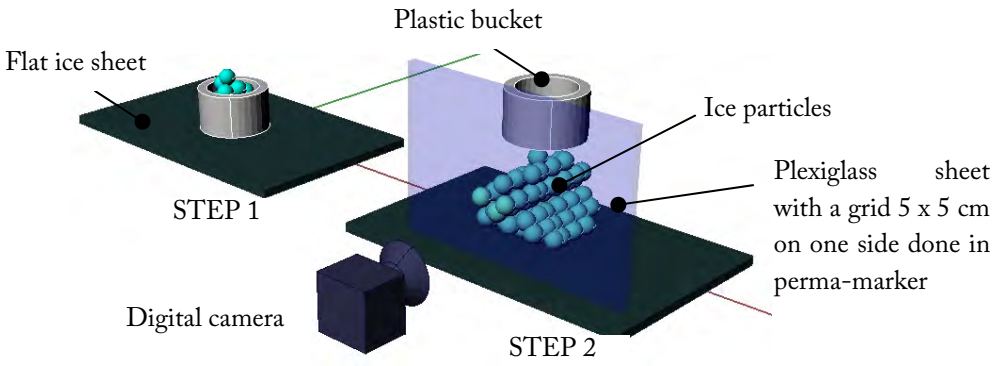

Figure 39: Sketch showing the main features of the AOR experiments.

3.2.2 Results and discussion

A total of 67 tests were conducted. The AOR experiments showed that at the testing temperatures, the small ice particles (0.85–1 mm) were highly cohesive and formed an approximately 90° angle with the horizontal; see Figure 40a.

The largest particles (16–19 mm) exhibited non-cohesive behavior and resulted in an AOR that was close to zero (Figure 40b).

(a) 0.85 – 1 mm (b) 16 – 19 mm

Figure 40: Photographs taken during the AOR experiments at –10°C: (a) ice particles of size 0.85 – 1 mm; (b) ice particles of size 16 – 19 mm.

To examine in more detail this transition from non-cohesive to cohesive behavior a time factor was introduced. The time lapse between pouring ice particles into the bucket and lifting the bucket was roughly measured by the digital watch. The averaged AOR obtained from all experiments is given in Table 8. The average measurement error is 2°. The measurement error is the standard deviation of the AOR estimates from series of photographs taken during a single experiment. The measurement error is mainly the result of the experimental setup and the AOR measurement technique.

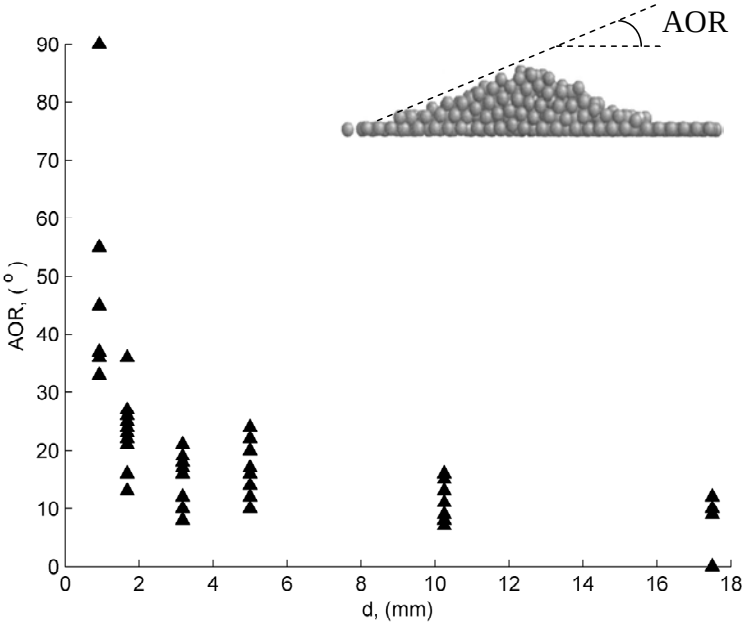

Figure 41: AOR versus particle size (a summary of all AOR data in Table 8).

A summary of all the measurements of AOR (67 tests) is presented in Figure 41. Figure 41 shows that AOR increases nonlinearly with decreasing particle size. This is in agreement with earlier observations in other materials (Carstensen and Chan, 1976; Taylor et al., 2008; Wouters and Geldart, 1996) and can be explained by an increase of cohesive force with decreasing particle size.

In general, mechanical behavior of a granular medium at both engineering scale (O[m]) and small-scale (O[mm]) can be explained by a combination of interlocking of particles, cohesion and friction. Interlocking of particles is influenced mainly by the shape of particles. Since the shape of ice particles did not vary significant from one test to another, further discussion will be mainly on the role of cohesion and friction during the AOR experiments.

Cohesion

At the engineering scale, cohesion is usually quantified by the "tau"-axis intercept of the Mohr-Coulomb failure envelope plotted in "tau-sigma" space, where "tau" is the shear stress acting on the failure plane, and "sigma" is the normal stress to that plane. Ice-rubble cohesion is a strength parameter associated with freeze-bonding of ice fragments/consolidation and is a function of contact time, compressive pressure, ice temperature, salinity, shape and size of the blocks. At this scale, the term "cohesion" is defined as the attractive force between two or more particles. For ice particles, cohesion is associated with sintering (sub-sintering) of ice and depends on temperature, time, salinity, presence of a liquid-like layer, normal force acting at the ice-ice interface, particle size and shape.

At the engineering scale, ice-rubble cohesion is proportional to the size of the block (Bruneau, 1996; Liferov and Bonnemaire, 2005). This study showed that at small-scale, the cohesive force was inversely proportional to the particle size (d). A theoretical formulation by Tomas (2003) was used to bridge this inconsistency in scale. At both scales, the total cohesive force F_c^{tot} can be written in the following form:

$$F_c^{tot} = iF_c + jF_n \tag{16}$$

where i and j are time-dependent coefficients. F_c is the cohesive force between particles ($F_c \propto d^{-1}$), and F_n ($F_c \propto d^3$) is the external normal force. If $d \ll 1$ m, the first term on the right side of Equation (16) dominates causing the total cohesive force F_c^{tot} to increase (and consequently the angle of repose) with decreasing particle size. This behavior was observed in our findings. If $d \geq 1$ m (with corresponds to the engineering scale), the second term dominates, leading to an increase in F_c^{tot} with d. This behavior was observed in studies by Bruneau (1996) and Liferov and Bonnemaire (2005).

Another important factor in building cohesive forces between particles during AOR experiments is the elapsed time between pouring the ice particles into the bucket and lifting the bucket. Figure 42 shows that the time factor played a significant role in the formation of the AOR. The results showed that the AOR increased with time. This observation can be explained by the results of a study by Szabo and Schneebeli (2007) in which ice grains bonded together in less than a second, and the bond strength increased with time and temperature. In the present experiments, temperature was not found to affect the AOR (Figure 43). This result may have been caused by the experimental apparatus and the absence of proper time control during the experiments. The results in Figure 42 showed that even a slight variation in the time (e.g., ±1 s) significantly changed the AOR. Imprecise time recording during the experiment may have caused measurement errors in excess of the actual temperature effect.

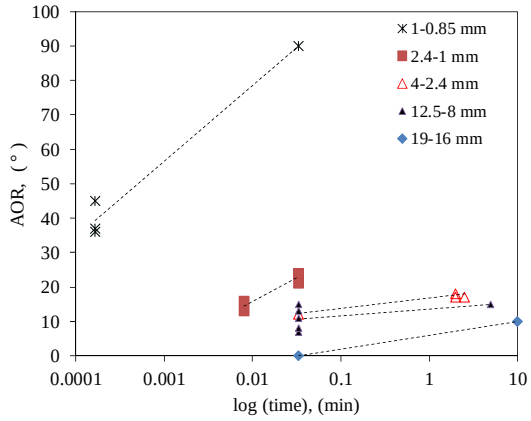

Figure 42: AOR experiment, effect of time at –10°C.

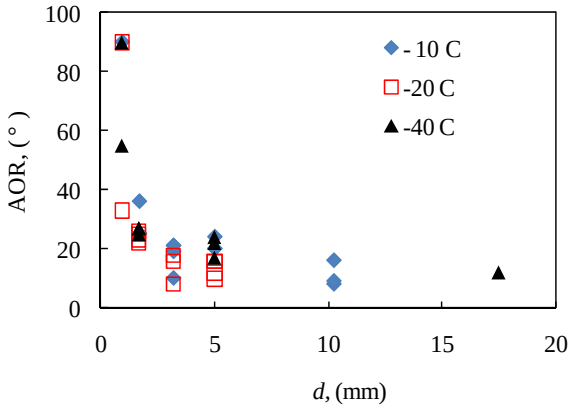

Figure 43: AOR experiment, effect of temperature.

Nevertheless, it is interesting to note from Figure 42, that the rate of increase AOR with time is higher for smaller ice particles. This is a signature that smaller ice particles form bonds between each other more rapidly and this bonding process (sub-second sintering of ice) is both time and size dependent. In turn, similar ice behavior (ice sintering, regelation of ice blocks, freeze-bonding) is observed at different time and length scales over centuries; see, e.g., (Chen and Baker, 2010; Ettema and Schaefer, 1986; Faraday, 1859; Kingery, 1960; Marchenko and Chenot, 2009; Shafrova and Høyland, 2008; Szabo and Schneebeli, 2007).

Friction

The frictional contribution between the ice particles and between the particles and the horizontal surface was studied during the AOR experiments. Figure 44 shows the main findings.

Despite the fact that ice–ice static friction is higher than that between ice and steel (Ryvlin, 1973), no static friction effect was found. For sliding speeds $>10^{-4}$ m/s at the experimental temperatures, almost no difference was observed between the steel-ice and ice-ice kinetic friction values of 0.04–0.08 and 0.1, respectively (see Frederking and Barker (2002) and Kennedy et al. (2000)). Thus, the dominance of kinetic friction, could account for the similar AOR values found for the two different surfaces in the present experiments.

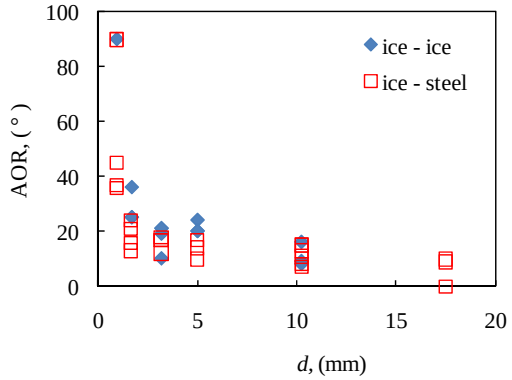

Figure 44: Effect of bottom friction at –10°C.

3.2.3 Summary

This work describes flow behavior of crushed ice in terms of angle of repose. In summary, the angle-of-repose experiments showed that the flowability of the crushed ice particles was mainly controlled by the contact forces between the grains and varied with the particle size and time. The experiments showed that a slight change in the operating conditions (i.e., the particle size and time) effectively changed the flow

characteristics from very cohesive (AOR=90°) to almost free flow conditions (AOR → 0°).

3.3 Drop tests of ice blocks on stiffened panels

The drop tests carried out at NTNU and Aalto University are presented in this section. These tests are an attempt to address the research question Q2 (see Section 2.3). In the experiments, the focus was on simultaneous inelastic deformations of ice and a steel structure. In the analysis of the results, the focus was on the energy dissipation mechanisms during the drop tests and on the impact characteristics of the stiffened panels. Uncertainties, the limitations of the experimental apparatus and the role of different factors that affect the experiments are also discussed. We also recommend that the experiment procedure be repeated (with some modifications) to improve the accuracy of the experimental results. The information presented in this section is important for planning experiments of ice-structure interaction scenario in which both the ice and the structure undergo significant deformations.

3.3.1 Experimental apparatus

Drop tests were conducted using laboratory-grown freshwater ice blocks and stiffener steel panels of varying characteristics. The aim of the experiments was to study the ice-structure interaction under conditions similar to those that are present during accidental collisions (i.e., high deformation rates, brittle-like ice failure and inelastic structural deformations). The tests at NTNU may be regarded as pilot tests for those conducted at Aalto. In turn, the drop tests at Aalto were performed to study the effects of removing the hydrodynamic aspects of moored-structure tests. In the moored-structure tests (see Section 3.4), a stiffened panel was mounted onto a moored structure and impacted with an approximately one ton ice block at speeds of 1 and 2 m/s.

Ice sample preparation

The ice samples were manufactured using a mix of water and commercially available crushed ice pieces. The pieces of crushed ice (Figure 45a and Figure 45c) were purchased from a third party. The crushed ice pieces that were 1–10 mm (Figure 45a) and 10–40 mm (Figure 45c) were used for ice sample preparation at NTNU and Aalto, respectively. Additionally, to facilitate specimen handling, a metal rod was frozen into the ice.

The samples were grown in the cold room, which was maintained at approximately −20°C. Moulds with partly flexible edges were used to allow thermal expansion of ice

during freezing. The moulds were filled with crushed ice and water, which was pumped in through hoses at the mould bottom to minimise the risk of trapped air. The moulds had dimensions of 0.8×0.6×0.4 m and 1.2×1.0×0.9 m at NTNU and Aalto, respectively. The manufacturing procedure resulted in ice microstructures as shown in Figure 45b and Figure 45d. Once an ice sample was completely frozen, it was removed from the mould and cut into the desired shape. Examples of produced ice blocks are shown in Figure 46.

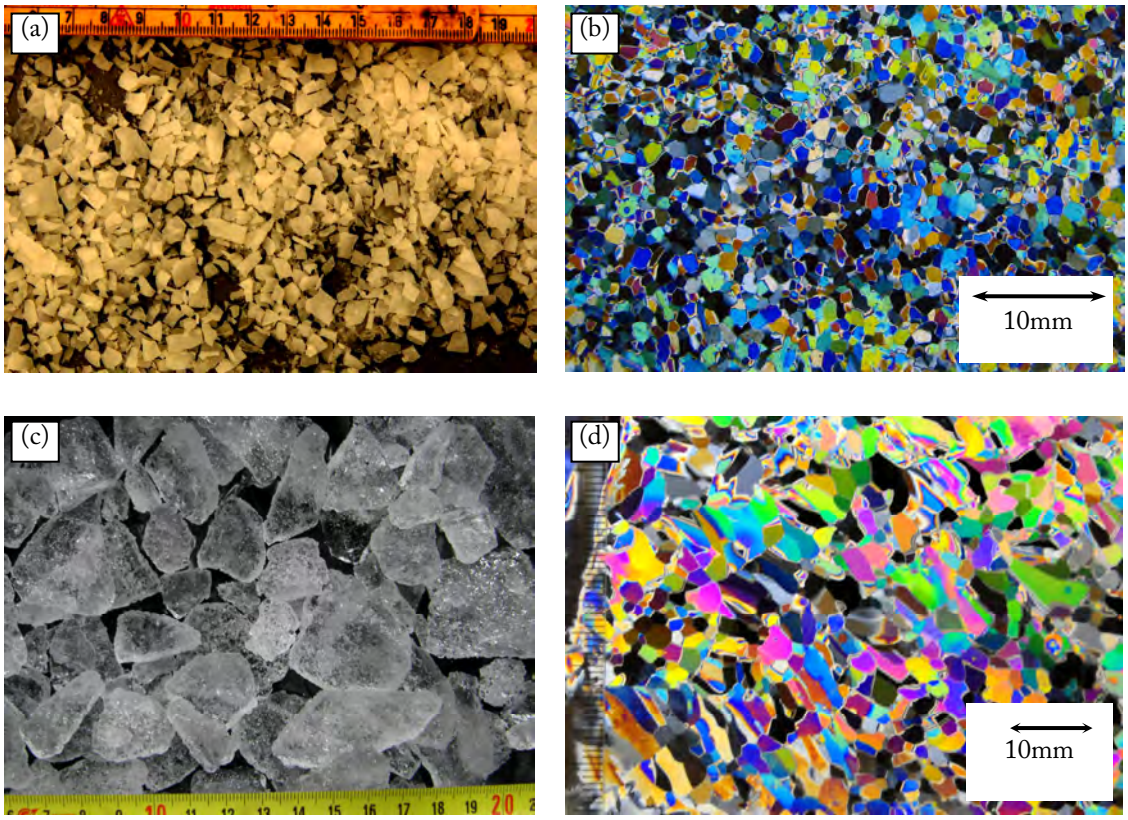

Figure 45: Photographs of ice used during the experiments: (a) and (c) crushed ice pieces used at NTNU and Aalto, respectively; (b) and (d) thin sections of ice at NTNU and Aalto, respectively; the thin sections of ice were photographed between two sheets of polaroid material.

The grain sizes of ice samples, used in the drop tests at NTNU and Aalto, were approximately 1–2 mm (see Figure 45b) and 2–10 mm (see Figure 45d), respectively. Figure 45 shows that the grain size of the produced ice depends on the type of the underlying crushed ice (i.e., the third-party manufacturing process of the crushed ice).

The ice at NTNU did not contain any visible cracks or large voids, whereas the ice at Aalto contained cracks that were sealed with water a few days before testing. The corners of the ice block were cut before the test to prevent interaction between the flat contact surfaces. Uniaxial compression tests were performed on ice samples that were extracted from the ice blocks at Aalto. Rectangular prisms and cubes of two different

sizes were prepared using a milling machine and were tested at an ambient temperature of approximately 0°C at an average loading speed of approximately 17 mm/s. The maximum nominal pressure (compressive strength) and density for each sample size are listed in Table 9. For comparison, the crushing strength of polycrystalline ice at 0°C (10-mm grains) in the brittle range is 0.94 MPa (Michel, 1978).

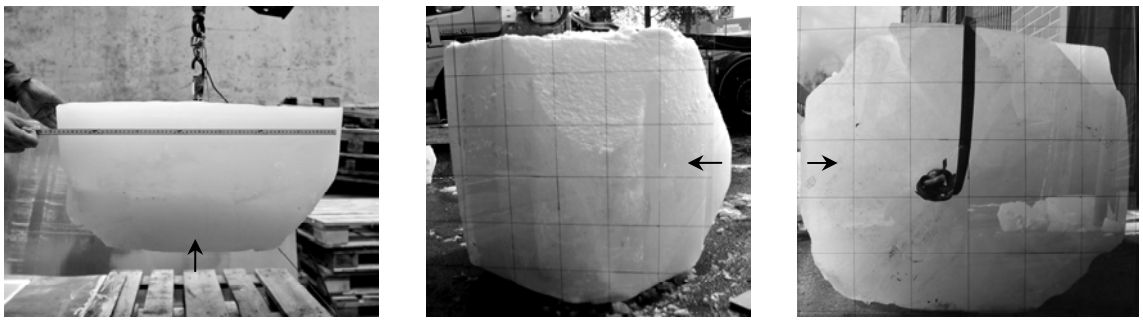

(a) NTNU 104 kg (b) Aalto 706 kg (c)Aalto 601 kg

Figure 46: Representative ice blocks; black arrows indicate the direction of impact; in (b) and (c), the grid lines are 0.15 m apart.

Table 9. Measured compressive strength under the uniaxially applied load in the brittle-like failure mode and the density of ice used in the tests at Aalto; the brittle-like failure mode was characterized by a sharp decrease in the load after ice failure.

Ice samples	Area [mm^2]	Height [mm]	Density [kg/m^3]	Strength[a] [MPa]
rectangular prisms[28]	50±2 by 50±2	141±12	880±23	0.89±0.32
small cubes[9]	49±1 by 49±1	49±1	898±18	0.71±0.28
large cubes[4]	129±3 by 127±4	109±24	891±7	0.92±0.15

The superscripts in the column "Ice samples" correspond to the total numbers of samples tested.
[a]The strength of brittle material is not always a meaningful quantity because it is not constant but varies with geometry, specimen size and lateral pressure; see Kendall (1978) for a discussion on this subject. However, the strength is used here to demonstrate the similarities/differences between the laboratory-grown freshwater granular ice and freshwater granular ice found in nature.

Stiffened panels

The stiffened panels used in this study exhibited in-plane dimensions of 1.1 m × 1.1 m (excluding L-profiles). The plates were stiffened with six flat-bar stiffeners 0.15 m in height with 0.15 m spacing and two flat-bar frames 0.15 m in height with 500 mm spacing (Figure 47). Additionally, two L-profiles were welded to the plate, as shown in Figure 47, and acted as supports (rigid boundaries) during the tests. Characteristics of the test panels are shown in Table 10.

Table 10. Characteristics of test panels.

Panel	Material	t_p–t_s–t_f (mm)
P1 (NTNU)	S235	4–2–4
P2 (Aalto)	S235	2–2–2
P3 (Aalto)	S235	4–4–4

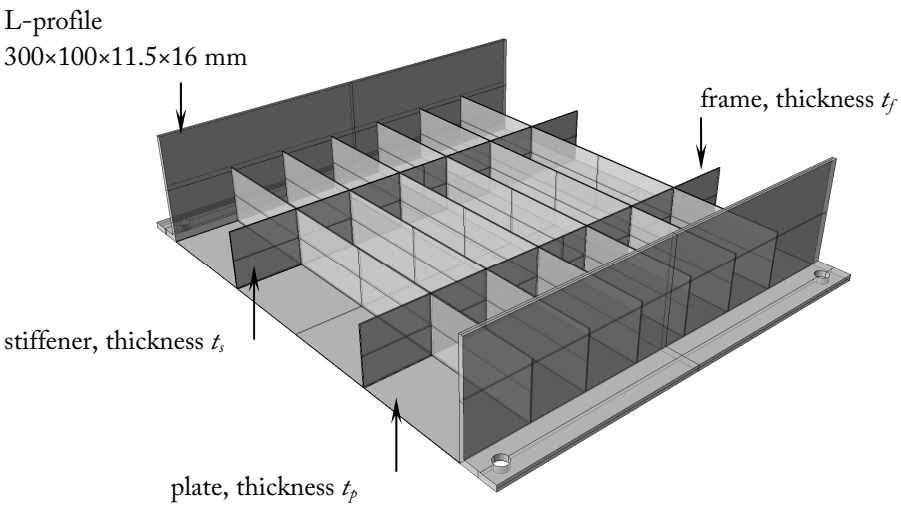

Figure 47: Stiffened panel with the main structural components.

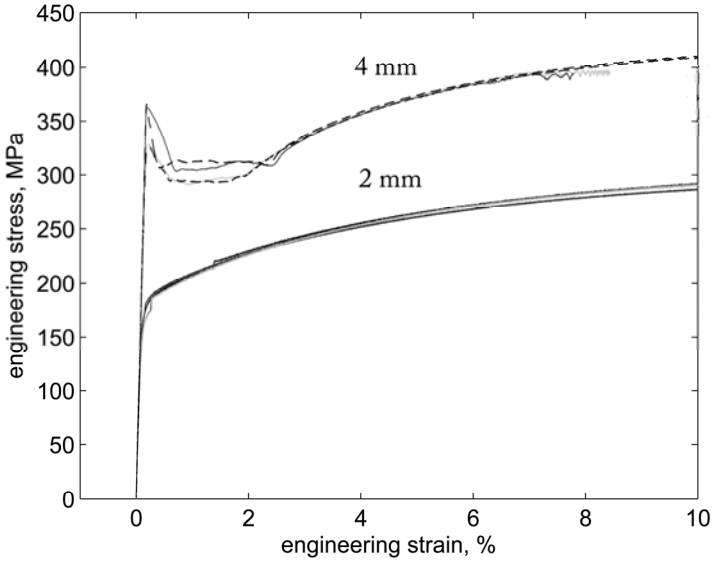

Figure 48: Inhomogeneous yielding of mild steel with the corresponding engineering stress-strain curves for 2 mm and 4 mm thick specimens; the capacity of the testing machine was limited to 25 kN, and the engineering strains were limited to 10%.

Tensile tests on steel samples were performed to characterize the behavior of the test panels. The test coupons were extracted from the same material that was used to manufacture the panels at Aalto. Tensile specimens were prepared in accordance with DNV Rules for Classification of Ships/High Speed, Light Craft and Naval Surface

Craft (2011). For each type of coupon (i.e., the 2-mm and 4-mm-thick specimens), the samples were prepared and tested parallel with and normal to the rolling direction at room temperature. The specimens were loaded at a constant speed of 0.0008 mm/s up to a yield point. After the yield point, the loading speed was increased to 0.08 mm/s. The stress-strain curves for the 2- and 4-mm-thick specimens are given in Figure Figure 48).

Experimental setup

Figure 49 shows a sketch of the experimental apparatus. The apparatus consisted of wooden supports, a test panel, the ice and a system for the lifting and quick release of the ice (i.e., a snap shackle and a release rope). The stiffened panel was placed on the top of wooden pallets. There were slight differences between the experimental configurations at Aalto and NTNU. These differences are shown in Figure 49. For example, at Aalto, four constraints (extra weights, total 1594 kg) were used to keep the stiffened panel in position.

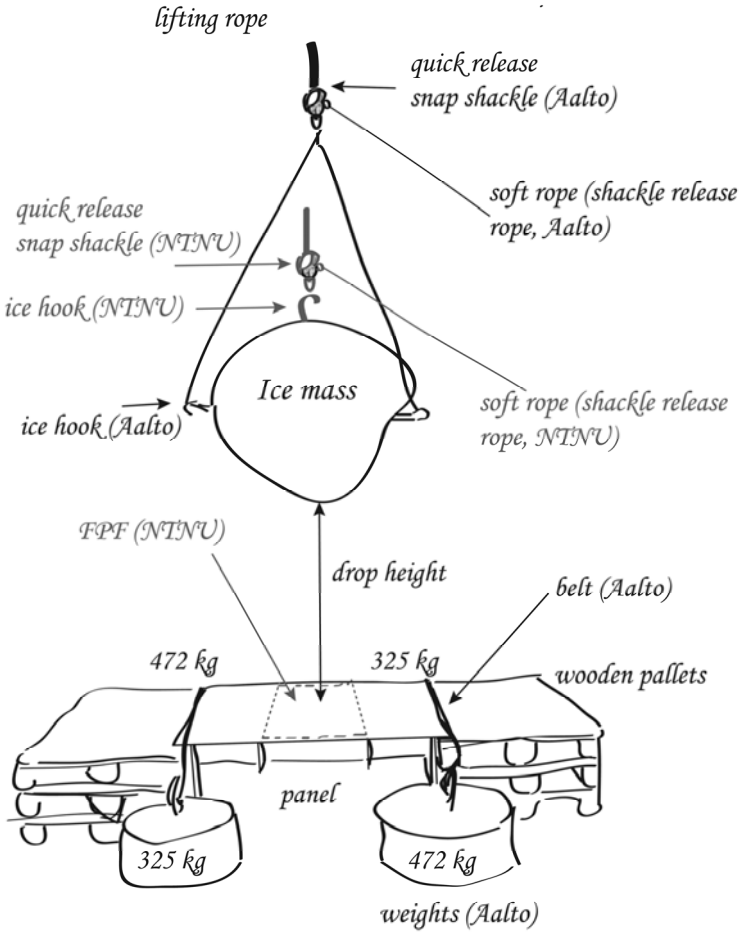

Figure 49: Schematic of drop test apparatus at Aalto and NTNU (FPF denoted Fuji Prescale Film; the FPF was attached to the test panel and used to record the contact pressures during impact).

The tests were performed at an ambient temperature of approximately 3°C. The ice masses were attached via a quick release shackle to the lifting mechanism. At NTNU, a tractor equipped with a front loader was used. In the first two tests, the loader bucket was removed, and the ice masses were attached to a bucket link (at the end of the lifting arms), as shown in Figure 50a. In the final test, the bucket was connected back to the lifting arms to increase the drop height (Figure 50b). A crane truck (shown in Figure 50c) was used as a lifting mechanism at Aalto. The ice blocks were lifted to a certain height and then dropped on the test panel using the shackle release rope (see Figure 49). At NTNU, the ice block (Figure 46a) was dropped onto the panel P1 (Table 10) from heights of 1.1 m, 1.6 m and 3 m. The drop height (see Figure 49) is defined as the clearance between a test plate and the bottom surface of the ice block. The mass of the ice block was measured before and after the drop test. At Aalto, the ice block weighing 706 kg (Figure 46b) was dropped onto a 2–mm thick panel P2 from a height of 0.5 m, and the ice-block of 601 kg (Figure 46c) was dropped onto a 4–mm panel P3 from the height of 3.0 m.

At NTNU, the ice pressure was measured using Fuji Prescale Film (FPF). The drop tests at NTNU were recorded using a FASTCAM-APX high-speed video camera. The recording speed was 1500 frames per second with 1024×512 resolution.

(a) (b) (c)

Figure 50: Photographs of the experimental apparatus (a and b) at NTNU and (c) at Aalto.

Table 11. Summary of drop tests.

Test no.	Plate thickness [mm]	Drop height [m]	Kinetic energy [kJ]	Max. length of dent [mm]	Max. depth of dent [mm]
1[c]	2.0 (NTNU)	1.1	1.1	not visible	not visible
2[c]	2.0 (NTNU)	1.6	1.6	not visible	not visible
3[s]	2.0 (NTNU)	3.0	3.0	~150[*]	~8
4[c]	2.0 (Aalto)	0.5	3.5	~600	~13
5[s]	4.0 (Aalto)	3.0	17.7	~750	~8

[c] crushing ice failure mode; [s] splitting ice failure mode; [*] visual observation

The masses of the ice blocks were measured before impact at Aalto. At NTNU, the ice masses were measured before and after the tests. At NTNU, an accelerometer was also attached to the ice hook shown in Figure 49 using a tape. Later, the accelerometer was observed to have disconnected from the hook immediately after the first ice-plate

contact. Thus, the acceleration history measurements were considered to be unreliable and were not used further. A total of five drop tests were conducted. Three different panels were used altogether. The extent of plate damage was measured after each test. Table 11 summarizes the test conditions and the primary test results.

The kinetic energy reported in Table 11 is the kinetic energy of the ice block immediately before the impact. The maximum length of the dent in the panel and the maximum depth of the dent (see Table 11) were estimated based on the measured deflections of the plate. The measurements were performed before and after each drop test. To measure the deflections, a plunger-type dial gauge was used.

For Test nos. 1, 4 and 5 the energy dissipated within the structure were determined from the measured plate deflections and the high-speed video recordings. Analytical and numerical approaches were used to assess the energy dissipated within the wooden supports and in the steel panel, respectively. For Test no. 1, the energy dissipated within the ice was estimated from the measured pressure and the high-speed video recordings. The energy dissipated within the ice was estimated using two different methods (Methods I and II). In Method I, the predominant energy dissipation mechanism was assumed to be the formation of fine powdery spherical fragments, and the energy was considered to be dissipated in producing a pure free surface. In Method II, a pressure-area relationship was assumed that involved the contact area and the penetration distance. Detailed descriptions of the calculation procedures can be found in Section 3.3.3.

Pressure measurements

FPF indicates the applied pressure differences as a red color density variation. FPF is composed of an A-Film which is coated with a micro-encapsulated color-forming material and a C-Film coated with a color-developing material (see Figure 51). The size of the micro-capsule and the strength of its walls are a function of the applied pressure. The volume of the color-forming material and the color-developing material determines the color density. The micro-encapsulated color-forming layer was designed to react to pressures in the range 2.5–10 MPa with accuracy ±10% (FUJIFILM Instruction Manual). The minimum measurable area was 0.1 mm^2, and the minimum measurable pressure application speed was 1.0 ms.

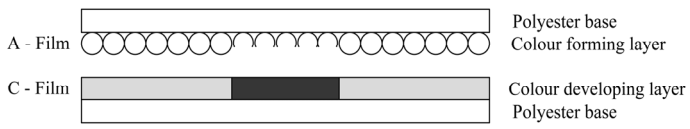

Figure 51: Structure of FPF.

The FPF was cut into the desired rectangular shape and placed over the impacted panel. To avoid sliding of the A-film along the C-film during testing, two sheets were bonded together with adhesive material outside the measurement area. Besides, FPF was also attached to the impacted panel using the tape.

3.3.2 Results

An image sequence from the ice-panel interaction during Drop Test no. 1 is shown in Figure 52.

The HSV showed that the ice-crushing process continued for at least 16 ms at an average speed of 1.0 m/s. The speed was 4–5 times lower than the speed of the ice immediately before the impact (4.6 m/s). The average crushing speed (1.0 m/s) was calculated as the ice-crushing distance, u, divided by the duration of the crushing event, Δt, (Δt=0.016 s was taken from HSV).

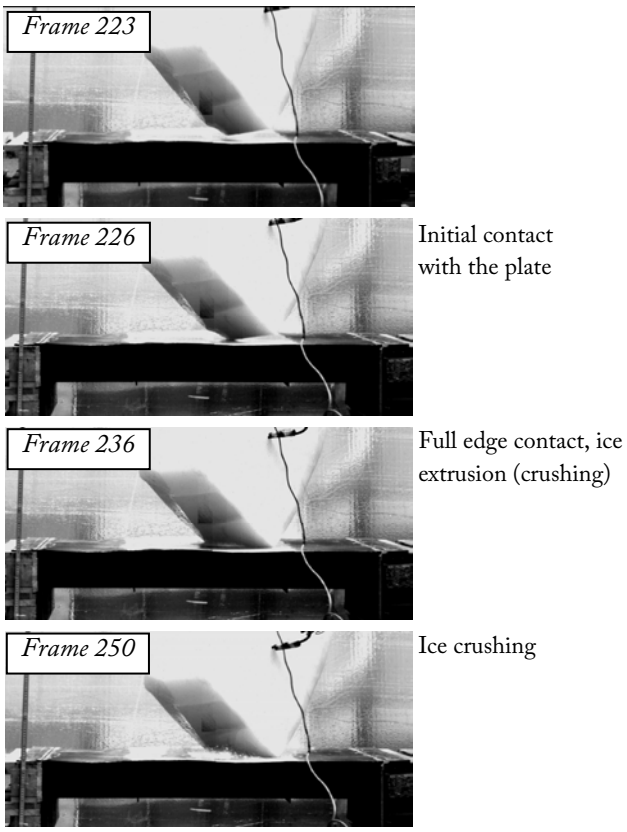

Figure 52: Sequence of images extracted from a high-speed video recording for Drop Test no. 1; the time interval between each frame is 0.67 ms.

The ice behavior during drop tests could be classified into two categories: crushing-dominated and splitting-dominated failure modes, as shown in Figure 53a and Figure 53b, respectively. The observed failure modes are indicated in Table 11.

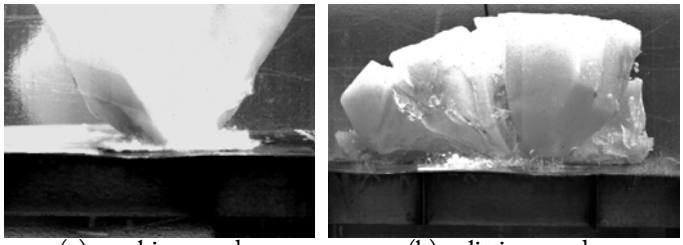

(a) crushing mode (b) splitting mode

Figure 53: Representative frames of ice failure modes (a) crushing-dominated mode and (b) splitting-dominated mode obtained during Test nos. 1 and 3, respectively.

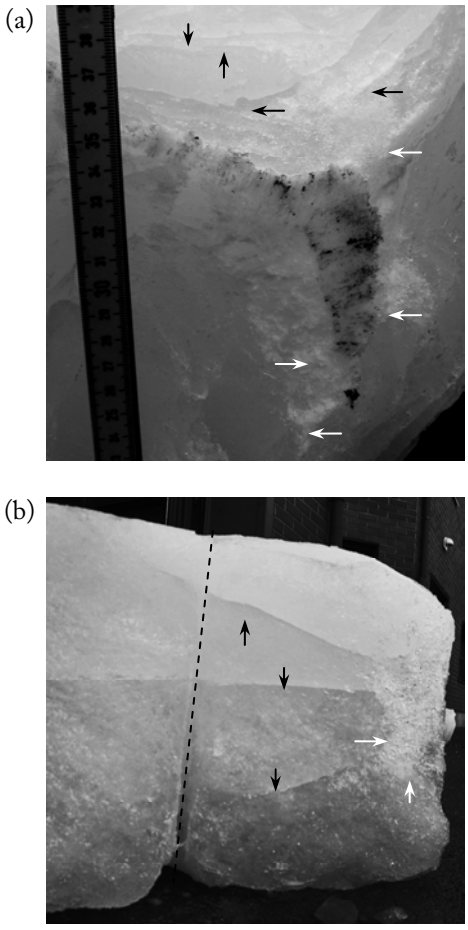

Figure 54: Ice damage after Test nos. 1 (a) and 5 (b); black arrows indicate freshly-formed splitting cracks, and white arrows indicate crushed and extruded ice; in (a), the ice-plate contact surface exhibits a grimy appearance; in (b), the dashed line indicates the position of the metal rod, which was frozen into the ice to facilitate specimen handling.

Ice crushing was localized specifically at the contact zone and characterized by the formation of fine powdery ice particles from the bulk ice and the ejection of these particles away from the contact zone. During localized crushing, the ice block remained intact except for a crushed region. The splitting mode was dominated by axial splitting and shear failure mechanisms and characterized by complete shattering of the ice block upon impact. The crushing failure mode produced finer fragments than those generated during splitting failure. Figures Figure 54a and Figure 54b are a close-up view of the ice damage zone after Test nos. 1 and 5, respectively.

Ice pressure

In Figure 55, a pressure distribution map at the end of Test no. 1 is plotted using data obtained from the FPF. For Test no. 1, the measurements of the FPF were processed using a method similar to the method described in Kim et al. (2012a). Pixel values were converted to the actual pressure levels, p_{film} using Equation (17). The equation was derived using the standard momentary pressure vs. color density curve and the color sample provided by FUJIFILM. The color sample was scanned and saved as an image file. The image file was processed in Matlab to determine the average pixel value corresponding to the color density. Pressure-color density data were converted to the pressure-pixel value relationship

$$p_{film} = 5744x^{-1.455} \tag{17}$$

where x is the pixel value and p_{film} is pressure in MPa.

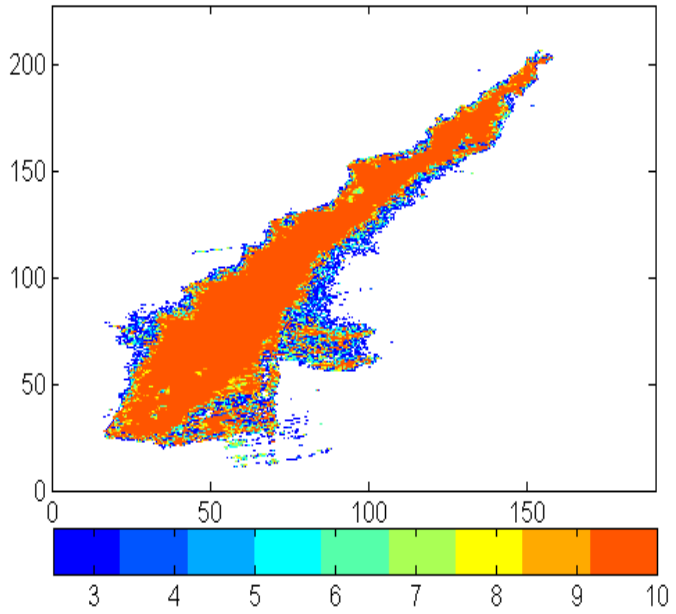

Figure 55: Pressure distribution map for Test no. 1 (crushing failure mode): the plane dimensions are given in mm, and the pressure is given in MPa.

The pressure map in Figure 55 reflected the events shown in Figure 52 and the contact surface in Figure 54a. The average pressure on the measured contact area with a local pressure of 2.5 MPa $<p_{film}<10$ MPa, was approximately 10 MPa. The presence or absence of high-pressure zones during the ice crushing event shown in Figure 52 and Figure 55 could not be confirmed due to FPF limitations. A better method to record the distribution of contact pressures could incorporate several FPFs of different sensitivities stacked vertically, as performed by Kim et al. (2012a).

Panel deformations

The level of damage for each test panel is shown in Table 11. The maximum extent of damage was achieved in Test no. 5. Figure 56 shows plate deformations for Test no. 5. Figure 57 shows plate deflections after Test no. 5. The last figure was obtained by plotting the measured deflections in 3D space using Matlab.

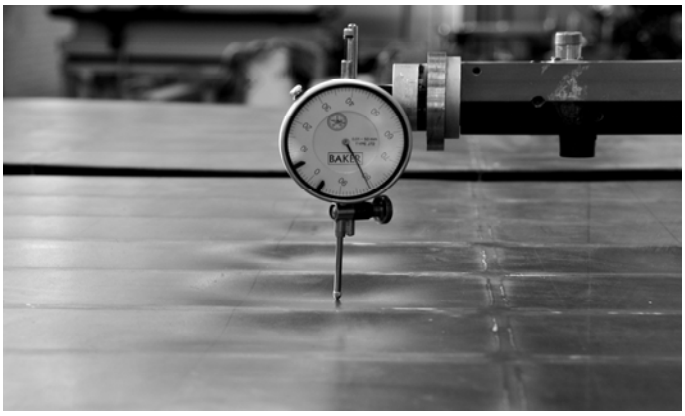

Figure 56: A photograph of the plate damage after Test no. 5.

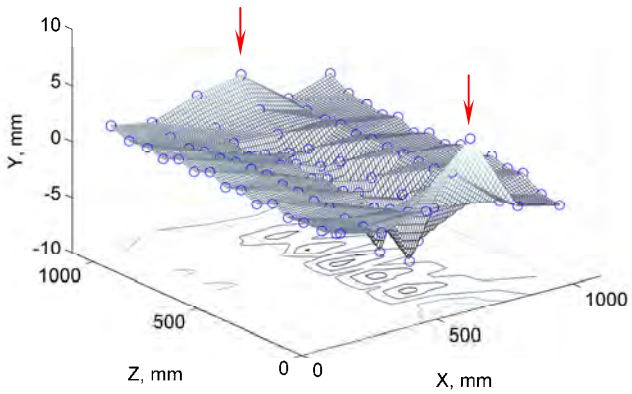

Figure 57: Plate deflections after Test no. 5; the circles indicate measured values; arrows indicate the locations, where the measured deflections may contain a contribution from the plate handling after the test.

The maximum length of the dent in Figure 56 is 750 mm (which is five times the spacing of the stiffeners), and the maximum depth is 8 mm.

3.3.3 Analysis and discussion

Energy of the process

The ice-structure interaction consisted of two interrelated response mechanisms: that of the ice and that of the test panel. The response mechanism of ice (or structure) is a collection of elementary processes. The response mechanism of ice consists of a rotation of the block, local elastic, viscous and plastic deformations of the ice, internal ice damage and fragmentation (crushing failure mode). The response mechanisms of steel structures consist of elastic and, to the extent required plastic deformations.

To further understand the ice response mechanism during collision, the energy involved in the elementary processes can be evaluated. The energy balance can be written as:

$$E_{kin} = E_{cr} + E_{bc} + E_{rot} + E_{platedef} \tag{18}$$

E_{kin} is the kinetic energy of the ice block immediately before impact (see Table 11); E_{cr} is energy dissipated within the ice block; E_{bc} is energy dissipated through flexibility of the wooden supports; E_{rot} is energy dissipation due to rotation of the ice block during collision; $E_{platedef}$ is energy dissipated in the steel structure. Energies E_{cr} and $E_{platedef}$ depend on the different energy-absorbing mechanisms activated during the interaction event.

Energy dissipated within the ice block

All the calculations in this section refer to Test no. 1. For this test, it was possible to obtain a rough estimate of the energy involved in the fragmentation process. Energy dissipation E_{rot} and $E_{platedef}$ were neglected because the impact direction passed through the centre of gravity of the ice mass, and after the impact, there were no permanent plate deformations.

For the case of the crushing failure mode in Figure 53a, it is possible to calculate the total energy dissipation within the ice using the following methods.

Method I. The energy dissipated during crushing failure mode will be dissipated by different energy-absorption mechanisms: (i) internal deformations, (ii) formation of cracks, (iii) formation of fine powdery ice particles from bulk ice and (iv) friction between fragmented surfaces and between the ice and the panel. During the crushing failure mode, the formation of fine ice particles can be seen in Figure 53a. The energy dissipation during the formation of these ice particles can be estimated by multiplying

the surface energy by the total surface area created, similar to that performed by Jordaan and Timco (1988).

The predominant cause of energy dissipation is assumed to be the formation of fine powdery ice particles from the bulk ice. The size of both the crushed zone and the ice fragments in the zone may be estimated from HSV records and photographs taken during the experiment. Considering spherically-shaped ice fragments of 2 mm in diameter, it is possible to predict the energy that is dissipated within the ice block, E_{cr} as:

$$E_{cr} = G_s \cdot 4\pi \cdot r_{is}^{\,2} \frac{V_{cr\_total}}{V_{is}} \tag{19}$$

where G_s is energy required to create a new crack surface of unit area; r_{is} is radius of a crushed particle; V_{cr_total}/V_{is} is total number of fragments (total crushed volume divided by the volume of a single particle). The effect of porosity was not included in the calculations. The assumed particle size corresponds to the grain size of the ice in Figure 45b.

G_s=0.8 J/m^2 was measured by Timco and Frederking (1986) and was used by Jordaan and Timco (1988) to assess the crushing energy during the indentation tests on level ice sheets. Michel (1978) reported G_s=0.109 J/m^2, and Schulson and Duval (2009) estimated G_s ranging between 0.138 – 0.218 J/m^2. The energy E_{cr} was calculated using different values of G_s found in the literature. Calculated E_{cr} values vary in the range between 0.73 and 5.33 J (see Table 12). Note that E_{cr} is the energy dissipated in pure free-surface production.

Table 12. Crushing energy calculation for Test no. 1.

Parameters	Value
Total mass, kg	~2*
Ice density, kg/m^3	900
Volume, m^3	0.0022
Particle radius, mm	1
Number of particles	530516
Total surface area, m^2	6.7
Gs, J/m^2	0.109 – 0.8
Crushing energy, J	0.73 – 5.33

* the difference between the ice mass before and after the impact

Method II. Another method for estimating the total energy dissipation within ice is based on the assumption of the pressure-area relationship:

$$E_{cr} = \int F du = \int p \cdot A \, du \tag{20}$$

where F is the impact force, u is the crushing (penetration) distance; A is the contact area A=f(u); p is contact pressure. Tests have shown that during ice crushing against a rigid surface the contact pressure varies over time and over the contact area. For simplicity, the following assumptions have been made:

(i) At every penetration distance, the pressure is constant over the contact area.
(ii) Pressure decreases with increasing area:

$$p = 3.2A^{-0.26} \tag{21}$$

Equation (21) is derived in Appendix C using experimental data on confined freshwater and multiyear ice at two different scales.

(iii) There is a linear relationship between the contact area, A, and the penetration distance, u.

$$A = cu = \frac{\Delta A}{\Delta u}u;\ \ c = \frac{\Delta A}{\Delta u} \tag{22}$$

where c=0.364 m was obtained from the experimental data (FPF).

$$E_{cr}\ \left[MJ\right] = \int_0^{u_i} 3.2A^{-0.26}Adu = 3.2\int_0^{0.0167}(cu)^{0.74}du = \\ 3.2c^{0.74}\frac{1}{1.74}u^{1.74}\Big|_0^{0.0167} = 0.7\cdot 10^{-3} \tag{23}$$

In Equation (23), the ice crushing distance, u≈0.0167 m was obtained from experimental data (HSV).

The ice impact force F=p·A=3.2$A^{0.74}$=3.2(cu)$^{0.74}$ corresponding to Equation (21) was 73 kN.

Using the upper bound of the pressure-area relationship p=5.0$A^{-0.46}$ and the lower bound p=0.51$A^{-0.46}$ found in Appendix C, the energy dissipation E_{cr} was found to be in the range between 3.44 kJ and 0.35 kJ. The lower bound estimate of energy E_{cr} appears to be more similar to the actual value of energy dissipated due to ice crushing in Test no. 1.

The ice impact force corresponding to the upper bound and the lower bound pressure-area relationship was 316 kN and 32 kN, respectively. Another method for estimating the ice impact force is to use the FPF data:

$$F = p_{film}\cdot A = 10\left[MPa\right]\cdot 6.08\cdot 10^3\left[mm^2\right] = 61\ kN \tag{24}$$

In Equation (24), a constant value of p_{film}=10 MPa was used. This value corresponds to the p_{film} distribution in Figure 55.

Energy dissipated within the wooden supports

All calculations in this section refer to Test no. 1. In Equation (18), the energy dissipated through the flexibility of the wooden supports was determined using the following considerations:

(i) a linear force-displacement relationship,
(ii) the work required to stop the ice mass can be expressed as:

$$E_{bc} = \frac{1}{2} F_{bc} u_{bc} \tag{25}$$

F_{bc} is the peak force at the wooden supports; u_{bc} is the vertical displacement of the impacted panel. The vertical displacement of the impacted panel *P1* was 10–15 mm (HSV data). The value of F_{bc} was assumed to be the same as the ice impact force F in Equation (20), corresponding to a pressure-area relationship (Equation (21)) and equal to 73 kN.

The energy dissipated due to flexibility of the supports was 0.37 – 0.55 kJ.

Energy dissipated in the steel structure

From the data collected during Test nos. 2 – 5, it was not possible to estimate the ice-crushing energy as for Test no. 1. However, for Test nos. 4 and 5, it was possible to estimate the energy dissipation due to deformations of the panel. The estimation was based on the simplified non-linear static analysis of transverse impact on panels as described below.

A rising uniform pressure distributed over an area of 0.325 × 0.75 m was applied to the test panel in Figure 47, and L-profiles were not included in the simulations. Translations of the plate were not allowed at points where the plate is welded to the L – profile (i.e., along two opposite plate edges and short edges of the stiffeners). The calculations were performed with ABAQUS v6.9–2 (Step: static, Riks) using S4R shell elements of approximately 25×25 mm. Mild steel S235 was modelled as elastic-plastic material with parameters obtained from the tensile tests (Figure 48). The effect of welds and initial imperfections was not considered. The dissipated energy in the structure was calculated for the deformed state (Figure 58a)) closest to the measured deformations (Figure 58b).

The results of the calculations are summarised in Table 13.

Table 13. Energy of the process.

Test no.	Available kinetic energy E_{kin} (kJ)	Energy dissipated within the ice E^*_{cr} (kJ)	Energy dissipated within the structure $E_{platedef}$ (kJ)
1	1.1	0.35 – 3.44	0.37 – 0.55
4	3.5	unknown	0.6
5	17.7	unknown	1.2

*as estimated by Method II

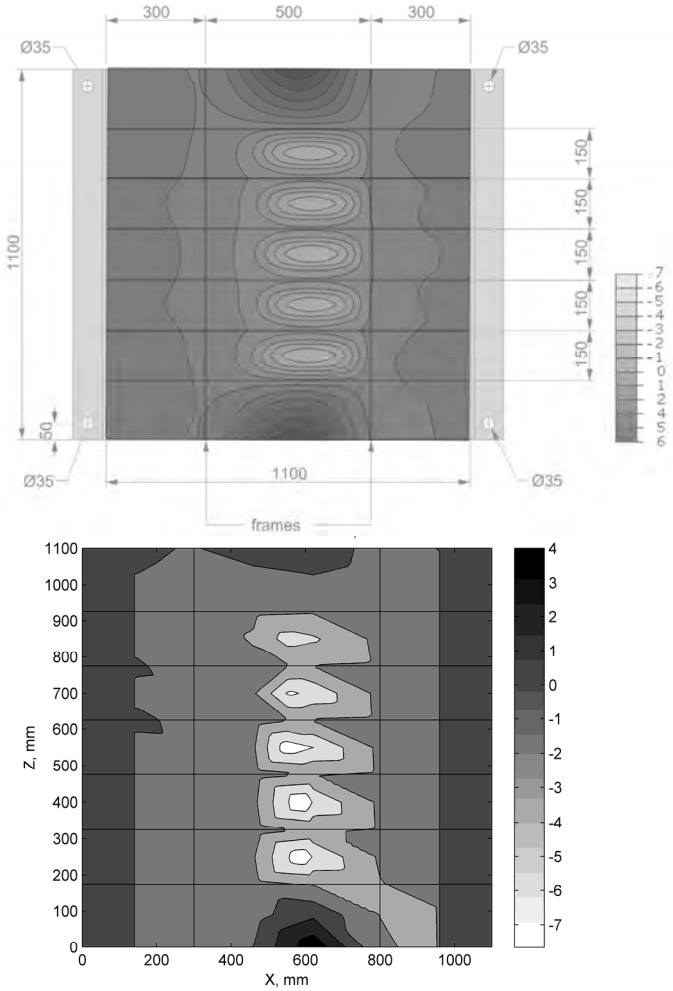

Figure 58: Dents on the steel plate (plate thickness of 4 mm): (a) calculated dents assuming uniform pressure distribution; (b) measured dents (Test no. 5); the pressure distribution during the test is unknown; all dimensions are in millimetres.

Based on the results in Table 13 and considering the energy balance, Equation (18), most of the collision energy (approximately 70 – 80%) was dissipated within the ice block, and approximately 20 – 30% was dissipated within the structure (including panel

deformations and flexibility of the supports). The calculation example (Method II) shows that the pressure-area relationship $p = 3.2A^{-0.26}$ derived using data from confined ice at two different scales can be used for predicting the energy dissipation within the ice during the drop test.

The effect of internal stresses

We attempted to directly observe fracture evolution in ice during the tests using HSV records. Only the outward appearance of the failure phenomena can be observed because of the opacity of the ice. As the failure process progressed, the pulverised/extruded ice influenced the visual observations. The response mechanism of ice in Test nos. 1, 2 and 4 was compressive failure and in Test nos. 3 and 5, the failure mechanism was predominantly axial splitting and shear.
The crushing energy of 0.73 – 5.33 J (in Table 12) obtained earlier using Equation (19) is three orders of magnitude smaller than the total collision energy involved in the process (1.1 kJ). Similar observations were made by Jordaan and Timco (1988), who reported a total energy for crushing of 6 mJ and an estimated total energy of 8 J for ice crushing using force-time series. The authors contended that the viscous extrusion process (a mechanism for the clearing of crushed ice) was the major energy-absorbing process during indentation by flat indenters (see Jordaan and Timco (1988) for a detailed discussion).

In our test, the process of ice fragmentation started due to intense stress conditions. Calculations indicated that the production of new free surfaces did not originate from the major energy-dissipation mechanisms for the crushing failure mode in Figure 53a. For example, the fine ice particles formed would eject outward from the surface. In the calculations (Method I), the energy absorbed by the ice particles moving out of the surface was not considered. In addition, when the ice block strikes the plate, the ice material at the ice/plate interface is under triaxial stress with the hydrostatic component largest near the centre of the contact area. The ice failure mechanism (or the energy-absorption mechanism) will depend on the stress state that arises due to complex loading (or boundary conditions).

The effect of internal stresses is illustrated by an example in Figure 59, which compares the available experimental data from the ice indentation tests of Masterson and Frederking (1993), Wells et al. (2007), Section 3.1 (see tests with rigid indenters in Figure 59) and from Daley (1994) (i.e., the Hobson's Choice pressure-area data for the ice wedge versus the flat flexible indenter) with Drop Test no. 1 and the unconfined compressive strength of the ice.

The truncated square is the point corresponding to the distribution of the pressure over the contact area at the end of Test no. 1. This point was obtained using the pressure

distribution map in Figure 55. Despite the differences in scale, as shown in Figure 59, the data point from the drop test agreed very well with laboratory-scale ice indentation tests under confinement and medium-scale ice indentation field-tests.

Furthermore, data from the compressive tests on standard prismatic ice samples including small 5-mm-width ice-cubes and large (10–15)-mm ice-cubes (see Table 9) are also shown in Figure 59. These ice samples were extracted from the ice blocks at Aalto. Pressure values were calculated as the maximum force divided by the cross-sectional area. Local pressures in Figure 59 are the maximum local pressures registered by the tactile pressure sensor during compression tests under uniaxial loading at Aalto. Figure 59 shows that the pressure values for unconfined tests (uniaxial compression) are lower than the values for the indentation tests (rigid and flexible indenters) at similar contact areas.

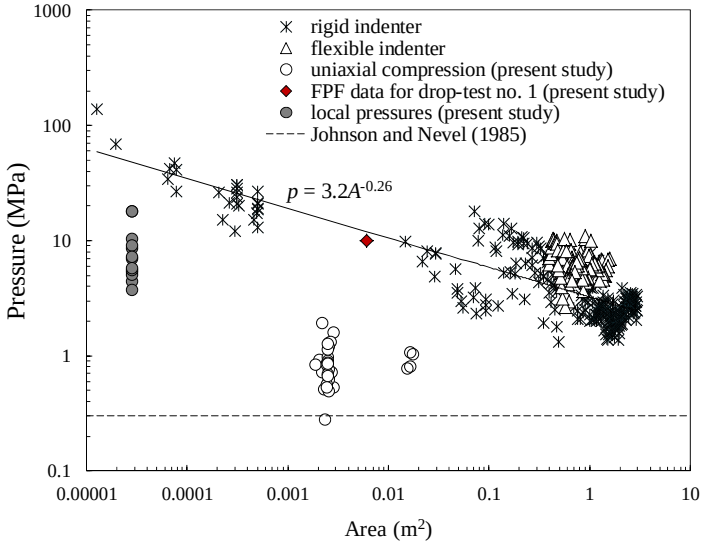

Figure 59: Log-log plot of pressure versus area for confined and unconfined ice; the flexible indenter resembled a ship-side structure (digitized data from Daley, (1994)).

There are two main reasons for the decreased values:

1. The compression tests were conducted at 0°C. The ice samples were close to the melting point and exhibited lower strength than ice used in laboratory-scale indentation tests conducted at lower temperatures.
2. The uniaxial test data corresponded to the failure of ice under low or no confinement, while the ice during indentation tests was confined and exhibited higher resistance.

Additionaly, it is possible to estimate the ice strength, σ, using the expression of Johnson and Nevel (1985) and compare the value with empirical compressive strength

of ice under uniaxial loading and empirical pressures. According to Johnson and Nevel (1985), when an ice feature collides with a structure, the kinetic energy of the ice feature is dissipated due to the work done in crushing ice (E_{cr}). The product of σV_{cr_total} represents E_{cr}. In our case, the kinetic energy of the ice block is also dissipated within the structure and therefore, $E_{cr}=0.7E_{kin}=\sigma V_{cr\_total}$ gives us σ=0.3 MPa. This level of σ is plotted in Figure 59 as the dashed line.

In summary, the drop-test results showed that most of the collision energy (70 – 80%) was dissipated within the ice with no or little plastic deformation of the structure. The maximum structural damage obtained for the experimental apparatus corresponded to a kinetic energy of approximately 18 kJ (see Table 11). Calculating the energy dissipated within the ice revealed that the production of new free surfaces was not the major energy dissipation mechanism for the crushing failure mode presented in Figure 53a.

If the kinetic energy immediately before impact is high relative to the size of the ice block (e.g., as in Test no. 5, where $0.5m_iv_i^2/l_i\approx$18 kJ/0.9 m, and l_i denotes the vertical dimension of an ice block of mass m_i , with an initial velocity v_i), the interaction is mainly governed by the ice shape and size (i.e., the global confinement or the boundary conditions of the ice block). In our case, the interaction resulted in ice shattering. In turn, if the impact energy is sufficiently small relative to the size of the ice block (e.g., as in Test no. 4, for which $0.5m_iv_i^2/l_i\approx$3.5 kJ/0.9 m), the interaction is influenced by the local confinement of the ice at the contact zone. The local confinement of the ice at the contact zone is a function of the local ice shape at contact and the flexibility and structural arrangement of the impacted structure, which complicates realistic analyses of collision scenarios.

3.3.4 Discussion of uncertainties and limitations

The collision between the ice mass and a structure is a rather complex process involving the deformation and motion of two bodies. The objective of the drop tests was to simulate an ice structure collision scenario in which both the ice and a structure undergo inelastic deformations. Conducting a full-scale collision experiment using small icebergs (or bergy bits) with kinetic energies on the order of 1 MJ to 1 GJ (Cammaert and Muggeridge, 1988) would most likely produce more information related to the ALS. However, full-scale tests are costly and difficult to control. In addition, no global expertize is available on how to conduct such tests. The available expertise (from bergy-bit impact trials, iceberg towing impacts, growler impact tests and tests at Pond Inlet, and Hobson's Choice Ice Island) is limited to cases in which the structure was considered to be rigid (or elastic). Only recently has attention been shifted toward the coupled behavior of ice and a structure (see Manuel et al. (2013), for example). To

balance the accuracy of the results with the total costs, the drop tests and collision experiments (Section 3.4) were conducted at scales approaching a full-scale ice impact. Possible uncertainties in the results, which are related to the experimental configuration, are listed below.

(a) *Size effects in welds and initial imperfections* The microstructure and mechanical properties of steel are altered by welding. Steel exposed to intense localized heat tends to recrystallize and soften in the heat-affected area, while the weld filler metal remains strong. Photographs of typical tee and cross weld joints are shown in Figure 60. The figure shows that the ratio between the half-width of the heat-affected area (≈15 mm) and the stiffener spacing (150 mm) was not the same in the laboratory and at full-scale. In addition, the ratio between the size of the weld (i.e., the weld length of 3–5 mm) and the thickness of the stiffener (e.g., 2 mm) in the laboratory was different from that at full-scale. The effective stiffener spacing was reduced by a few percent because of welds. This reduction affected the load bearing capacity of the plate.

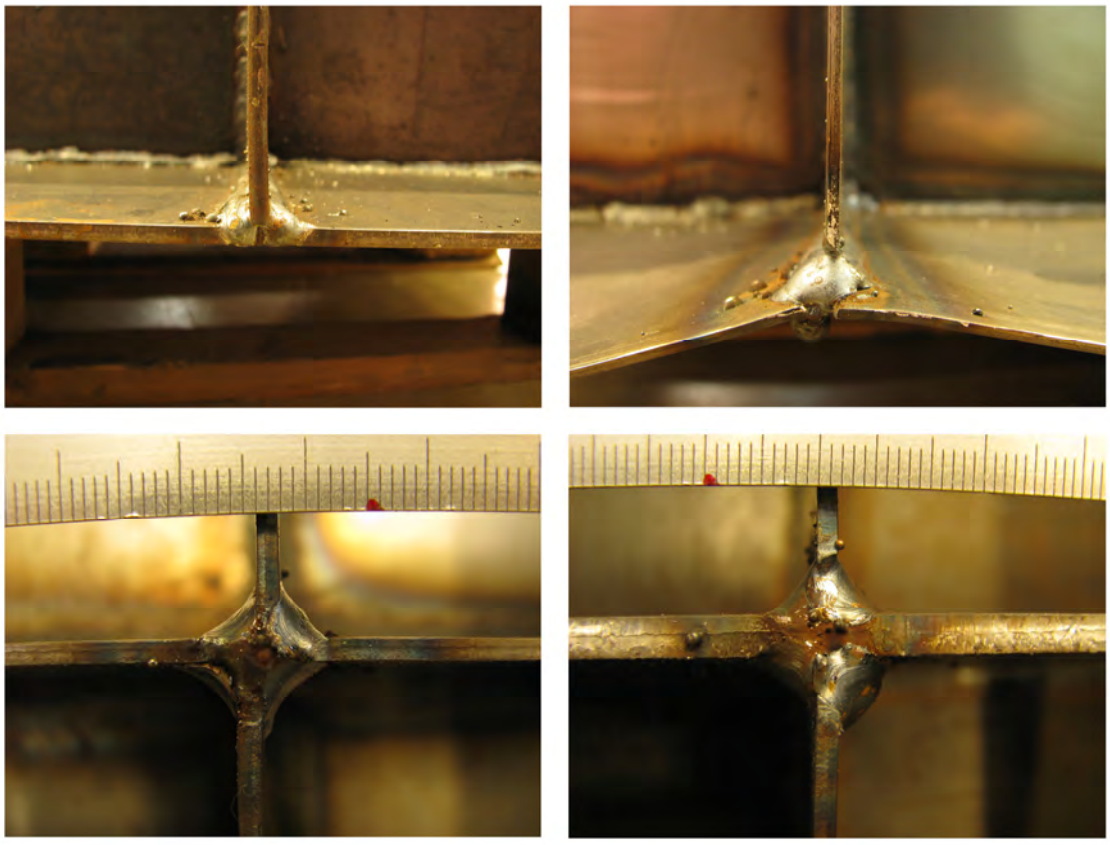

Figure 60: Close-up photographs of the tee- and cross-fillet welds in the manufactured panels.

Nevertheless, the overall deformations of the plate were relatively small compared to those immediately prior to plate rupture. The size effect of the welds on the plate' behavior was considered to be negligible in the present study. The extent of the initial imperfections was larger for the thinner plates and could be clearly observed with the naked eye. In the plate deformation analysis, we subtracted the initial imperfections from the total deflections of the plate.

(b) *Effect of laboratory-grown ice* The larger the size of the ice blocks, the more challenging it is to maintain a uniform ice microstructure. The size of the ice block made it difficult to maintain control of the freezing direction. Freezing the large blocks of ice at Aalto created internal stresses in the ice and large cracks. Additional measures were necessary to ensure stable ice growth and to prevent open cracks. Several holes were drilled through the ice to release the internal ice pressure. Cracks formed during freezing. These cracks were sealed with freshwater a few days before testing. In addition, to facilitate specimen handling, a threaded metal rod (at Aalto) with a hook welded to a metal plate (at NTNU) was frozen into the ice. The presence of this "artificial inhomogeneity" was not believed to affect the localized crushing behavior of the ice, which was sufficiently far from the metal (Figure 53a). However, the cracking patterns during the splitting-dominated failure mode (see Figure 53b) could have been affected by the metal rod because (1) the rod may have acted as an additional source of crack nucleation, and (2) the rod may have acted as a physical barrier to crack propagation. We cannot elaborate further on the effect of a metal object frozen in the ice without comparing the splitting behavior of the ice with and without the metal rod.

A better means of producing freshwater ice blocks would be to use unidirectional freezing. Such a scheme could be realized by isolating the sides and top of the ice molds, following Gudimelta et al. (2012), for example. However, this manufacturing technique would require a longer freezing period that should be taken into consideration during planning if the experiments.

(c) *HSV limitations* The HSV recordings were used to visualize, analyze and measure high-speed ice-structure interaction events in which the ice underwent crushing (or splitting), and the structure deflected plastically. The framing rate was used in conjunction with the resolution to set the total time of an event that could be recorded by camera until the camera memory was full. For example, the velocity of cracks in freshwater ice (or the rate of ice fragmentation) is approximately 1000 m/s, as measured by Petrenko and Gluschenkov (1996). To record a crack running through an ice sample that is 1.0 m in size, the framing rate must be at least 5000 frames per second. This rate enables five snapshots to

be recorded over a crack propagation distance of 1.0 m. Choosing such a high frame rate for the given HSV camera meant that events lasting over 1.0 s could not be recorded while satisfying the image resolution requirements. Moreover, the higher the frame rate, the brighter the object needs to be or an additional light source may be required. Thus, for the NTNU experiments, we chose an optimum recording speed of 1500 fps with a 1024 × 512 resolution. No HSV recordings of the ice-structure impact were made at Aalto. For the chosen frame rate, we could not track the crack propagation in the splitting failure mode. Only the external appearance of the failure phenomena could be observed because of the opacity of the ice. As the failure process progressed, the pulverized and extruded ice affected the visual observations. This behavior limited our understanding and analysis of the ice failure process during impact to some extent.

(d) *Accuracy of pressure measurements* The uncertainties in the pressure measurements were primarily related to the calibration of the FPF and its operational limits. The FPF shows the applied pressure differences as a red color density variation, which was converted to a pressure distribution map (shown in Figure 55) using the standard momentary pressure vs. color density curve (and a color sample) provided by FUJIFILM. A direct calibration of the pressure film for the ice-steel contact interface was not performed, and there may have been an uncertainty in the pressure records. The pressure measurement film was designed to react for pressures in the 2.5–10 MPa range with a 10% accuracy for a minimum measurable area of 0.1 mm^2. Thus, contact pressures below 2.5±0.25 MPa and above 10±1.0 MPa were not recorded. The actual contact area for Test no. 1 may also have been larger than that reported in Figure 55. Note that the pressure record reflected the entire process (or to some extent, an envelope of contact pressures during the impact event). The pressure record should not be confused with the spatial pressure-area distribution defined in Section 2.2. A better way of recording contact pressures would be to use several FPFs of different sensitivities, one on the top of the other, following Kim et al. (2012a). Alternatively, Tekscan tactile pressure sensors could be used provided that the response time of the sensor is known and satisfactory, and the pressure mat (and each censil) is properly calibrated with respect to the total force and the total contact area. The pressures during ice crushing can vary rapidly from 0 to 100 MPa; thus, the calibration of the pressure sensors could be an important issue.

It is unlikely that the uncertainties described above altered the primary conclusions drawn from the experiments (see Chapter 5). However, the reader should be aware of the limitations associated with these types of tests.

3.3.5 Summary

The work has presented results from drop tests of ice blocks on stiffened steel panels, with emphasis on ice failure mode and processes of energy dissipation, highlighting the importance of internal stresses on the crushing process during collision. The relevance of the recorded contact pressure to that calculated from laterally confined ice was demonstrated.

The pilot drop-tests results were as follows: (1) the behavior of the laboratory-grown ice resembled that of freshwater granular ice; (2) the pressures corresponding to the actual contact areas were generally within the assumed limits; (3) the ice dissipated most of the available collision energy during crushing; and (4) the structural deformations were limited to small (or moderate) dents on the impacted panel.

3.4 ACCIDENTAL COLLISIONS BETWEEN AN ICE BLOCK AND A FLOATING STRUCTURE

In this section, issues related to the planning (and execution) of the collision experiments are discussed. This section describes laboratory-scale ice block/stiffened panel impact tests performed in a 40 m × 40 m ice basin at Aalto University. The stiffened panels were mounted onto a flat-bottomed floating structure. During testing, the moored floating structure was impacted with an approximately one-ton ice block. The collision scenario was designed to simulate the coupled behavior of the ice and the impacted structure, i.e., both the ice and the structure deform inelastically during a collision event. The impacts were conducted at speeds of 1 and 2 m/s for panels of different stiffnesses. The objectives of the tests were as follows: (i) to obtain data for the development and verification of existing analytical and numerical models of full-scale ice block/structure collisions, (ii) to build expertise in modeling accidental collisions under laboratory conditions and (iii) to advance the development of a testing procedure for a full-scale collision scenario. A total of 18 impact tests were conducted using structures of varying rigidities and ice masses. The towline force, the strains and the accelerations of the impacted structure were recorded continuously during each run. Each collision event was video-taped from five different angles. After the test runs with the flexible structures, the damage to the ice and the structure was observed. The impact locations and times were determined from the collected data, and the impact velocities and forces were computed. This section describes the tests and presents the major test results, including a description of the structural damage resulting from collision with the ice blocks at 2 m/s. The laboratory tests presented in this section are one of a few experiments on simultaneous inelastic deformations of ice and a structure.

The present study was motivated by the limited amount of available experimental data for validating existing numerical and analytical models of damage to the ice and to the structure; see Section 2.3. The test procedure, instrumentation, impacted structure, ice manufacturing process and other experimental aspects are described in the next subsections. Additional issues related to the planning of the collision experiments under laboratory conditions can be found in Kim et al. (2012b).

3.4.1 Experimental methodology

In a realistic collision scenario, the location of the impact and the geometric properties of the ice feature depend on the methods used to detect ice masses and the management procedures used to prevent collisions. The "human element" can also play a negative (or positive) role in a collision scenario. An example of a negative human element would be if a large ice mass (e.g., an iceberg) was detected by radar but no substantial action was taken by the captain and crew to prevent a full-speed collision. An example of a positive human element would be if the system failed to detect an ice mass, but the captain attempted to reduce the speed of the vessel at the last moment such that only a slow-speed collision occurred. The global shape (and local shape at contact) of the ice feature is also an important parameter. The global shape is important for overall response while the local shape is important with respect to penetration of plating.

A collision process involves the motion and deformations of two bodies (i.e., the ice and the steel structure). Thus, "true" modeling of a full-scale collision event in a laboratory must include proper scaling of the geometrical and mechanical properties of both the ice and the structure. Unfortunately, it is uncertain which of the mechanical properties of ice should be scaled and how this scaling should be performed. Tests of physical models in scenarios where the ice fails in compression (or crushing) cause additional complications because of uncertainties associated with the mechanics of ice failure at full- and model-scales (Jordaan et al., 2012). Sazonov (2011) noted that there are no reliable methods to precisely scale of the crushing strength of ice and the nominal pressure that are used in the "process" pressure area model. Timco (1986) reported that model ice is not sufficiently brittle to simulate real ice. Kendall (1978) considered that the compressive strength is not a very useful parameter for describing brittle behavior because of compression cracking does not always take place at the same stress. In addition, there are complications associated with scaling the behavior of a steel structure. If model ice (i.e., Froude scaling) is used and the elastic modulus and yield strength of steel are not properly scaled, the ice mass becomes too soft relative to the impacted structure. Using a material other than steel may lead to erroneous deformation mechanics.

In this study, the choice of the collision scenario (and the experimental apparatus) was limited by the testing facilities (e.g., the maximum speed allowed by the towing carriage, the strength of the concrete floor and the walls of the ice basin). No "standard" scaling laws were used in the aforementioned tests. Instead, emphasis was placed on selecting an appropriate collision scenario to simulate the coupled behavior of the ice and the impacted structure, that is:

(i) both the ice and the structure deform during a collision event;
(ii) the ice behavior at impact should approximate that in nature; the ice block should be strong (and large) enough to cause permanent deformations in the impacted structure;
(iii) the impacted steel plate should be sufficiently stiff to produce similar deformation patterns (including plastic deformations of a plate, local and global buckling of stiffeners, etc.) as at full-scale impact.

The following collision scenario was considered: an impact of an approximately 1000-kg ice block (a truncated cube) onto a vertical stiffened plate at a speed of 2.0 m/s. By comparison, the "Canadian Bulker" and the "Overseas Ohio" collided with an iceberg at speeds of 7.5 m/s and 5 m/s, respectively (Westmar, 2001). Cammaert and Muggeridge (1988) noted that the small ice masses could be accelerated by waves to reach kinetic energies on the order of 1 MJ to 1 GJ. The aforementioned considerations (i–iii) were accounted for in performing the following actions to simulate a full-scale ice-structure collision scenario.

Test apparatus

The experimental apparatus balanced the accuracy of the results with the total costs. The tests were conducted in a 40 m by 40 m Aalto Ice Tank facility that can operate with water depths as high as 2.8 m. Figure 61 and Figure 62 present a schematic and a photograph of the experimental apparatus, respectively.

A system of ropes (consisting of towing and steering ropes, as shown in Figure 61) was used to tow an ice block into a purpose-built target. The ice motions (predominantly sway) were controlled by the steering rope to obtain a "good" collision with a direct impact on the target. An ancillary rope (see the white rope in the plan view in Figure 61a) was used to position the ice block before each test. The ice was towed at speeds of approximately 1 and 2 m/s against the moored structure shown in Figure 62. It may be argued that this collision scenario is unrealistic in the sense that the ice mass is being towed to impact the structure. In a realistic collision scenario, small ice masses could be accelerated by waves to reach higher kinetic energies and hit a fully loaded tanker above the design draft. Alternatively, a vessel could collide with a submerged part

of an ice mass (or an iceberg) at a full sea-service speed of 6 m/s (Yamaguchi et al., 2002).

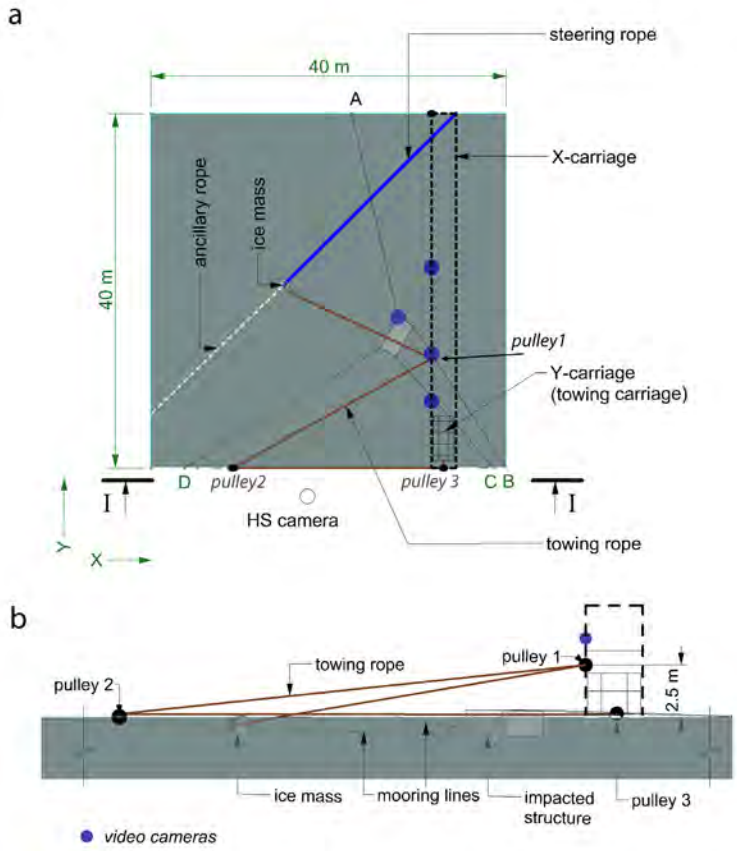

Figure 61: Schematic of the experimental configuration: (a) plan view ("A, B, C and D" are mooring lines); (b) side view I–I; the slack in the mooring lines is not shown in the drawings.

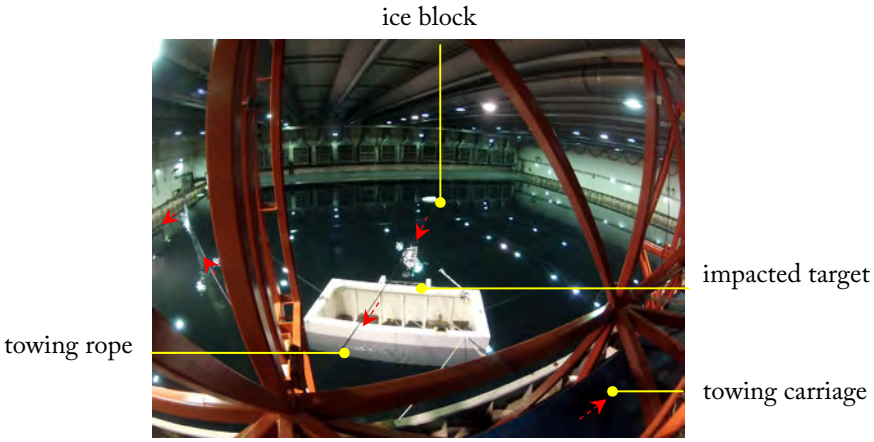

Figure 62: Photograph of experimental apparatus, arrows indicate the direction of the towing arrangement.

Under laboratory conditions, e.g., Gagnon (2004) was able to perform tests where free-floating glacial ice masses were impacted with a heavy apparatus designed to simulate a ship bow. In field tests at Newman's Cove, Newfoundland (Bruneau et al., 1994), glacial ice pieces were towed into a fixed structure. Our selection of the collision scenario (and experimental setup) considers the restrictions imposed by the testing facility such as limitations on adverse operating conditions of the towing carriage, i.e., the maximum speed allowed by the towing carriage and the safe deceleration rate of the carriage, maximum allowable load per unit surface area of the basin floor, ultimate strength of the walls, etc. The goal of the experimental setup was to create conditions for inelastic deformations of the ice and the structure during interaction. To reproduce a realistic hydrodynamic interaction between the ice block and the structure was beyond the scope of this study.

A towing test was conducted using the following procedure: the ice block was manually positioned at the desired location using the ancillary rope (see Figure 61a). A start-position was selected to enable the carriage to reach the desired steady-state velocity and to enable the ice block to reach the designated impact position. The ice block was controlled by a steering rope to ensure that the impact occurred near the center of the target plate. A V-towing scheme was used to prevent the ice hook from hitting the panel as shown in Figure 63. A towing-rope release mechanism, i.e., a weak-link (see Figure 64) attached to the towing rope, was used to prevent high dynamic loads on the towing carriage at impact.

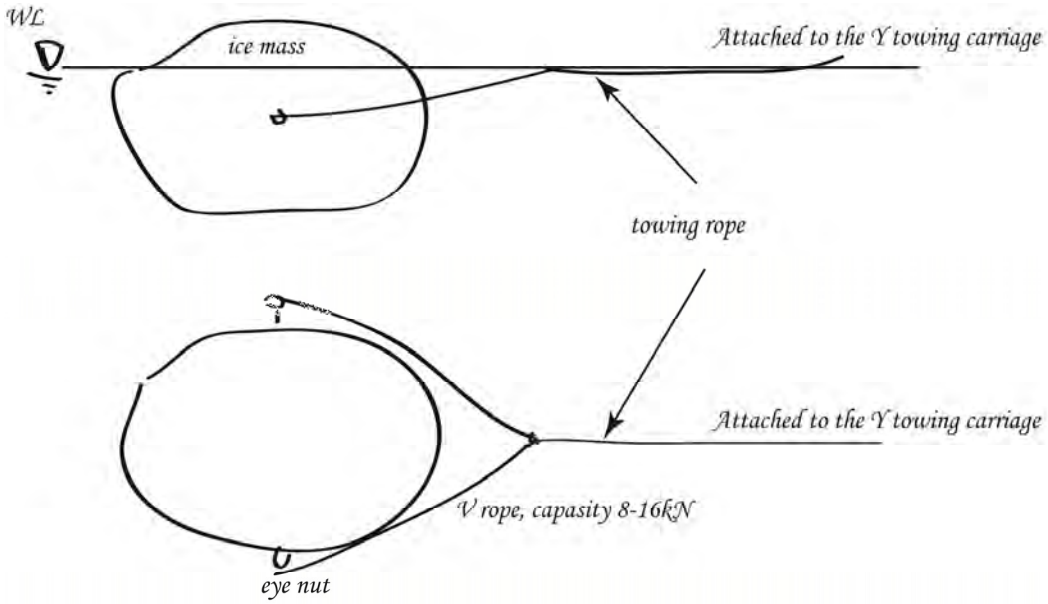

Figure 63: Side and plan view schematics of the towing arrangement.

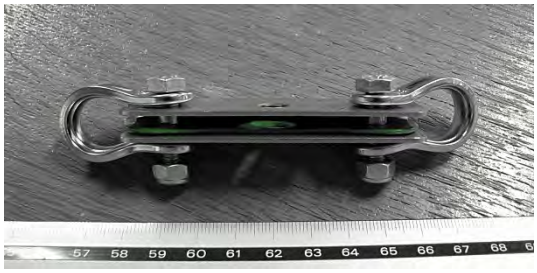

(a) capacity 3 kN and 5 kN

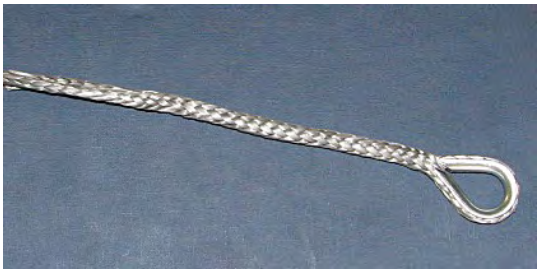

(b) capacity <4 kN and <8 kN

Figure 64: Photographs of the weak-links used during the experiments: (a) TOST weak link that was placed between the towing rope and the *Y* towing carriage and (b) a portion of the V-rope that was used to connect the ice block to the towing rope.

The temperature of the water in the ice tank was approximately 0°C. As far as possible, the ice block was placed in the water before the impact test. Nevertheless, the size of certain ice blocks diminished because of melting as the test program progressed over many days.

Description of the impacted target

It was important to choose the stiffness of the impacted structure in order to produce a similar deformation pattern (i.e., the plastic deformations of the plate, the local and global buckling of stiffeners) as in a full-scale impact. In the early stages of impact, the panel crushes the ice. The total force increases with the contact area. At a certain stage, the plate deforms plastically. If the kinetic energy of the impact is sufficiently large, failure ideally occurs in the web stiffener adjacent to the contact area.

Figure 65 shows the geometry of the impacted structure. The impacted structure, shown in Figure 65a, consisted of a stiffened panel (Figure 65b) bolted to a moored floater.

The global dimensions of the floater at the water plane were 2 m × 4 m, with a draught of approximately 0.9 m and a total height of 1.25 m. Table 14 lists the ballasted loading conditions used in the experiments for the floater including the 12-mm-thick impact panel. The floater was moored with four 10–16 mm ø polyester mooring lines, as shown in Figure 61a. The mooring lines were attached to the bottom corners of the floater at one end and to the basin wall (a rail of the *X* carriage) at the other end. All of the lines were equipped with 20-kg weights at mid-span to provide a soft mooring response with low forces until there was significant sway and surge displacement of the floater. Thus, the soft mooring arrangement did not affect the measured impact loads or

velocities but served to properly align the floater and ensure the safety of the basin during testing.

Four flexible panels of varying stiffnesses were used to simulate the desired interaction between the ice block and the structure. Figure 65c presents a plan view of the impacted panel, highlighting the different structural elements of the panel.

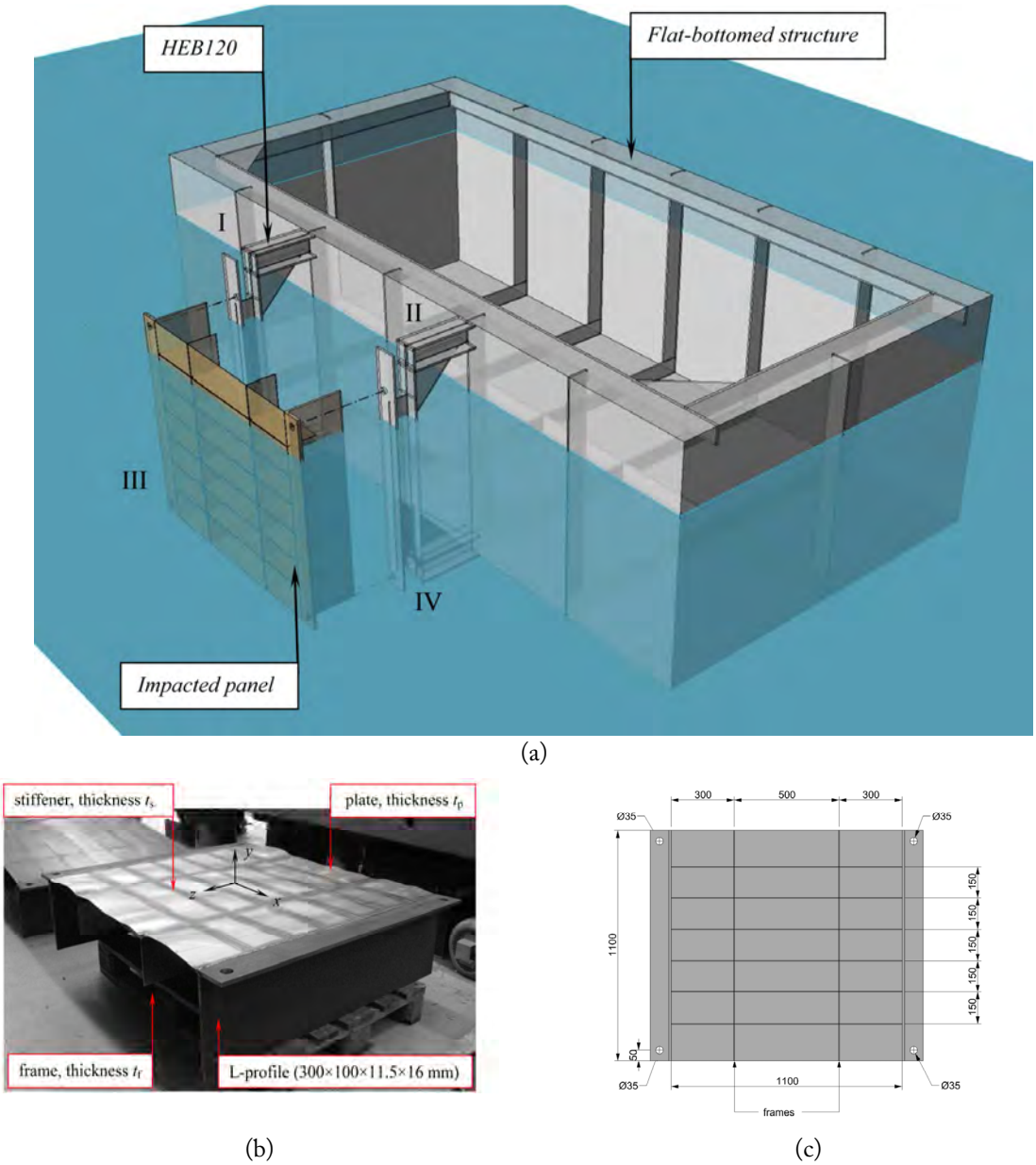

Figure 65: Geometry of the impacted structure: (a) attachment scheme of a stiffened panel with the floater; (b) photograph of a stiffened panel showing the main structural components (the flat-bar stiffeners and the flat-bar frames of height 0.15 m); and (c) detailed drawing of the impacted panel (xz–view, where all dimensions are in mm).

Table 14. Floater ballast conditions used in the experiments (panel D was included in the calculations).

Total weight (kg)	7537
Draught (m)	0.95
Vertical center of gravity (m)	
X_G	0.00
Y_G	0.01
Z_G	0.23
Roll period (s)	≈2
Radii of gyration (m)	
R_x	0.8
R_y	1.2
R_z	1.4

The overall dimensions of the panel were 1.1 m × 1.3 m. All of the welds were fillet welds. The actual weld throat was estimated from close-up photographs to be approximately 3–4 mm. The panel was supported by six transverse flat-bar stiffeners with a height of 150 mm and a spacing of 150 mm and by two flat-bar frames with a height of 150 mm and a spacing of 500 mm, as shown in Figure 65b and Figure 65c. The total plate area of 1100 × 1100 mm^2 (excluding the L-profiles) was wider than the expected ice crushing area. Table 15 lists the panel parameters.

Table 15. Test panel characteristics.

Panel	Material	Thickness, t_p–t_s–t_f (mm)
A	Mild steel S235	4–2–4
B*	Mild steel S235	2–2–2
C*	Mild steel S235	4–4–4
D	Mild steel S235	12–12–12

*Used in drop tests

The initial plate deflections were measured on a flat, vibration-free surface using a plunger-type dial gage. The final deformations of the A–C panels were computed as the difference between the measured plate deflections before and after the impact.

The dimensions of the structural elements (i.e., the plate thickness, the stiffener spacing and the frame spacing) were determined based on the following considerations.

(a) The ice pressure was assumed to be uniformly distributed over the $s \times s$ loading patch (where s denotes the stiffener spacing).

(b) The experimental data obtained for ice indentation at medium and small scale were assumed to be representative in estimating the ice pressure within the $s \times s$ contact area (see Appendix, Figure C2). For a stiffener spacing of 0.15 m, an ice pressure of approximately 2.0–3.0 MPa was considered to be realistic.

(c) The plate-strip analogy was used to predict the onset of irreversible deformations. (d) Three different numerical methods were used to predict structural deformations during the collision event. These methods were as follows: (1) a simplified nonlinear static analysis; (2) an integrated (or coupled) quasi-static (displacement control) analysis and (3) an integrated (coupled) dynamic (velocity-controlled) analysis. The techniques and the assumptions on which these methods were based are described below. In addition, the uncertainty in the ice material properties was investigated using a sensitivity study of an ice collision with a flat rigid (i.e., analytical rigid) plate. The results of the sensitivity study are given in Appendix D.

1. Simplified nonlinear static analysis of transverse impact on panels

A rising uniform pressure, distributed over an area of 0.15×0.15 m^2, was applied to the center of a test panel in Figure 65b, L – profiles were not included in simulations. Translations of the plate were not allowed at points where the plate is welded to the L – profile (i.e., along two opposite plate edges and short edges of the stiffeners). The calculations were carried out in the finite element software ABAQUS v6.9–2 (Step: static, Riks) using S4R shell elements of size approximately 50×50 mm. Mild steel S235 were modeled as elastic-plastic material with a bilinear isotropic hardening rule (E_s=210 GPa; v_s=0.3; σ_y=235 MPa; plastic hardening modulus h_p=625 MPa). Calculations were done for all panels in Table 15. Figure 66 shows results of the calculations. In Figure 66 the energy absorption capacity of the panels (internal energy) is plotted as a function of plate displacement at the impact point. The plate displacement is defined as the nodal displacement in the direction of the impact. The horizontal line in Figure 66 corresponds to the calculated difference in kinetic energy before and after a collision (G_s). In Figure 66, the grey area represents a loss of energy solely by ice crushing process and limited by the lower (upper) bound pressure-area estimates shown in Appendix C (Figure C2). The total energy loss (G_i) during ice crushing and the difference in kinetic energy before and after a collision (G_s) were estimated as:

$$G_s = \frac{1}{2}(m_i + A_i)v_i^2\left(\frac{1}{1+\frac{m_i + A_i}{M_s + A_s}}\right) \qquad (26)$$

$$G_i = \int_0^{u_i} C(\pi u(2R_i - u))^{1+x}\,du$$

where m_i is the ice mass; A_i is the hydrodynamic added mass of the ice; v_i is the ice velocity; M_s is the mass of a structure; A_s is the hydrodynamic added mass of the structure; C, x are empirical constants; u is the ice crushing distance.

For simplicity, we assumed a perfect ice sphere with radius R_i. Mean energy of ice crushing (Figure 66) corresponds to a pressure-area relationship $p=3.2A^{-0.26}$.

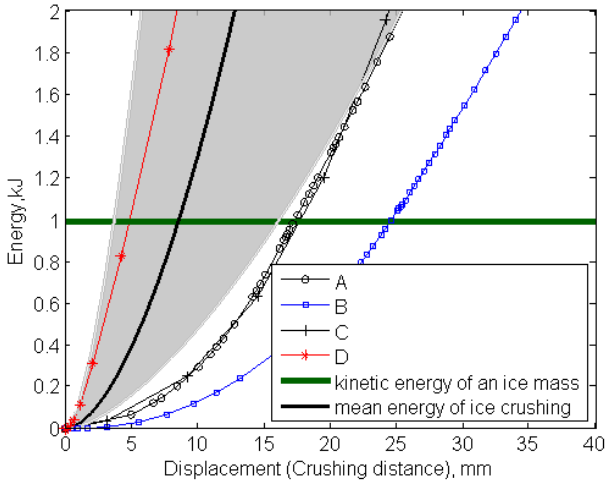

Figure 66: Energy dissipation in ice (grey area) and steel panels; horizontal line corresponds to the calculated difference in kinetic energy before and after the collision (G_s), assuming a spherical ice mass (R_i=0.45 m).

2. Integrated nonlinear dynamic analysis (displacement control) of transverse impact on panels

Integrated analysis of an ice mass collision with the steel panel A (Table 15) was performed in accordance with the procedure described in Liu (2011) for the case when a 0.45 m-radius ice semi-sphere strikes a stiffened steel panel with a velocity of 2 m/s. The dynamics of ice-panel collision was split into external and internal mechanics. From external mechanics the kinetic energy that should be dissipated as strain energy was calculated ($G_s \approx 1.0$ kJ), which is the difference between kinetic energy before and after the collision. The following assumptions have been made: (1) a central, perfectly plastic impact; (2) a spherical ice mass (R_i=0.45 m, ρ_i =900 kg/m^3); (3) initial velocity of 2 m/s; (4) added mass is constant and equal to $0.5m_i$ for the ice and $1.0M_s$ for the floating structure; and (5) total mass of the floating structure 7.0 t.

From internal mechanics, using nonlinear numerical simulations, energy dissipation by the ice and by the steel panel was found. In numerical simulations, instead of initial velocity, displacements were applied to the ice mass as shown in Figure 67a.
Calculations were performed in LS-DYNA ls971s, revision 7600.129. The ice mass was modeled using material model and input parameters proposed by Liu et al. (2011). For the steel panel, a power-law plasticity model developed by Alsos et al. (2009) was used with RTCL damage criterion. Input material parameters to both models are given in Table 16. The edges of the panel and the stiffeners were fixed in the same manner as

described in Pt. 1 above. Modeling of contact was done as shown in Liu et al. (2011) (same contact definitions and contact parameters were used). The results of the calculations are presented in Figure 68.

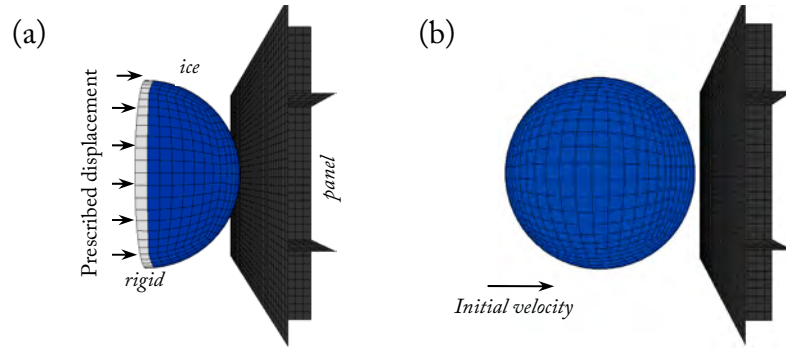

Figure 67: Numerical models: (a) displacement controlled simulations and (b) velocity controlled simulation.

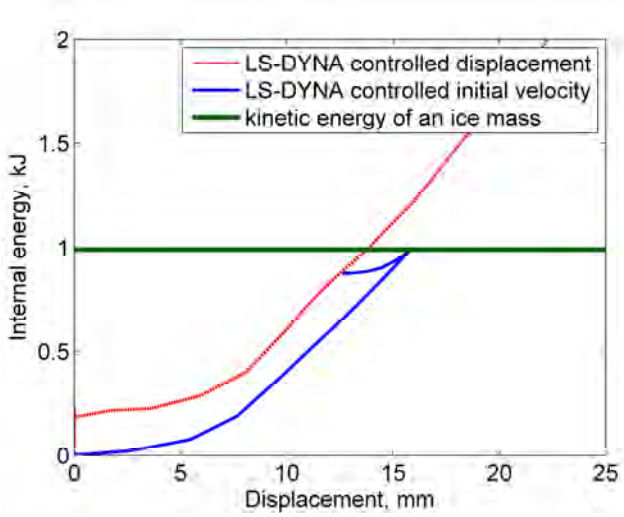

Figure 68: Energy dissipated during integrated behavior of ice and the steel panel A. A horizontal line corresponds to energy $G_s \approx 1.0$ kJ.

3. Integrated nonlinear dynamic analysis (velocity control) of transverse impact on panels

Numerical simulations of a spherical ice-mass collision with the stiffened panel A was performed for the case when a 0.45 m-radius ice sphere strikes a steel stiffened panel 1.1×1.1 m with an initial velocity of 2 m/s. Effect of water was accounted only through added mass.

Calculations were run in LS-DYNA ls971s, revision 7600.129. The numerical model is shown in Figure 67b. The material parameters and the boundary conditions were the same as in Pt. 2 above. Ice density was set to 1350 kg/m^3 to account for added mass. The added mass varies with time during a collision. For simplicity, the added mass

coefficient was assumed constant and equal to 0.5 for the ice mass and 1.0 for the floating structure. It should be noted, that in all three methods described above, the effect of welds was not included. Energy dissipation due to hydrodynamic effects was disregarded. Results are presented in Figure 68.

Table 16: Material parameters for integrated analysis (s_{el} – characteristic element size; ρ_s , ρ_i – density; E_s , E_i – elasticity modulus; ν_s , ν_i – Poisson ratio; σ_y – yield stress, a_0 , a_1 , a_2 – constants; K – strength index, n – strain index; ε_{plat} – yield plateau strain; p_c – pressure cutoff, compression is positive; ε_0 – initial failure strain).

Mild steel S235, s_{el}=30 mm[a]		Ice, s_{el}=45–60 mm[b]	
ρ_s	7890 kg/m^3	ρ_i	900 kg/m^3
E_s	210 GPa	E_i	9.5 GPa
ν_s	0.3	ν_i	0.3
σ_y	235 MPa	a_0	22.9 MPa[2]
K	700 MPa	a_1	2.06 MPa
n	0.24	a_2	–0.023
ε_{plat}	0.005	p_c	–2.0 MPa
Mesh exponent	0.71	ε_0	0.008

[a]Belytchko-Tsay shell elements with five integration points through the thickness;
[b]fully integrated solid eight-node elements

For the panel D, during the collision event the major part of the energy will be dissipated by the ice with no or very little plastic deformations of the steel plate. Conversely, plates A, B and C will deform plastically (maximum deflection 15–25 mm). A comparison of methods 1, 2 and 3 described above showed that for the panel A, simplified nonlinear static analysis (Pt. 1) predicts slightly higher displacements than integrated nonlinear dynamic analyses (Pt. 2 and Pt. 3).

Pilot drop tests were conducted at NTNU (see Section 3.3, Test nos. 1–3 in Table 11) to verify the ice manufacturing process and the ice-structure interaction scenario.

Ice specimen preparation

It was important to produce an ice mass that resembled natural ice formations i.e., multiyear ice floes and glacial ice-masses. The ice mass needed to be sufficiently strong (and large) to cause permanent deformations in the impacted structure. The objective of the ice specimen preparation was to reproduce as closely as possible the ice-crushing failure in a full-scale test for freshwater or iceberg ice.

The mechanical behavior of granular ice is known to be similar to that of glacier ice (Montgnat et al., 2009). A mixture of freshwater and commercially crushed ice was used.

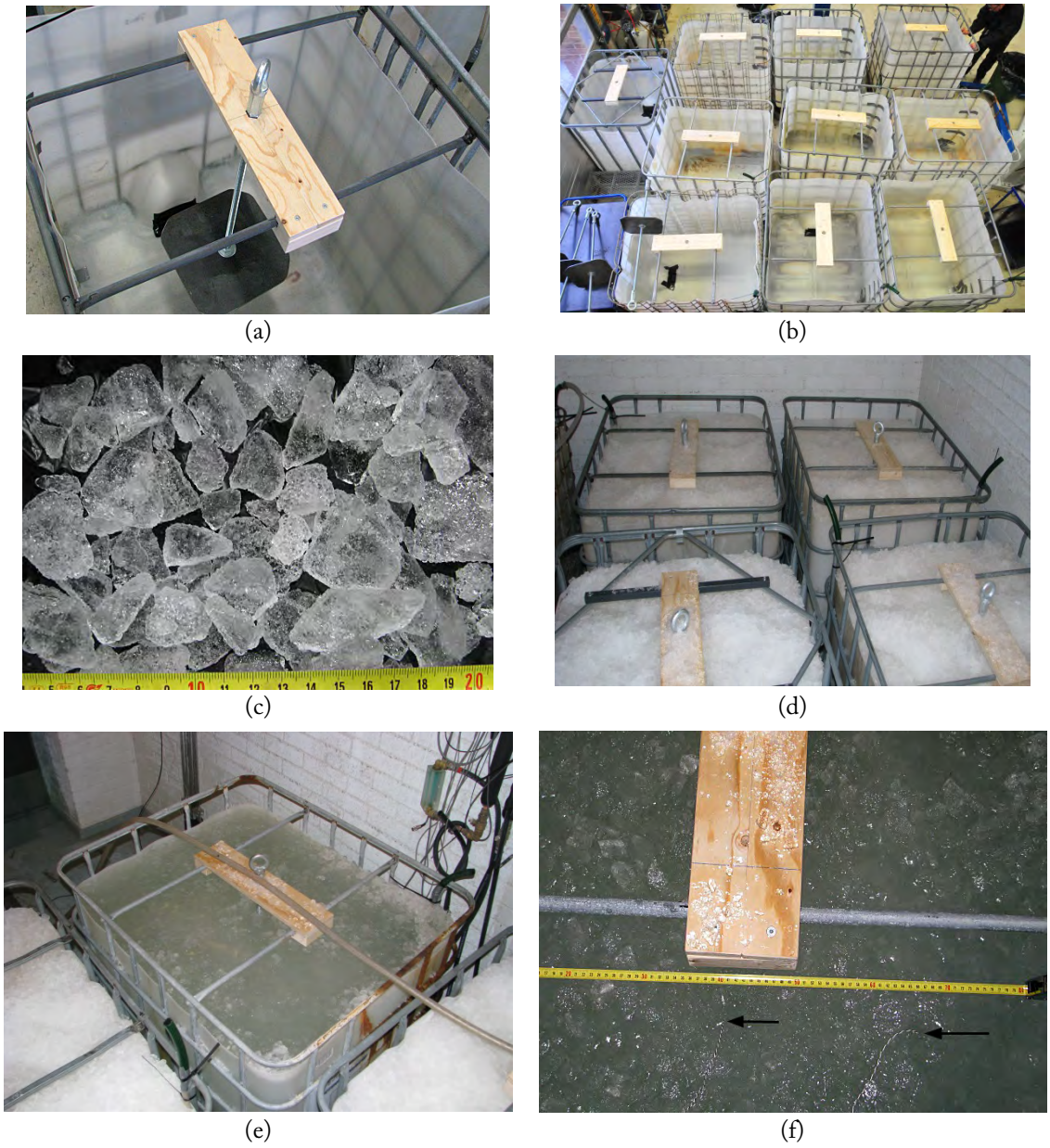

Figure 69: Photographs of the ice manufacturing process: (a) a mold, showing a threaded 1-m-long bar with an attached eye nut and a metal plate (the eye nut is an attachment point for the steering rope; the plate is an ice anchor during the lifting/towing of the ice block); (b) ten empty molds during the ice preparation phase; (c) crushed ice pieces used to fill the molds. On the ruler, longer lines with numbers are in centimeters and shorter lines are in millimeters; (d) molds filled with crushed ice (ice block at fabrication stage); (e) molds filled with a mixture of crushed ice and water; and (f) close-up top view of a mold (the black arrows indicate the location of temperature sensors).

The ice blocks were manufactured in molds with in-plane dimensions of 1.0 m × 1.2 m and a height of 0.9 m (see Figure 69a and Figure 69b). The partially flexible plastic walls of the molds allowed some expansion of the ice during the freezing-process. To facilitate specimen handling, a threaded metal rod (Figure 69a) was frozen into the ice,

as shown in Figure 69d. The threaded rod, with eye nuts attached to both ends, provided connection points for the system of ropes that was used during the ice towing and lifting. A total of 10 molds were filled and packed with commercial crushed ice (see Figure 69d). The crushed ice was ordered from a third-party company and had a piece size of approximately 10–40 mm (see Figure 69c). Subsequently, water was added to the crushed and packed ice from the bottom to avoid air entrapment (Figure 69e). The molds, filled with the mixture of water and crushed ice, were stored at −20°C to freeze completely. The freezing process was controlled by installing two temperature sensors in the ice at depths of approximately 0.4 m and 0.1 m (Figure 69f). The size of the ice block made it difficult to maintain control of the freezing direction within the available time frame. The freezing process was accelerated, and the internal stresses in the ice (which resulted from freezing the large blocks of ice) were decreased by drilling several holes, approximately 0.3 m deep, in the ice near the threaded bar. These holes enabled unfrozen water to flow to the surface of the block, releasing some of the internal pressure.

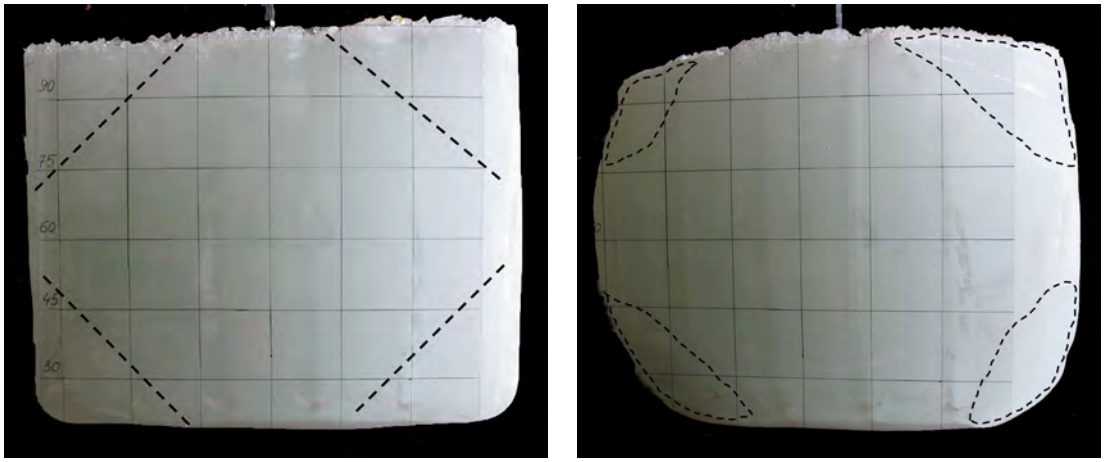

(a) Side view of the ice block before shaping; the dashed lines indicate where the ice sample was cut into the final shape.

(b) Final shape of the ice block; the dashed contours indicate the edges after shaping.

Figure 70: Photographs of the ice block: the grid lines are 0.15 m apart; the final shape of the ice shown in (b) was formed by cutting out four approximately equal-sized tetrahedrons from the corners of the prismatic ice block.

The ice block was considered to be frozen once the temperature at both sensors attained the ambient temperature of −20°C. It took approximately 5 days to completely freeze the samples. One to two days before testing, cracks that had formed during the freezing process were sealed with fresh water. The resulting ice was predominantly granular.

The ice block was examined for signs of open cracks and unfrozen water pockets before being placed in the basin. “Healthy” ice blocks were cut into the final test shape

(Figure 70) using a chain saw. Figure 70b is a photograph of a typical ice specimen used in the impact tests. The dashed lines in Figure 70a and Figure 70b indicate the locations of the target cuts and the actual cuts, respectively.

To estimate the ice compressive strength, uniaxial tests were performed on the resulting ice using a compression rig, as illustrated in Figure 71.

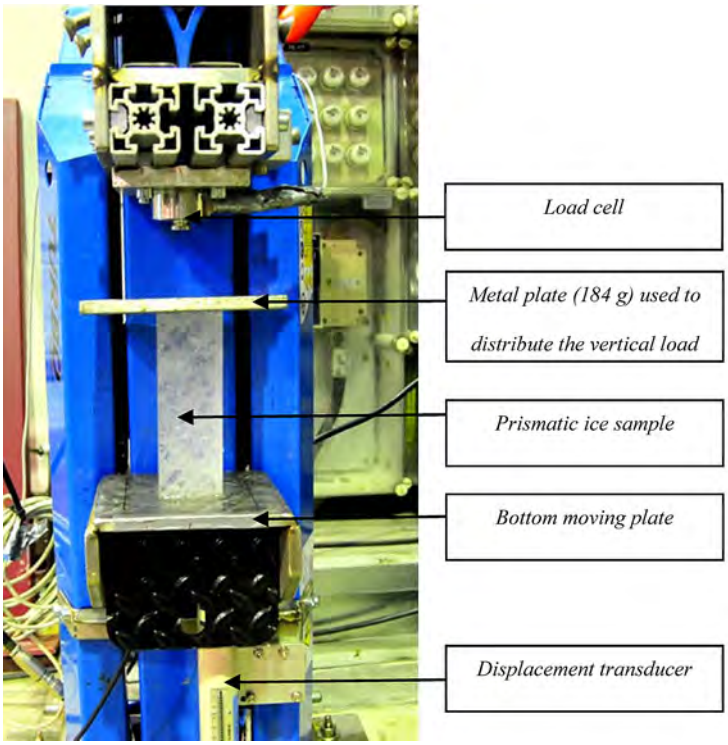

Figure 71: Compression machine.

The lower steel plate moved upwards with a near constant velocity, while the force was recorded by a load cell. The vertical displacement of the bottom plate was measured using a displacement transducer. Samples were cut from each tested ice block and machined to prismatic specimens of the desired size (approximately 5 cm × 5 cm × 15 cm). Each ice sample was weighed and measured before compression to estimate the ice density. After the peak load was reached, the test was terminated. The ice samples exhibited a density of 901±11 kg/m^3 (implying an average porosity of approximately 2%) and an unconfined compressive strength of 0.80±0.10 MPa in brittle-like failure mode. The ice was tested at a temperature of 0°C and at a loading speed of approximately 17 mm/s. The reported strength values were obtained by dividing the maximum load at failure by the sample cross-section area. The brittle-like failure mode was characterized by a sharp decrease of the load after ice failure. For comparison, the crushing strength of polycrystalline ice at 0°C in the brittle range is 0.94 MPa for a grain size of 10 mm and is 2.1 MPa for a grain size of 2 mm (Michel, 1978). Here, the compressive strength is

used to demonstrate the similarities and differences between our artificially grown ice and other published data. For example, the unconfined brittle compressive strength of freshwater granular ice of an approximately 1 mm grain size at 0°C is approximately 2–3 MPa (Schulson and Duval, 2009). These values of ice strength were obtained for ice samples that were carefully prepared for the laboratory tests, i.e., the grain size and the air content of the ice samples were carefully controlled during ice manufacturing.

Instrumentation

The impact event was recorded using a high-speed FASTCAM-APX video camera and four GoPro HD Hero 2 video cameras, which were mounted as shown in Figure 61. A video camera was mounted on the upper right side of the floating structure to record an oblique angle view of the impact zone and to provide additional information about the eccentricity of the impact and the orientation of the ice block prior to impact. The high-speed video camera was mounted on the side of the ice basin and recorded images at 500 frames per second.

The impact force transferred through each of the four HEB beams (denoted I–IV in Figure 65a) was measured by three uniaxial strain gages, which were attached along the beam flange, across the beam flange and at an angle of 45° to the beam web neutral axis. Figure 72 is a schematic of the strain gage locations on the HEB beam.

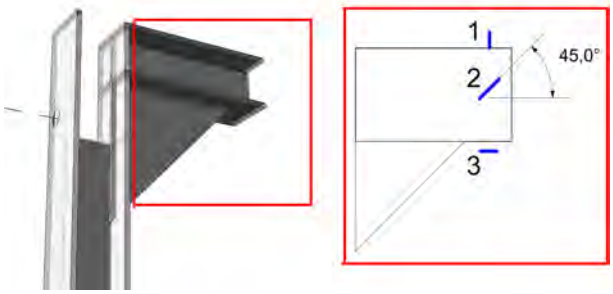

Figure 72: Schematic view of the portion of HEB beam II shown in Figure 65a; labels 1, 2, and 3 denote the locations of the strain gages.

A Crossbow dynamic motion unit recorded accelerations and the angular rates of the floater and the attached stiffened panel. The strains, accelerations and angular rates were recorded using a data acquisition system at a sampling frequency of 523 Hz, which was the highest sampling frequency possible with this equipment. This system ensured that the strain and acceleration measurements were synchronized. The towing force of the ice block was measured with a separate data acquisition system at a sampling frequency of 123 Hz using a load cell attached to the towing rope.

For Test nos. 10–18, a Tekscan 5513 tactile pressure sensor with a total sensing area of 157 mm by 416 mm at a sampling frequency of 100 Hz was used for a qualitative assessment of the pressure induced by the ice. Applicability considerations of tactile pressure sensors to dynamic pressure measurements are provided in Subsection "Pressure data". The sensor was placed on the impacted panel. The tab length of the sensor limited the depth to which the sensor could be placed without damaging the data logger. Thus, the pressure mat was only centered in the x-direction (see Figure 65b). The center of the sensing area was located approximately 0.2 m below the water line. Each sensor had a sensing area of approximately 28 mm^2. Paikowsky and Hajduk (1997) described the working concept of the pressure sensor. The sensing face of the pressure mat was covered with transparent watertight foil and fixed to the steel plate. Dacron fabric was attached with tape over the pressure sensor to protect the sensor during the impact experiments without adding extra stiffness.

Despite the wide use of pressure sensors for measuring ice pressures (e.g., Sodhi et al., 1998; Gagnon, 2004; Määttänen et al., 2011; Kujala and Arughadhoss, 2012 and Browne et al., 2013), only a few publications have described the calibration procedure and the uncertainties associated with the pressure measurements. The calibration procedure and some of the uncertainties associated with the use of tactile pressure-sensors are described below and are intended to alert other researchers of the possible uncertainties of tactile pressure sensor systems.

The tactile pressure-sensor was calibrated following the guidance provided by Tekscan (2010) as closely as possible. The calibration was limited to static loads because it was difficult to arrange a known calibration force with the same duration as an ice impact. The degree of contact is proportional to the applied load and was calibrated using I-Scan software bundled with the data logger. The calibration was conducted on the concrete floor of the ice tank at temperatures similar to that of the actual impact tests. Steel pieces of varying dimensions and shapes were pressed against the pressure panel using a 472-kg weight. A plywood sheet was placed between the concrete floor and the sensor to conform to the slight deformations in the concrete floor during loading. In addition, a 2-mm-thick silicon mat was placed between the point of pressure application and the sensor. This configuration provided a fairly uniform pressure during calibration. The entire sensing area could not be loaded during calibration because accurate pressure measurements up to approximate 20 MPa were required.

Each individual element of a grid-based pressure sensor has its own sensitivity (Tekscan, 2010). Therefore, partial loading of the sensor during calibration may introduce measurement errors. These errors can be minimized using a method recommended by Tekscan (2010), known as equilibration, whereby hydrostatic pressure is applied to the sensing area. This procedure was not conducted in this study. However,

the reliability of the calibration (or the uncertainty of the measurements) was ascertained by conducting two series of validation tests, which are described below:

(i) A known force was applied to a known area at various points over the sensing area; the saturation pressure of a single sensing cell was 18 MPa. Table 17 provides the validation results.
(ii) The peak force during the uniaxial compressive tests was measured using a small portion of the pressure sensor and compared with the force measured by a traditional load cell. The uniaxial tests were performed with ice extracted from a manufactured ice block. The ice specimens tested under uniaxial compression had different sizes and shapes (see Table 9). Figure 73 presents the results of the comparison.

Table 17. Pressure-sensor validation data.

		Actual			Measured			Relative error, %			
Test #	Position	Force, kg	Area, mm^2	Pressure, MPa	Force, kg	Area, mm^2	Pressure, MPa	Force	Area	Pressure	Pressure*
1	right[a]	472	3822	1.2	475	2219	2.1	1	42	73	43
2	right[a]	472	6072	0.8	572	3926	1.4	21	35	87	56
3	right	472	1131	4.1	527	1394	3.7	12	23	9	35
4	left	472	1131	4.1	359	1081	3.3	24	4	20	28
5	right	472	1131	4.1	453	996	4.5	4	12	9	16
6	left	472	1131	4.1	391	967	4.0	17	15	3	32
7	left	472	1131	4.1	428	996	4.2	9	12	3	21
8	left	472	1131	4.1	335	882	3.7	29	22	9	51
9	left	472	1131	4.1	422	1167	3.5	11	3	13	14
10	left	472	1131	4.1	363	1053	3.4	23	7	18	30
							Average error, %	15	18	25	33

* error calculated using the provisional rule for error propagation (see Taylor (1997))

[a]denotes validation tests in which the loaded area was different from that used in the pressure sensor calibration

From Figure 73, it can be observed that the average relative error between the measurements of the load cell and the pressure sensor for the ice-steel interface was 23%. This error was larger than that for the validation procedure (i). This result can be explained by the slightly lower sensitivity that was selected for the pressure sensor during the calibration than that required for an ice-steel contact. Under the given calibration conditions, a lower sensitivity value was selected to obtain a relatively high saturation pressure (approximately 18 MPa in this study) for a single sensil. The objective of the calibration was to tune the sensing area to the rather high localized

pressures that occur during ice crushing. Such calibration settings can cause errors in measurements of the contact area, the total force and, consequently, the average pressures. Table 17 shows the possible uncertainties in the values. Figure 73 demonstrates that the actual measurement error during ice loading could be larger than the estimates in Table 17 because the characteristics of the ice interface at the contact zone may differ from those of the interface used during the calibration.

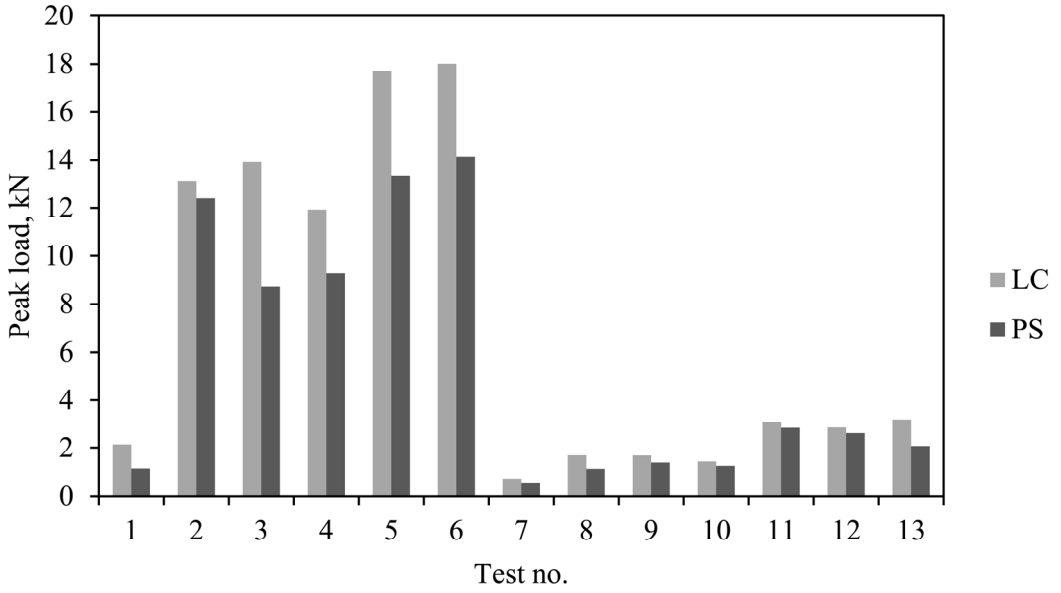

Figure 73: Plot comparing the peak load measured by a pressure sensor and a load cell during uniaxial compressive tests on prismatic ice samples; (LC denotes the peak load measured by the load cell and PS denotes the peak load measured by the pressure sensor).

In addition to the towing tests described, two drop tests in air were conducted (i.e., Test nos. 4 and 5 in Table 11). A detailed description of the drop tests can be found in Section 3.3. These tests characterized the ice-stiffened panel interaction in the absence of hydrodynamic effects. In Drop Test no. 4 (see Table 11), the kinetic energy and the global shape of the ice block before impact were similar to those for the impact tests in water at 2 m/s. The kinetic energy was approximately 3.5 kJ in Drop Test no. 4 and approximately 2.6–3.6 kJ for impact Test nos. 8 and 9 (for tests in water, there is an uncertainty contribution that originates from the uncertainty of the hydrodynamic coefficients of the ice mass).

3.4.2 Data analysis and discussion

A total of 18 impact tests were conducted in water. Of these, 16 impacts were conducted using the 12-mm-thick panel (panel D in Table 15) to determine whether reproducible results could be obtained with the experimental configuration.

Table 18 presents the parameters for each test and the corresponding ice properties. Table 18 lists the test identification numbers along with the type of the impacted panel, the initial ice velocity, the mass of the striking ice, the compressive strength of the ice under uniaxial loading and the density. This table also indicates whether either of the weak links was broken in the impact and whether the evolution of the contact pressures was measured during the test. The tabulated values of the initial ice velocity correspond to the speed of the *Y*–towing carriage immediately before the impact.

The significant data measured in the impact tests are listed in Table 19. The table includes the maximum plate deflections that were measured after the test, the impact load, the impact duration and the maximum acceleration of the target in the direction of the impact.

During the test period, the water temperature was maintained at approximately 0°C; however, the difference in the size of ice block "C" tested on 29.03.2012 and 04.04.2012 was visible to the naked eye. The ice block was only weighed once after it was shaped and before it was placed into the water.

Table 18. List of parameters and corresponding ice properties.

Date 2012	Test no.	Panel	Velocity (m/s)	Ice mass (kg)	σ_C (MPa)	Ice density (kg/m^3)	Weak link	Pressure sensor
29/03	1	D	1	C = 920	-	-	No	None
29/03	2	D	2	C	-	-	Yes, 3 kN	None
30/03	3	D	1	C	0.77 ± 0.16 [i]	914 ± 15 [i]	Yes, 8 kN	None
30/03	4	D	1	C	0.77 ± 0.16	914 ± 15	No	None
30/03	5	D	2	C	0.77 ± 0.16	914 ± 15	No	None
30/03	6	D	2	C	0.77 ± 0.16	914 ± 15	No	None
30/03	7	D	2	C	0.77 ± 0.16	914 ± 15	No	None
02/04	8	B	2	E = 897	0.71 ± 0.18 [j]	894 ± 7 [j]	Yes, 16 kN	None
03/04	9	A	2	F = 850	-	-	Yes, 5 kN	None
04/04	10	D	2	F	0.91 ± 0.29 [k]	896 ± 9 [k]	Yes, 16 kN	map 5513
04/04	11	D	2	F	0.91 ± 0.29	896 ± 9	Yes, 5 kN	map 5513
04/04	12	D	2	F	0.91 ± 0.29	896 ± 9	Yes, 5 kN	map 5513
04/04	13	D	2	G = 636	-	-	Yes, 8 kN	map 5513
04/04	14	D	2	G	-	-	No	map 5513
04/04	15	D	1	G	-	-	No	map 5513
04/04	16	D	2	C	-	-	No	map 5513
04/04	17	D	2	C	-	-	No	map 5513
04/04	18	D	2	C	-	-	No	map 5513

[i, j, k] number of tested ice samples (i=5, j=6, k=7)

Table 19. Summary of partial test results.

Test no.	Maximum panel deflection (mm)	Loads via I beams [a], % I	II	III	IV	Peak load [b*] (kN)	Impact duration [a*] (ms)	Impact duration [b] (ms)	Velocity before impact [c(d)] (m/s)	Common velocity after impact [d(e)] (m/s)	Maximum sway acceleration (floater) (m/s^2)
1	-	-	-	-	-	-	-	-	-	-	-
2	-	-	-	-	-	-	-	-	-	-	-
3	-	-	-	-	-	-	-	-	0.9 (-)	0.3 (-)	-
4	-	37	45	8	10	146	29	33	0.9 (0.0)	0.2 (0.1)	13.8
5	-	-2	-2	49	55	172	27	25	1.9 (0.0)	0.4 (0.3)	16.3
6	-	-	-	-	-	-	-	-	1.5 (-)	-	-
7	-	-1	-4	45	60	171	31	29	2.0 (0.0)	0.5 (0.2)	16.2
8	≈5	18	17	33	31	190	36	31	1.5 (0.0)	0.4 (0.3)	18.5
9	≈3	31	28	19	22	226	35	36	1.5 (0.1)	0.3 (0.4)	21.9
10	-	31	51	6	12	203	25	34	1.5 (0.0)	0.1 (0.2)	19.2
11	-	15	28	23	33	222	27	21	1.8 (0.1)	0.2 (0.2)	21.0
12	-	1	13	45	41	238	20	8	1.8 (0.0)	0.2 (0.1)	22.6
13	-	32	40	12	16	104	34	38	1.7 (0.0)	0.1 (0.1)	9.9
14	-	12	24	28	35	85	26	17	1.5 (0.1)	0.3 (0.2)	7.7
15	-	45	42	3	10	35	38	40	0.7 (0.0)	0.1 (0.1)	3.3
16	-	67	76	-27	-17	-	14	10	1.7 (0.0)	- (0.1)	20.3
17	-	18	19	28	35	-	27	29	- (0.0)	- (0.1)	3.8
18	-	27	21	24	29	-	26	21	1.7 (0.0)	0.1 (0.1)	4.7

[a] Unfiltered data from strain gages at 45°, expressed in terms of % distribution of the force in each beam for each impact run.

[a*] Impact duration, as estimated from strain gages at 45°.

[b*] Unfiltered data from DMU, $F = (M_s + 0.4M_s)a_s$, a_s is the peak sway acceleration of the floater.

[b] Measured from acceleration data integrated over time.

[c] Ice-block velocity from high speed video records.

[d] Velocity of the floater, as estimated from high speed video recording.

[e] Velocity after impact, as estimated from the acceleration data.

For each ice blocks, the number of tested samples in uniaxial compression varied between 5 and 7 (see Table 18). The measured compressive strength values (σ_c) were slightly lower than those of freshwater ice (2–10 mm grain size) tested under similar conditions (i.e., Michel, 1978). Our ice was quite porous. As evidenced from the measured densities (Table 18) and from the observations of thin sections of virgin ice (see Figure 74), the ice porosity was high (approximately 2%), unlike the porosity of the laboratory-grown ice (<0.2%) made from presieved seeds and distilled, deionized and degassed water under controlled freezing process, e.g., see Wiess and Schulson (1995). These differences in porosities and strengths are not surprising because our ice was produced without careful control of freezing direction, air content and grain size.

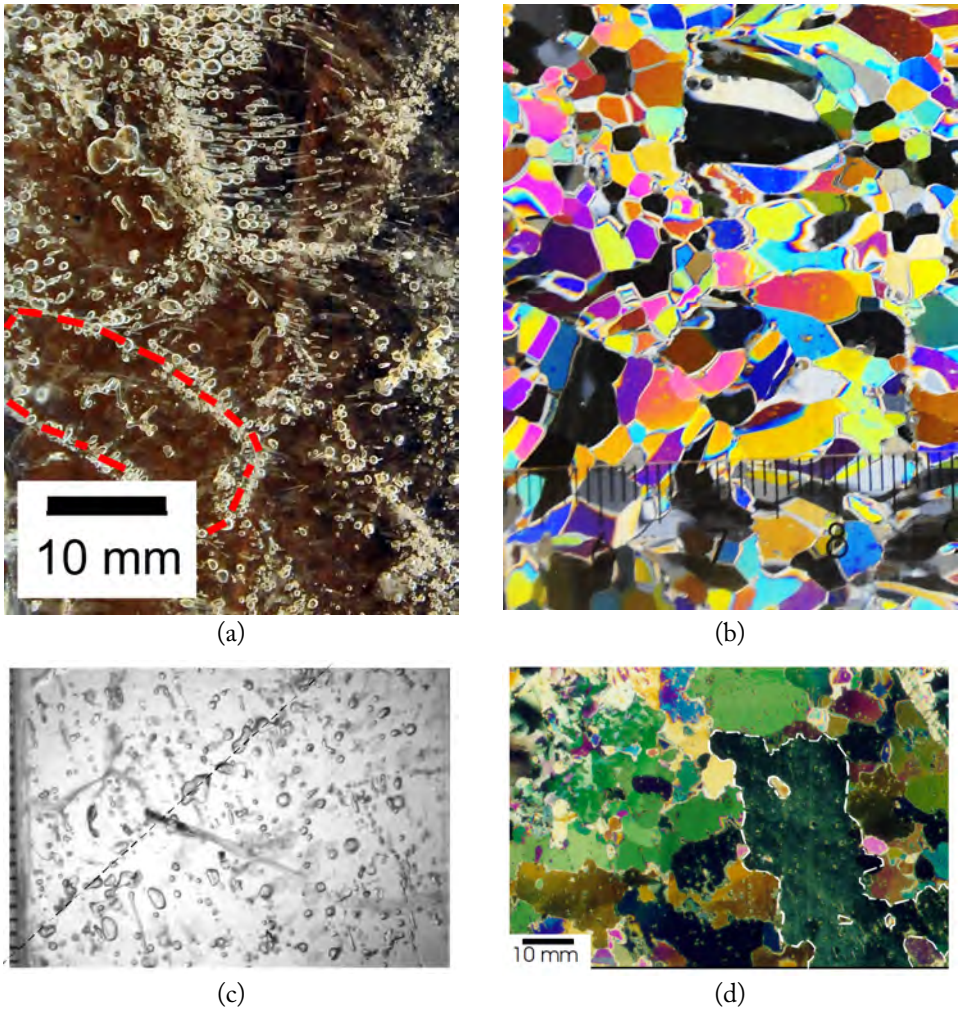

Figure 74: Photographs of manufactured ice and iceberg ice: (a) an example of air entrapped in manufactured ice; the dashed contour line indicates ice-piece boundaries with entrapped air; (b) heterogeneity in the grain size of manufactured ice (section of ice photographed between cross polaroids from the manufactured ice sample); the scale at the bottom is in millimeters. (c) an example of air entrapment in iceberg ice from Barrette and Jordaan (2001); the scale to the right is in millimeters. (d) heterogeneity in the grain size of iceberg ice from Barrette and Jordaan (2001).

Figure 75 shows a sequence of images taken during Test no. 9 (the test with the highest impact load). Towing the ice block toward the target generated a progressive disturbance (a bow wave) that caused a water pile-up in front of the target before the actual impact. This result could be observed in a sequence of images extracted from the high-speed-video recordings for Test no. 9 (see Figure 76).

Figure 76 illustrates the ice-structure interaction for a typical test. The target exhibited a lateral, negligible vertical, response to the bow wave. A very slow drift of the floater in the direction of the impact was registered before the impact. This drift may have been caused by the water pile-up. Strain measurements revealed that the target

ahead of the moving ice experienced negligibly small forces until contact was imminent. In addition, as the ice block approached the target, the increase in the vertical towing angle (i.e., the angle between the towing line and the towing course) resulted in rotations of the ice block prior to the actual impact (see frames 336 and 388 in Figure 76). At impact, the ice block was stopped by the target (see frame 484 in Figure 76), breaking the weak-link in some cases. The weak-link did not break in some of the other tests because of the slack in the towing arrangement. After the impact, the ice block experienced a slight rotation, and both the ice and the floater moved in the direction of the impact (see frames 668 and 912 in Figure 76). In all of the cases using the 12-mm panel, the structure was sufficiently strong to crush the ice with relatively little or no permanent deformation of the impacted plate.

Figure 75: Sequence of images taken for Test no. 9.

Figure 76: Sequence of images extracted from a high-speed video recording for Test no. 9 at a frame rate of 500 fps.

The velocity of the ice block before the collision and the common velocity of the ice block and the floater after the collision were estimated using images extracted from the high-speed video recordings. These results are presented in Table 19. This table demonstrates that the ice block approached the target with a slightly lower velocity than

the towing speed (see the column entitled "Velocity before impact" in Table 19). The lower velocity may have resulted from the slack in the towing arrangement and the variation in the towing angle.

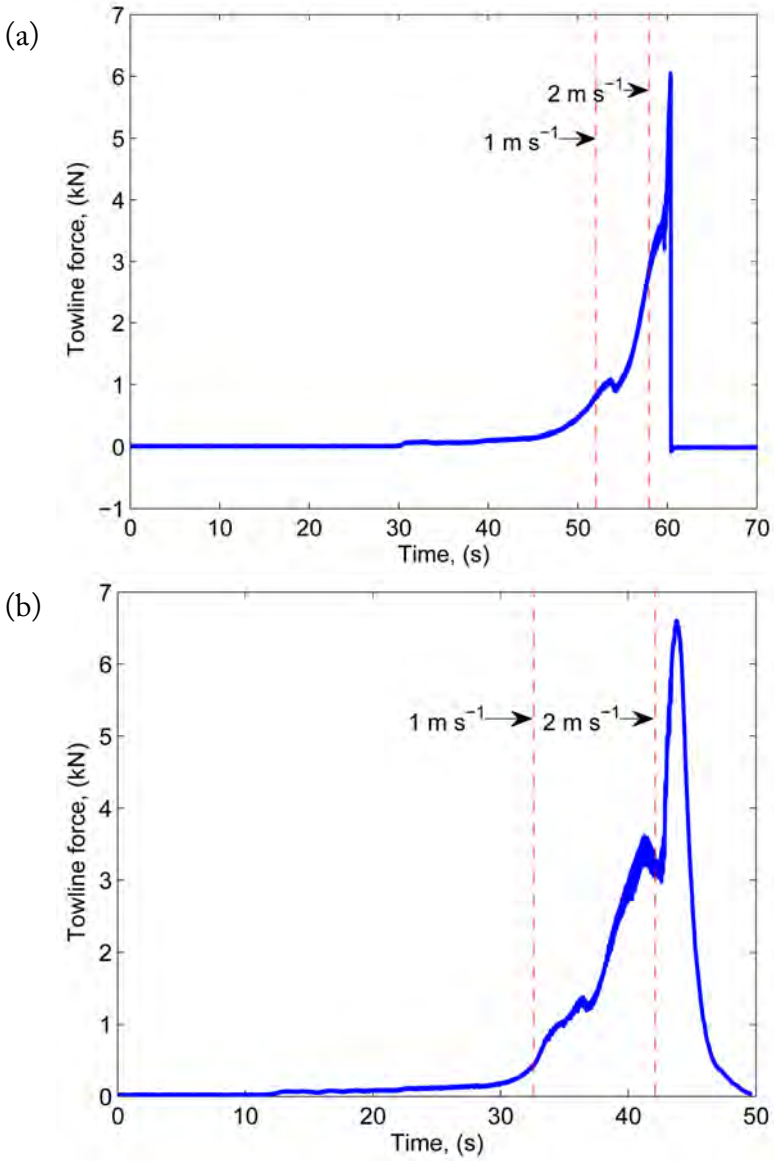

Figure 77: Towing force versus time for Test nos. 7 and 9, where the dashed vertical lines correspond to times when the speed of the towing carriage reached 1 m/s and 2 m/s, respectively; (a) Test no. 9: the weak-link with a capacity of 5 kN broke after the impact; (b) Test no. 7: the polyester rope absorbed the impact strains in the towing system, and the weak-link did not break after the collision.

The towing force history for impacts nos. 9 and 7 is plotted in Figure 77a and Figure 77b, respectively. Figure 77a presents a case in which the weak-link (with a capacity of 5 kN) broke after the impact, and Figure 77b presents a case in which the towline strains caused by the impact were taken up by the flexible polyester towing rope.

The weak-link breakage was characterized by a peak and a subsequently sharp drop in the load. For the case in which the weak-link did not break, the towing force gradually decreased after the peak. This descending branch of the towing force corresponded to the deceleration of the towing carriage after the impact. In Figure 77a, the difference between the peak force (approximately 6 kN) and the capacity of the weak link (5 kN) was within the 10% tolerance margin of the weak link and the accuracy of the load cell measurement. The towing force data are summarized in Figure 78 in the form of a plot of the towing force versus the towing speed for different ice blocks.

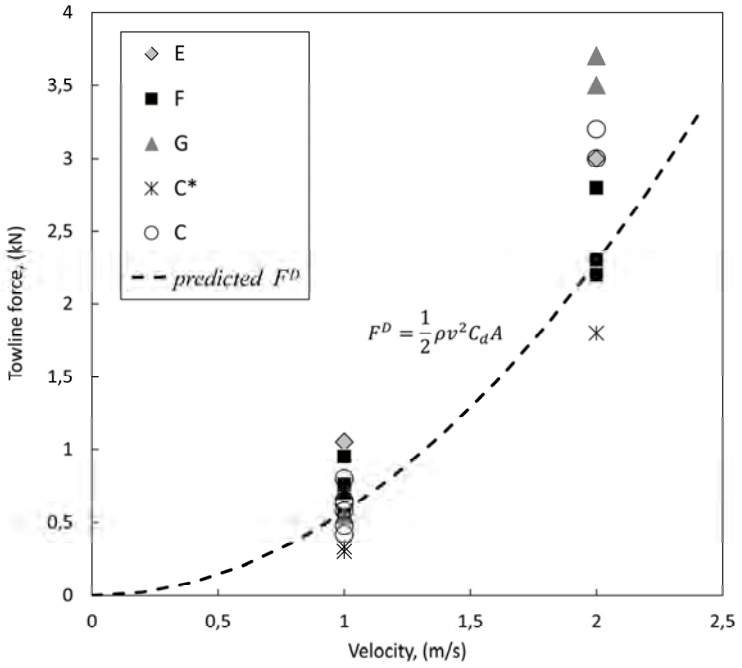

Figure 78: Towing force versus towing speed; the ice block C melted during several days of testing, i.e., label C* corresponds to tests on 04.04.2012; (the value of the towing force F^D was predicted using the well-known drag equation, where v denotes the towing speed, ρ=999 kg/m^3 is the density of water and C_d denotes the drag coefficient; C_d =0.8 was assumed, corresponding to an angled cube with a reference area A=1.3×1.1 m^2).

The impact duration could not be evaluated from the towing force measurements because of the low sampling frequency and the elasticity of the towing rope. In order to determine the impact duration, the data from strain gages and the dynamic motion unit (DMU) were used. A partial summary of the test results is given in Table 19.

Low-frequency drift and high-frequency noise were present in some of the registered signals from the strain gages. Post-processing a signal that contains drift and noise always produces additional uncertainties associated with the numerical method selected to compensate for the noise and the drift. The peak force that was estimated from the

strain gages depended on the signal post-processing technique. Thus, only the distribution of the maximum total load via the beams I–IV (expressed as a percentage) is reported in Table 19 (in the column "Load fraction via beams"). The percent values were least affected by the signal post-processing and indicate the eccentricity of an impact event.

Figure 79 presents the impact force histories for Test no. 8. The force from beams I–IV was calculated using unfiltered measurements from the 45° strain gages and represented the panel response to the impact. For simplicity, the following assumptions were used in the calculations: the impact load was only transferred through the beams; each HEB beam exhibited a linear elastic response with an elastic modulus of 210 GPa; and the stress was uniformly distributed over the cross-section of each HEB beam. Figure 79 shows a plot of the total load obtained by summing the load records for each beam. The peak force (estimated from strain gages) was affected by the signal processing method and, therefore, only values in percent are shown in Figure 79. Figure 79 shows the basic events in the load histories. These events included the impact and the damped dynamic response of the panel. These events are similar to those reported by Bruneau et al. (1994) and are common to all tests. The primary hit and the peak loads were emphasized. The damped dynamic response is not discussed here.

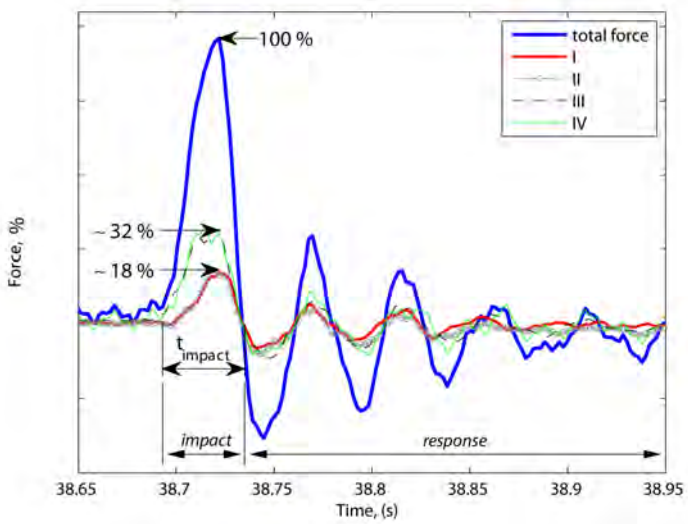

Figure 79: Impact force versus time for the collision interaction between the approximately 900-kg ice block and panel B (Test no. 8); the impact force was calculated using unfiltered measurements from the 45° strain gages; the labels I, II, III and IV correspond to different strain gage locations (see Figure 65a); note that the reported force was normal to the floater side surface.

The peak impact load for each run (F_p, see the column "Peak load" in Table 19) was also estimated from the measured sway acceleration of the floater as $F_p=(M_s+A_s)a_s$, where M_s is the total mass of the impacted structure, A_s is the hydrodynamic added mass of the structure in the sway direction ($A_s=0.4M_s$) and a_s is the maximum acceleration of the

floater in Table 19. Only the peak force for each run is reported. The column "Peak load" provides information about the reproducibility of a single run.

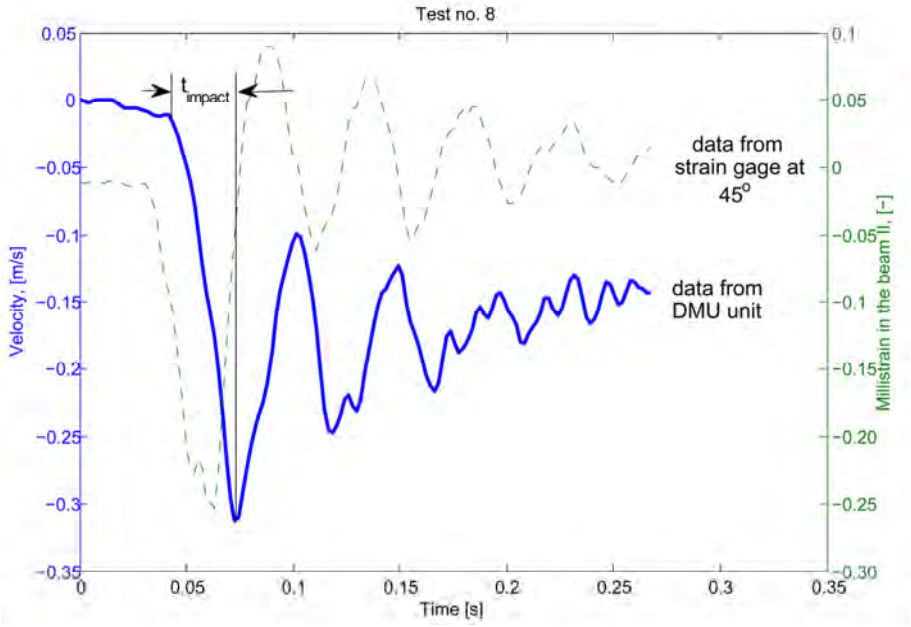

Figure 80: Velocity and strain time series; note that the velocity, estimated from the measured acceleration of the floater, was in the direction of the impact, and the strain time-series were measured by the strain gages (unfiltered signal) located at 45° on beam II.

The duration of the impact listed in Table 19 was defined using two different data sources: the strain gages and the DMU. Only the strain signals with a minimum noise were used in determining the impact duration. Figure 79 and Figure 80 illustrate how the impact duration (t_{impact}) was determined from the strain gage data and the DMU data, respectively. From Table 19, it can be deduced that the floater had no time to obtain a significant global response because of the short impact duration. Therefore, the major part of the impact energy was absorbed locally by panel denting and ice crushing. Some of the kinetic energy was transferred to global motions of the ice and the floater. According to the collision mechanics, the overall loss in kinetic energy at the collision must be absorbed by ice crushing and by deformations of the floater. For all tests (except Test nos. 8 and 9), the energy was dissipated by elastic vibrations and by ice crushing; however, for Test nos. 8 and 9, the energy was also dissipated by plastic deformation of the plate. Assuming an inelastic collision and considering that all acting motions between the structure and the ice occurred along the normal to the impact plane at the point of collision, the principles of collision mechanics can be adopted (i.e., the principle of conservation of momentum) to determine the common velocity of the ice/floater after the collision (v_c), see Equation (27). The hydrodynamic effects from the surrounding water in the vicinity of the collision are treated as added masses.

$$v_c = \frac{(m_i + A_i)v_i + (M_s + A_s)v_s}{m_i + A_i + M_s + A_s} \tag{27}$$

m_i is the ice mass (Table 18), M_s is the mass of the floater (including the panel), A_i and A_s are the hydrodynamic added masses of the ice (surge motion) and of the floater (sway motion), respectively and v_i and v_s are the velocities of the ice mass (Table 18) and the floater before the impact. The floater velocity before the impact was zero except for Test nos. 9, 11 and 14, where the floater had a velocity of 0.1 m/s (HSV records).

In general, the added mass of a floating body is associated with the mass of the fluid accelerated by the body oscillating in water. The added mass depends on the size and shape of the body, oscillating frequency and proximity of a neighboring body (including the size and shape of the neighboring body). Chwang (2003) analytically demonstrated that surge added mass may increase with decreasing distance between the colliding objects.

Due to the difference in size of the ice and floater, the added mass associated with the ice may be more affected by the presence of the floater than the other way around. In Equation (27), for simplicity, the added mass of the ice feature and floater is taken as a constant. For an ice block of an almost square shaped cross-section experiencing a unidirectional surge motion, its added mass can be approximated as A_i=0.5m_i (Bass and Sen, 1986). The added mass of the floater for sway motion was taken as A_s=0.4M_s. This approximation is reasonable when the duration of the impact is less than 50 ms (Petersen and Pedersen, 1981).

Figure 81 presents a comparison between the velocities predicted by Equation (27) and the values estimated from HSV records and DMU data.

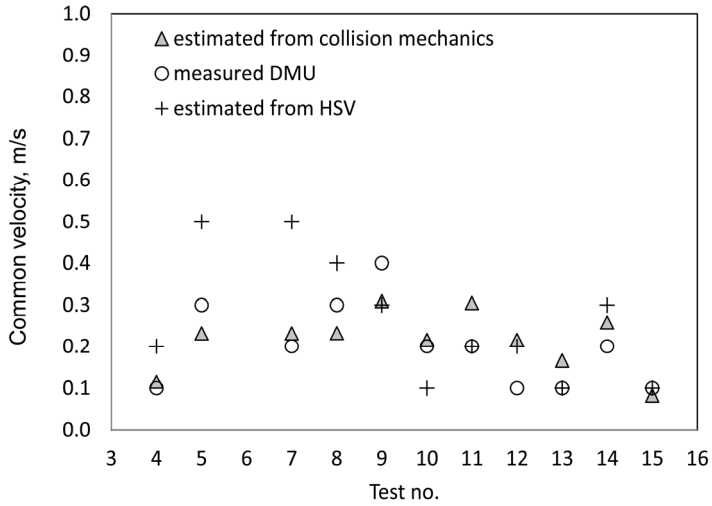

Figure 81: Common velocity of the ice block and the floater after the collision. A comparison between the velocity predicted by collision mechanics (Equation (27)) and measured values (DMU and HSV records).

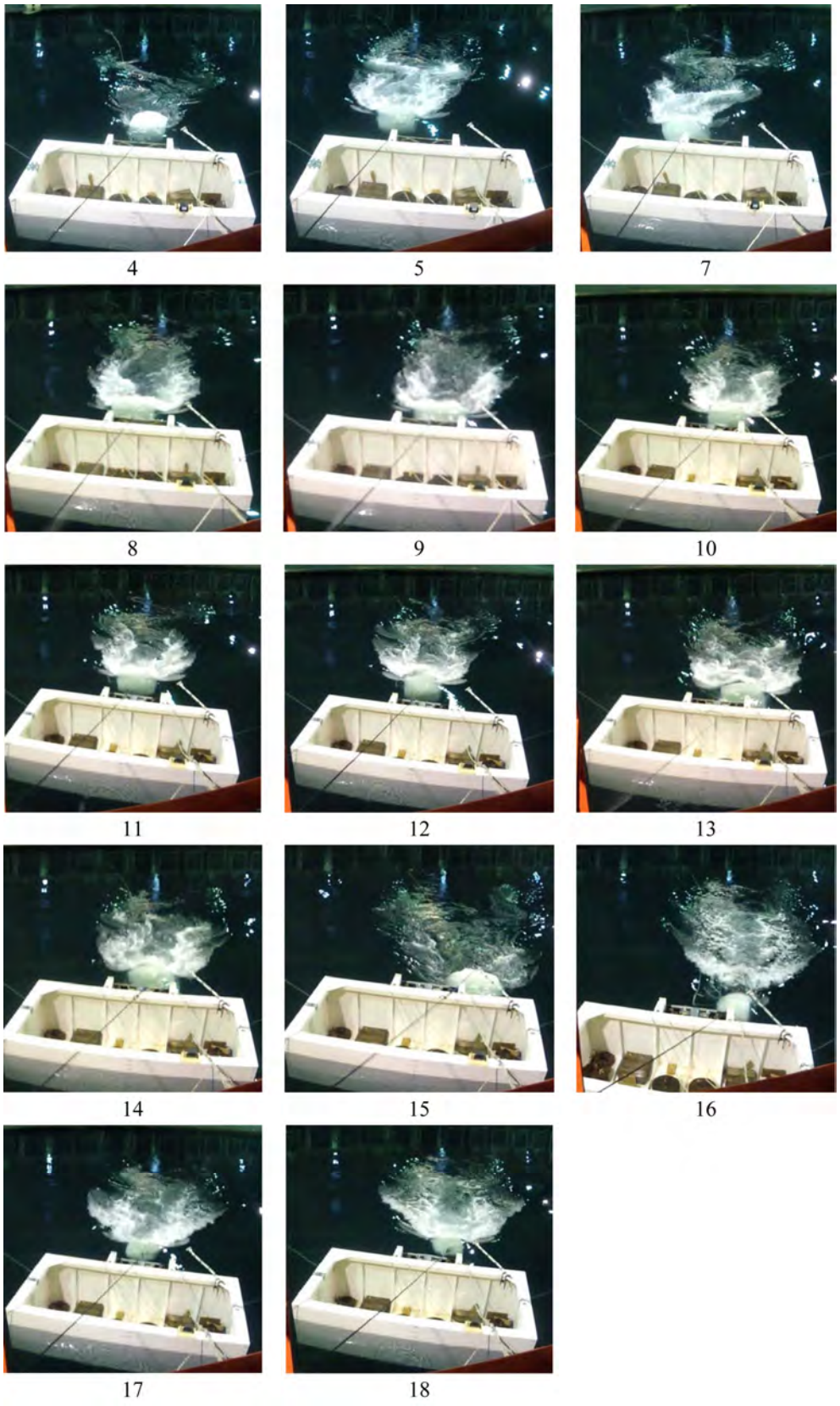

Figure 82: Impact events for all of the towing tests.

The common velocity calculations for Test nos. 16–18 are not presented due to the uncertain ice mass. In Test nos. 16–18, the ice significantly melted during several days of tests, resulting in an unknown mass. The scatter of data in Figure 81 reflects difficulties in ensuring similar impact conditions for each test and the uncertainty of the added mass. For example, oblique and eccentric impacts were the rule rather than the exception.

Impacts with a glancing character will also affect the estimation of the common velocity. Figure 82 presents video recording images immediately before the impact event for each test. These images provide visual information on the eccentricity of the impact for comparison with the load data in Table 19. From Figure 82, it can be seen that the eccentricity is most noticeable in Test nos. 5, 7 and 16. This observation can also be deduced from Table 19 (see "Load fraction via beams"), where the collision resulted in tension of the HEB webs. The high eccentricity is an explanation of the large scatter between HSV and DMU data in Test nos. 5 and 7 (Figure 81).

Figure 81 indicates that the velocity data from the DMU (and hence the acceleration) are more reliable than those obtained from HSV records. Overall, there is good agreement between the velocity predicted by collision mechanics and the velocity registered by the DMU.

Ice structure

Several samples were harvested from the manufactured ice to characterize the internal structure and the flaw structure of the ice. After repeated impacts on 30.03.2012 (see Table 18), a few ice samples were collected from ice block "C". These ice samples were stored at −10°C before their structure was examined. Thin sections of all of the samples were obtained using the technique described in the subsection entitled "Examination of microstructure" (see Section 3.1.1). It was difficult to obtain a true representation of the internal structure of an entire 1-m^3 ice feature. A thin section only represents a single plane in a specimen of a limited size. The samples collected from the virgin ice (the ice as manufactured) and from the ice that was tempered in the ice basin were only partial representations of the internal structure of all of the ice blocks described in this work. The following observations were based on photographs of the thin sections under various lighting conditions.

The internal structure of the ice specimens did not exhibit large variations in texture, except for the top most layer of the ice block. This top layer formed because of the actions performed during the freezing of the ice (see Section 3.4.1, the subsection entitled "Ice specimen preparation"). The ice in the top layer was very porous with predominantly columnar grains. The V-towing scheme used during the impact tests

(see Figure 63) prevented any interaction between the structure and this layer; therefore, the top layer will not be discussed further. The manufactured ice was relatively homogeneous in all of the thin sections, with grain sizes varying between 2 and 10 mm (see Figure 74b). The flaw structure included entrapped air, which occurred as bubbles with diameters of 1 mm or less (see Figure 74a) that were mainly concentrated along the boundaries of the ice piece used during the manufacturing process (see Figure 69c). Large fractures, which may have been induced by stress, were visible on some of the photographs of the ice blocks (e.g., black arrows indicate the location of pre-existing flaws in Figure 83b,) and could also be attributed to the flaw structure. Figure 74c and Figure 74d provide an example of the internal structure of iceberg ice for comparison.

Comparing the internal structure of the laboratory-manufactured ice to that of iceberg ice, as described by Gagnon and Gammon (1995b) and Barrette and Jordaan (2001), revealed that the laboratory-grown ice had a smaller grain size but similar porosity (2%). The fractional porosity (%) of iceberg ice varies between 0.7±0.20 and 3.5 ±0.38 (Gagnon and Gammon, 1995b). Iceberg ice grains are generally irregular in shape, while the grains of the artificial ice were more rounded. The laboratory-manufactured ice also had fewer interlocking grains. Unlike artificial ice, Gagnon and Gammon (1995b) noticed that for iceberg ice, there was no significant accumulation of air bubbles at grain boundaries. Note that in the thin sections from the manufactured ice blocks, a pattern of crisscrossing planar features (or healed cracks) was not observed. These planar features are one of the most distinguishing characteristics of iceberg ice (for more information, see Barrette and Jordaan (2001)). However, healed cracks were present in the ice blocks as the result of ice manufacturing (e.g., Figure 83b).

There was an inherent randomness in the manufactured ice blocks in terms of the heterogeneity of the grain orientations and sizes, the uneven distribution of the bubble density and the presence of fractures. Randomness of the fracture has been observed in full-scale data (Jordaan et al., 2012); however, the extent to which the inherent distribution of the flaws in the ice affects the ice loads during a full-scale collision scenario is unclear.

In summary, the observations indicate that the laboratory-manufactured ice exhibited a few similar characteristics as iceberg ice (i.e., the presence of air bubbles of different sizes, nonuniform grain size, healed cracks), and at the same time, the shape of the grains, the character of air bubble accumulation and the amount of grain-interlocking were different from those in iceberg ice.

Immediately following impact Test nos. 8 and 9, several photographs were taken under different lighting conditions, angles and magnifications. Figure 83 compares an idealized ice-solid body impact (Figure 83a) with observations of the ice damage zone immediately after the impact between the ice and flexible panel B (Figure 83b).

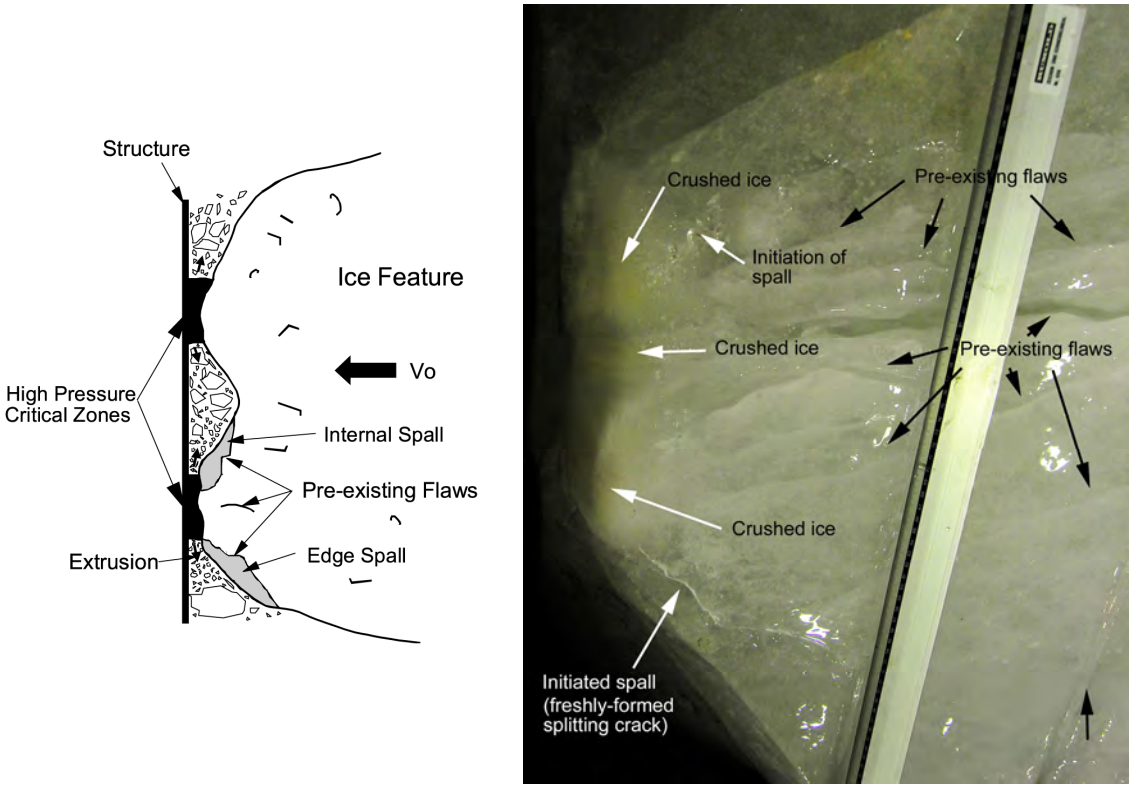

(a) (b)

Figure 83: Interaction area: (a) a schematic representation from Jordaan (2001) and (b) a close-up photograph taken just after impact for Test no. 8.

The black arrows show pre-existing flaws in the ice. These flaws may have resulted from the internal stresses that built-up while the ice was freezing in the mold. The flaws in laboratory-manufactured ice could be avoided by growing 1 × 1 × 1 m^3 ice samples using unidirectional freezing. This process could be performed by isolating the sides and the top of a mold, e.g., as done by Gudimelta et al. (2012). However, for unidirectional freezing, the freezing time can be expected to be more than 5 days. For comparison, in Gudimelta et al. (2012), 3 to 4 days were required to grow an ice sample (i.e., a cylinder with a diameter of 1 m and a height of 0.3 m and a cone with a height of 0.3 m on the top of the cylinder).

The white arrows in Figure 83b show the effect of the ice-panel interaction. In Figure 83, zones of crushed ice and freshly-formed splitting cracks (initiated spalls) are visible to the naked eye.

Figure 84 shows the ice damage zone for Test nos. 8 and 9 and the corresponding measured plate deflections. The black horizontal and vertical lines in Figure 84 (i.e., the photographs showing plate deflections) highlight the locations of the stiffeners and the frames. From the photographs, HPZs could not be conclusively identified in the damaged region. This ambiguity may be attributed to the glossy appearance of the ice surface in the presence of water, which reflects more light and makes it difficult to judge

the location or presence of HPZ in the damage zone. The ice blocks appeared to be resistant to impacts during testing. This result is similar to the growler impact tests described by Gagnon (2004), in which the growler could withstand many impacts without significant damage to bulk ice under prescribed impact conditions. In both Test nos. 8 and 9, the ice damage zone was highly localized, and it may be argued that the presence of healed cracks in ice samples did not significantly affect the response of the ice for these two tests.

Panel deformations

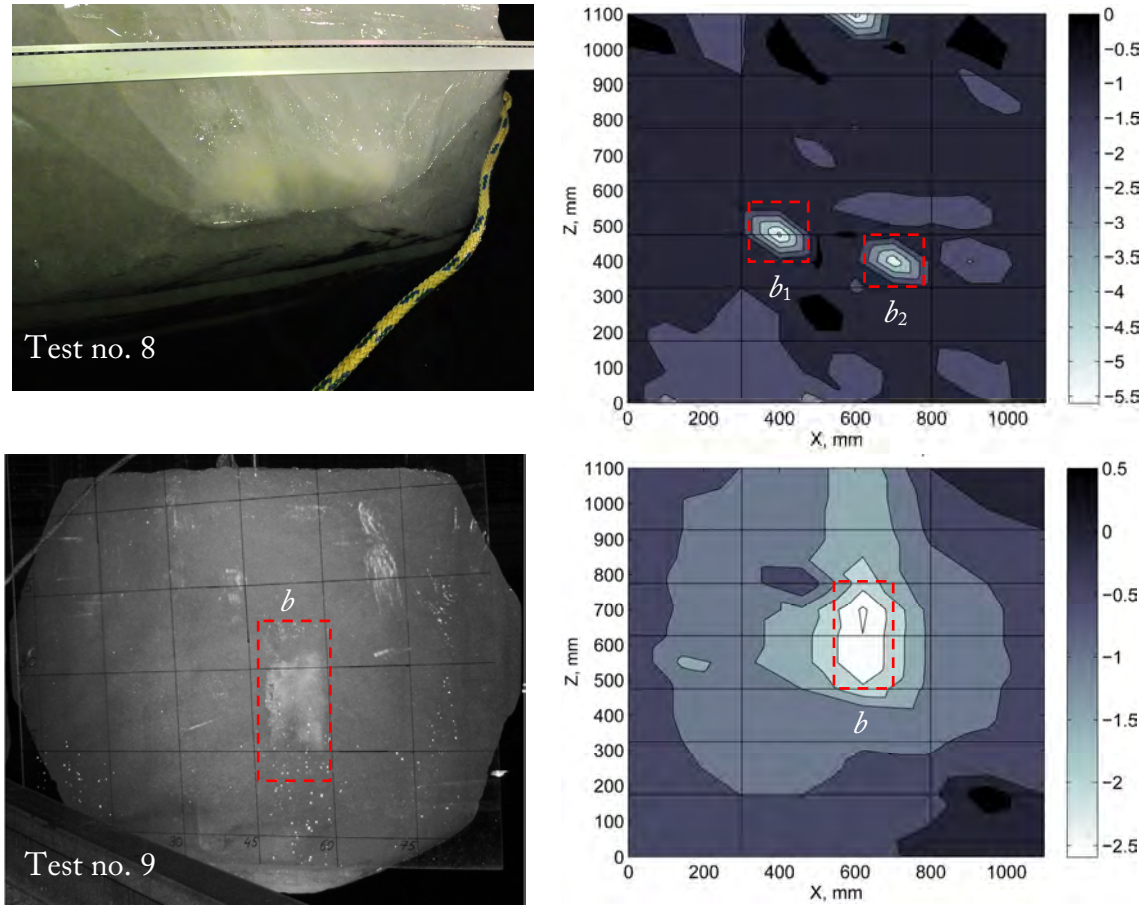

Figure 84: Photograph showing the ice damage zone in Test nos. 8 and 9 (for a grid size of 0.15 m) and the resulting deflections of the 2-mm plate in Test no. 8 and the 4-mm plate in Test no. 9; the deflections are given in mm; the total load path is shown by the dashed lines, b, b_1 and b_2 are the widths of the load patches.

Figure 84 shows the measured plate deflections after the impact tests in water. For the purpose of comparison, the measured plate deflections after the drop tests in air are provided in Figure 85a and Figure 85b. The black horizontal and vertical lines indicate

the locations of the stiffeners and the frames. From Figure 84, it can be observed that the plastic deformations in the panel occurred near the location of the ice impact.

Figure 56 (see Section 3.3) is a photograph of the plate damage resulting from the drop test from 3 m. For comparison, Figure 86 shows permanent dents on the plating of a chemical tanker caused by a collision with multi-year ice.

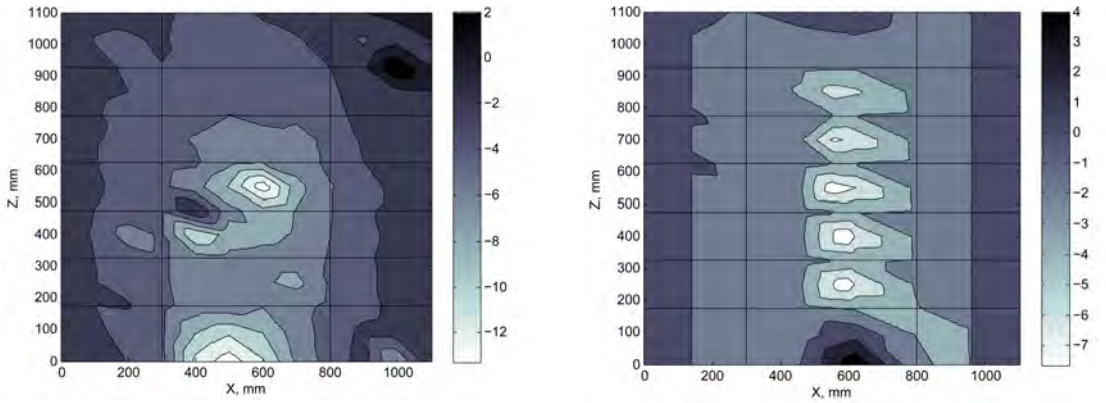

(a) Drop Test no. 4 in Table 11, panel B. (b) Drop Test no. 5 in Table 11, panel C.

Figure 85: Plate deflections after an ice impact in air, deflections are given in millimeters (mm).

Figure 86: Damage to steel structure caused by ice: permanent deflections of a ship plating caused by ice (from Hänninen (2005)).

Comparing damage to the panels in Figure 56 and Figure 86, it can be observed that Drop Test no. 5 reproduces similar deformation patterns as those observed in full-scale and typically called "hungry horse" deformations. During Drop Test no. 4, the local ice behavior was similar to that in water (i.e., the ice block did not split). The interaction caused local ice crushing and plastic deflections of the 2-mm plate (with a stiffener spacing of 150 mm) up to 13 mm (see Figure 85a). In comparison, data gathered by Hänninen (2005) for different types of ice-related incidents revealed that dents caused by ship-ice interaction in the Baltic Sea were between 10 and 100 mm deep.

Hänninen (2005) commented that traverse framing was used in the bow and aft areas of the ship (Figure 86). The ship had 30-mm dents in the bow, mid and aft areas. The frame spacing on the bow ice belt was 350 mm, and the thickness of the plating was 24

mm. Hänninen (2005) did not report on the structural arrangement in the mid area. The damaged areas had a length of four frame spacings and a height of three stringer spacings (see Hänninen (2005) for more details). Jennings et al. (1991) reported a maximum permissible ratio of 0.05 between the indent and the minimum span length between the stiffeners as one of the existing criteria for in-service allowance of hull plating. The ratio between the maximum plate deflection and the stiffener spacing was 0.087 in the laboratory tests. This value was similar to the ratio of 0.086, which was calculated using data in Hänninen (2005). The fact that both calculated ratios are larger than 0.05 suggests that the level of damage in the laboratory is interesting in terms of the severity of the structural damage. In turn, the similarity of the ratios (0.087 in the laboratory versus 0.086 in the full-scale) suggests that damage in the laboratory is reasonable compared with the full-scale data.

The maximum dent in the plate after the impact test in water (Figure 84, Test no. 8) was less than that during the drop test in air (Figure 85a), despite the similar kinetic energies (approximately 3 to 3.5 kJ) of the ice mass before the impact. This result may be attributed to the additional resistance provided by the water between the impacted panel and the side of the floater. Moreover, the boundary conditions during the tests in water and air were not precisely the same. The local ice shape at contact was also different in water and in air. For the drop test in water, the rotation of the ice block and global motions of the floater dissipated some of the available kinetic energy.

In drop Test no. 5 (Table 11), the impact of the ice block on the panel at a higher kinetic energy (17.7 kJ) resulted in the complete shattering of the ice block rather than local ice crushing. The shape of the plate deformations (Figure 56) was different from the ice shape (see, Figure 46c). This result suggests that there was some amount of local ice crushing before ice shattering. This local ice crushing caused the plate damage shown in Figure 85b and Figure 56. The dents on the plate for Drop Test no. 5 were less deep than those for Drop Test no.4; however, a larger damage area was observed for Drop Test no. 5 than for Drop Test no. 4.

Analysis of the plate deformations (see Table 13) reveals that in the drop tests, the major part of the collision energy (70–80%) was dissipated within the ice with little plastic deformations in the panel. The maximum structural damage was achieved at a kinetic energy level of 17.7 kJ (Drop Test no. 5). The maximum length of the dent in the 4-mm thick panel was 750 mm (five times the spacing of the stiffeners), and the maximum depth was 8 mm.

The differences between the ice-panel interaction and the damage for Drop Test nos. 4 and 5 highlight the importance of the kinetic energy level (the initial velocity) and the local/global ice shape in terms of the plate deformations and the energy dissipation. It is

essential to determine the conditions under which the structure will sustain the most damage. For example, a certain level of damage can be sustained under the following conditions: (i) local confinement at the interaction zone caused by the local ice shape and (ii) global confinement of an ice mass caused by the size (global shape) of the ice block and its boundary conditions. The level of local (or global) confinement is determined by the ice block size, the internal stresses caused by temperature gradients, the flaw structure, etc. This problem may be elucidated by recent studies by Bruneau et al. (2012) and Gudimelta et al. (2012) on the behavior of ice samples of various sizes and shapes during ice-structure interaction and by further work (see Section 5.3).

Pressure data

In the impact tests with the tactile pressure sensors, the ice block impacted the stiffened panel in areas where the pressure sensing mat was able to record data in only three out of nine tests. Since the tactile sensor did not cover the entire plate surface, it is uncertain whether the actual contact area extended outside the sensing panel. Due to the limited calibration of the pressure sensor and low data acquisition rate, only a rough, qualitative assessment of the contact pressures can be performed. Figure 87 shows the contact pressure distribution for Test no. 10 provided for the illustration of the pressure patterns only.

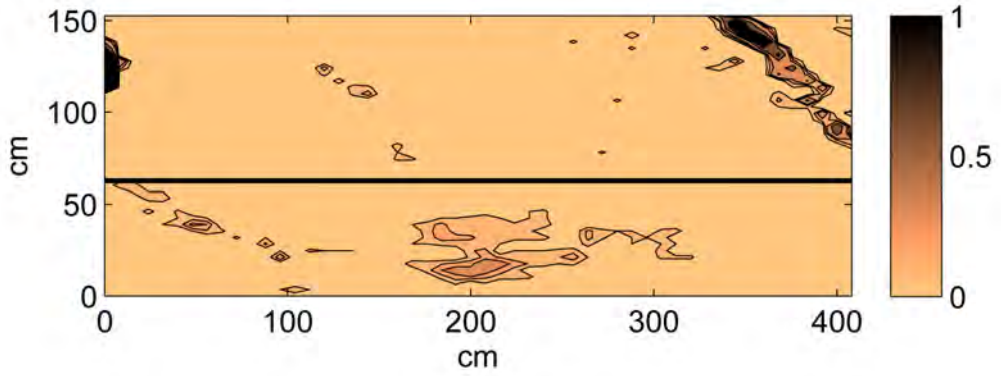

Figure 87: Data recorded by the pressure sensor during Test no. 10, showing pressure contours; pressure values are reported in MPa, the black horizontal line denotes the stiffener position relative to the pressure sensing area.

The measured values of pressure and contact areas are highly uncertain. At this point, applicability concerns regarding the use of tactile sensors for dynamic pressure measurements may be raised. The pressure sensing system (Tekscan, 2010) not only responds to the applied pressure but can also be affected by the contact conditions (surface roughness and hardness), temperature, load duration, etc. The pressure may vary over a wide range (e.g., 0–100 MPa) during the ice crushing process. According to Tekscan (2003), a single load calibration provides good accuracy for a range of

pressures, approximately ±20% of the single calibration load. However, a quantitative assessment of the system accuracy during impact load measurements is not provided in the manual. The necessity of nonlinear calibration for the pressures that rapidly vary over the range of 0–100 MPa may introduce uneven errors in the measurements of pressure over this range. In addition, there are uncertainties related to the sensor response time. For example, the dynamic response time of an F–Scan testing system is delayed by a mean of 0.32 s (Sumiya et al., 1998). This delay would be unacceptable for events with duration of a few milliseconds (e.g., the present study). For the sensor system (Tekscan 5513), we did not verify whether there is a delay between the actual time of load application and the time registered by the sensor. For a similar sensor system, Määttänen et al. (2011) mentioned the possibility of a time lag in the physical behavior of the sensor. Määttänen et al. (2011) also noted that during ice crushing, this time lag is likely to attenuate sudden changes of pressure.

From our experience with the tactile pressure sensor, we recommend that the time lag issues be addressed before deciding to use a similar pressure sensor system to quantitatively assess dynamic contact pressures. The reliability tests presented in Subsection "Instrumentation" reveal some additional shortcomings of the technology related to the measurements of quasi-static ice pressures.

Impact force

The total peak impact force was estimated using the data from the DMU (see Table 19) for each run, assuming that the added mass coefficient is constant and equal to 0.4 for sideways motion, adopted from Petersen and Pedersen (1981). The force was determined by multiplying the mass of the ice (including hydrodynamic added mass) by the maximum acceleration of the floater in the sway direction. As expected, the impacts at a speed of 1 m/s produced smaller loads than those at 2 m/s.

The eccentricity of the impact was quantified by comparing the loads acting on the web of each HEB beam. Table 19 provides the web load fractions for each test run. Impact nos. 5, 7 and 16 (see Figure 82 and Table 19) were extremely off-centered. For these impacts, the ice/panel interaction produced tension in the webs.

To access the impact events causing inelastic deformations of the plate (see Test nos. 8 and 9 in Table 19), simplified theoretical methods were applied to the experimental data to back-calculate the maximum impact load. The theoretical models were based on a plastic limit analysis. The load was determined by assuming the formation of a plastic mechanism and equating the external work to the internal work. The load cases and the deformation mechanisms were based on the measured plate deflections and the ice damage zone (Figure 84). For simplicity, isotropic, rigid and perfectly plastic material behavior was assumed in the calculations. The yield stress of the panel elements (σ_Y) was determined from the tensile coupon tests on steel samples and was equal to

approximately 300 MPa for the 4-mm plate and 190 MPa for the 2-mm plate (see Figure 48). The effects of strain hardening and the membrane stresses were neglected. For Test no. 9, the impact load was estimated using a fully loaded plate-strip model and an end-loaded stiffener model.

Plate-strip model

A stiffened plate spanning a distance (b) of approximately 0.15 m with a uniform stiffener spacing (s) of 0.15 m was considered. The plate was subjected to a uniformly distributed load (p). Plate-strip theory was applied, and a fully clamped beam model with a rectangular cross section (Figure 88) was used in the theoretical model to simulate the stiffened plate. The shear deformation of the plate web and the deformations of the stiffeners were neglected.

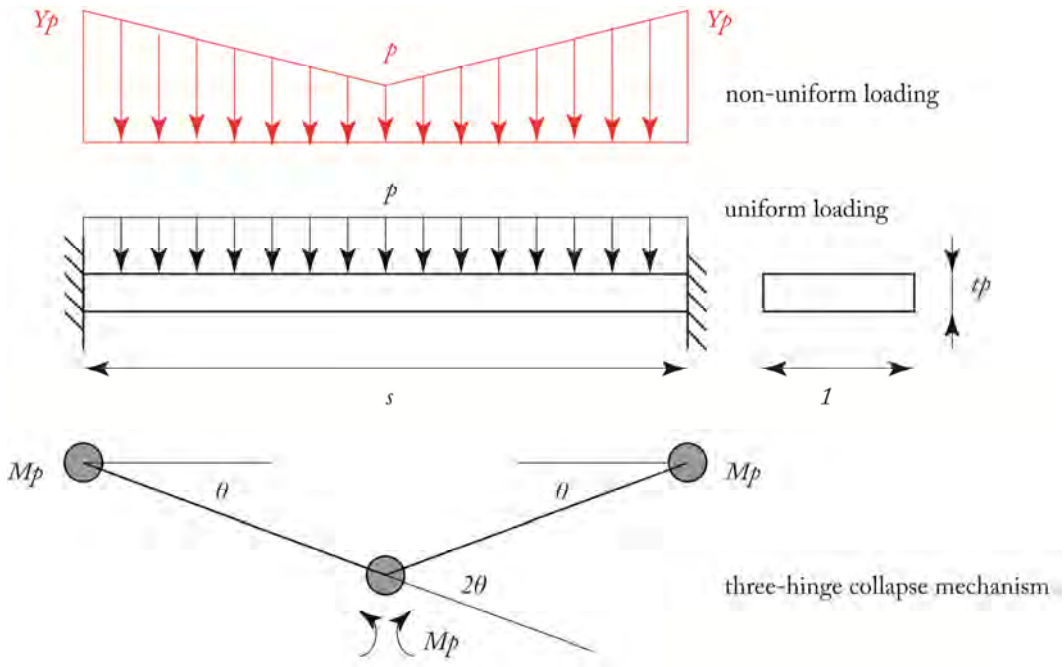

Figure 88: Beam model in which a plastic deformation mechanism was assumed (s – stiffener spacing, t_p – plate thickness, M_p – plastic bending moment, p – pressure, Y – non-uniformity factor and θ – rotation angle of the beam).

The critical pressure for a plate strip of unit width is given as follows

$$p_c = 4\sigma_Y \left(\frac{t_p}{s}\right)^2, \tag{28}$$

where σ_Y is the material yield stress. The dynamic yield stress was used for strain-rate effects. In the Cowper-Symonds equation (see e.g., Amdahl (1983)), the dynamic stress is defined as a function of the static yield stress (σ_Y) and the strain rate ($\dot{\varepsilon}$)

$$\sigma_{Yd} = \sigma_Y \left(1 + \left(\frac{\dot{\varepsilon}}{40} \right)^{0.2} \right). \tag{29}$$

The strain rate in the calculations was assumed to be 1/s. This value corresponded to a strain of 2% following an impact that lasted 20 ms.

Next, the actual plate width (b) was included, and the ice pressure was considered to extend over the plate supports (see Figure 84, Test no. 9). Equations (28) and (29) were combined to yield the total critical load (or impact load)

$$F = 2 p_c b s = 8 \sigma_Y \left(1 + \left(\frac{\dot{\varepsilon}}{40} \right)^{0.2} \right) \left(\frac{t_p^2}{s} \right) b . \tag{30}$$

Stiffener model

A stiffened plate spanning a distance (L) of 0.5 m with a uniform stiffener spacing (s) of 0.15 m was considered. A beam model with a tee cross-section was used to replace the stiffened plate. One-half of the distance to each neighboring stiffener was taken as the effective width of the beam, and a uniform pressure was applied, as shown in Figure 89. The plastic hinge along the length of the beam was loaded at the middle of the applied load. Our model was similar to the "*end loaded fixed-fixed frame model*" formulated by Daley (2002). Our model differed from the Daley's model in that the plastic work done by the plastic bending moments in the left part of the beam was neglected to yield the following expression for the internal work

$$\begin{aligned} IW &= t_s h \frac{\sigma_{Yd}}{\sqrt{3}} (a + 0.5b) \theta_1 + 2 M_p \theta_2 , \\ \theta_2 &= \theta_1 \frac{a + 0.5b}{L - (a + 0.5b)}, \end{aligned} \tag{31}$$

where t_s denotes the thickness of the stiffener. The location of the plastic hinge was also assumed in our model, whereas Daley (2002) determined the location of the hinge by minimizing the internal work.

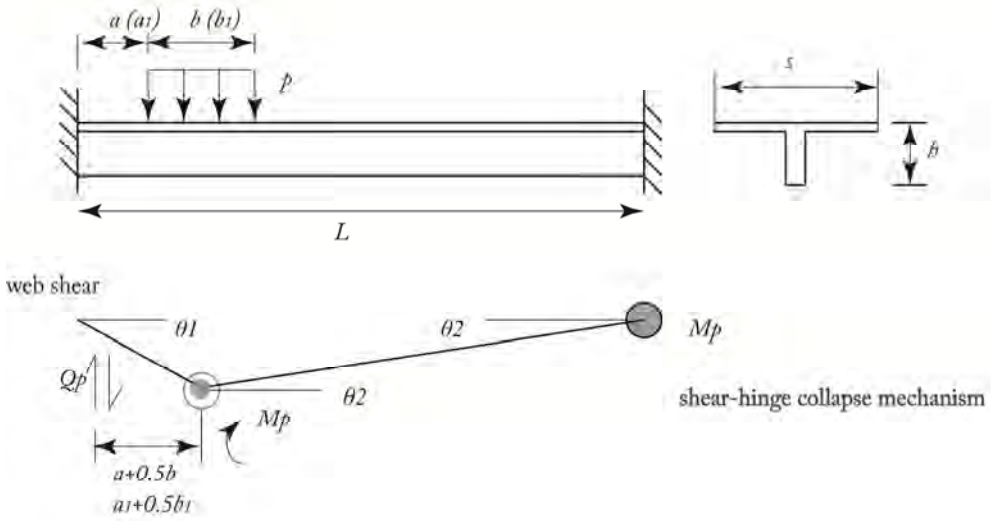

Figure 89: End-loaded fully clamped stiffener model assuming a plastic deformation mechanism (L – frame spacing; M_p – plastic bending moment of tee section; p – pressure; θ_1 and θ_2 – rotation angles of the beam; Q_p – shear force; and h – stiffener height).

The critical pressure was given as follows

$$p_c = \frac{Q_p x + 2M_p \frac{x}{y}}{s\left(0.5(x^2 - a^2) + \frac{x}{y}(a + b - x)(L - 0.5(x + a + b))\right)}, \tag{32}$$

$$Q_p = t_s h \frac{\sigma_{Yd}}{\sqrt{3}}$$
$$x = a + 0.5b$$
$$y = L - x$$

The calculations for M_p were simplified by considering the stress in the cross-section to be the yield stress for the 2-mm-thick plate and assuming a plastic neutral axis at the plate/web connection. Accounting for the size of the load patch produced, the following expression for the total load (impact load) in Test no. 9 (see Figure 84) becomes

$$p_c bs \le F \le 3 p_c bs\,. \tag{33}$$

The smallest value of the force corresponded to the collapse of one stiffener. This value corresponded to the pressure acting over a square area of 0.15 × 0.15 m^2 and most likely underestimated the load patch in Figure 84. The load corresponding to the collapse of

three stiffeners overestimated the load patch and was considered to represent an upper bound.

In Test no. 8, the plate deformations were highly localized (Figure 84). A *yield line model* for a plate (Figure 90) was used. Clamped boundaries were assumed.

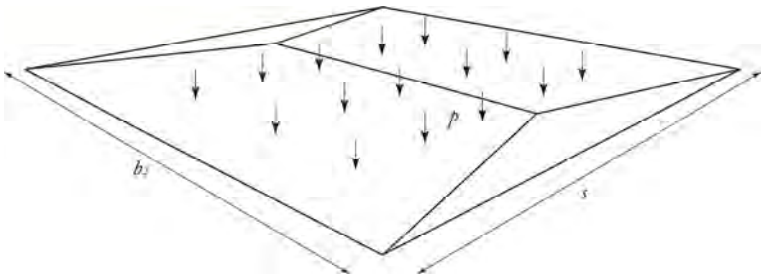

Figure 90: Yield line model for a square plate subjected to a uniform pressure (b_2 – load patch width, s – stiffener spacing and p – pressure).

The plastic loading capacity in bending for b_2=s was predicted as follows

$$p_c = \frac{12\sigma_{Yd}\, t_p^2}{b_2^{\,2}}, \tag{34}$$

The critical load was given as follows

$$F = p_c b_2 s\,. \tag{35}$$

Next, 25% of the load in Equation (35) was assumed to be carried by the stiffener. In this case, the stiffener model in Figure 89 should also have included a concentrated load of 0.25F at a distance (c) of approximately 0.1 m from the right end. For Test no. 8, Equation (32) was written as follows

$$p_c = \frac{Q_p x + 2M_p \frac{x}{y} - 0.25F\frac{x}{y}c}{s\left(0.5(x^2 - a_1^{\,2}) + \frac{x}{y}(a_1 + b_1 - x)(L - 0.5(x + a_1 + b_1))\right)}, \tag{36}$$

$$x = a_1 + 0.5b_1$$

$$y = L - x$$

For Test no. 8, the total load (impact force) was the sum of the critical load from the yield-line model and the load from the stiffener model.

The results of the calculations are presented in Table 20.

Table 20. Summary of calculation results.

Test ID	Impact force, kN	Measured (DMU estimates), kN
8	13[3]+104[4]	190
9	57[1] (228±114) [2]	226

[1] plate-strip model (b=0.15 m, contact over two stiffener spacing); [2] stiffener model (a =b=0.15 m); [3] yield-line model (b_2=s=0.15 m) and [4] stiffener model with extra external load (a_1=0.03 m; b_1=0.15 m)

Note that the derivations given above are simplified and idealized, e.g., the reduction in the effective width of the stiffener spacing from the welds was not considered. In addition, a uniform pressure distribution was assumed. The ice-plate interaction in Test nos. 8 and 9 most likely resulted in a non-uniform pressure distribution (i.e., the pressure increased in the direction of the stiffeners), but the exact form of the pressure distribution was difficult to describe. For example, assuming a non-uniform pressure distribution in Test no. 9 (see Figure 88 in which Y ranges between 2 and 4) could increase the impact load in the plate-strip model by 50% – 150%. The size of the load patch may have been slightly bigger than the assumed value. In addition, a portion of the total impact load may have been supported by the closest frame.

In Figure 91, the theoretical force for Test nos. 8 and 9 is compared to the force estimated from the DMU data (i.e., measured force) and Timco's empirical formula (Timco, 2011). For Test no. 9, the results from Daley's asymmetrical shear-collapse model (Daley, 2002) are also presented for comparison. For detailed information about the model, refer to the end-loaded fixed-fixed frame model in Daley (2002), Figure 6. The load width for Daley's model was estimated from Figure 84 and was equal to 0.15 m.

Timco (2011) analyzed all of the available data for ice-floe impacts on structures (including forces from small icebergs impacting test structures at Grappling Island and Newmans Cove) and found that the impact force was well-correlated with the energy at impact and could be expressed by the following functional form.

$$F = BE_{imp}^{0.532}, \tag{37}$$

where F is in MN and E_{imp} is in GJ. The coefficient B was determined to be 61.7 for the probable impact force and 388 for the upper limit of the impact force. In this

formulation, the hydrodynamic added mass was neglected in the calculations of kinetic energy.

Figure 91 shows that assuming a uniform pressure distribution in the plate-strip model resulted in an underestimate of the load. The agreement between the theoretical and measured force was not perfect. The predicted loads only partially reflected the measured values. There were also uncertain factors that could affect the impact force, e.g., the added mass, the impact eccentricity and the roll rate of the impacted target at impact. Note that the experimental data were scattered for similar impact conditions (see Table 19). The scatter in the data was most likely a reflection of the difficulty in controlling the exact impact geometry. Oblique and eccentric impacts were the rule rather than the exception. For example, the impact force could be significantly reduced by changing the eccentricity of the impact.

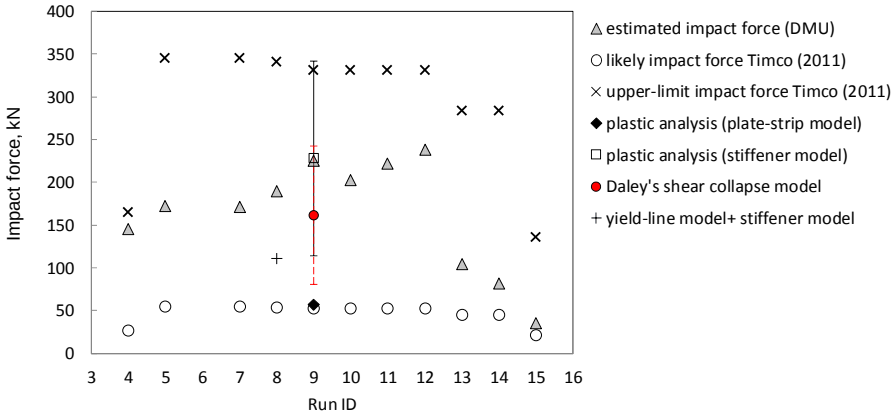

Figure 91: Comparison between experimental and theoretical data; error bars for Test no. 9 correspond to lower and upper bounds in Equation (33).

To gain insight into the possible effect of the roll rate, a few runs were selected for careful inspection (see Table 21). The data presented in Table 21 indicate that accounting for the roll rate in the calculations can influence the estimates of the impact force by approximately 5-10%.

Table 21. Possible effects of the roll rate for selected tests.

Run ID	ζ – vertical distance between center of gravity and the collision point (estimated from video recordings)	Roll rate $\dot{\omega}_x$ at peak sway acceleration	Rolling linear speed $v_R = \dot{\omega}_x \zeta$	Common velocity after impact[1]
	(m)	(°/s)	(m/s)	(m/s)
4	0.3	1	0.0052	0.12
8	0.5	3	0.026	0.23
9	0.4	3	0.021	0.31

[1]The common velocity after impact was calculated using collision mechanics and accounted for the hydrodynamic added mass of the ice block and the floating structure (see Equation (27), Section 3.4.2).

The data in Figure 91 and the aforementioned uncertainties led to the conclusion that the measurements validated the theoretical considerations of the present study and those of Daley (2002). The force estimated from the DMU measurements was in the range of the values predicted by the empirical formula given by Timco (2011).

Comparison with numerical predictions

The numerical models used to predict the structural deformations after an ice impact have been described in Subsection "Description of the impacted target". Note that all of the numerical simulations were conducted before the actual material parameters of the ice (including the shape of the ice blocks) and the steel were determined. The selection of the ice/steel properties was based on available experimental data and the avaliable experience. The purpose of the numerical studies was to predict whether the ice action would be sustained by the stiffened plates rather than to simulate the details of the damage. Numerical studies were conducted using a simplified nonlinear static analysis with the ABAQUS (2007) finite element code and an integrated nonlinear dynamic analysis using LS-DYNA, Hallquist (2006). Details can be found in Subsection "Description of the impacted target".

A constant impact speed of 2 m/s was used in the LS-DYNA simulations. The ice mass was placed symmetrically in front of the impacted target. In this study, the numerical predictions were compared with the experimental data for the maximum depth of the dents on the impacted panel.

The maximum predicted deflection for panel A was 15–20 mm (assuming that all of the collision energy was dissipated only by the panel and that the ice pressure was uniformly distributed over a contact area of 0.15 m by 0.15 m) and 10–15 mm (assuming that the collision energy was dissipated by both the ice and the panel and that the ice shape was spherical).

The predictions of the finite-element simulations were larger than the experimental values (see Figure 84 for Test no. 8 in water). However, the maximum predicted deflection was very close to the measured deflection for Drop Test no. 4 in air (Figure 85a).

The deflection estimates obtained from the finite element analysis were consistent with the experimental results, which suggests that the ice model and the modeling procedure have reasonable accuracy. However, these preliminary numerical models did not account for physical factors that may have affected the results (e.g., a part of the impact energy was transferred to the global motions of the ice and the floater, hydrodynamic added mass of the floater, stress triaxiality, flexibility of the wooden supports in drop tests).

3.4.3 Summary

The primary findings of this ice-structure collision study in which the structure and the ice were allowed to deform inelastically are given below.

- The characteristics of the ice impact zone compared fairly well with data from full-scale observations. For example, features such as crushed (pulverized) ice and splitting cracks were observed in both this study and the full-scale results. More ice splitting was observed for events with higher collision energies.
- The data showed that the peak impact load increased with the impact speed and the ice mass. The force values estimated from the peak acceleration were within the range reported by Timco (2011) using full- and laboratory-scale data. For the inelastic ice-structure interaction, the maximum force was also estimated based on plastic deformations of the panel observed after the impact and using the plastic mechanism analysis developed by Daley (2002). The calculated force agreed well with the force estimated from the peak acceleration. This result confirms Daley's theoretical formulation.
- The impacts of ice blocks at speeds of 1–2 m/s with panels of different stiffnesses produced a variety of results, ranging from no visible marks (on a 12-mm-thick plate) to dents in 2-and 4-mm-thick plates. A maximum dent depth of 13 mm that was observed for a stiffener spacing of 150 mm was within the range of the typical dent values caused by ship-ice contact in the Baltic Sea. The ratio between the dent depth and the stiffener spacing was larger than the maximum allowable in-service plate-deformation ratio for vessels.
- The extent of energy dissipation (both the ice and the structure deformed inelastically) was less pronounced than desired. However, the ice crushing process is very uncertain, and thus, it was extremely difficult to design experiments to obtain the desired results. In addition, it was also difficult to obtain a sufficiently high kinetic energy for the towing cases to create significant plastic deformations in the steel panels without using very thin panels.

Additional uncertainties in the results associated with the experimental apparatus used were similar to those listed for the drop tests in Section 3.3.4, with the exception of the pressure measurements. The uncertainties in and the limitations of the pressure measurement system (i.e., the delayed sensor response, sensor calibration for a wide range of pressures) are outlined in Subsection "Instrumentation". It is unlikely that the overall trends in the reported results (including the coupled behavior of the ice and the impacted structure) will be altered by the aforementioned uncertainties.

3.5 Concluding remarks

In summary, experimental studies were conducted at two different scales. Ice indentation tests and AOR studies were conducted at small-scale (O[cm]) while the drop tests and collision experiments were conducted at scales approaching a full-scale ice impact (O[m]).

Small-scale ice-indentation experiments were conducted on laboratory-grown freshwater ice. Remarkable similarities were observed between events observed at full and medium scales. Coulombic and plastic fault zones were created by indentation. In the absence of confinement, the flow properties of the crushed ice particles were controlled by contact forces, the particle size and time. These data may serve as additional data in ice-structure interaction problems and may improve our understanding of ice failure processes at larger scales.

The impact tests were conducted using structures of various rigidities and different ice masses. The ice blocks used in the collision experiments (and the drop tests) were manufactured using a mixture of water and commercially crushed ice. Both the ice and the structure underwent permanent deformations during impact. In the drop tests, most of the collision energy was dissipated within the ice with no (or little) plastic deformations in the 4-mm-thick panel. The collision experiments simulated deformations of the ice and the structure at full-scale (i.e., "hungry horse" deformations); however, the deformations of the structure were limited to moderate plastic dents on the impacted plate and represented the ultimate limit state of the structure rather than the accidental limit state. We did not obtain sufficient information to be able to comment on the effect of structural deformations on the contact pressure distribution.

The experimental data obtained in this study may be used for (a) the development and validation of ice material models (primarily for granular ice) for engineering applications and (b) verification and further development of existing design tools for water-ice-steel interactions and structural damage, in particular.

The major findings were communicated to the relevant research community through the scientific publications, i.e., Kim et al. (2012c) and Kim et al. (2013).

Chapter 4

Numerical studies

"Essentially, all models are wrong, but some are useful."
Box, G. E. P. and Draper, N. R., 1987
"Empirical Model Building and Response Surfaces"

This work considers the ice material model in Liu et al. (2011), which was primarily developed to simulate ship-iceberg impacts and is an isotropic, elastic-plastic model with failure. This chapter presents findings related to the physical interpretation of the input material parameters and evaluation of the ice material model by a potential end user of this model. The main objectives were to provide an understanding of the input parameters and to determine recommendations for the appropriate choice of the values in engineering applications. The results of the calculations were used to quantify uncertainties related to applications of the model and to aid in defining the applicability of the model for integrated (coupled) finite element analysis of ice-structure interaction problems in which local deformations of the structure and ice crushing are considered. In addition, improvements (modifications) to the ice material model are suggested based on the results of model evaluation.

4.1 Design material model of ice

The main characteristics of Liu's ice model are the isotropic constitutive equations, a pressure-dependent elliptical yield surface defined with two stress invariants and elastic-perfectly plastic behavior with a strain-based element erosion criterion. For details, please refer to the work by Liu et al. (2011). To reduce the number of input parameters, the assumption of plastic incompressibility is applied, which is physically incorrect for brittle ice failure. Temperature and strain-rate effects are not included. For quasi-static analysis, strain-rate dependence for the yield or failure surfaces can be included by varying the corresponding material constants. An element deletion technique is used to remove failed elements from the calculation. The material model is implemented as a user subroutine in the explicit solver LS-DYNA.

4.1.1 Model description

Within the model, additive decomposition of strains and stresses is assumed. The stress and strains are expressed in terms of their deviatoric and spherical components $\boldsymbol{\sigma}=\mathbf{s}+p\mathbf{1}$

and $\boldsymbol{\varepsilon}=\mathbf{e}+\varepsilon_m\mathbf{1}$, where $p=\frac{1}{3}\mathrm{tr}\,\boldsymbol{\sigma}$ and $\varepsilon_m=\frac{1}{3}\mathrm{tr}\,\boldsymbol{\varepsilon}$. It is also assumed that the strain tensor can be split into an elastic and plastic components $\boldsymbol{\varepsilon}=\boldsymbol{\varepsilon}^{el}+\boldsymbol{\varepsilon}^{pl}$. The plastic-strain components ($\boldsymbol{\varepsilon}^{pl}$) are calculated using a classical elastic predictor/cutting-plane return-mapping scheme. The yield surface is a function of stress variables defined via two stress invariants as

$$F(p, J_2)=J_2-a_0-a_1p-a_2p^2 \tag{38}$$

where $J_2=\frac{1}{2}\,\mathbf{s}:\mathbf{s}$ ($\mathbf{s}$ – deviatoric stress tensor) and the hydrostatic pressure is $p=\frac{1}{3}I_1$. The material parameters (a_0, a_1 and a_2) are derived from experimental data and are related to the ice strengths. The yield surface represents an ellipsoid in the principal stress space with a pair of equal semi-axes of lengths $BC=(2J_{2\max})^{0.5}$ and a distinct third semi-axis CA oriented along the hydrostatic axis, as shown in Figure 92.

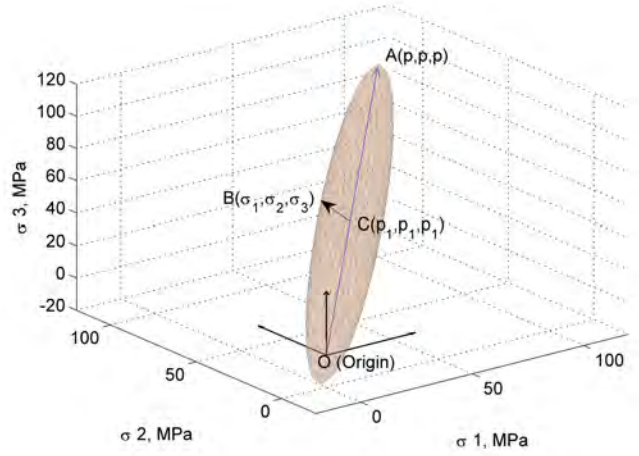

Figure 92: Schematic representation of an elliptical yield surface defined by Equation (38) in the principal stress space; OA is the hydrostatic axis where $\sigma_1=\sigma_2=\sigma_3$, BC indicates a semi-minor axis and CA indicates the semi-major axis.

The element loses all strength (stiffness), and element erosion occurs after $p\leq p_{cut\ off}$ (compression is positive, $p_{cut\ off}$ is negative) or $\varepsilon^p_{eq}>\varepsilon_f$, where $p_{cut\ off}$ is a material parameter, ε_f is a function of stress variables and material constraints $\varepsilon_f=f(p)$, and ε^p_{eq} is the equivalent plastic strain defined as

$$\varepsilon^p_{eq}(j)=\int_0^{t_j}\dot{\varepsilon}^p_{eq}dt\,,\ \dot{\varepsilon}^p_{eq}=\frac{2}{3}\sqrt{\dot{\boldsymbol{\varepsilon}}^{pl}:\dot{\boldsymbol{\varepsilon}}^{pl}} \tag{39}$$

The model was developed as a FORTRAN subroutine and incorporated into the LS-DYNA solver by Dr. Zhenhui Liu. A flowchart showing the details of the implementation is presented in Figure 93. Note that the model has limitations when

used within the implicit finite element framework due to the chosen stress-update algorithm. For details, please see the discussion on the cutting-plane algorithm in de Souza Neto et al. (2008).

The limitations of the material input data include the following:

- No direct measurements of ice strengths for conditions close to hydrostatic compression and tension, and no direct measurements of ice failure strain under different degrees of triaxiality or confinement.
- No proof that the erosion limit is a material property and can be set independently of the mesh size.
- The approach used to evaluate the model is an estimation of the missing (uncertain) material input parameters via LS-DYNA correlations with known (available) impact and indentation data. The values of the material properties provided by Liu et al. (2011) are treated as default input parameters.

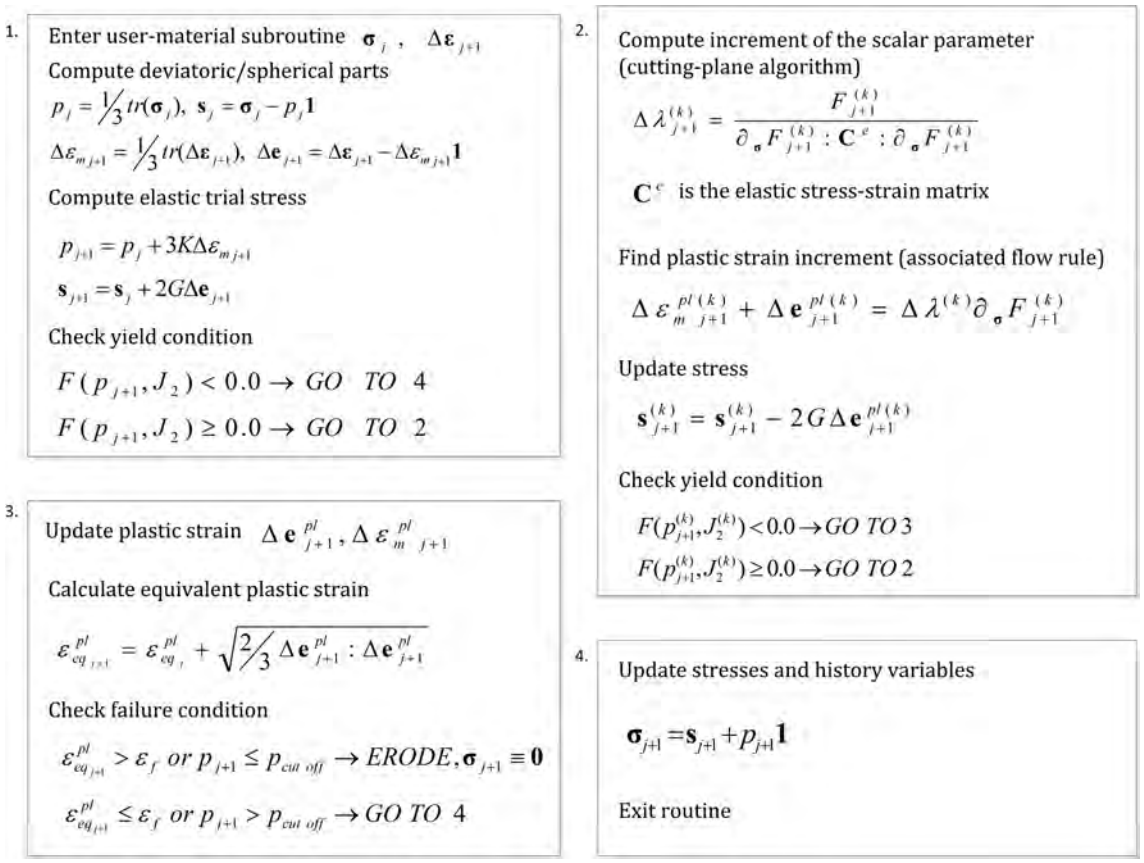

Figure 93: Flowchart highlighting details of the implementation of the elastic-plastic model with failure. Tensor notation is applied, i.e., $\boldsymbol{\sigma}_j$ is the Cauchy stress tensor at time j, and the strain increment is $\Delta\boldsymbol{\varepsilon}=\Delta t\dot{\boldsymbol{\varepsilon}}$. In Step 2, the maximum number of iterations (k) was set to 15. K denotes the bulk modulus, and G is the shear modulus.

Figure 94 presents the yield/failure surfaces for two different sets of material parameters (a_0, a_1 and a_2) used by Kierkegaard (1993) and Liu et al. (2011). The surfaces were obtained from different experimental data sets. The shape of the yield surface is only in partial agreement with the experimental findings by Schulson and Duval (2009), i.e., increasing ice strength with increasing level of confinement. The material parameters a_0, a_1 and a_2 in Figure 94 imply that a hydrostatic pressure of approximately 50–100 MPa will cause a certain amount of melting at the grain boundaries, and the ice material will no longer withstand shear stresses.

The values of a_0, a_1 and a_2 may be related to the ice strengths, i.e., compressive strength, shear strength and (or) tensile strength; see Equation (40). The details of the derivation of Equation (40) are provided in Appendix B.

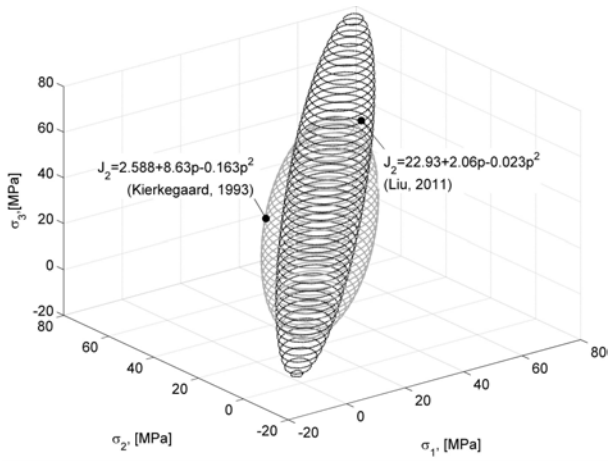

Figure 94: Ice yield surfaces used by Kierkegaard (1993) and Liu (2011). Data are shown in the principle stress-space.

$$a_0 = \tau^2;\ a_1 = -3a_0\left(\frac{1}{\sigma_c}+\frac{1}{\sigma_t}\right);\ a_2 = 9a_0\left(\frac{1}{\sigma_t}\frac{1}{\sigma_c}+\frac{1}{3a_0}\right) \tag{40}$$

At this point, the effect of temperature and (or) deformation speed (or a strain rate) can be included in the model by entering the strength values that correspond to a certain ice temperature and (or) deformation speed. The effect of deformation speed may be implicitly included only for quasi-static analysis (i.e., only for the analysis in which a constant displacement is prescribed for the ice component). In an analysis in which the initial velocity of the ice component is given, the deformation rate of the ice will not be constant throughout the analysis, and hence, the effects of the deformation rate should be explicitly included in the user material subroutine. It is possible to show (see Appendix B) that the yield surface used by Liu (2011) is a special (isotropic) case of the yield surface developed by Tsai and Wu (1971) for anisotropic materials.

Alternatively, one may obtain Liu's yield surface by extending the von Mises yield criterion; see, e.g., Reinicke and Remer (1978).

4.1.2 Model evaluation

The evaluation consisted of a series of numerical analyses using Liu's implementation of the ice material model in LS-DYNA (version 971 release R6.1.0 single precision) for the MS-Windows platform. The model evaluation consisted of two steps:

1 First, the ice material model was used in quasi-static crushing analysis of a spherical (1.5–m radius) ice-mass against a rigid, flat surface with a speed of 2.0 m/s. The calculations were performed to verify that the model can successfully reproduce the empirical process/spatial pressure-area relationships and to confirm that the results are similar to those obtained with earlier LS-DYNA versions for a different platform (Linux). Furthermore, a parametric study was performed to evaluate the model sensitivity against variations of the key parameters (i.e., size of the yield surface, shape and size of the failure curve, coefficient of friction between ice and steel).

2 Second, the effect of local ice geometry was studied by reducing the radius of the ice mass to 0.45 m.

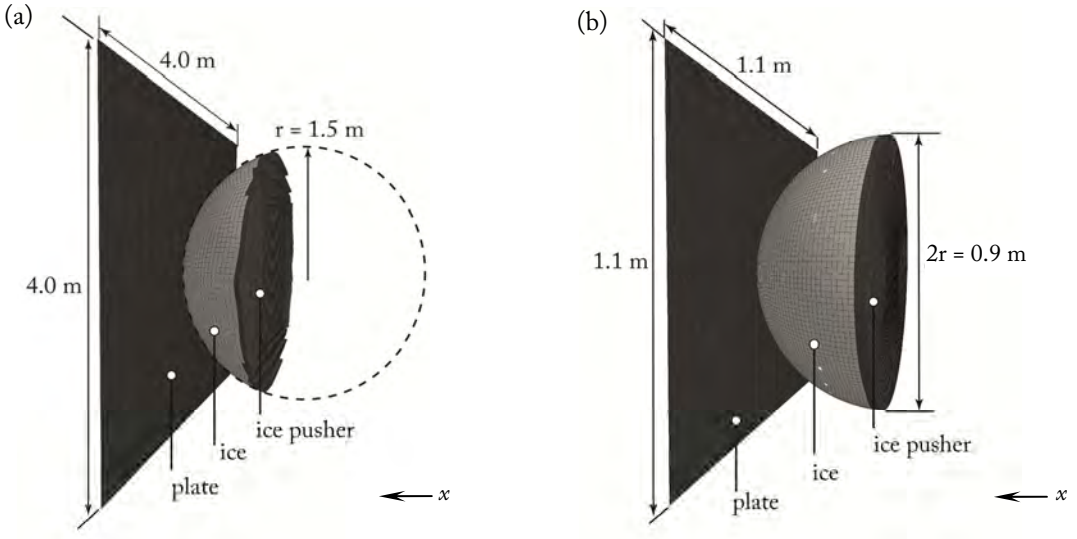

Figure 95: Finite element models: (a) model used to study the effects of material input parameters and friction; (b) model to study geometry effect; *x* is the direction of a prescribed displacement.

The two finite element models that were used in the evaluation studies are presented in Figure 95a and Figure 95b. To save computation time, only a portion of the ice mass

was modeled. The models consisted of three components, one component represented the deformable ice, the second component represented the impacted structure and the last component represented a rigid object pushing the ice during the analysis. The model shown in Figure 95a was created by Simen Bøhlerengen. The mesh size and ice material parameters for this model were verified by Liu (2011) and Bøhlerengen (2013) against Pond Inlet indentation tests with a 2-m radius indenter described in Frederking et al. (1990). The model in Figure 95b was used to study the effect of geometry. Both models contained the same contact formulations, element types and boundary conditions.

Mesh

The plate was modelled as a rigid material employing shell elements. The plate in Figure 95a (and Figure 95b) was modelled by 80 (and 70) elements over the width and 80 (and 70) elements over the height, respectively. The spherical ice component was modelled using eight-node solid elements with reduced integration and viscosity based hourglass control. The hourglass energy was less than 15% of the total energy during simulations. The characteristic length of a hexahedral element was roughly 50 mm in the regular part of the mesh (Figure 95a). In the model shown in Figure 95b, three meshes with characteristic element lengths of 44 mm, 22 mm and 15 mm were considered (see the subsection entitled "Size effect in ice").

Boundary conditions

The displacement corresponding to a velocity of 2 m/s was applied in x-direction to the rigid body labeled as "ice pusher" while displacements in two other directions and the rotations were fixed. The plate component was also fixed. Contact between the ice part and the plate was implemented through the contact-eroding-surface-to-surface formulation which was used with the segment-based contact option (SOFT=2) in LS-DYNA. A static friction coefficient of 0.15 was used in the contact formulation between the ice component and the plate. Self-contact of the ice component was implemented through the contact-eroding-single-surface formulation with a static friction coefficient of 0.15. After the simulations, it was checked that the sliding energy remained positive during simulations.

For the model in Figure 95a, the simulations required approximately 1.5 h to run on an Intel 2.5-GHz processor work station (8 CPU, 8.0 GB RAM), which corresponds to 0.35 s of real time.

Sensitivity study and uncertainty quantification

1. *Material parameters and size of the failure criterion*

To perform the sensitivity study, it was necessary to generalize the failure criterion. The function (Equation 41) originally proposed by Liu et al. (2011) requires only one input parameter (ε_0) and hence may be too simple for certain applications.

$$\varepsilon_f = \varepsilon_0 + \left(\frac{p}{p_2} - 0.5 \right)^2 \tag{41}$$

In Equation (41), p_2 is the largest root of $F(p, J_2)=0$ given by Equation (38).
A more general form of Equation (41) was incorporated into the user material subroutine:

$$\varepsilon_f = \varepsilon_0 + \left(\frac{p}{M \cdot p_2} - \frac{N}{M} \right)^2, \tag{42}$$

where ε_0, M and N are the dimensionless material parameters such that $N \cdot p_2$ determines the pressure at which the failure strain reaches its minimum equal to ε_0. The vertex of the parabolic failure function has the coordinates $(N \cdot p_2, \varepsilon_0)$. The leading coefficient $M \cdot p_2$ indicates how quickly the failure strain decreases with increasing pressure. For M=1.0 and N=0.5, the failure criterion in Equation (42) becomes identical to that of Liu et al. (2011).
A summary of the input parameters used in the parametric studies is given in Table 22. Figure 96 presents the yield surface and the failure curves for the selected runs. The last column in Table 22 gives the process pressure-area relationship obtained from the simulation runs. Pressure (p) was calculated by dividing the contact force by the area of contact (A) at the corresponding time step. In turn, the area of contact is assumed to be equal to the projected area of the ice component at the corresponding time step.

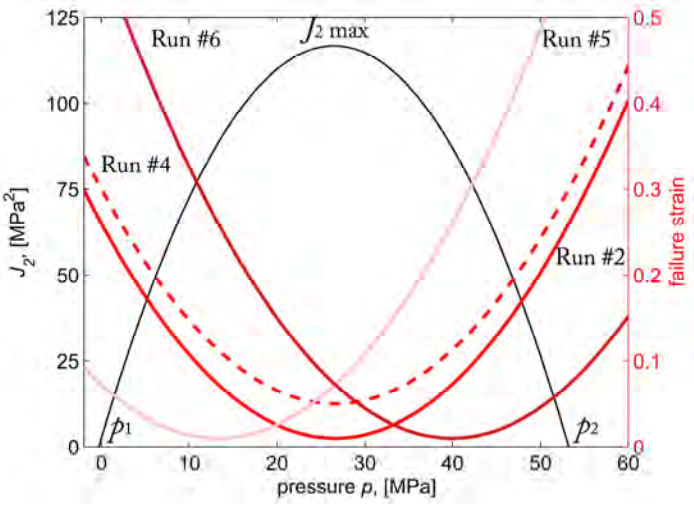

Figure 96: Yield function in $J_2 - p$ space and selected failure curves for different runs in Table 22; p_1 and p_2 are the smallest and the largest root of $F(p, J_2)=0$, respectively, and J_2max indicates the vertex of the yield function.

For all test runs in the list, the density of ice, elastic modulus and Poisson's ratio of ice were held constant and equal to 900 kg/m^3, 9.5 GPa and 0.3, respectively. The tensile pressure cut-off and ice-steel friction coefficient remained constant and were equal to –2.0 MPa and 0.15, respectively.

Table 22. Summary of input parameters and corresponding process pressure-areas relations.

Run ID	σ_c [MPa]	σ_t [MPa]	τ [MPa]	ε_0 [-]	M [-]	N [-]	$p=CA^{-x}$ [MPa]
1	9.35	–7.30*	4.79	0.008	1.0	0.5	$p=2.4A^{-0.15}$
2	9.00	–0.82	1.61	0.01	1.0	0.5	$p=3.4A^{-0.36}$
3	9.00	–0.82	1.61	0.005	1.0	0.5	$p=3.4A^{-0.44}$
4	9.00	–0.82	1.61	0.05	1.0	0.5	$p=5.2A^{-0.42}$
5	9.00	–0.82	1.61	0.01	1.0	0.25	$p=0.7A^{-0.41}$
6	9.00	–0.82	1.61	0.01	1.0	0.75	$p=7.8A^{-0.25}$
7	9.00	–0.82	1.61	0.01	0.8	0.5	$p=4.4A^{-0.34}$
8	9.00	–0.82	1.61	0.01	1.3	0.5	$p=2.5A^{-0.47}$

* Element erosion limits the tensile pressures to –2 MPa;

Figure 97 presents a comparison between the calculated contact force and the forces obtained from the empirical pressure-area relationships in ISO, Ritch et al. (2008), Appendix C and Palmer and Croasdale (2013).

- The pressure-area relationship given in ISO 19906 ($p=7.4A^{-0.7}$) was assembled from field measurements and is purely empirical.
- The pressure-area relationship $p=3.5A^{-0.56}$ was obtained by Ritch et al. (2008) using data from impacts between bergy bits and the CCGS *Terry Fox*. The relationship was constructed for the contact areas within the range of 0.12–2.4 m^2 and can be considered as an empirical maximum pressure-area envelope curve for all considered events.
- The pressure-area relationship $p=4.8A^{-0.5}$ was recommended by Palmer and Croasdale (2013) for local ice pressures for first-year ice and is a combination of the CSA and ISO approach.
- The pressure-area relationship $p=3.2A^{-0.26}$ was derived in Appendix C (i.e., see Figure C2) using data from two different scales (small- and medium-scale indentation tests).

The discussed pressure-area relationships are purely empirical, and the mechanics underlying these relationships are not clearly understood. For example, in Section 3.1.3 (Table 6), a power-type relationship $p=0.10A^{-0.64}$ was found from small-scale indentation of freshwater granular ice. This relationship was related to the behavior of a

single high-pressure zone (HPZ). It was assumed that HPZs account for the majority of the ice load, and it was argued that the pressure-area relationship at larger scales could be found using small-scale data.

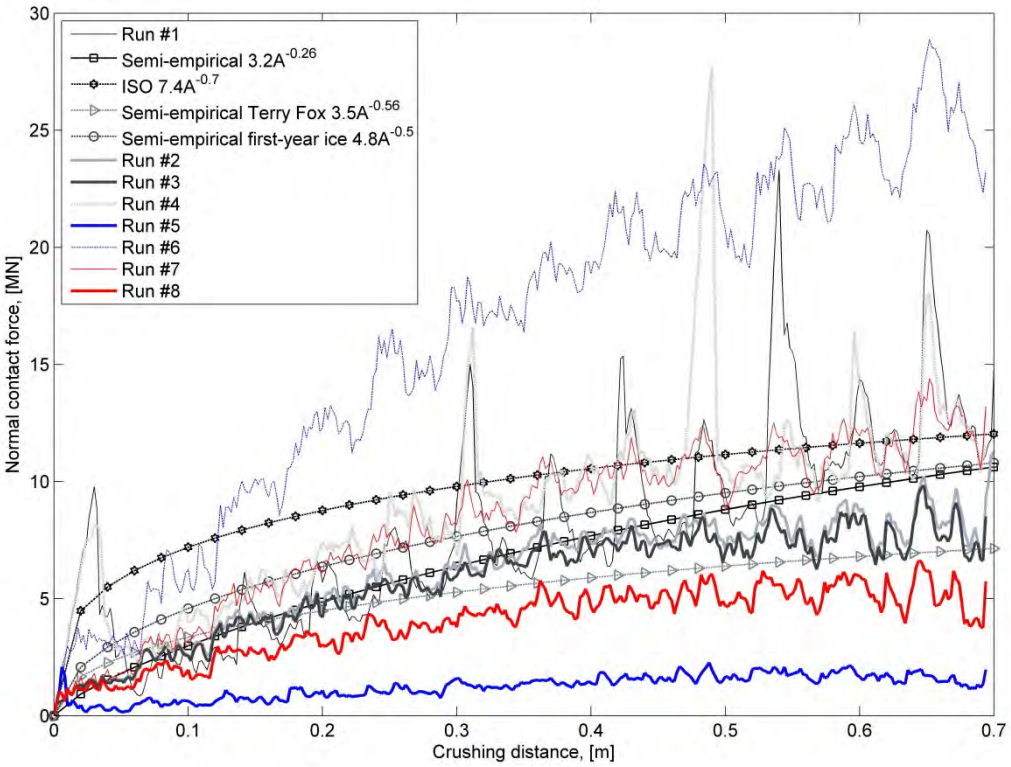

Figure 97: Normal contact force vs. crushing distance.

We apply similar thinking to our case in which a spherical ice mass strikes the structure. Taking into account that the number of HPZs in the full-scale is approximately 1/m^2 (Jordaan, 2001) and considering a spherical ice mass with a radius of 1.5 m, one could expect to observe a total of approximately five fully developed HPZs over the contact area $A_{full}=u\pi(2r-u)$. The value of A_{full}=5 m^2 corresponds to the maximum crushing distance (u) of 0.7 m. For the described collision, the pressure-area relationship becomes $p=5\cdot0.10A^{-0.64}=0.5A^{-0.64}$. The force corresponding to this relationship is close to that of Run no. 5. However, from Figure 97, it can be observed that the computed force in Run no. 5 is much smaller than that estimated from an empirical full-scale pressure-area curve, e.g., in Ritch et al. (2008). Perhaps the number of HPZs cannot explain the difference between forces (or pressure-area relationships) at different scales. The mechanics of interaction are more complex, and hence, the pressure-area relationship (or the force-displacement relationship) is controlled by such different factors as size and local ice shape, degree of ice confinement, shape of the impacted structure, indentation speed, etc.

Figure 97 and Table 22 demonstrate that the contact force is greater for higher values of N as defined in Equation (42). Low values of M correspond to greater forces. In practical design, it is recommended to use ε_0=0.01 because higher values of ε_0 may result in sharp force jumps (or numerical instabilities) that are closely related to the element erosion technique (see, e.g., Figure 97, Run no. 1).

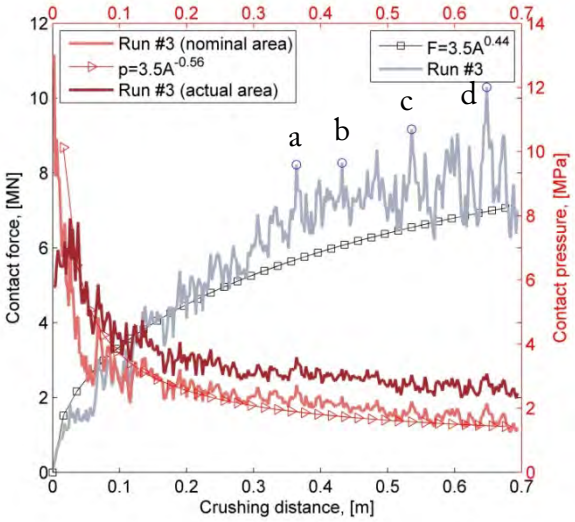

Figure 98: Force vs. crushing distance and the corresponding contact pressure vs. contact distance. The nominal contact area was calculated from known displacements and the radius of the ice block. The actual contact area corresponds to the total area of *non-zero* contact pressures.

From Figure 97, it can be observed that for glacial ice, the material parameters in Runs no. 2 and 3 resulted in a better estimate of the contact forces. The numerical estimate is close to the force computed using the empirical pressure-area curve in Ritch et al. (2008).

Figure 98 presents a comparison between the measured and calculated forces for Run no. 3. Contact pressures from the numerical simulations and from field measurements (Ritch et al., 2008) are also compared in Figure 98. In the numerical simulations, the contact pressure was defined as the force per nominal area or per actual contact area. The nominal area was computed from the known radius of the ice mass and the crushing speed. The actual area corresponds to the total area of *non-zero* contact pressures.

Spatial pressure distributions for Run no. 3 are shown in Figure 99 (see events “a”, “b”, “c” and “d” highlighted in Figure 98)

The element deletion technique resulted in sudden drops of the contact force, and the sawtooth load variations were of short duration. Numerical simulations of ice crushing generated “non-physical pockets” of zero contact pressure that were created upon the deletion of elements and can be observed in Figure 99.

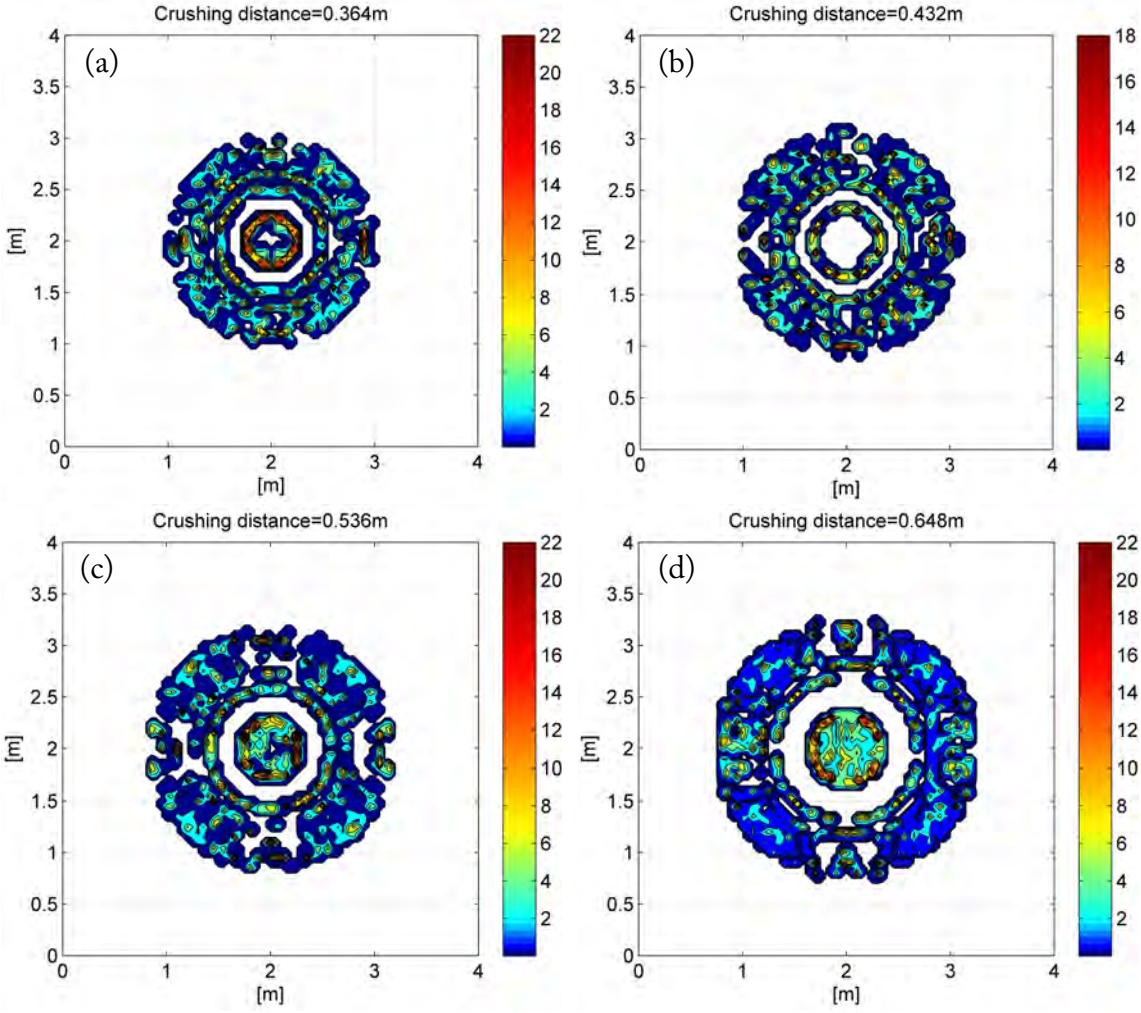

Figure 99: Spatial pressure distribution for the events marked in Figure 98; pressure is given in MPa.

Figure 100 shows a contour plot of the pressures in Run no. 3 and the pressure measured in a quasi-static ice-cone crushing test. The contour plot in Figure 100a was developed as follows:

- For each point on the contact surface (a node or an integration point), select the maximum contact pressure at all times.
- Generate a contour plot of maximum pressures as a function of the point location.

In this manner, the envelope of all spatial pressure distributions was constructed for Run no. 3. This approach can be compared with the mechanism of action through which the contact pressure distribution is produced by a pressure-indicating film used by Kim et al. (2012a).

From Figure 100, it can be observed that good agreement exists between the numerical calculations and the experiment in terms of the main characteristics of the pressure distribution, i.e., clustering of HPZs near the center of the contact zone. Note

that in Figure 100b, pressures above 2.5 MPa are shown, and hence, there is uncertainty in the actual contact area in the crushing test.

The computed local pressures in Figure 99 and Figure 100 can also be compared with the measurements of the confined compressive strength for icebergs reported by Fenco Engineers Inc. for depths up to 3.0 meters, i.e., 30 MPa and 26.8 MPa, as reported in Cammaert and Muggeridge (1988).

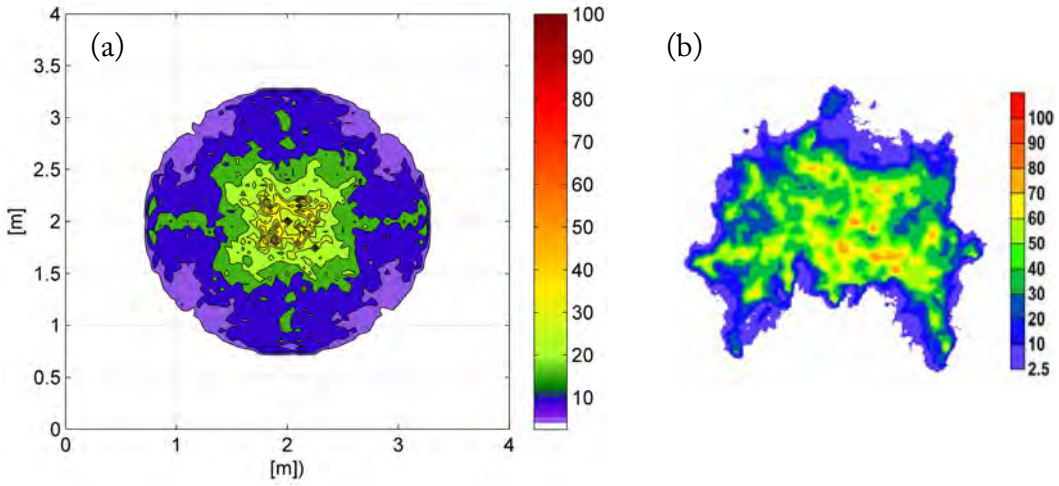

Figure 100: Contour plots of the contact pressure distribution envelope (MPa): (a) scattering of pressures from numerical simulations (the model in Figure 95a); (b) scattering of contact pressures from cone crushing experiments (Kim et al., 2012a) obtained using a pressure-measurement film. The pressure patterns on the right correspond to the sample diameter of 0.1 m.

To summarize, the ice model with the generalized strain-based failure criterion is able to reproduce various process pressure-area curves that are in agreement with experimental data at the full scale. However, for each time instance, the spatial pressure distribution suffers from non-physical zero-contact-pressure zones.

2. Shape of the failure criterion

Let us extend the pressure-dependent strain-based failure criterion such that it captures stress triaxiality. The degree of stress triaxiality (σ^*) can be defined as the ratio between the hydrostatic pressure (p) and the effective stress $(3J_2)^{0.5}$ and can be expressed as a function of the ratio between the principal stresses $\sigma_2=\alpha\sigma_1$ and $\sigma_3=\beta\sigma_1$:

$$\sigma^* = \frac{p}{\sqrt{3J_2}} = \frac{1+\alpha+\beta}{3\sqrt{1-\alpha-\beta-\alpha\beta+\alpha^2+\beta^2}}, \tag{43}$$

where α and β define the degree of confinement, and $\sigma^* > 0$ indicates a state of compression. A pure shear stress state is characterized by zero stress triaxiality.

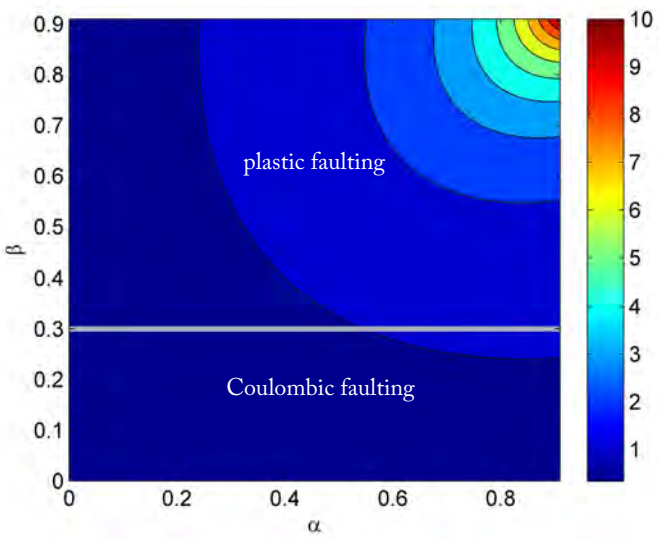

Figure 101: Stress triaxiality (σ^*) as a function of confinement ratios $\alpha=\sigma_2/\sigma_1$ and $\beta=\sigma_3/\sigma_1$. A higher degree of triaxiality (i.e., for $\beta > 0.3$) triggers the plastic faulting mode, and a lower triaxiality results in the Coulombic faulting mode.

From Figure 101, it can be observed that the degree of triaxiality increases with increasing confinement α, β. The function σ^* has a singularity ($\sigma^*=\infty$) at $\alpha=\beta=1.0$. For $\alpha=\beta=0$, $\sigma^*=1/3$ defines a state of uniaxial compression. The horizontal line in Figure 101 defines a stress state described by $\sigma_3=0.3\sigma_1$ and corresponds to the transition between two deformation modes, namely, the Coulombic and plastic faulting modes. These modes are described in Golding et al. (2010) and observed during freshwater-ice indentation tests at –10°C (see Chapter 3, Section 3.1). The micromechanical processes underlying these two faulting modes are different. Coulombic faulting is primarily characterized by microcracking, whereas plastic faulting is accompanied by plastic flow, deformation-induced heat and solid-state recrystallization (Schulson, 2009). Golding et al. (2010) defined ice strength as $\sigma_1-\sigma_3$ and found that the strength increases with increasing β but is almost constant for $\beta>0.3$. For the condition $\sigma_3/\sigma_1=0.3$, the triaxiality increases with increasing σ_2 and reaches the maximum value of 1.1 for $\sigma_1=\sigma_2$.

The failure condition $\varepsilon_f=f(p)$, Equation (42) may be expressed as $\varepsilon_f=f(\sigma^*)$ because $J_2=f(p)$ according to Equation (38) and $\sigma^*=f(p, J_2)$ according to Equation (43). Figure 102a presents the failure curve $\varepsilon_f=f(\sigma^*)$ that was redefined from Equation (42) for Run no. 2. The descending (or ascending) branch of the failure criterion $\varepsilon_f=f(\sigma^*)$ can be approximated by the generalized logistic function as shown in Equation (44).

$$\varepsilon_f = n_1 + \frac{n_2 - n_1}{1 + e^{-n_3\sigma^* + n_3 n_4}} \tag{44}$$

where n_1, n_2, n_3 and n_4 are material parameters; n_1 and n_2 define the lower and upper asymptote of the failure strain, respectively; n_3 characterizes the growth rate of the

failure strain with confinement; and n_4 characterizes the confinement of the maximum growth rate. Note that n_1, n_2, n_3 and n_4 are dimensionless quantities. Equation (44) can be considered as an original contribution to the field of constitutive ice modeling.

Figure 102a illustrates how the descending branch of the Liu's failure criterion $\varepsilon_f = f(\sigma^*)$ may be approximated using Equation (44) (see the curve labeled "Run #1s"). For $n_1 > n_2$, the strain at failure decreases with increasing triaxiality, and for $n_2 > n_1$, it increases with triaxiality.

Six runs were carried out to evaluate the sensitivity of the force-displacement relationship to the various ice failure parameters. In all test runs, only the parameters defining the shape of the failure curve (n_1, n_2, n_3 and n_4) were varied, whereas the parameters defining the elastic properties and the ice yield surface (ρ, E, ν, σ_c, σ_t, τ) were held constant and equal to those used in Run no. 2 (Table 22). The varied parameters are listed in Table 23. Note that the failure curve corresponding to Run no. 1s mimics the descending branch of the failure curve $\varepsilon_f = f(p)$ used in Run no. 2 and redefined as $\varepsilon_f = f(\sigma^*)$. The results of the calculations for the runs listed in Table 23 are presented in Figure 102b.

The ice behavior is more brittle in the absence of (or low) confinement ($0 < \sigma^* \leq 0.3$), and hence, the plastic strains should be close to zero. As the confinement increases ($0.3 < \sigma^* < \infty$), the development of microcracks is suppressed, and the ice may undergo plastic faulting for $\sigma^* > 0.5–1.1$. In this case, the plastic strains are expected to be greater than that in the case of low (or no) confinement. Therefore, from a physical point of view, the failure strain is expected to increase with the increasing degree of triaxiality.

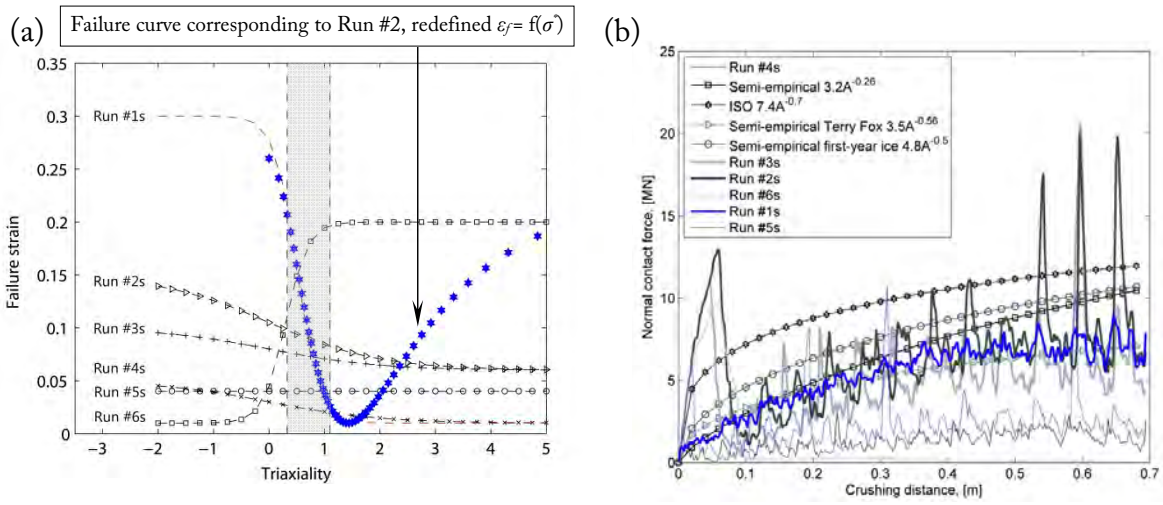

Figure 102: (a) Ice failure curves and (b) the corresponding force-displacement relationships.

The increasing failure strain as a function of triaxiality was used in Run no. 6s ($n_2 > n_1$, Table 23). This $n_2 > n_1$ approach resulted in the development of large splitting cracks radiating away from the ice/panel interface. This behavior produced the non-physical

force-displacement relationship shown in Figure 102b, perhaps because the elements were deleted from the analysis immediately after the failure strain was reached.

Table 23. Input parameters for the ice failure curve.

Run ID	n_1	n_2	n_3	n_4
Run 1s	0.3	0.01	5.0	0.5
Run 2s	0.15	0.06	1.0	0.0
Run 3s	0.1	0.06	1.0	0.0
Run 4s	0.05	0.01	1.0	0.0
Run 5s	0.04	0.04	1.0	0.0
Run 6s	0.01	0.2	5.0	0.3

It is interesting to report that Run no. 1s (the failure strain decreases with triaxiality, Figure 102a) resulted in almost the same force-displacement relationship as that of Run no. 2 (the failure strain decreases with pressure up to a certain value and subsequently increases, as in Liu's model); see Figure 102b and Figure 97. This similarity of the forces indicates that the response of ice is primarily controlled by the descending portion of the failure criterion for a given ice mass and shape. Despite the different shape of the failure criteria, the force-displacement records in Figure 97 (for Equation (42)) can be reproduced using Equation (44).

To summarize, Equation (44) is able to capture the effect of stress triaxiality, whereas Equation (42) lacks this information. The ice model displays several shortcomings with respect to the modeling of macroscopic ice behavior (i.e., microcracking, recrystallization) that limit the use of Equation (44) with $n_2>n_1$. Both Equations (42) and (44) and $n_2<n_1$ are able to reproduce various process pressure-area relationships that are in agreement with experimental pressure-area curves at the full scale.

3. Effect of contact friction

Figure 103 presents the contact force vs. crushing distance for friction coefficients between the ice and the rigid structure of μ_s=0.0, μ_s=0.15 and μ_s=0.5. For comparison, the forces corresponding to different pressure-area relationships have also been plotted in the same figure. The image to the left is a magnification of the force-crushing distance curve shown on the right.

It can be observed that at the beginning of the interaction, before significant element erosion take place, the effect of friction is insignificant. However, considering the entire crushing distance, it can be observed that the contact force decreases with increasing friction coefficient. From a physical point of view, the contact force is expected to

increase with increasing friction. The explanation for such erroneous behavior is thought to be the following:

The presence of friction introduces additional forces that shift the stress state in the ice towards states with higher pressures and, hence, lower failure strains, eventually leading to element erosion and to a decrease in the contact force.

The above explanation was driven by the following observations:

- In the numerical model, the net contact energy (i.e., the work performed by normal and surface contact forces) increased when the friction was included in the contact definition. (The contact energy was less than 12% of the total internal energy. In the absence of friction, the contact energy was less than 2% of the total internal energy.)
- The number of eroded elements increased with increasing friction.
- The net internal energy of the eroded elements for the contact with friction was lower than that for a frictionless contact.

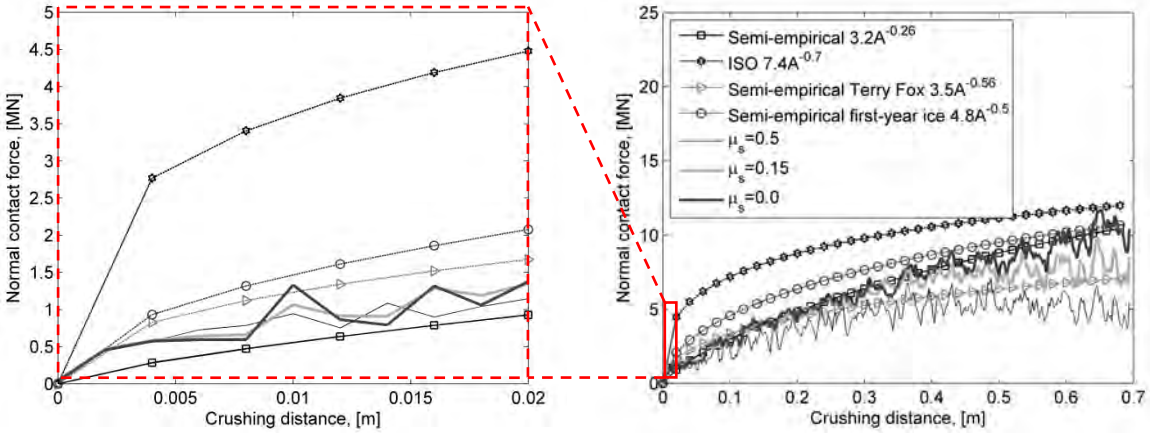

Figure 103: Effect of contact friction for the eroding surface-to-surface contact type with option SOFT=2.

To summarize, the effect of friction on the contact load seems to be unrealistic. It is suggested that a given fixed value of the friction coefficient must be applied during the analysis of an ice/structure interaction.

4. Size effect in ice

Figure 104 presents the force-displacement curves for the scenario in which a hemispherical ice mass (r=0.45 m) is crushed against a flat rigid plate at a speed of 2 m/s (see Figure 95b). The material parameters for this model were those used in Run no. 1

and shown in Table 22. Figure 104a shows the force-time history for the characteristic element length of 44 mm. Figure 104b presents the results of a mesh sensitivity study for characteristic element lengths (l_c) of 44 mm, 22 mm and 15 mm.

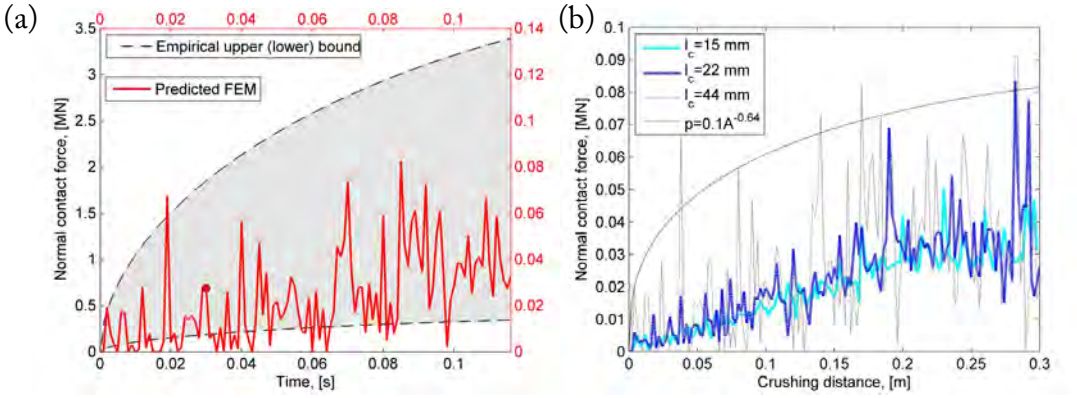

Figure 104: Force vs. crushing distance for the ice mass of radius r=0.45 m (the finite element model is presented in Figure 95b); in (a), the area between the upper- and lower bound is highlighted in gray.

Because the ice mass has a radius of only 0.45 m, it was difficult to compare the computed forces (process pressure-area curves) with those suggested in ISO or by Ritch et al. (2008). Instead, lower- and upper-bound empirical estimates were used. These estimates are based on the data from two different scales and were derived in Appendix C for an ice mass of a similar size. The lower bound corresponds to the pressure-area relationship $p=0.51A^{-0.46}$, and the upper bound is $p=5.0A^{-0.46}$ (see Figure C2 in Appendix C for additional details). Furthermore, the computed force can also be compared with the force corresponding to the empirical pressure-area relationship obtained in Chapter 3 from small-scale indentation tests (see $p=0.1A^{-0.64}$ in Figure 104b). This pressure-area curve corresponds to the behavior of a single HPZ and was discussed previously in the subsection entitled "Material parameters and size of the failure criterion".
From Figure 104a and Figure 104b, it can be observed that the calculated force for a 0.45-m ice mass is significantly lower than that predicted from the upper/lower bound pressure-area relationships and is also slightly lower than that for $p=0.1A^{-0.64}$.

We face an inherent uncertainty in the numerical simulations that is not entirely based on ice physics. The question arises as to whether the numerical model can adequately reproduce the ice crushing process at scales for which it was not calibrated. Is the constitutive behavior (or material constants) of the ice within the solid volume of 50×50×50 mm^3 (engineering-scale) the same as those for the ice volume of 15×15×15 mm^3 (laboratory-scale)?

From Figure 104b, it can be observed that the numerical force-displacement curve converges to a certain pressure-area relationship for the characteristic element length of

15 mm; however, the predicted force is significantly less than the experimental force at the full scale. Will the small ice volume be stronger than the ice large volume? Do we need to "scale up" the material parameters to match the experimental results?

According to Cammaert and Muggeridge (1988), the compressive and tensile strengths of ice will be controlled by the ratio of the sample size to the crystal size. To avoid scale/size effects, the authors recommend using sample' widths that are approximately 15 to 20 times the crystal diameter. At the same time, glacial ice may have individual crystals with cross-sectional areas ranging from 2–5 mm^2 (in the upper portions of the glacier) and from 100–1000 mm^2 (in the lower sections) (Cammaert and Muggeridge, 1988). The assumption of the same ice behavior within the volumes of 15×15×15 mm^3 and 50×50×50 mm^3 may not be entirely correct. It can be argued that a scale dependency exists that is caused by the change of underlying physical mechanisms within the smaller ice volume. The material parameters of the model (or the ice behavior) may express multi-scale characteristics.

To minimize uncertainties related to the element size and assumptions of the model, the following stepwise procedure is suggested for the analysis of structural deformations due to ice crushing:

1. Select the appropriate value of the ice-steel friction for a given interaction scenario (μ_s=0.15 in this study).
2. Choose the ice material parameters: For a given ice type (e.g., iceberg ice, freshwater ice, multiyear ice) E, v, a_0, a_1 and a_2 can be taken from uniaxial compression, tensile and (or) shear tests at the given deformation rate and temperature (see Appendix B). The parameters for the failure criterion, ε_0, M and N in Equation (42) or n_1, n_2, n_3 and n_4 in Equation (44), should be determined from analysis of the interaction between the ice of a given size and shape and a flat, rigid surface. The parameters should correspond to the assumed process pressure-area relationship. The possible set of parameters and the corresponding process pressure-area curves can be found in Table 22.
3. Once the material parameters are established, run the analysis of deformable ice versus deformable structure.

4.1.3 Combined SPH and FEM

This section explores the possibility of an increase in the model fidelity level by replacing failed solid elements with "water-like" SPH particles that are coupled to solid elements. The FEM-SPH coupling can be viewed as an alternative approach to the element erosion technique.

The SPH is a "mesh-free" method invented to solve gas dynamic problems in astrophysics (e.g., see Lucy, 1977). Since then, the method has been applied to solve various engineering problems, primarily modeling of fluid flows, e.g., modeling of incompressible fluid flow (Monaghan, 1994), high velocity impact problems (Libersky et al., 1993) and slope stability analysis (Bui et al., 2011).

In this study, the SPH method is applied for the first time to simulate ice crushing using LS-DYNA. This approach was used to avoid zero-contact pressures resulting from the deletion of finite elements. The theory behind SPH approximation can be found elsewhere, e.g., Hallquist (2006).

The model in Figure 95b was discretized using hybrid elements. Each hybrid element was composed of two layers: a solid layer (FEM component) and a particle layer (SPH component). The behavior of the solid layer was governed by the constitutive model described at the beginning of this chapter. Once the equivalent plastic strain in a solid element reached a critical level defined by Equation (42), the element was replaced with a number of SPH particles (1, 8 or 27). The parameters for the SPH component were taken from Otsuka et al. (2004) and represent liquid water (or a flow of crushed ice particles). The behavior of particles was controlled by the Mie-Grüneisen equation of state *EOS GRUNEISEN with c=1489 m/s; s_1=1.79 and γ=1.65 and by the material model *MAT NULL with the density of 1350 kg/m^3, a pressure cut-off of −1.0 MPa and a dynamic viscosity coefficient of μ=1.0·10^{-3} N·s/m^2. A comparison between the pure finite element analysis and the coupled FEM-SPH analysis is presented in Figure 105.

To investigate the stability of the FEM-SPH approach, the effect of the two numerical parameters FORM (in *CONTROL SPH card) and NQ (in *DEFINE ADAPTIVE SOLID TO SPH) was studied. The effect of three different SPH approximation-theories, namely, FORM=0 (LS DYNA default), FORM=5 (fluid particle approximation) and FORM=6 (fluid particle with renormalization approximation), is shown in Figure 106.

Figure 106 presents the spatial pressure distributions at time 0.03 s. It should be noted that the analysis with FORM=6 was computationally less efficient than that with the default value (FORM=0). For example, with FORM=6, the analysis corresponding to 0.05 s of real time took approximately two days to complete.

The difference between the computed contact forces was insignificant for the considered types of particle approximations. The parameter FORM affected the fluidic behavior of crushed (pulverized) ice, i.e., the contact forces were computed based on the chosen contact algorithm and hence, were unaffected by FORM.

The effect of particle density (number of particles) was studied using three different options NQ=1 (adapt one solid to one SPH element), NQ=2 (adapt one solid to eight

SPH elements) and NQ=3 (adapt one solid to 27 SPH elements). Figure 107 shows the contact force vs. crushing distance for different NQ options. The forces corresponding to the lower (and upper) bound pressure estimates are also plotted in Figure 107. The area between the lower and upper estimates is highlighted in gray.

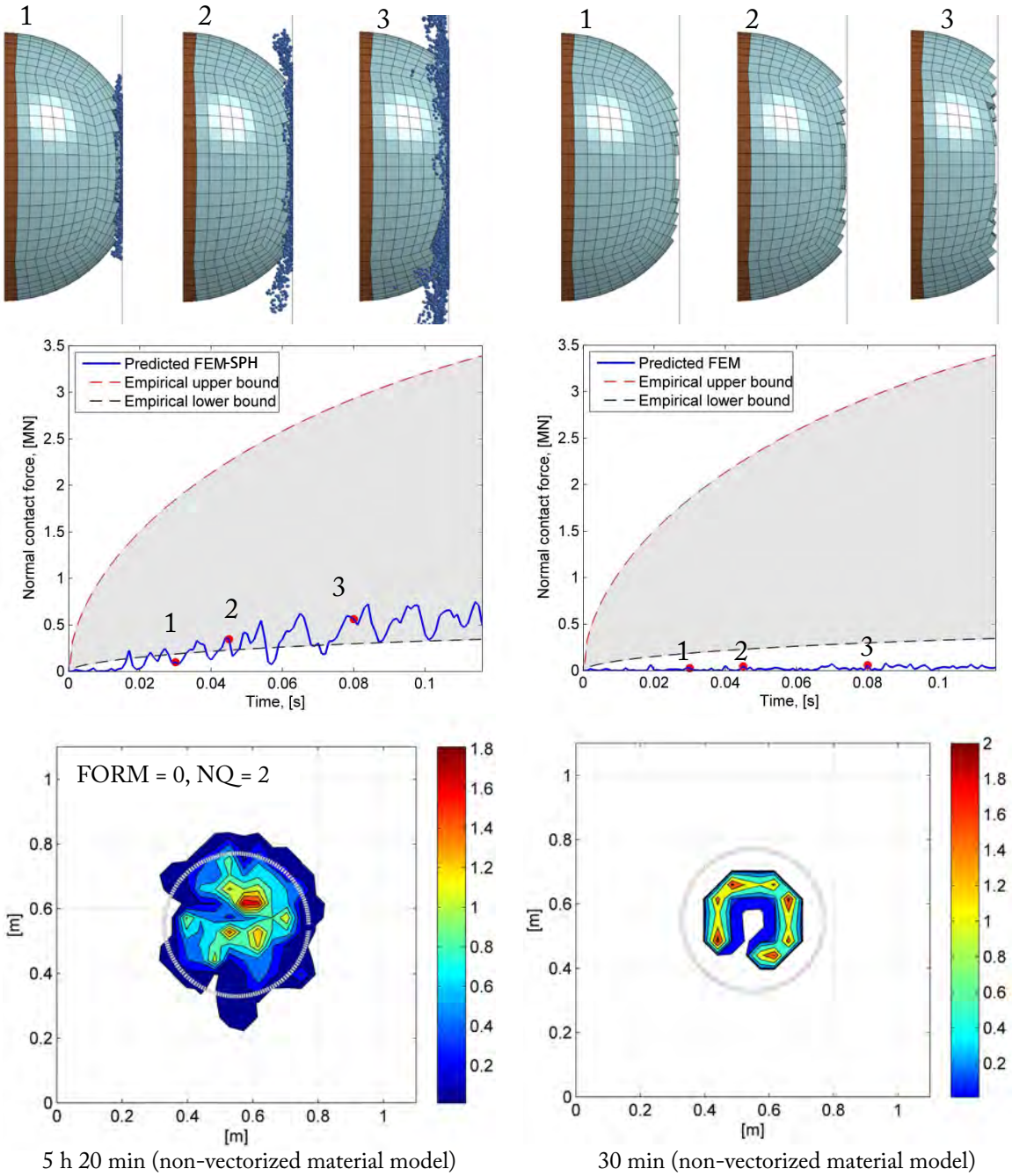

5 h 20 min (non-vectorized material model) 30 min (non-vectorized material model)

Figure 105: Comparison between the conventional FEM approach (plots on the right) and coupled FEM-SPH analysis (plots on the left); the gray circles correspond to the nominal (analytical) contact area, and the contact pressures are given in MPa.

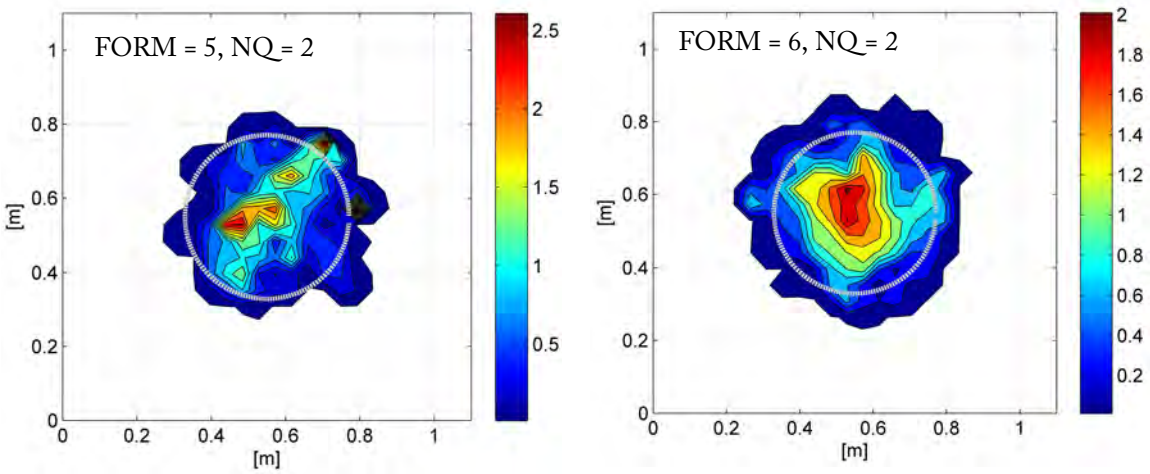

Figure 106: Effect of the particle approximation theory on the spatial pressure distribution at a time of 0.03 s (a global displacement of 0.06 m); the pressure values are given in MPa.

For comparison, the model with NQ=3 required approximately 12 h 30 min to simulate a 0.15-s ice crushing event, whereas the model with NQ=1 took only 1 h 20 min.

For a geometrically symmetric problem and homogeneous isotropic ice, a symmetrical pressure pattern is expected as opposed to the pressure patterns shown in Figure 105 and Figure 106. The randomness in Figure 105 and Figure 106 is a purely numerical effect. The FEM-SPH contains an inherent uncertainty related to the implementation of SPH method/contact algorithm within LS-DYNA that must be further investigated.

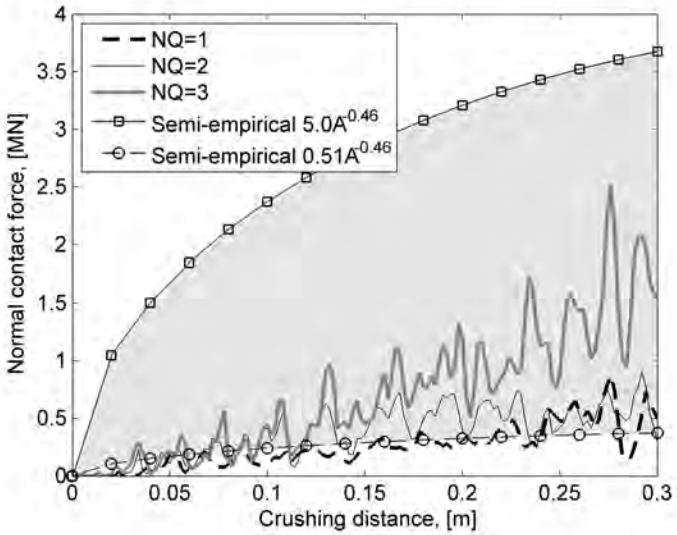

Figure 107: Effect of particle density (FORM=0).

Comparing the element erosion technique within FEM with the hybrid FEM-SPH approach, it can be concluded that the FEM-SPH approach is more computationally demanding; however, the pressure patterns from FEM-SPH appear more realistic than those from pure FEM. The visual representation of ice crushing is also better with the FEM-SPH approach.

4.1.4 Engineering-scale model validation

In Section 4.1.2 it was shown that Liu's constitutive ice model described in Section 4.1.1 was able to represent the force-displacement curves obtained in ice crushing tests. This section aims to explore whether the material model is able to predict energy absorption capacity of ice during crushing.

To characterize an idealized ice-structure collision, Bruneau et al. (2013) used the measure of energy consumed per unit of crushed volume. The authors argue that this measure used on a volumetric average may be more adaptable for the irregular ice shapes encountered in nature. The results presented by Bruneau et al. (2013) indicate that the energy measure is more reliable compared with conventional pressure measurements. Tsupric (2013) proposed calculation of the ice loads on structures using the "specific energy of mechanical fracture of ice" as a strength criterion. An analysis of the test results was presented in Chapter 3 (Section 3.1) and in Figure 37. The analysis indicated that the energy absorption during ice crushing is a scale-independent characteristic.

It is known that the presence of confinement affects the ice failure strength. Different boundary conditions resulting from ice/structure deformations, local shapes of the structure and ice, and global shape and size of the ice mass will promote/suppress splitting of ice. For example, under impact conditions, brittle-like failure of ice via tensile spalling occurs at relatively low degrees of confinement (i.e., sharp ice protrusion vs. a flat rigid surface). With an increasing level of confinement (blunt ice edge versus a structure or indentation into an ice wall), the ice exhibits Coulombic and plastic faulting. Therefore, for a given structural layout, it is important to realize the "most critical" loading conditions. The local ice shape is a concern, and it is reasonable to assume that the degree of confinement (or local ice shape) will affect energy consumption during ice crushing.

Figure 108a presents an illustration of strength versus confinement for freshwater granular and columnar ice.

According to Golding et al. (2010), Renshaw et al. (2011) and test results in Section 3.1, the plastic faulting dominates the failure process for granular ice when $\sigma_3/\sigma_1>0.3$ (σ_3 is the smallest or least compressive stress, and σ_1 is the largest principal stress). A comparison among indentation tests (Figure 108b), quasi-static impact tests and drop-

ball tests revealed that indentation (and impact) into an ice wall resulted in the highest value of SEA, whereas local crushing of a sharp ice edge gives lower values of SEA. The concept of SEA was defined in Section 3.3.1. The sharper the ice mass (i.e., smaller the attack angle), the less energy required to crush a unit volume of ice.

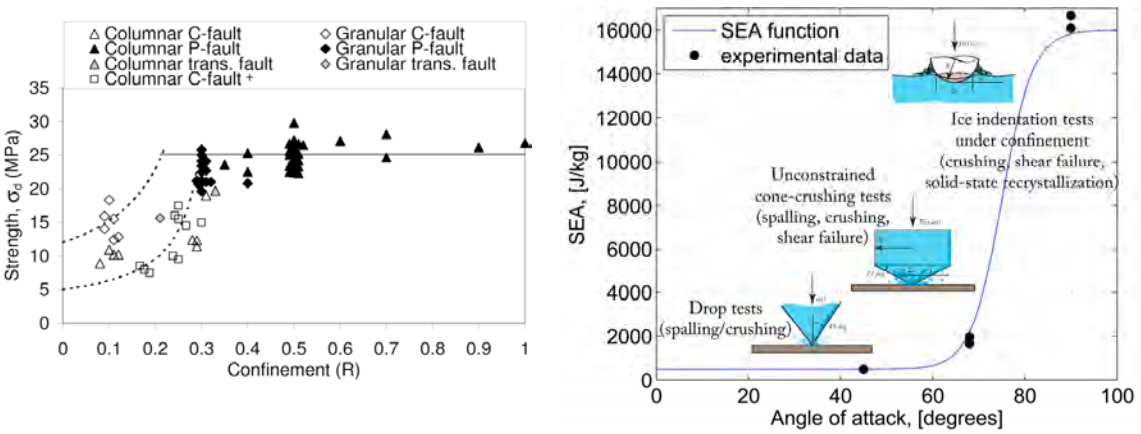

Figure 108: (a) Ice strength as a function of confinement, C-fault (Coulombic faulting) and P-fault (plastic fault) from Renshaw et al. (2011); (b) schematics of the proposed validation curve.

In this section, an empirically derived envelope (shown in Figure 108b) was used as an additional validation criterion for the engineering-scale model in Figure 95a. The envelope assumes that the spalling process is inhibited for increasing levels of confinement, and additional energy is required to crush the same amount of ice. This assumption is based on the fact that frictional sliding in ice (as opposed to sliding between ice and indenter) is suppressed under high degrees of confinement. The confinement tends to enforce crack closure and to hinder their propagation (Schulson and Duval, 2009), causing an increase in SEA.

The envelope for different stress regimes (attack angles) is shown in Figure 108b. The envelope can be modeled using a geometry-dependent version of SEA as described by the expression

$$SEA = m + \frac{n-m}{1+e^{-b\alpha^{*}+bc}} \tag{45}$$

where the attack angle is denoted α^{*}. The attack angle is defined as the angle between the tangent to an ice surface at the point of contact and the normal to the surface of the structure. Additionally, m is the lower asymptote of the SEA under a low degree of confinement ($\alpha^{*}<45^{o}$), and n is the upper asymptote of the SEA of fully confined ice ($\alpha^{*}=90^{o}$). The parameter b controls the growth rate of SEA, and the parameter c indicates

the α^* of maximum SEA growth. Note that m and n have units of J/kg, whereas b and c are dimensionless quantities. The criterion is empirical and only supported by limited data:

- data from drop tests (Section 3.3);
- unconfined cone-crushing tests (the average SEA value for Test nos. 11 and 12 derived from data in Ulan-Kvitberg et al., 2011); and
- the average value of SEA from medium-scale drop tests and small-scale indentation tests by Timco and Frederking (1990) and Section 3.1, respectively.

Because the constants m, n, b and c were calibrated from a limited number of data, they might not be representative for all ice masses and (or) boundary conditions that are experienced during ice-structure interactions.

The semi-analytical curve SEA vs. attack angle for m=500 J/kg, n=16000 J/kg, b=0.3 and c=75 is presented in Figure 108b. Numerical predictions of SEA and empirical data are compared in Figure 109 for the scenario of a spherical ice mass (r=1.5 m) crushed against a flat rigid surface (Run no. 3 in Table 22). It is important to note that the parameters for the ice model were established independently from the tests used to validate the model.

For each time step, the attack angle was calculated as the angle between the tangent to the ice surface at the point of contact and the normal to the surface of the structure. The digitized experimental data from Bruneau et al. (2013) are also shown in Figure 109. The comparison in Figure 109 indicates that the material parameters used in Run no. 3 result in an SEA that is in a close agreement with the experimental data.

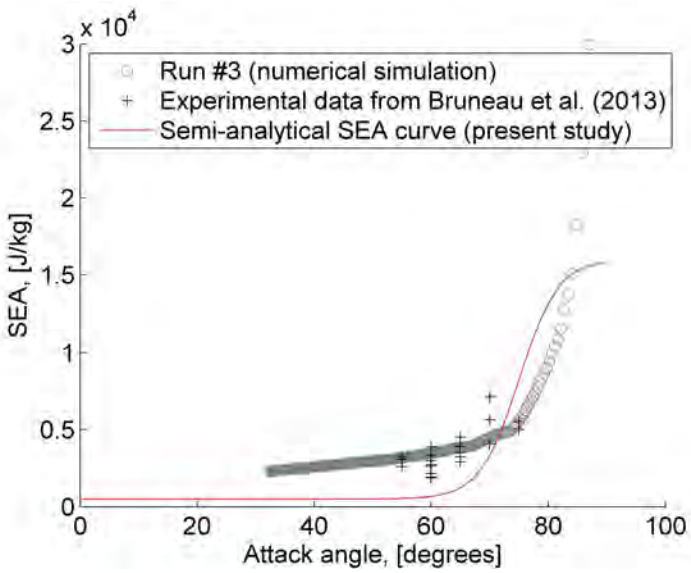

Figure 109: Results of the model validation.

The ice model is not only able to reproduce the pressure-area relationship of the process but can also reproduce an increase of SEA as a function of the attack angle. The numerical and experimental results indicate the importance of the local ice shape with respect to SEA. Crushing of blunt ice features requires additional energy compared with that of sharp ice features.

4.2 APPLICATION EXAMPLE

In this section, the ice model described in Section 4.1.1 was used to analyze three collision events, namely, *strength*, *ductile* and *coupled events* (a reference is made to Section 2.1). A *strength event* constitutes a collision between a relatively rigid plate and a deformable ice mass. This event is often considered for the ULS design of the structure, i.e., no permanent deformation of the impacted structure is allowed, and the ice-mass dissipates most of the available collision energy. A *ductile event* constitutes a collision between a deformable steel plate and a relatively stiff ice-mass, and a *coupled event* constitutes a collision between two deformable bodies (ice and the structure). The last two events may be considered for ALS design in which the structure is allowed to deform plastically under the ice load. During a ductile event, the plate absorbs a major component of the available collision energy, whereas in the coupled event, both the ice and the structure contribute to the energy dissipation.

Table 24. Summary of selected input parameters.

Parameter name	Parameter value		
	Strength event	*Ductile event*	*Coupled event*
Ice material model			
Density, kg/m^3	900	900	900
Elasticity modulus, GPa	9.5	9.5	9.5
Poisson ratio	0.3	0.3	0.3
Compressive strength, MPa	9.0	9.0	9.0
Tensile strength, MPa	–0.82	–0.82	–0.82
Shear strength, MPa	1.61	1.61	1.61
Failure constants $\varepsilon_0/M/N$	0.01/1.0/0.5 (**0.01/1.0/0.25**)[a]	0.01/1.0/0.5 (**0.01/1.0/0.25**)[a]	0.01/1.0/0.5 (**0.01/1.0/0.25**)[a]
Steel material model			
Yield strength (σ_y), MPa	NA(**NA**)[a]	235 (**235**)[a]	460 (**355**)[a]
Strength coefficient (K), MPa	NA(**NA**)[a]	670 (**670**)[a]	820 (**760**)[a]
Hardening exponent (n)	NA(**NA**)[a]	0.24 (**0.24**)[a]	0.13 (**0.23**)[a]
Plate thickness (t_p), mm	36(**36**)[a]	36 (**36**)[a]	50 (**36**)[a]
Coefficient of friction between ice and steel (μ_s)	0.15	0.15	0.15

[a] Parameters correspond to the events with soft ice (i.e., failure constant N=0.25)

A spherical ice mass with a radius of 1.5 m impacts an initially flat square plate (4.0×4.0 m^2) at a speed of 2.0 m/s. Fixed boundary conditions were applied to the plate edges. To reduce computational time, only a portion of the ice mass was modeled. The contact between the ice and the panel was modeled using *CONTACT ERODING SURFACE TO SURFACE with option SOFT=2, and the friction coefficient was set to 0.15. The ice parameters were defined accordingly as μ_s=0.15 and represent a soft and a hard ice mass. The soft ice was modeled using N=0.25 in Equation (42), and the hard ice was modeled using N=0.5. Table 24 summarizes important input parameters.

Forces vs. global displacements for the hard and soft ice are presented in Figure 110a and Figure 110b, respectively. The process of collision for the various events is illustrated in Figure 111.

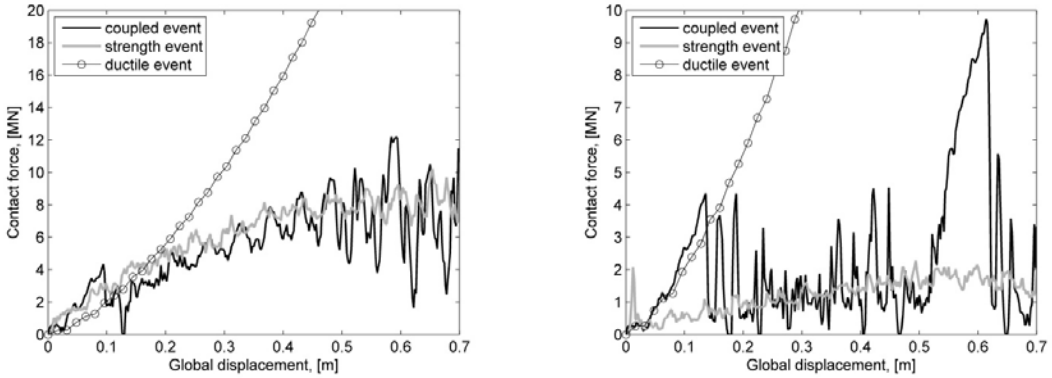

Figure 110: Force vs. global displacement for various ice and plate stiffness: (a) hard ice, (b) soft ice.

Comparing the force-displacement relationship during the strength event in Figure 110 with that in Figure 97, it can be observed that for the hard ice, the force-displacement relationship corresponds to the pressure-area curve $p=3.4A^{-0.36}$. For comparison, the force-displacement curve corresponds to $p=0.7A^{-0.41}$ for the soft ice during the strength event.

The force-displacement curves from the *ductile event* (for both hard and soft ice in Figure 110) represent simply the resistance of a fully clamped 36-mm-thick plate. Consequently, there is no difference between the force-displacement curves in Figure 110a (hard ice) and Figure 110b (soft ice). During the *coupled event*, an interesting interaction between the ice and the plate can be observed (Figure 110b). Initially, it is mainly the plate that deform, which results in the sharp increase of the contact force. The force-displacement relationship is close to that of a ductile event. At a global displacement of approximately 0.15 m, the structure becomes stronger than the ice, which subsequently begins to crush. A period of dominant ice crushing takes place for global displacements within the range of approximately 0.15–0.5 m.

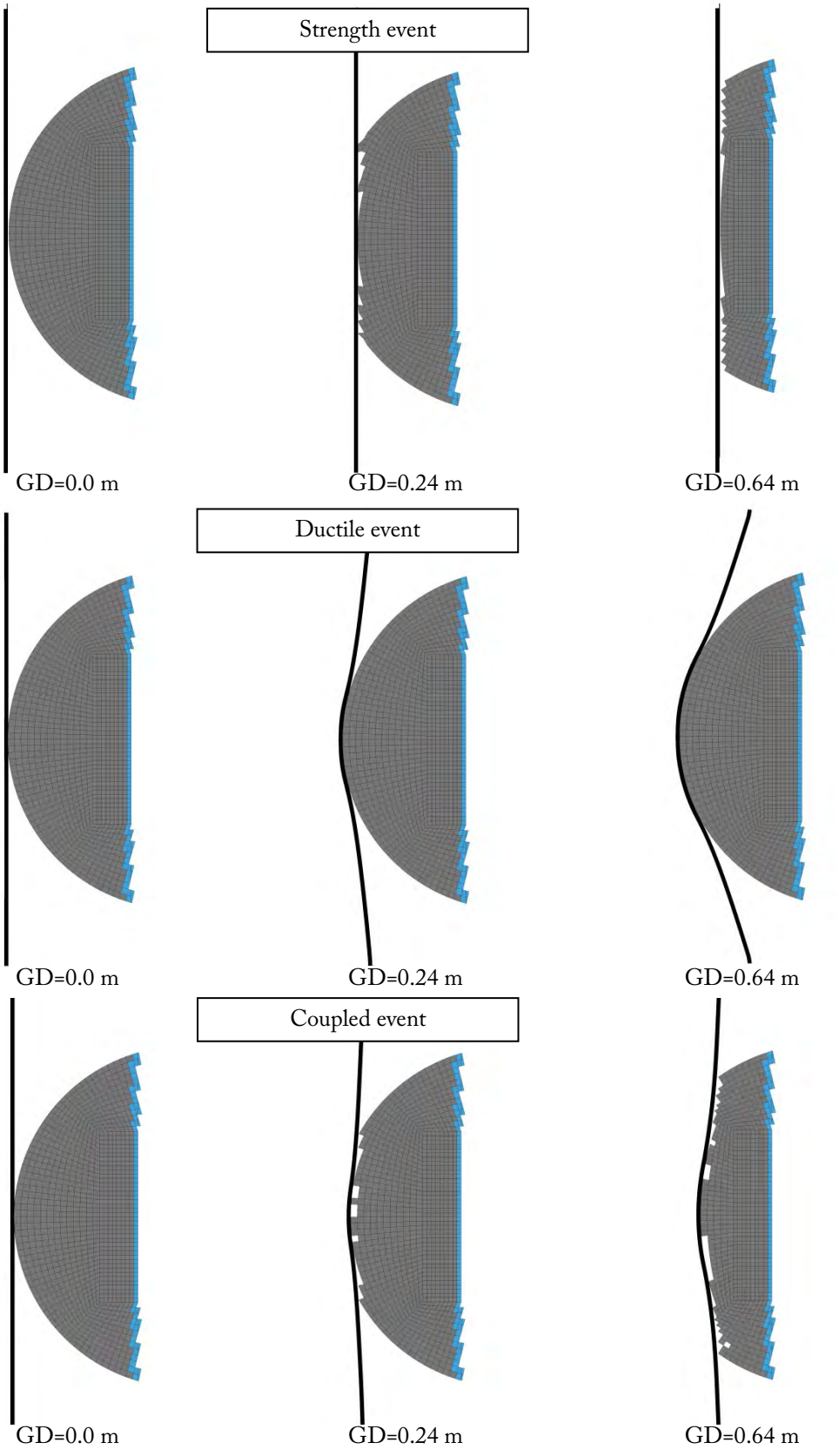

Figure 111: Process of ice-structure interaction; GD is the global displacement.

This process results in a force-displacement relationship that is close to that of the strength event. At 0.5 m, the contact area becomes too large, and the ice is so strong that the plate once again starts to deform. For the hard ice (Figure 110a), it is difficult to distinguish the periods of dominant ice crushing/plate deformations.

The force-displacement curves in Figure 110 illustrate that the coupled behavior of ice and the structure is characterized by the mutually dependent response of the ice and the structure. At a given moment, the instantaneously weaker ice or the structure will deform.

Another example of the damage predicted for a coupled event was discussed in Section 3.4 (i.e., the subsection entitled "Description of the impacted target" and the subsection "Comparison with numerical predictions"). The calculations were performed to plan the impact tests conducted at Aalto. All of the numerical simulations were conducted before the actual material parameters of ice and steel were determined. The numerical procedure used to access the structural damage was described in the subsection entitled "Description of the impacted target". The subection entitled "Comparison with numerical predictions" compares the numerical prediction to the experimental data for the maximum dents on the impacted panel. The deflection estimates obtained from the finite element analysis were consistent with the measurements (see discussion in Subsection "Comparison with numerical predictions").

4.3 Concluding remarks

The ice model evaluation was based on two ice geometries (a spherically shaped ice component with a diameter of 3.0 m and a hemispherical component with a diameter of 0.9 m). Based on the comparison between the numerical simulations and small-, medium- and full-scale data, improvements to the model are suggested and include the following:

1 A generalized version of the pressure-dependent strain-based failure-criterion.
2 A new alternative confinement-dependent, strain-based failure criterion to improve the physical understanding (or interpretation) of the model parameters.
3 An improved representation of physical ice behavior using the coupling between the FEM and SPH. However, uncertainties related to the implementation of the SPH method and the contact algorithm exist that must be further investigated.

An important aspect of the modifications was to introduce as few as possible "new" input material parameters but at the same time, provide users better control of the model performance.

Table 25. Summary of the ice model input.

Material constants	*Short description*
Ice density (kg/m^3) Elasticity modulus (Pa) Poisson's ratio (–)	Physical properties of the material
Yield condition a_0 (Pa^2) a_1 (Pa) a_2 (–)	Defines the boundaries of elastic behavior Input parameters are governed by the ice compressive, tensile and (or) shear strengths; see Equation (40). For a quasi-static analysis, the choice of these parameters may be based on the ice temperature and deformation rate.
Strain-based element erosion criteria (a) pressure-dependent ε_0, N, M (b) triaxiality-dependent n_1, n_2, n_3, n_4	Both criteria define how far the stress-state travels along the yield surface before element erosion occurs. Failure by splitting is suppressed (a) by using a U-shaped relationship between the failure strain and pressure or (b) by using a form of the generalized-logistic function to model decay of the failure strain with increasing triaxiality. The parameters for the element erosion criterion may be defined from a known pressure-area relationship.
Tensile pressure cut-off (Pa)	If one decides to take into consideration the effect of ice pressure melting under hydrostatic compression, the yield condition may become overly conservative for the stress states that are dominated by tension. The use of tensile pressure cut-off eliminates conservatism of the model. In this case, the tensile pressure cut-off may be set to the tensile strength of the ice for a given strain rate and temperature. For fine-grained polycrystalline ice at –7°C, Cammaert and Muggeridge (1988) report a value of approximately 2.0 MPa.
Ice-steel friction (–)	For a given ice material model and the chosen contact algorithm, the friction coefficient should be viewed as a default parameter rather than a physical quantity. Values other than 0.15 should be used with caution. Alternatively, the ice material parameters may be recalculated for a certain friction coefficient.

The design ice model is able to reproduce the Pond Inlet test (see work by Liu (2011)) and the pressure-area relationship from the Terry Fox trials (Ritch et al., 2008). The model was validated against the energy criterion that was established independently using data from the small and medium scales. The application of the model was

illustrated for two case studies: (1) the coupled behavior of ice/flexible structure at the engineering scale and (2) the coupled behavior of ice/stiffened panel at the laboratory scale.

The coupled FEM-SPH approach is a useful numerical technique for improving the spatial pressure distributions and perhaps a process pressure-area relationship for problems with insufficient mesh refinements. The visual impression of the ice crushing process is also improved by this approach. Because it is a numerical remedy to the great distortion of Lagrange meshes, the coupled FEM-SPH approach may be considered as a tool for reproducing a realistic spatial pressure-area relationship.

Application of damage mechanics might be considered as an alternative to the suggested improvements. In this case, the criterion for damage initiation might be based on the triaxiality ratio in which less plasticity is allowed before the initiation of damage for lower degrees of triaxiality/confinement. For simplicity, isotropic softening might be considered. For lower triaxiality values, less softening might be assumed (i.e., ductility increases with increasing confinement). Reduction in the remaining ductility might be assumed due to propagation of microcracks. Furthermore, a damage-based failure criterion might be chosen. In general, such implementation of a damage criterion is complex and will introduce additional input parameters. The difficulties in determining these parameters restricted the application of the damage mechanics in this work. However, the application of damage mechanics may be attractive because it might increase understanding of the qualitative nature of the ice failure process.

The following interpretation of the model input parameters is suggested; see Table 25. Note that the material constants may change during the life of a glacial ice mass as a result of various thermo-mechanical processes. Furthermore, the element erosion function is not a true material property.

Chapter 5

Conclusions and suggestions for future work

"Science, like art, is not a copy of nature but a re-creation of her."
Jacob Bronowski,
"Science and Human Values"

The current study has addressed the coupled behavior of ice and steel structures during collisions with a specific focus on situations in which the ice and the structure may undergo inelastic deformations simultaneously. An emphasis has been placed on the evaluation and improvement of the ice material model (including various failure criteria) for representation of the process of an extreme ice load on a steel structure during collisions (impact events). An existing continuum model for ice has applied and further developed. Furthermore, a new approach based on coupled FEM-SPH theories has been investigated with respect to improving the modeling of ice crushing (fragmentation). It has been realized that during collision, the structure may deform inelastically, encompass the ice mass and create conditions of ice confinement. In turn, the response of the confined ice is different from that of unconfined ice. Hence, for the scenarios in which the structure is allowed to deform inelastically, the response mechanism of ice should be viewed as a function of the structural response.

To verify the ice behavior under conditions of rapidly applied stresses and to increase our understanding of the physical processes taking place during an ice-structure impact, experimental studies were conducted at different scales (O[cm] and O[m] scales). The experimental investigations include small-scale laboratory indentation of freshwater granular and columnar S2 and S1 ice, drop tests of ice blocks on stiffened panels constructed of steel and laboratory experiments on collisions between ice blocks and a floating structure at a scale "mimicking" a full-scale collision. The experimental work has produced new fundamental knowledge of ice failure mechanisms that occur beneath the indenter, information on the behavior of crushed (powdered) ice in the absence of confinement and knowledge of energy absorption during ice crushing.

The knowledge from the experimental studies laid the foundation for the numerical studies and for further development of the ice model. Findings from the numerical studies may be integrated into a numerical model for the analysis of collisions between an ice mass and a floating steel-structure in the full-scale.

5.1 CONCLUSIONS

Despite differences in scales, similar patterns of ice failure behavior were observed in both small- and medium-scale tests, i.e., the visible presence of spalls, formation of fine powdery ice and its extrusion. It was found that ice appears to fail in the dominating brittle-like regime at higher indentation rates. Additional ice splitting was observed for events with higher collision energies. The damage to the structure observed in the laboratory ("hungry horse"-type deformations) mimics that of the full scale.

The small-scale laboratory ice indentation tests with a rigid indenter showed that during indentation, regions of Columbic and plastic faulting occur that are controlled by the degree of confinement. For freshwater granular ice at a temperature of –10°C, the transition between these two regimes occurs when the ratio between the minor and major principal stresses is approximately equal to 0.3. This observation is in agreement with earlier published data.

The crushed ice has greater mobility than the parent ice. It was found that the flow properties of unconfined crushed ice are primairly controlled by the contact forces between ice particles. Indeed, these forces depend on the particle size and contact duration. The experiments revealed that a slight change in the operation conditions (particle size and time) could effectively change the flow characteristic from highly cohesive to almost free flow.

A strong effect of confinement exists on the energy absorption capacity of ice. The experiments showed that confined ice subjected to global failure by suppressed splitting could absorb greater energy during crushing (approximately 17 kJ/kg). The calculations showed that the production of new free surfaces is not the major energy dissipation mechanism. The energy absorption capacity during crushing (fragmentation) of ice expresses a multi-scale character and can be considered as a parameter of the ice/indenter system. The energy absorption (J/kg or m^2/s^2) is independent of the interaction scenario; both the drop-weight tests and the indentation tests gave similar energies. Analysis of experimental data revealed that the energy absorption depends on the geometry, size and ice temperature. If the ice crystals are sufficiently small compared to the penetration depth and indenter size, and the sample size (width and thickness) is sufficiently large compared with the indenter size and the penetration depth, the energy absorption can be considered as a scale-independent and size-invariant characteristic. This work demonstrates that the energy absorption can be used as an additional validation criterion for the numerical models of collision between an ice mass and a structure.

Knowledge from the experimental studies was used to evaluate and further develop the ice material model for finite element analysis of isolated-ice-floe/structure collisions. Two different failure criteria were established and implemented in LS-DYNA 971: the

generalized strain-based, pressure-dependent criterion and as alternative, the strain-based, triaxiality-dependent criterion. A parametric study was performed to evaluate the model sensitivity to various key parameters. The varied parameters were the size of the yield surface, the shape and mathematical formulation of the failure curve and the coefficient of friction between ice and steel.

The study showed that the pressure-dependent and triaxiality-dependent criteria produce similar ice crushing loads. The most accurate reproduction of the target process pressure-area relationship was achieved by generalizing the one-parameter failure criterion to the three-parameter criterion; however, at each time instance, the spatial pressure distribution suffered from non-physical zones with zero contact-pressures. It is suggested to use a given, fixed value of the contact friction between ice and steel.

Coupling between SPH and FEM enabled improvement in the realization of the spatial pressure distribution and produced an improved visual impression of the crushing process compared with that of the conventional FEM with the element deletion technique. Good qualitative agreement was observed between the numerical simulations and experimental data in terms of clustering of high-pressure zones near the center of the contact zone. Based on the results of the numerical study, a physical interpretation of the model input parameters is proposed. The numerical procedure used to access damage to the structure due to collision with an ice mass is also suggested.

The attractiveness of the presented design-ice-model is that is rather simple and does not require sophisticated experimental procedures for validation of the input parameters.

5.2 SUMMARY OF ORIGINAL CONTRIBUTIONS

The primary objective of this dissertation, as stated in Chapter 1, has been achieved. The following contributions of this doctoral study to the fields of ice mechanics and ice-structure collision analysis are believed to be original:

1. Knowledge of the mechanisms governing the failure of ice beneath a spherically shaped indenter, i.e., the micromechanical processes underlying the indentation pressure as a function of penetration speed, penetration depth and the size of the indenter and the relevance to those processes at the larger scale (Section 3.1).
2. Knowledge of the flow properties of crushed (pulverized) ice in the absence of confinement, i.e., transition from non-cohesive to cohesive behavior and the role of cohesion and friction (Section 3.2).
3. A basis for the consideration of specific energy absorption during the ice crushing process as a scale-independent and size-invariant parameter of the ice/indenter system (Section 3.1, Subsection "Energy absorption capacity of ice during crushing"), and furthermore, a proposal of a new energy-based validation criterion for models of ice crushing (Section 4.1.4).

4. Experimental data for the development and validation of existing analytical and numerical models of full-scale ice mass/structure collisions in which both the ice and the structure can undergo inelastic deformations (Sections 3.3 and 3.4, recognizing that there is always room for improvement). It should be noted that hardly any experimental works exist and published on this topic.
5. Improvements to the numerical model of ice crushing for analysis of the coupled behavior of ice and the structure during collisions. Related items:

    5.1. Proposal of a generalized pressure-dependent, strain based-failure criterion.
    5.2. Proposal of an alternative, confinement-dependent, strain-based failure criterion.
    5.3. Proposal of coupling between the FEM and SPH to model the ice crushing process.
    5.4. Interpretation of model input parameters, including recommendations on how to determine them.

5.3 Recommendations for future work

Neither the work presented nor the conclusions put forth an end to the understanding of the coupled behavior of ice and the structure. One can always wish for a better model or better experimental data. Suggestions for continued improvement but not perfection are presented below.

History shows that rapid advancements in technology and constantly changing ice conditions eventually lead to an increase in the amount of ice-damage to the hulls of vessels. Hence, it is important to establish applicable design rules and methodologies, which means that the assumptions behind the various design formulations and associated design factors should be explicitly stated in the rules. With respect to the design of the offshore structures against rare and extreme ice actions, there is a strong need for improved design rules.

For the scenario of a collision with a free floating ice mass, in which the structure is allowed to deform inelastically, a need exists for detailed full-scale data on simultaneous inelastic deformations of the ice and the structure for validation, calibration and further development of non-linear numerical approaches and simplified analytical methods.

1. The coupled FEM-SPH approach should be studied further, and a study of the computational efficiency of this approach should be performed. For example, vectorization of the ice material subroutine or a limited SPH calculation domain might be considered. Incorporating damage mechanics into the ice model and

randomization of certain ice input parameters might also be considered as a tool to improve spatial pressure distribution.

2. A combination of FEM-DEM also should be investigated. Knowledge from angle-of-repose experiments can be used to validate the behavior of the powdered ice extruded during crushing or to determine the material parameters for DEM. To identify the material parameters of crushed (pulverized) ice under confinement, the information in Singh and Jordaan (1999) may be useful. However, a trade-off will be required between the model accuracy and simplicity.

3. No commonly accepted approach is available for characterizing the local ice shape. The question of how to parameterize the local/global ice shape and determine a structural layout should be addressed. The global ice shape is important for external mechanics, whereas the local ice shape is more important for internal mechanics. Different local/global ice shapes should be considered. The ice-shape sensitivity study is of particular interest. It is important to determine the most critical local ice shape for a given structural layout. The ice shape must be considered together with the structural layout.

4. For the ice model, only a preliminary validation against experiments at Aalto was conducted. To improve reliability of the model, additional research should be carried out in this direction. For example, the ice model (and numerical procedure) should be validated against the experimental data presented in Manuel et al. (2013). Alternatively, the modeling approach presented in Lee and Zhao (2013) and Gagnon and Wang (2012) could be checked against the collision scenario at Aalto.

5. In the tests at Aalto, only moderate damage to steel panels was observed. It would be useful to conduct tests with the steel panels that undergo larger deformations, even up to full plate rupture. In the new tests, an emphasis should be placed on improved fabrication of ice, more accurate shaping of ice blocks and improved instrumentation (i.e., the ability to record steel/ice deformations, dynamic contact-pressures).

6. Small-scale indentation of ice with a non-convex indenter should be performed to investigate whether the ice response mechanism will be altered by the additional confinement that is introduced. In addition, it would be interesting to arrange the experimental setup and instrumentation in a manner that allows recording of the crushing process at the ice/indenter interface using high-speed

video. The knowledge obtained from such tests could be vital in understanding of ice failure mechanisms.

7. The experimental studies have focused on laboratory-grown freshwater granular ice. However, ice of different origin exists, i.e., iceberg ice (of glacial origin), multiyear ice. The ice features may have different microstructures (size and shape of crystals, level of grain interlocking, presence of healed cracks, etc.), and hence, the ice properties may be different. Further experiments with ice of different origins should also be conducted.

References

ABAQUS (2007). Abaqus theory manual. Dassault Systmes.

Aldwinckle, D.S. & Lewis, K.J., 1984. Prediction of structural damage, penetration and cargo spillage due to ship collisions with icebergs. Proceedings of the 3rd International Conference on Icebreaking and Related Technologies.

Alsos, H.S., Amdahl, J. & Hopperstad, O.S., 2009. On the resistance to penetration of stiffened plates, Part II: Numerical analysis. International Journal of Impact Engineering 36 (7), 875–887.

Amdahl, J., 1983. Energy absorption in ship-platform impacts. Doctoral thesis, Department of Marine Technology, Norges Tekniske Høgskole, Trondheim.

AMSA, 2009. Arctic marine shipping assessment report. Arctic Council.

Appolonov, E.M., Didkovsky, A.V., Kuteinikov, A.M. & Nesterov, A.B., 2011. Improvement in design models for ice load evaluation under vessel impact against ice. Ships and Offshore Structures 6 (3), 249–256.

Arockiasamy, M., El-Tahan, H., Swamidas, A.S.J., Russell, W.E. & Reddy, D.V., 1984. Semisubmersible response to transient ice forces. Ocean Engineering 11 (5), 463–490.

Ashton, G.D., 1986. River and lake ice engineering. Water Resource Publications, Littleton, Colorado, 485p.

Barrette, P.D. & Jordaan, I., 2001. Beam bending and fracture behaviour of iceberg ice. PERD/CHC report 4-78, Ocean Engineering Research Center, Memorial University of Newfoundland.

Barrette, P.D. & Jordaan, I.J., 2003. Pressure-temperature effects on the compressive behaviour of laboratory-grown and iceberg ice. Cold Regions Science and Technology 36 (1–3), 25– 36.

Barrette, P., Pond, J. & Jordaan, J., 2002. Ice damage and layer formation in small-scale indentation experiments. Proceedings of the 16th IAHR International Symposium on Ice 3, 246–253.

Barrette, P., Pond, J., Li, C. & Jordaan, I., 2003. Laboratory-scale indentation of ice. PERD/CHC Report 4-81. St. John's, Canada.

Barnes, P. & Tabor, D., 1966. Plastic flow and pressure melting in the deformation of ice I. Nature 210 (5039), 878–882.

Bass, D. & Sen, D., 1986. Added mass and damping coefficient for certain “realistic” iceberg models. Cold Regions Science and Technology 12 (2), 163–174.

Bøhlerengen, S., 2013. Probabilistic material modeling of iceberg for analysis of accidental impacts with ships and offshore structures. Master thesis, Department of Marine Technology, Norwegian University of Science and Technology, Trondheim, Norway, 78p.

Browne, T., Taylor, R., Jordaan, I. & Gürtner, A., 2013. Small-scale ice indentation tests with variable structural compliance. Cold Regions Science and Technology 88, 2–9.

Brown, R. & Daley, C., 1999. Computer simulation of trans-verse ship-ice collisions. PERD/CHC Report 9-79 prepared for National Research Council of Canada.

Bruneau, S.E., 1996. Development of a first-year ridge keel load model. Doctoral thesis, Memorial University of Newfoundland, St. John's, Canada, 307p.

Bruneau, S.E., Cammaert, A.B. & Croasdale, K.R., 1994. Field tests for iceberg impact loading. Proceedings of the 12th International Symposium on Ice 1, 187–197.

Bruneau, S., Colbourne, B., Dragt, R., Dillenburg, A., Ritter, S., Pilling, M. & Sullivan, A., 2013. Laboratory indentation tests simulating ice-structure interactions using cone-shaped ice samples and steel plates. Proceedings of the 22nd International Conference on Port and Ocean Engineering under Arctic Conditions, Espoo, Finland, Paper POAC13_146.

Bruneau, S.E., Dillenbeurg, A.K. & Ritter, S., 2012. Ice sample production techniques and indentation tests for laboratory experiments simulating ship collisions with ice. Proceedings of the 22rd International Offshore, Ocean and Polar Engineering Conference. Paper ISOPE-2012-TCP-0104.

Bui, H.H., Fukagawa, R. Sako, K. & Wells, J.C., 2010. Slope stability analysis and discontinuous slope failure simulation by elasto-plastic smoothed particle hydrodynamics (SPH), Géotechnique 61 (7), 565–574.

Burg, J.P., Wilson, C.J.L. & Mitchell, J.C., 1986. Dynamic recrystallization and fabric development during the simple shear deformation of ice. Journal of Structural Geology 8 (8), 857–870.

Cammaert, A.B. & Muggeridge, D.B., 1988. Ice interaction with offshore structures. Van Nostrand Reinhold, New York, 432p.

Cammaert, A.B. & Tsinker, G.P., 1981. Impact of large ice floes and icebergs on marine structures. Proceedings of 6th International Conference on Port and Ocean Engineering under Arctic Conditions 2, 653–662.

Cammaert, A.B., Wong, T.T. & Curtis, D.D., 1983. Impact of icebergs on offshore gravity and floating platforms. Proceedings of 7th International Conference on Port and Ocean Engineering under Arctic Conditions 4, 519–536.

Carney, K.S., Benson, D.J., Du Bois, P. & Lee, R., 2006. A phenomenological high strain rate model with failure for ice. International Journal of Solids and Structures 43 (25–26), 7820–7839.

Carstensen, J.T. & Chan, P.C., 1976. Relation between particle size and repose angles of powders. Powder Technology 15 (1), 129–131.

Chen, S. & Baker, I., 2010. Structural evolution during ice-sphere sintering. Hydrological Processes 24 (14), 2034–2040.

Christensen, R.M., 1997. Yield functions/failure criteria for isotropic materials. Proceedings of the Royal Society A: Mathematical, Physical and Engineering Sciences 453 (1962), 1473–1491.

Chwang, A.T., 2003. Interaction hydrodynamics of two bodies. Proceedings of the 13th International Offshore and Polar Engineering Conference, Honolulu, Hawaii, USA.

Cunliffe, B., 2002. The extraordinary voyage of Pytheas the Greek. Walker & Co., New York, 195p.

Daley, G., 1984. BAFFIN – A dynamic ship/ice interaction model. Proceedings of the 3rd International Conference on Ice-breaking and Related Technologies, Calgary.

Daley, C.G., 2002. Derivation of plastic framing requirements for polar ships. Marine Structures 15 (6), 543–559.

Daley, C.G., 2007. Reanalysis of ice pressure-area relationships. Marine Technology 44 (4), 234–244.

Daley, C.G., 1994. Compilation of MSI tests results and comparison to ASPPR. Report by Daley R&E to National Research Council of Canada. Transport Canada Report TP 12151E.

Daley, C., 1999. Energy based ice collision forces. Proceedings of the 15th International Conference on Port and Ocean Engineering under Arctic Conditions 2, 674–686.

Daley, C. & Kim, H., 2010. Ice collision forces considering structural deformation. Proceedings of ASME 29th International Conference on Ocean, Offshore and Arctic Engineering (OMAE2010), Paper OMAE2010-20657.

Dempsey, J.P., Palmer, A.C. & Sodhi, D.S., 2001. High pressure zone formation during compressive ice failure. Engineering Fracture Mechanics 68 (17–18), 1961–1974.

de Souza Neto, E.A., Perić, D. & Owen, D.R.J., 2008. Computational Methods for Plasticity: Theory and Applications. John Wiley & Sons, Ltd., 814p.

Derradji-Aouat, A., 2003. Multi-surface failure criterion for saline ice in the brittle regime. Cold Regions Science and Technology 36 (1–3), 47–70.

DNV, 2011 Rules for Classification of Ships/High Speed, Light Craft and Naval Surface Craft, Part 2, Chapter 1, General requirements for materials. Det Norske Veritas.

DNV, 2011. Rules for Classification of Ships. Ships for Navigation in Ice. Det Norske Veritas.

DNV-RP-C204, 2010. Design against accidental loads. Recommended practice, Det Norske Veritas, Norway.

Doherty, R.D., Hughes, D.A., Humphreys, F.J., Jonas, J.J., Juul Jensen, D., Kassner, M.E., King, W.E., McNelley, T.R., McQueen, H.J. & Rollett, A.D., 1998. Current issues in recrystallization: A review. Materials Today 1 (2), 14–15.

ECON, 2007. Arctic shipping 2030: From Russia with oil, stormy Passage, or Arctic great game? Report 2007–070, Oslo.

Eicken, H., Gradinger, R., Salganek, M., Shirasawa, K., Perovich, D. & Leppäranta, M., 2009. Field techniques for sea-ice research. University of Alaska Press, Fairbanks, 588p.

El-Tahan, H., Swamidas, A.S.J. & Arockiasamy, M., 1988. Impact/indentation strength of iceberg and artificial snow ice. Journal of Offshore Mechanics and Arctic Engineering 110 (1), 87–93.

EPOA, 1971. Iceberg impact effects on drillship. Eastcoast Petroleum Operators' Association, Research project report no. 4 by FENCO and German & Milne.

ESA, 2013. Sea ice information for navigation and offshore operations. Retrieved from http://earth.esa.int/applications/data_util/hrisk/ice/ice.htm

Ettema, R. & Schaefer, J.A., 1986. Experiments on freeze-bonding between ice blocks in floating ice rubble. Journal of Glaciology 32 (112), 397–403.

Fischer-Cripps, A.C., 2000. Introduction to contact mechanics. Springer-Verlag New York, Inc., New York, 221p.

Faraday, 1859. XXIV. On regelation, and on the conservation of force. Philosophical Magazine Series 4 17 (113), 162–169.

Fish, A.M. & Zaretsky, Y.K., 1997. Ice strength as a function of hydrostatic pressure and temperature. CRREL Report 97-6. US Army Cold Regions Research and Engineering Laboratory, Hanover, 23p.

Flores-Johnson, E.A. & Li, Q.M., 2010. Indentation into polymeric foams. International Journal of Solids and Structures 47 (16), 1987–1995.

Foschi, R., Isaacson, M., Allyn, N. & Yee, S., 1996. Combined wave-iceberg loading on offshore structures. Canadian Journal of Civil Engineering 23, 1099–1110.

Frederking, R., 1998. The pressure area relation in the definition of ice forces. Proceedings of the 8th International Offshore and Polar Engineering Conference 2, 431–437.

Frederking, R., 1999. The local pressure-area relation in ship impact with ice. Proceedings of the 15th International Conference on Port and Ocean Engineering under Arctic Conditions 2, 687–696.

Frederking, R. & Barker, A., 2002. Friction of sea ice on steel for condition of varying speeds. Proceedings of 12th International Offshore and Polar Engineering Conference, Kitakyushu, Japan, 766–771.

Frederking, R., Jordaan, I.J. & McCallum, J.S., 1990. Field tests of ice indentation at medium scale Hobson's Choice ice island, 1989. Proceedings of the 10th International Symposium on Ice, Espoo, Finland, 931–944.

Fricke, W. & Bronsart, R. (Eds.), 2012. ISSC Committee V.6: Arctic technology, Proceedings of the 18th International Ship and Offshore Structures Congress, 243–274.

Fuglem, M.K., Muggeridge, K. & Jordaan, I., 1999. Design load calculations for iceberg impacts. Offshore and Polar Engineering 9 (4), 298–306.

Fuglem, M.K., Duthinh, D., Lever, J.H. & Jordaan, J., 1991. Probabilistic determination of iceberg collision design loads for floating production vessels. Proceedings of IUTAM-IAHR Symposium on Ice-Structure Interaction, 459–482.

FUJIFILM. Pressure Measuring Film. Instruction manual. Tokyo, Japan.

Fundamentals of Planetary Materials, 2013. Lecture notes. California Institute of Technology, Retrieved from http://www.gps.caltech.edu/classes/ge131/notes/Ch3.pdf

Gagnon, R.E. & Bugden, A., 2007. Ice crushing tests using a modified novel apparatus. Proceedings of the 19th International Conference on Port and Ocean Engineering under Arctic Conditions, 235–244.

Gagnon, R.E. & Gammon, P.H., 1995a. Triaxial experiments on iceberg and glacier ice. Journal of Glaciology, 41 (139), 528–540.

Gagnon, R.E. & Gammon, P.H., 1995b. Characterization and flexural strength of iceberg and glacier ice. Journal of Glaciology 41 (137), 103–111.

Gagnon, R.E. & Gammon, P.H., 1997. In situ thermal profiles and laboratory impact experiments on iceberg ice. Journal of Glaciology 43 (145), 569–582.

Gagnon, R.E., 1994. Generation of melt during crushing experiments on freshwater ice. Cold Regions Science and Technology 22 (4), 385–398.

Gagnon, R.E., 1999. Consistent observations of ice crushing in laboratory tests and field experiments covering three orders of magnitude in scale. Proceedings of the 15th International Conference on Port and Ocean Engineering under Arctic Conditions 2, 858–869.

Gagnon, R.E., 2004. Analysis of laboratory growler impact tests. Cold Regions Science and Technology 39 (1), 1–17.

Gagnon, R.E., 2007. Results of numerical simulations of growler impact tests. Cold Regions Science and Technology 49 (3), 206–214.

Gagnon, R.E, 2008a. Analysis of data from bergy bit impacts using a novel hull-mounted external Impact Panel. Cold Regions Science and Technology 52(1), 50–66.

Gagnon, R.E., 2008b. High-speed imaging of mechanisms responsible for sawtooth cyclic loading during ice-crushing. Proceedings of the 19th IAHR International Symposium on Ice 2, 983–991.

Gagnon, R.E., 2011. A numerical model of ice crushing using a foam analogue. Cold Regions Science and Technology 65 (3), 335–350.

Gagnon, R.E. & Mølgaard, J., 1991. Evidence for pressure melting and heat generation by viscous flow of liquid in indentation and impact experiments on ice. Annals of Glaciology 15, 254–260.

Gagnon, R.E. & Wang, J., 2012. Numerical simulations of a tanker collision with a bergy bit incorporating hydrodynamics, a validated ice model and damage to the vessel. Cold Regions Science and Technology 81, 26–35.

Garcia, N.B., Farrell, D. & Mellor, M., 1985. Ice penetration tests. Cold Regions Science and Technology 11 (3), 223–236.

Gately, D., Adelman M.A. & Griffin, J.M., 1986. Lessons from the 1986 oil price collapse. Brookings Papers on Economic Activity 2, 237–284.

Gold, L.W., 1977. Engineering properties of freshwater ice. Journal of Glaciology, 19 (81), 197–212.

Golding, N., Schulson, E.M. & Renshaw, C.E., 2010. Shear faulting and localized heating in ice: the influence of confinement. Acta Materialia 58 (15), 5043–5056.

Golding, N., Schulson, E.M. & Renshaw, C.E., 2011. Shear faulting and the ice-structure interaction problem. Proceedings of 21st POAC Conference, Paper 15, Montréal, Canada.

Goodman, D.J., 1980. Critical Stress Intensity Factor (KIc) Measurements at high loading rates for polycrystalline ice. Physics and Mechanics of Ice (Ed. P. Tryde), Springer-Verlad New-York Inc., 129–146.

Grace, I.M., 2011. Analytical and experimental investigations of ships impact interaction with one-side barrier. Doctoral thesis, Wayne State University, Detroit, USA.

Grape, J.A. & Schulson, E.M., 1992. Effect of confining stress on brittle indentation failure of columnar ice. International Journal of Offshore and Polar Engineering 2 (3), 212–221.

Greshunov, E.M., 1986. Collision of large floating ice feature with massive offshore structure. Waterways, Port, Coastal and Ocean Engineering 112 (3), 390–401.

Gudimelta, P.S.R., Colbourne, B., Daley, C., Bruneau, S.E. & Gagnon, R., 2012. Strength and pressure profiles from conical ice crushing experiments. Proceedings of the ICETECH Conference, Paper ICETECH12-132-RF.

Gudmestad, O.T, Løset, S, Alhimenko, A.I, Shkhinek, K.N, Tørum, A. & Jensen, A., 2007. Engineering aspects related to Arctic offshore developments. LAN St. Petersburg, 256p.

Gürtner, A., 2009. Experimental and numerical investigations of ice-structure interaction. Doctoral thesis, Department of Civil and Transport Engineering, Norwegian University of Science and Technology, Trondheim, Norway, 183p.

Hagan, J.T. & Swain, M.V., 1978. The origin of median and lateral cracks around plastic indents in brittle materials. Journal of Physics D: Applied Physics 11 (15), 2091–2102.

Hallquist, J., 2006. LS-DYNA theory manual. Livermore Software Technology Co.

Han, S., Lee, J.Y., Park, Y.I. & Che, J., 2008. Structural risk analysis of an NO96 membrane-type liquefied natural gas carrier in Baltic ice operation. Journal of Engineering for the Maritime Environment 222, 179–194.

Hänninen, S., 2005. Incidents and accidents in winter navigation in the Baltic Sea, winter 2002 – 2003. Technical Report Winter Navigation Research Board, Helsinki. Research Report no. 54.

Herodotus, The history of Herodotus (Tr. Macaulay, G.C.), London & New York: Macmillan, 1890.

Hilding, D., Forsberg, J. & Gürtner, A., 2011. Simulation of ice action loads on off shore structures. Proceedings of 8th European LS-DYNA User Conference, Strasburg, Germany.

Hill, B., 2005. Ship collisions with iceberg database, Report to PERD: Trends and analysis, TR-2005-17.

Hobbs, P.V., 1974. Ice Physics, Clarendon Press, Oxford, 837p.

Horrigmoe, G., Zeng, L.F. & Andersen, R., 1994. Modelling ductile behavior of columnar ice using computational plasticity. Proceedings of the 12th International Symposium on Ice, Trondheim, Norway, 282–291.

ISO 19904–1, 2006. Petroleum and natural gas industries – Floating structures - Part 1: Monohulls, semi-submersibles and spars. International Standardization Organization, Geneva, Switzerland.

ISO 19906, 2010. Petroleum and natural gas industries – Arctic offshore structures. International Standardization Organization, Geneva, Switzerland.

Jebaraj, C., Swamidas, A.S.J. & Jones, S.D., 1988. Dynamics of ship/ice interaction. Proceedings of International Conference on Technology for Polar Areas (Polar Tech) 1, 89–100.

Jefferies, M.G. & Wright, W.H., 1988. Dynamic response of Molikpaq to ice-structure interaction. Proceedings of the 7th International Conference on Offshore Mechanics and Arctic Engineering 4, 201–220.

Jennings, E., Grubbs, K., Zanis, C. & Raymond, L., 1991. SSC–364 inelastic deformation of plate panels. Technical report SR–1322, Ship Structure Committee.

Johannessen, O.M., Alexandrov, V., Frolov, I.Y., Sandven, S., Pettersson, L.H., Bobylev, L.P., Kloster, K., Smirnov, V.G., Mironov, Y.U. & Babich, N.G., 2007. Remote sensing of sea ice in the Northern Sea Route, studies and applications. Springer, 472p.

Johnson, K.L., 1985. Contact Mechanics. Cambridge University Press, Cambridge.

Johnson, R.C. & Nevel, D.E., 1985. Ice impact structural design loads. Proceedings of the 8th International Conference on Port and Ocean Engineering under Arctic Conditions 2, 569–578.

Johnston, M.E., Croasdale, K.R. & Jordaan, I.J., 1998. Localized pressures during ice-structure interaction: relevance to design criteria. Cold Regions Science and Technology 27 (2), 105–117.

Johnston, M., Timco, G.W. & Frederking, R., 2003. In situ borehole strength measurements on multi-year sea ice. Proceedings of 13th International Offshore and Polar Engineering Conference, Honolulu, Hawaii, USA, 445–452.

Jones, S.E. & Rule, W.K., 2000. On the optimal nose geometry for a rigid penetrator, including the effects of pressure-dependent friction. International Journal of Impact Engineering 24 (4), 403–415.

Jones, S.J. & Sinha, N.K., 1990. Crystallography of impacted ice. Proceedings of 10th International Symposium on Ice 2, 652–660.

Jones, S.J., 1978. Triaxial testing of polycrystalline ice. Proceedings of Third International Conference on Permafrost 1, 671–675.

Jones, S.J., 1982. The confined compressive strength of polycrystalline ice. Journal of Glaciology 20 (98), 171–177.

Jordaan, I.J., 2001. Mechanics of ice structure interaction. Engineering fracture mechanics 68 (17-18), 1923–1960.

Jordaan, I.J., Maes, M.A., Browne, P.W. & Hermans, I.P., 1993. Probabilistic analysis of local ice pressures. Journal of Offshore Mechanics and Arctic Engineering 115 (1), 83–89.

Jordaan, I., Taylor, R. & Derradji-Aouat, A., 2012. Scaling of flexural and compressive ice failure. Proceedings of the 31st International Conference on Ocean, Offshore and Arctic Engineering. Rio de Janeiro, Brazil, Paper OMAE2012-84033.

Jordaan, I.J. & Timco, G.W., 1988. Dynamics of the ice-crushing process. Journal of Glaciology 34 (118), 318–326.

Karr, D.G. & Das, S.C., 1983. Ice strength in brittle and ductile failure modes. Journal of Structural Engineering 109 (12), 2802–2811.

Kendall, K., 1978. Complexities of compression failure. Proceedings of the Royal Society A 362, 245–263.

Kennedy, F.E., Schulson, E.M. & Jones, D.E., 2000. The friction of ice on ice at low sliding velocities. Philosophical Magazine A 80 (5), 1093–1110.

Kheisin, D.E. & Likhomanov, V.A., 1973. Experimental determination of the specific energy of the mechanical ice crushing during impact. Problemy Arktiki i Antarktiki 41, 55–61 (in Russian).

Kheisin, D.E. & Cherepanov N.V., 1970. Change of ice structure in the zone of impact of a solid body against the ice cover surface. Problemy Arktiki i Antarktiki 34, 79–84 (in Russian).

Kierkegaard, H., 1993. Ship collisions with icebergs. Doctoral thesis, Department of Ocean Engineering, The Technical University in Denmark, 149p.

Kim, H., Daley, C. & Ulan-Kvitberg, C., 2012a. Reappraisal of pressure distribution induced by ice-structure interaction using high-precision pressure measurement film. ICETECH12-114.

Kim, E., Storheim, M., von Bock und Polach R. & Amdahl, J., 2012b. Design and modeling of accidental ship collisions with ice masses at laboratory scale. Proceedings of the 31st International Conference on Ocean Offshore and Arctic Engineering, 495–506.

Kim, E., Golding, N., Schulson, E.M., Løset, S. & Renshaw C.E., 2012c. Mechanisms governing failure of ice beneath a spherically shaped indenter. Cold Regions Science and Technology 78, 46–63.

Kim, E., Storheim, M., Amdahl, J., Løset, S. & von Bock und Polach, R., 2013. Drop test of ice blocks on stiffened panels with different structural flexibility. Proceedings of the 6th International Conference on Collision and Grounding of Ships and Offshore Structures, CRC Press, 241–250.

Kingery, W.D., 1960. Regelation, surface diffusion, and ice sintering. Journal of Applied Physics 31 (5), 833–838.

Kitami, E., Fujishima, K., Taguchi, Y., Nawata, T., Kawasaki, T. & Sakai, F., 1984. Iceberg collision with semisubmersible drilling unit. Proceedings of IAHR Ice symposium, 45–53.

Koehler, P.E. & Jorgensen, L., 1985. Ship impact analysis. Proceedings of 4th Symposium Offshore Mechanics and Arctic Engineering, 344–350.

Kolari, K., 2007. Damage mechanics model for brittle failure of transversely isotropic solids. Finite element implementation. Doctoral thesis. VTT Publications no. 628, Espoo, Finland, 195p.

Kormann, J.P. & Brown, T.G., 1990. A modified Nadreau yield function. Cold Regions Science and Technology 19 (1), 89–92.

Korzhavin, K.N., 2002. Action of ice on engineering structures. Books for Business, New York–Hong Kong, 319p.

Kujala, P. & Arughadhoss, S., 2012. Statistical analysis of ice crushing pressures on a ship's hull during hull-ice interaction. Cold Regions Science and Technology 70, 1–11.

Kujala, P. & Ehlers, S., 2013. Limit state identification for ice strengthened hull structures using measured long-term loads. Proceedings of the 22nd International Conference on Port and Ocean Engineering under Arctic Conditions.

Kuutti, J., Kolari, K. & Marjavaara, P., 2013. Simulation of ice crushing experiments with cohesive surface methodology. Cold Regions Science and Technology 62, 17–28.

Lachance, J. & Michel, B., 1987. Experimental study of the brittle behaviour of iceberg ice. Proceedings of the 9th International Conference on Port and Ocean Engineering under Arctic Conditions, 11–19.

Langhaar, H., 1951. Dimensional analysis and theory of models. John Wiley & Sons., 166p.

Laughlin, G.R., 1970. Failure analysis of clamped rectangular plates under idealized ice-loads. Thesis for Degree of Naval Engineer and Master of Science in Naval Architecture, Massachusetts Institute of Technology, 128p.

Lee, S.G. & Nguyen, H.A., 2011. LNGC collision response analysis with iceberg considering surrounding seawater. Proceedings of 21st International Offshore and Polar Engineering Conference, Hawaii, USA.

Lee, S.G. & Zhao, T., 2013. Structural safety assessment of LNGC CCS under iceberg collision using FSI analysis technique. Proceedings of the 23rd International Offshore and Polar Engineering Conference, Anchorage, Alaska, USA, 1145–1155.

Leppäranta, M., 2005. The drift of sea ice. Springer-Praxis, Heidelberg, Germany, 290p.

Li, Y. & Somorjai, G.A., 2007. Surface premelting of ice. Journal of Physical Chemistry C 111 (27), 9631–9637.

Li, C., Barrette, P. & Jordaan, I., 2004. High pressure zones at different scales during ice-structure indentation. Proceedings of ASME Conference, Vancouver, Canada, 887–894.

Libersky, L.D., Petschek, A.G., Carney, T.C., Hipp, J.R. & Allahdadi, F.A., 1993. High strain Lagrangian hydrodynamics: A three-dimensional SPH code for dynamic material response. Journal of Computational Physics 109 (1), 67–75.

Liferov, P. & Bonnemaire, B., 2005. Ice rubble behavior and strength: Part I. Review of testing and interpretation of results. Cold Regions Science and Technology 41 (2), 135–151.

Likhomanov, V., Stepanov, I., Frederking, R. & Timco, G.W., 1998. Comparison of results of impact tests on laboratory and natural freshwater ice with hydrodynamic model predictions. In Proceedings of the Eighth International Offshore and Polar Engineering Conference, 452–459.

Likhomanov, V.A. and Kheisin, D.E., 1971. Experimental investigation of solid body impact on ice, Problemy Arktiki i Antarktiki 38, 105–111 (in Russian).

Liu, Z., 2011. Analytical and numerical analysis of iceberg collisions with ship structures. Doctoral thesis, Department of Marine Technology, Norwegian University of Science and Technology, Trondheim, Norway, 160p.

Liu, Z., Amdahl J. & Løset S., 2011. Plasticity based material modelling of ice and its application to ship-iceberg impacts. Cold Regions Science and Technology 65 (3), 326–333.

Liukkonen, S. & Kivimaa, S., 1991. FE-modelling of ice failure load during ship bow indentation into multi-year ice. Research Reports 725, Technical Research Center of Finland, Espoo.

Lobanov, V.A., 2011. Numerical evaluation of ice vessel convenience. Strength. Vestnik nauchno-technicheskogo razvitiya 12 (52), (in Russian).

Løset, S. & Kvamsdal, T., 1994. Iceberg/structure interaction. Effects of ice temperature on the impact force. Proceedings of 12th IAHR International Symposium on Ice 1, 205–218.

Løset, S., Shkhinek, K.N., Gudmestad, O.T. & Høyland, K.V., 2006. Actions from ice on arctic offshore and coastal structures. LAN, St. Petersburg, 271p.

Lucy, L.B., 1977. A numerical approach to the testing of the fission hypothesis. The Astronomical Journal 82 (12), 1013–1024.

Lu, W., Løset, S. & Lubbad, R., 2012. Simulating ice-sloping structure interactions with the cohesive element method. Proceedings of the ASME 31st International Conference on Ocean, Offshore and Arctic Engineering, Rio de Janeiro, Brazil.

Määttänen, M., Marjavaara, P., Saarinen, S. & Laakso, M., 2011. Ice crushing tests with variable structural flexibility. Cold Regions Science and Technology 67, 120–128.

Mackey, T., Wells, J., Jordaan, I. & Derradji-Aouat, A., 2007. Experiments on the fracture of polycrystalline ice. Proceedings of 19th International Conference on Port and Ocean Engineering under Arctic Conditions. Dalian University of Technology Press, Dalian, China, 339–349.

Magidovich, I.P. & Magidovich, B.I., 1982. Studies of the history of geographical discoveries (Part I). Prosveshenie, Moscow, 286p. (in Russian).

Makarov, S.O., 1901. The Ermak in the ice fields: Description of the construction and voyages of the icebreaker Ermak and a summary of scientific results from the voyages. St. Petersburg, 507p. (in Russian).

Manuel, M., Gudimetla, P.S.R., Daley, C. & Colbourne, B., 2013. Controlled plastic deformation of a grillage using artificial freshwater ice at large scale. Proceedings of the 22nd International Conference on Port and Ocean Engineering under Arctic Conditions, Espoo, Finland, Paper POAC13_157.

Marchenko, A. & Chenot, C., 2009. Regelation of ice blocks in the water and on the air. Proceedings of 20th International Conference on Port and Ocean Engineering under Arctic Conditions, Paper 67, Luleå, Sweden.

Masterson, D.M. & Frederking, R.M.W., 1993. Local contact pressures in ship/ice and structure/ice interactions. Cold Regions Science and Technology 21 (2), 169–185.

Masterson, D.M., Frederking, R.M.W., Wright, B., Kärnä, T. & Maddock, W.P., 2007. A revised ice pressure–area curve. Proceedings of the 19th International Conference on Port and Ocean Engineering under Arctic Conditions. Dalian University of Technology Press, 305–314.

Matskevitch, D.G., 1997a. Eccentric impact of an ice feature: linearized model. Journal of Cold Regions Science and Technology 25 (3), 159–171.

Matskevitch, D.G., 1997b. Eccentric impact of an ice feature: non-linear model. Journal of Cold Regions Science and Technology 26 (1), 55–66.

Matsushi, M. Ikeda, J.-I., Kawakami, H. and Hirago, M., 1984. Ship-ice floe collision analysis considering the elastic deflection of hull girder. Proceedings of the 3rd International Conference on Icebreaking & Related Technologies, Calgary, Canada.

McKenna, R.F., 2004. Development of iceberg shape characterization for risk to Grand Banks installations, PERD/CHC Report 20-73, Canada.

McTaggart, K.A., 1989. Hydrodynamics and risk analysis of iceberg impacts with offshore structures. Doctoral thesis, The University of British Colombia.

Mellor, M., 1980. Mechanical properties of polycrystalline ice. Physics and Mechanics of Ice, IUTAM Symposium, Copenhagen, 217–245.

Michel, B. & Toussaint, N., 1977. Mechanisms and theory of indentation of ice plates. Journal of Glaciology 19 (81), 285–300.

Michel, B., 1978. Ice mechanics. Les Presses De L'Université Laval, Qubéc, 499p.

Moan, T., 2009. Development of accidental collapse limit state criteria for offshore structures. Structural Safety 31 (2), 124–135.

Monaghan, J.J., 1994. Simulating free surface flows with SPH. Journal of Computational Physics 110 (2), 399–406.

Montagnat, M., Durand, G. & Duval, P., 2009. Recrystallization processes in granular ice. Supplement Issue of Low Temperature Science 68, 81–90.

Moore, P.F., Jordaan, I.J. & Taylor, R.S., 2013. Explicit finite element analysis of compressive ice failure using damage mechanics. Proceedings of the 22nd International Conference on Port and ocean Engineering under Arctic Conditions, Espoo, Finland, Paper POAC13_121.

Mravak, Z., Rudan, S., Tryaskin, V. Coache, D. de Lauzon, J. & Dudal, A., 2009. Iceberg collision with offshore unit. Proceedings of the 20th International Conference on Port and Ocean Engineering under Arctic Conditions, Paper POAC09-140.

Nadreau, J.-P. & Michel, B., 1986. Yield and failure envelope for ice under multiaxial compressive stresses. Cold Regions Science and Technology 13 (1), 75–82.

Nansen, F., 1905. The Norwegian North polar expedition, 1893-1896; scientific results, Vol. 6. Christiania, 659p.

Nawata, T., Sakai, F., Imakubo, Y., Kawasaki, T. & Taguchi, Y., 1984. Iceberg collision for semi-submersible drilling unit. 西部造船会会報 68, 135–146 (In Japanese).

Neatby, L.H., 1958. In quest of the Northwest Passage. Apollo Editions, New York, 194p.

Nessim, M.A., Murray, A., Maes, M.A. & Jordaan, I.J., 1984. Risk analysis methodology for mobile offshore units operating in ice-fested waters. Proceedings of the 3rd International Conference on Icebreaking and Related Technologies.

Nesterov, A.B., 2010. Регламентация аварийной прочности крупнотоннажных арктических газовозов. Труды ЦНИИ им. акад. А.Н. Крылова 55, 5–20 (in Russian).

Noble, P.G., Tam,W.K., Menon, B. & Bayly, I.M., 1979. Ice forces and accelerations ona polar class icebreaker. Proceedings of 5th International Conference on Port and Ocean Engineering under Arctic Conditions 2, 1003–1022.

NORSOK N-004, 2004. Design of steel structures, Appendix A: Design against accidental actions. Standards, Norway.

Online Etymology Dictionary, 2013. Retrieved from http://www.etymonline.com/

Otsuka, M., Matsui, Y., Murata, K., Kato, Y. & Itoh, S., 2004. A study on shock wave propagation process in the smooth blasting technique. The 8th International LS-DYNA User Conference, Detroit.

Paikowsky, S.G. & Hajduk, E.L., 1997. Calibration and use of grid-based tactile pressure sensors in granular material. Geotechnical Testing Journal 20, 218–241.

Palmer, A. & Croasdale, K., 2013. Arctic offshore engineering. World Scientific Publishing Co. Pte. Ltd., Singapore, 357p.

Parameswaran, V.R. & Jones, S.J., 1975. Brittle fracture of ice at 77 K. Journal of Glaciology 14 (71), 305–315.

Petersen, M.J., & Pedersen, T., 1981. Collisions between ships and offshore platforms. Proceedings of the Offshore Technology Conference, 163–172.

Petrenko, V.F. & Gluschenkov, O., 1996. Crack velocities in freshwater and saline ice. Journal of Geographical Research 101 (B5), 11541–11551.

Petrenko, V.F. & Whitworth, R.W., 1999. Physics of Ice. Oxford University Press, Oxford, New York, 373p.

Petrovic, J.J., 2003. Review. Mechanical properties of ice and snow. Journal of Material Science 38, 1–6.

Pettersen, T., 2012, November 23. 46 vessels through Northern Sea Route. Retrieved from http://barentsobserver.com/en/arctic/2012/11/46-vessels-through-northern-sea-route-23-11

Pettersson, O., 1883. On the properties of water and ice. Vega-expeditionens vetenskapliga iakttagelser bearbetade af deltagare i reisan och andra forskare utgifna af A. E. Nordenskiöld, F. & G. Beijers Förlag, Stockholm, 516p.

Popov, Y.N. Faddeev, O.N. Kheisin, D.E. & Yakovlev, A.A., 1967. Strength of ships navigating in ice. Sudostroenie Publ. House: Leningrad, (in Russian).

Pounder, E.R., 1965. Physics of ice. Pergamon Press Ltd., Oxford, 151p.

Quinton, B.W.T., Daley, C.G. & Gagnon, R.E., 2012. Response of IACS URI ship structures to real-time full-scale operational ice loads. Proceedings of International Conference on Performance of Ships and Structures in Ice, Paper ICETECH12-125.

Ralph, F., McKenna, R. & Gagnon, R., 2008. Iceberg characterization for the bergy bit impact study. Cold Regions Science and Technology 52 (1), 7–28.

Reinicke, K.M. & Remer, R., 1978. A procedure for the determination of ice forces-illustrated for polycrystalline ice. Proceedings of the IAHR Symposium on Ice, 217–238.

Renshaw, C.E., Golding, N. & Schulson, E.M., 2011. Systematic experimental investigation of the impact of increasing confinement on shear faulting. 45th US Rock Mechanics/Geomechanics Symposium, San Francisco, Paper ARMA 11–336.

Renshaw, C.E. & Schulson, E.M., 2007. Limits on rock strength under high confinement. Earth and Planetary Science Letters 258 (1–2), 307–314.

Riska, K., 1980. On the role of failure criterion of ice in determining ice loads. Technical Research Centre of Finland, Ship Laboratory, Report no. 7, Espoo, 36p.

Riska, K. & Frederking, R., 1987. Modelling ice loads during penetration into ice. Transport Canada Report TP82337E. Espoo, Finland, 57p.

Riska, K. & Kämäräinen, J., 2011. A review of ice loading and the evolution of Finish-Swedish ice class rules. In SNAME Transactions, A24.

Ritch, R., Frederking, R., Johnston, M., Browne, R. & Ralph, F., 2008. Local ice pressures measured on a strain gauge panel during the CCGS Terry Fox bergy bit impact study. Cold Regions Science and Technology 52 (1), 29–49.

Runeberg, R., 1889. On steamers for winter navigation and ice-breaking. Minutes of the Proceedings 97 (2371), 277 – 301.

Ryvlin, A., 1973. Experimental study of ice friction. Proceedings of the Arctic and Antarctic Research Institute 309, 186–199 (in Russian).

Sand, B., 2008. Nonlinear finite element simulations of ice floes on offshore structures. Doctoral thesis. Department of Civil, Mining and Environmental Engineering, Luleå University of Technology, Luleå, Sweden, 241p.

Sanderson, T.J.O., 1988. Ice mechanics: risks to offshore structures. Graham & Trotman, 253p.

Sayed, M. & Frederking, R.M.W., 1992. Two-dimensional extrusion of crushed ice. Part 1: experimental. Cold Regions Science and Technology 21 (1), 25–36.

Sazonov, K.E., 2011. On modeling of impact processes in ice tank. Transactions of the Krylov Shipbuilding Research Institute 63, 27–34 (in Russian).

Schulson, E.M. & Duval, P., 2009. Creep and fracture of ice. Cambridge University Press, 416p.

Schulson, E.M., 2002. Compressive shear faults in ice: plastic vs. Coulombic faults. Acta Materialia 50 (13), 3415–3424.

Schulson, E.M., 2009. Fracture of ice and other Coulombic materials. In Mechanics of Natural Solids (Eds. D. Kolymbas and G. Viggiani), Springer, 177–202.

Schulson, E.M., 2013. Personal communication.

Serré, N., 2011. Mechanical properties of model ice ridge keels. Cold Regions Science and Technology 67 (3), 89–106.

Shafrova, S. & Høyland, K.V., 2008. The freeze-bond strength in first-year ice ridges. Small-scale field and laboratory experiments. Cold Regions Science and Technology 54 (1), 54–71.

Singh, S.K. & Jordaan, I.J., 1996. Triaxial tests on crushed ice. Cold Regions Science and Technology 24 (2), 153–165.

Singh, S.K. & Jordaan, I.J., 1999. Constitutive behavior of crushed ice. International Journal of Fracture 97 (1), 171–187.

Singh, S.K., Jordaan, I.J., Xiao, J. & Spencer, P.A., 1995. The flow properties of crushed ice. Journal of Offshore Mechanics and Arctic Engineering 117 (4), 276–282.

Skarżyński, Ł. & Tejchman, J., 2012. Determination of representative volume element in concrete under tensile deformation. Computers and Concrete 9 (1), 35–50.

Small, M., 2007. From jellied seas to open waterway: redefining the northern limit of the knowable world. Renaissance Studies 21 (3), 315–339.

Smirnov, V.N., 1996. Dynamic processes in sea ice. Gidrometeoizdat, St. Petersburg, 162p. (in Russian).

Smith, L.C. & Stephenson, S.R., 2013. New Trans-Arctic shipping routes navigable by midcentury. Proceedings of the National Academy of Sciences 110, E1191–E1195.

Smith, T.R. & Schulson, E.M., 1993. The brittle compressive failure of fresh-water columnar ice under biaxial loading. Acta Metallurgica et Materialia 41 (1), 153–163.

Sodhi, D.S., 1998. Nonsimultaneous crushing during edge indentation of freshwater ice sheets. Cold Regions Science and Technology 27 (3), 179–195.

Sodhi, D.S., 2001. Crushing failure during ice-stricture interaction. Engineering fracture mechanics 68 (17–18), 1889–1921.

Sodhi, D.S., Takeuchi, T., Nakazawa, N., Akagawa, S. & Saeki, H., 1998. Medium-scale indentation tests on sea ice at various speeds. Cold Regions Science and Technology 28 (3), 161–182.

Strabo, 1877. Geographica (Ed. Meineke, A., Strabonis Geographica), Leipzig, Teubner.

Suh. Y., Ito, H., Chun, S., Han, S., Choi, J. & Urm, H., 2008. Ice collision analyses for membrane tank type LNG carrier. Journal of Ship and Ocean Technology 12 (1), 35–44.

Sumiya, T., Suzuli, Y., Kasahara, T. & Ogata, H., 1998. Sensing stability and dynamic response of the F-Scan in-shoe sensing system: A technical note. Journal of Rehabilitation Research and Development 35 (2), 192–200.

Swamidas, A.S.J., Arockiasamy, M. & Reddy, D.V., 1983. Bergybit impact forces on a moored semisubmersible. Proceedings of the 7th International Conference on Port and Ocean Engineering under Arctic Conditions 4, 591-619.

Szabo, D. & Schneebeli, M., 2007. Subsecond sintering of ice. Applied Physics Letters 90, 151916.

Tangborn, A., Kan, S. & Tangborn, W., 1998. Calculation of the size of the iceberg struck by the oil tanker Overseas Ohio. Proceedings of 14th International IAHR Symposium on Ice, Potsdam, USA.

Taylor, J.R., 1997. An introduction to error analysis. University Science Books, 327p.

Taylor, K., King, P.J. & Swift, M.R., 2008. Influence of magnetic cohesion on the stability of granular slopes. Physical Review E 78 (3), 031304.

Taylor, R.S., Jordaan, I.J., Li, C. & Sudom, D., 2010. Local design pressures for structures in ice: analysis of full-scale data. Journal of Offshore Mechanics and Arctic Engineering 132 (3), 031502-1–7.

Tekscan, 2003. I-Scan equilibration and calibration practical suggestions. Tekscan, Inc. South. Boston, Massachusetts.

Tekscan, 2010. I-Scan and high-speed I-Scan user manual. Tekscan, Inc. South. Boston, Massachusetts.

Timco, G.W. & Frederking, R.M.W., 1982. Comparative strength of freshwater ice. Cold Regions Science and Technology 6 (1), 21–27.

Timco, G.W. & Frederking, R.M.W., 1986. The effect of anisotropy and microcracks on the fracture toughness (K_{IC}) of freshwater ice. Proceedings of the 5th International Offshore mechanics and Arctic Engineering Symposium, Tokyo, Japan.

Timco, G.W. & Frederking, R., 1990. Drop impact tests on freshwater ice: spherical head. Proceedings of the 10th IAHR Ice Symposium 2, 776–787.

Timco, G.W. & Frederking, R.M.W., 1995. Experimental investigations of the behavior of ice at the contact zone. In: Selvadurai, A.P.S., Boulon, M.J. (Eds.), Studies in Applied Mechanics. Elsevier, 35–55.

Timco, G.W., 2011. Isolated ice floe impacts. Cold Regions Science and Technology 68 (1–2), 35–48.

Timco, G.W., 1986. Indentation and penetration of edge-loaded freshwater ice sheets in the brittle range. Proceedings of 5th Offshore Mechanics and Arctic Engineering 4, 444–452.

Timco, G.W. & Weeks, W.F., 2010. A review of the engineering properties of sea ice, Cold Regions Science and Technology 60 (2), 107–129.

Tomas, J., 2003. Flow properties of cohesive nanopowders. China Particuology 1 (6), 231–241.

Tsai, S.W. & Wu, E.M., 1971. A general theory of strength for anisotropic materials. Journal of Composite Materials 5 (1), 58–80.

Tsuprik, V.G., 2013.The method of experimental study of the energy criterion of the sea ice failure. Requirements to the method and to the criterion. Proceedings of the 23rd International Offshore and Polar Engineering, Anchorage, 1098–1103.

Tuhkuri, J., 1994. Analysis of ice fragmentation process from measured particle size distributions of crushed ice. Cold Regions Science and Technology 23 (1), 69–82.

Tuhkuri, J., 1996. Experimental investigations and computational fracture mechanics modelling of brittle ice fragmentation. Acta Polytechnica Scandinavica, Mechanical Engineering Series no. 120, Helsinki, 105p.

Ulan-Kvitberg, C., Kim, H. & Daley, C., 2011. Comparison of pressure-area effects for various ice and steel indenters. Proceedings of the 21st International Offshore and Polar Engineering, 1048–1055.

Varsta, P., 1983. On the mechanics of ice load on ships in level ice in the Baltic Sea. Technical Research Centre of Finland, Publication no. 11, Espoo, Finland, 91p.

Vershinin, S.A., Truskov, P.A. & Kuzmichev, K.V., 2005. Ice action on constructions of Sakhalin shelf. Institut Giprostroimost, Moscow, 208p. (in Russian).

Vershinin, S.A., Truskov, P.A. & Liferov, P.A., 2008. Ice Action on seabed and subsea structures. Russkaya Kniga, Moscow, 228p.

Vinogradov, A.M., 1987. Constitutive modelling of ice. Proceedings of 6th International Conference on Offshore Mechanics and Arctic Engineering 4, 181–188.

Wadhams, P., 2000. Ice in the ocean. Gordon and Breach Science Publishers, Australia, 351p.

Wang, B., Yu, H.C. & Basu, R., 2008. Ship and ice collision modeling and strength evaluation of LNG ship structure. Proceedings of ASME 27th International Conference on Offshore Mechanics and Arctic Engineering, Paper OMAE2008-57134.

Weeks, W.F., 1962. Tensile strength of NaCl ice. Journal of Glaciology 4 (31), 25–52.

Weeks, W.F., 2010. On sea ice. University of Alaska Press, Fairbanks, 664p.

Wells, J., Jordaan, I., Derradji-Aouat, A. & Budgen, A., 2007. Laboratory investigation of the fracture behavior of polycrystalline ice with embedded monocrystals - Phase I. Report TR-2006-25.

Wells, J., Jordaan, I., Derradji-Aouat, A. & Taylor, R., 2011. Small-scale laboratory experiments on the indentation failure of polycrystalline ice in compression: main results and pressure distribution. Cold Regions Science and Technology 65 (3), 314–325.

Westmar, 2001. Load estimates for ship damage due to impact with icebergs. PERD/CHC Report 20-60, Westmar Consultants Inc. Vancouver, Canada.

Weiss, J. & Schulson, E.M., 1995. The failure of fresh-water granular ice under multiaxial compressive loading. Acta Metallurgica et Materialia 43 (6), 2303–2315.

Wouters, I.M.F. & Geldart, D., 1996. Characterising semi-cohesive powders using angle of repose. Particle and Particle Systems Characterization 13 (4), 254–259.

Yamaguchi, H., Derradji, A.A., Izumiyama, K. & Wilkman, G., 2002. The specialist committee on ice. Final report and recommendations to the 23rd ITTC. Proceedings of the 23rd International Towing Tank Conference–Volume 2.

Yang, W.H., 1980. Generalized Von Mises criterion for yield and fracture. Journal of Applied Mechanics, Transactions ASME 47 (2), 297–300.

Zubov, N.N., 1963. Arctic ice (Tr. by U.S. Navy Oceanographic Office and American Meteorological Society). San Diego, California, U.S. Navy Electronics Laboratory, 491p.

Appendix

A. *ANALYTICAL MODEL OF INDENTATION*

The deformation of ice loaded by an indenter is usually complex. A typical force displacement relationship is shown in Figure B1a (see indentation Test EK8 in Table 5).

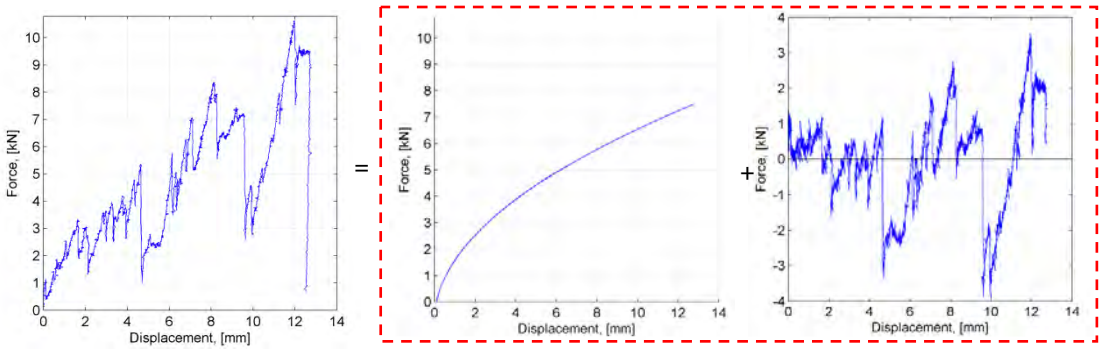

(a) (b) (c)

Figure B1: Force vs. displacement curves for the EK8 test.

The force in Figure B1a may be decomposed into the mean component (homogeneous, Figure B1b) and oscillatory component (localized behavior, Figure B1c), as shown in Figure B1. The mean component is the overall response of the bulk ice, whereas the oscillatory component is the localized response of ice (microcracking events, ejection of material, etc.). The frequency of the oscillations is related to the frequency of the local spalling events, and the amplitude of the oscillations is related to the size of the spalls. The theoretical model of indentation is presented below and describes the ice behavior in Figure B1a.

The indentation of ice is considered as schematically shown in Figure B2a.

We consider a rigid hemispherical indenter that normally penetrates a semi-infinite ice block. The cross-section of the indenter is shown in Figure B2a. Careful examinations of the indented ice specimens were performed. Figure B2b shows the damaged ice specimen after Test EK8. During indentation, a crushed zone (damage region) develops in the strong shear-compression zone below the contact. Macroscopically (cm- or m-scale), this deformation region may be treated as the inelastic zone, for example, see the phenomenological ice material model by Liu et al. (2011). However, at the mm-scale, the zone under the indenter may undergo recrystallization, shear (or plastic) faulting and microcracking or phase transformations. For a detailed discussion on the ice behavior in confined compression fields, see Schulson and Duval (2009). We assume that the forces involved in the indentation process are crushing, friction and splitting forces.

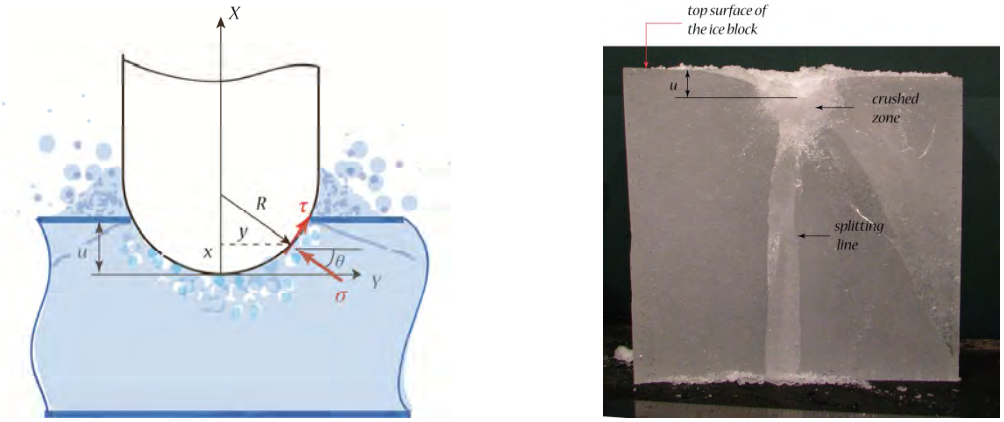

(a) (b)

Figure B2: (a) Schematics of the cross-section of the hemispherical indenter and (b) the photograph of the ice damage for Test EK8; σ is the normal pressure, τ is the friction force per unit area due to sliding and u is the penetration distance.

The shape function of the contact region between the indenter and the top ice surface is

$$y = y(x) = \begin{cases} \sqrt{R^2 - (R-x)^2}, & x \in [0, R) \\ R, & x \geq R \end{cases} \tag{B1}$$

where R is the radius of the indenter.

A similar indentation problem was treated earlier by Jones and Rule (2000). The coordinate system and notation used in Jones and Rule (2000) are used in this work with minor changes. The incremental force resisting the motion of the indenter can be expressed as

$$dF = 2\pi y(\sigma \sin\theta + \tau \cos\theta) ds\,, \tag{B2}$$

where ds is the increment of arc length on the surface of the indenter.

$$ds = \sqrt{dx^2 + dy^2} = \sqrt{1 + \frac{dy^2}{dx^2}}dx = \sqrt{1 + (\tan\theta)^2}\,dx \tag{B3}$$

Substituting Equation (B3) into Equation (B2), the increment force is rewritten as

$$dF = 2\pi y\left(\sigma \frac{\tan\theta}{\sqrt{1+(\tan\theta)^2}} + \tau \frac{1}{\sqrt{1+(\tan\theta)^2}}\right) ds = 2\pi y\left(\sigma \frac{dy}{dx} + \tau\right) dx$$

$$F = \int_o^u 2\pi y \sigma \frac{dy}{dx} dx + \int_o^u (2\pi y \tau) dx = F_{crushing} + F_{friction} \tag{B4}$$

Because the total resistance consists of the ice resistance against crushing, the ice resistance against splitting and the ice resistance against sliding (frictional resistance), we can write

$$F_{total} = F_{crushing} + F_{friction} + F_{splitting} \tag{B5}$$

The mechanics of crack initiation in ice are complex. Macroscopically (mm-scale), considering the microstructural features (residual internal stresses, trapped air, etc.), freshwater ice is a heterogeneous material, and inclusions of trapped air may act as weak internal interfaces. For simplicity, we assume that the splitting fracture begins from the edges of the indenter, and the fracture propagates downwards by flaring outward.

The splitting force can be defined as in Flores-Johnson and Li (2010)

$$\begin{aligned} dF_{splitting} &= 2\pi\Gamma \tan\theta \, dx \\ F_{splitting} &= \int_o^u 2\pi\Gamma \tan\theta \, dx \end{aligned} \tag{B6}$$

where Γ is the splitting energy per unit area. The value of Γ=0.109 J/m^2 was used by Michel (1978) and corresponds to the surface energy of ice in contact with its saturated vapor, and Γ=0.8 J/m^2 was used by Jordaan and Timco (1988) to access the energy of a fine grained (1–2 mm) columnar S2 ice crushing. For purely brittle fracture, Schulson and Duval (2009) reported Γ=0.138–0.218 J/m^2. Goodman (1980) estimated Γ=1.38 J/m^2 from the mode-I stress intensity factor and Young's modulus.

We assume that the friction is proportional to the normal stress

$$\tau = \mu\sigma \tag{B7}$$

For simplicity, the normal stress can be assumed to be relatively constant and equal to σ_c=11 MPa, and μ is the coefficient of static friction. The value for sea ice-steel, μ=0.2, was adopted from Frederking and Barker (2002). At −10°C, the friction coefficient ranges between μ=0.1 and μ=0.6 (Schulson and Duval, 2009).

Substituting Equation (B1) into Equations (B4) and (B6) and taking into account Equation (B7), we obtain

$$F_{crushing} = 2\pi\sigma_c \int_0^u (R-x)dx = \pi\sigma_c (R^2 - (R-u)^2) \tag{B8}$$

$$F_{splitting} = 2\pi\Gamma \int_0^u (2Rx - x^2)^{-0.5} (R-x)dx \tag{B9}$$

$$F_{friction} = 2\pi\mu\sigma_c \int_0^u (2Rx - x^2)^{0.5} dx \tag{B10}$$

The resistance force corresponding to Equation (B5) for μ=0.2, σ_c=11 MPa and Γ=0.1 J/m^2 is plotted in Figure B3. In Figure B3, the result of the calculations is compared with the experimental data.

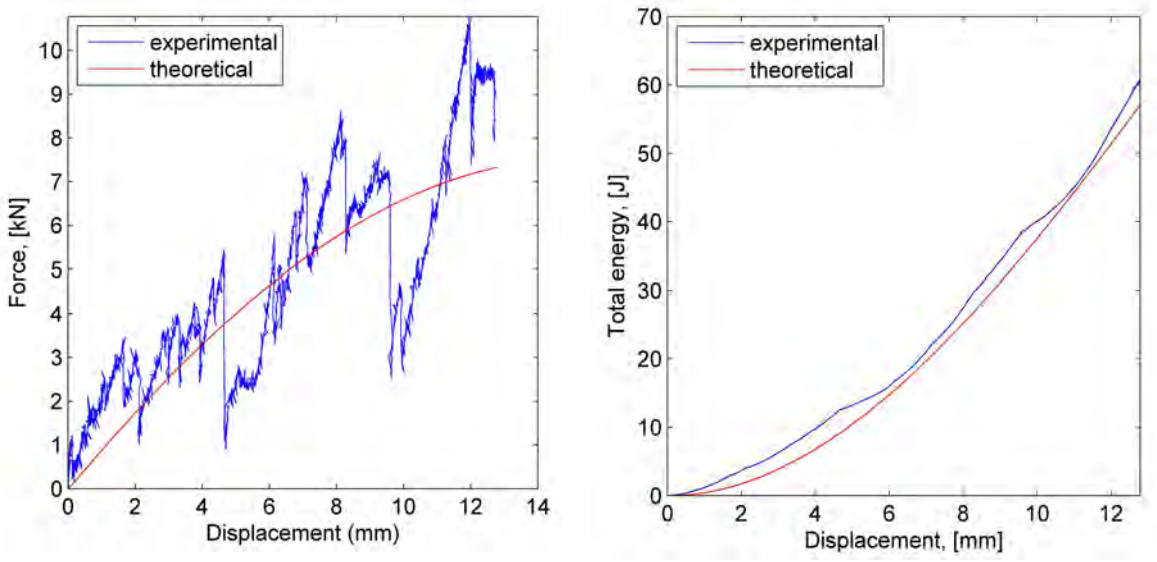

Figure B3: Comparison of the experimental- and analytical results for Test EK8. The total energy is calculated as an integral of the indentation force over the displacement range (σ_c=11 MPa, μ=0.2, Γ=0.1 J/m^2).

The crushing force appears to be a dominating force. If we only consider the crushing component of the force in Equation (B5), the selected value of σ_c=15 MPa gives the total force that satisfactory resembles the force-displacement curve for Test EK8. For comparison, the maximum contact pressures reported in Kheisin and Likhomanov (1973) are in the range of 4 MPa to 18 MPa.

The total crushing energy becomes

$$\Psi_{crushing} = \int_0^u F_{crushing} du = \pi\sigma_c R u^2 - \frac{1}{3}\pi\sigma_c u^3 \tag{B11}$$

For small contact areas, we assume geometric similarity and the following relationship between the prototype (p) and the model (m)

$$\sigma_c^{(p)} = \sigma_c^{(m)}; \rho^{(p)} = \rho^{(m)}; R^{(p)} = \lambda R^{(m)}; u^{(p)} = \lambda u^{(m)} \tag{B12}$$

Combining Equations (B11) and (B12), we rewrite the relationship between the energy in the prototype and in the model as

$$\frac{\Psi_{crushing}^{(p)}}{\Psi_{crushing}^{(m)}} = \frac{\sigma_c^{(p)} u^{2(p)} \left(R^{(p)} - 1/3\, u^{(p)} \right)}{\sigma_c^{(m)} u^{2(m)} \left(R^{(m)} - 1/3\, u^{(m)} \right)} = \lambda^3 \tag{B13}$$

Combining Equation (B11) and the expression for specific energy absorption (ε), we obtain

$$\varepsilon^{(p)} = \varepsilon^{(m)} = \frac{\sigma_c}{\rho} = \frac{15 \text{ MPa}}{900 \text{ kg/m}^3} \cong 1.7 \cdot 10^4 \text{ J/kg} \tag{B14}$$

The specific energy absorption was defined as the energy absorbed per unit mass of the crushed material.

B. *YIELD SURFACE. PARAMETRIC STUDY*

The yield surface used by Liu (2011) can be viewed as a special case of the yield surface for anisotropic materials proposed by Tsai and Wu (1971) or as an extension of the Von Mises criterion for granular ice (Riska, 1980). The general form of the Tsai-Wu surface is written in the stress–space as

$$F(\boldsymbol{\sigma}) = A_i \sigma_i + A_{ij} \sigma_i \sigma_j = 1 \tag{B15}$$

where A_i and A_{ij} are the so-called "interactive strength terms" and are the components of strength tensors $\mathbf{A}^*$ and $\mathbf{A}$, respectively; i, j=1, 2,…6. Equation (B15) may be expanded as

$$\begin{aligned} &A_1\sigma_1 + A_2\sigma_2 + A_3\sigma_3 + A_4\sigma_4 + A_5\sigma_5 + A_6\sigma_6 \\ &+ A_{11}\sigma_1^2 + A_{22}\sigma_2^2 + A_{33}\sigma_3^2 + A_{44}\sigma_4^2 + A_{55}\sigma_5^2 + A_{66}\sigma_6^2 \\ &+ 2A_{12}\sigma_1\sigma_2 + 2A_{13}\sigma_1\sigma_3 + 2A_{14}\sigma_1\sigma_4 + 2A_{15}\sigma_1\sigma_5 + 2A_{16}\sigma_1\sigma_6 \\ &+ 2A_{23}\sigma_2\sigma_3 + 2A_{24}\sigma_2\sigma_4 + 2A_{25}\sigma_2\sigma_5 + 2A_{26}\sigma_2\sigma_6 \\ &+ 2A_{34}\sigma_3\sigma_4 + 2A_{35}\sigma_3\sigma_5 + 2A_{36}\sigma_3\sigma_6 + 2A_{45}\sigma_4\sigma_5 + 2A_{46}\sigma_4\sigma_6 + 2A_{56}\sigma_5\sigma_6 = 1 \end{aligned} \tag{B16}$$

The ice yield function in Liu (2011) reads $F(p, J_2) = J_2 - a_0 - a_1 p - a_2 p^2 = 0$, where

$$J_2 = \frac{1}{6}\left[(\sigma_1 - \sigma_2)^2 + (\sigma_2 - \sigma_3)^2 + (\sigma_1 - \sigma_3)^2 \right] + \sigma_4^{\,2} + \sigma_5^{\,2} + \sigma_6^{\,2} \tag{B17}$$

$$p = \frac{\sigma_1 + \sigma_2 + \sigma_3}{3}$$

In the stress-space, Liu's function is written as

$$-\frac{1}{3}\frac{a_1}{a_0}(\sigma_1+\sigma_2+\sigma_3)+\left(\frac{1}{3}\frac{1}{a_0}-\frac{1}{9}\frac{a_2}{a_0}\right)(\sigma_1^2+\sigma_2^2+\sigma_3^2)-\ldots$$
$$\ldots\left(\frac{1}{3}\frac{1}{a_0}+\frac{2}{9}\frac{a_2}{a_0}\right)(\sigma_1\sigma_2+\sigma_2\sigma_3+\sigma_1\sigma_3)+\frac{1}{a_0}\left(\sigma_4^2+\sigma_5^2+\sigma_6^2\right)=1 \qquad \text{(B18)}$$

For isotropic ice, the Tsai-Wu strength terms A_i and A_{ij} may be expressed via material constants a_0, a_1 and a_2 and related to the ice strengths.

$$A_i\sigma_i+A_{ij}\sigma_i\sigma_j-1=J_2-a_0-a_1p-a_2p^2 \qquad \text{(B19)}$$

From Equation (B19) we obtain

$$A_1=A_2=A_3=-\frac{1}{3}\frac{a_1}{a_0}$$
$$A_{11}=A_{22}=A_{33}=\frac{1}{3}\frac{a_1}{a_0}-\frac{1}{9}\frac{a_2}{a_0};A_{44}=A_{55}=A_{66}=\frac{1}{a_0}$$
$$2A_{12}=2A_{13}=2A_{23}=-\left(\frac{1}{3}\frac{1}{a_0}+\frac{2}{9}\frac{a_2}{a_0}\right) \qquad \text{(B20)}$$
$$A_{44}=2(A_{22}-A_{23})=\frac{1}{a_0}$$

All other interactive strength terms are zero. Hence, $\mathbf{A}^*$ and $\mathbf{A}$ become

$$\mathbf{A}^*=\begin{Bmatrix}-\frac{1}{3}\frac{a_1}{a_0}\\-\frac{1}{3}\frac{a_1}{a_0}\\-\frac{1}{3}\frac{a_1}{a_0}\\0\\0\\0\end{Bmatrix} \qquad \mathbf{A}=\begin{bmatrix}\frac{1}{3}\frac{1}{a_0}-\frac{1}{9}\frac{a_2}{a_0} & -\frac{1}{2}\left(\frac{1}{3}\frac{1}{a_0}+\frac{2}{9}\frac{a_2}{a_0}\right) & -\frac{1}{2}\left(\frac{1}{3}\frac{1}{a_0}+\frac{2}{9}\frac{a_2}{a_0}\right) & 0 & 0 & 0\\ & \frac{1}{3}\frac{1}{a_0}-\frac{1}{9}\frac{a_2}{a_0} & -\frac{1}{2}\left(\frac{1}{3}\frac{1}{a_0}+\frac{2}{9}\frac{a_2}{a_0}\right) & 0 & 0 & 0\\ & & \frac{1}{3}\frac{1}{a_0}-\frac{1}{9}\frac{a_2}{a_0} & 0 & 0 & 0\\ & & & \frac{1}{a_0} & 0 & 0\\ & sym & & & \frac{1}{a_0} & 0\\ & & & & & \frac{1}{a_0}\end{bmatrix}$$

The Tsai-Wu stability conditions of the strength tensor $\mathbf{A}$ (that ensure that the ellipsoidal yield surface intercepts each stress axis) become

$$a_0>0$$
$$\frac{1}{3}\frac{1}{a_0}-\frac{1}{9}\frac{a_2}{a_0}>0 \;\Rightarrow a_2<3.0 \qquad \text{(B21)}$$
$$\left(\frac{1}{3}\frac{1}{a_0}-\frac{1}{9}\frac{a_2}{a_0}\right)^2-\left(\frac{1}{2}\right)^2\left(\frac{1}{3}\frac{1}{a_0}+\frac{1}{9}\frac{a_2}{a_0}\right)^2>0 \;\Rightarrow a_2<0.75$$

The magnitude of the uniaxial compression strength of ice (σ_c) is considered to be larger than the magnitude of the uniaxial tensile strength of ice (σ_t).

$$\sigma_c = \frac{\frac{1}{3}\frac{a_1}{a_0} + \sqrt{\left(\frac{1}{3}\frac{a_1}{a_0}\right)^2 + 4\left(\frac{1}{3}\frac{1}{a_0} - \frac{1}{9}\frac{a_2}{a_0}\right)}}{2\left(\frac{1}{3}\frac{1}{a_0} - \frac{1}{9}\frac{a_2}{a_0}\right)};\ \sigma_t = \frac{\frac{1}{3}\frac{a_1}{a_0} - \sqrt{\left(\frac{1}{3}\frac{a_1}{a_0}\right)^2 + 4\left(\frac{1}{3}\frac{1}{a_0} - \frac{1}{9}\frac{a_2}{a_0}\right)}}{2\left(\frac{1}{3}\frac{1}{a_0} - \frac{1}{9}\frac{a_2}{a_0}\right)}$$

$$A_{11} = -\frac{1}{\sigma_c}\frac{1}{\sigma_t};$$

$$A_1 = \frac{1}{\sigma_c} + \frac{1}{\sigma_t} \qquad \text{(B22)}$$

The shear strength derived from a direct simple shear test

$$\tau = \sqrt{a_0}$$

$$A_{44} = \frac{1}{\tau^2} \qquad \text{(B23)}$$

$$A_{23} = A_{22} - \frac{A_{44}}{2} = -\frac{1}{\sigma_c}\frac{1}{\sigma_t} - \frac{1}{2}\frac{1}{\tau^2}$$

For multiyear ice, Timco and Weeks (2010) gave the values of tensile ice strength in the range of 0.5–1.5 MPa, τ=0.2–4 MPa for the shear strength and σ_c=6–10 MPa for the uniaxial compressive strength for freshwater ice (Ashton, 1986). In current parametric study, σ_t =–1.0 MPa, τ =2.0 MPa and σ_c=8.0 MPa were selected and represent the iceberg ice at a temperature near –10°C and deformation rates greater than 10^{-3} m/s.

From Equations (B20) and (B22), parameters a_0, a_1 and a_2, corresponding to the ice strengths, are

$$a_0 = \tau^2; a_1 = -3a_0\left(\frac{1}{\sigma_c} + \frac{1}{\sigma_t}\right); a_2 = 9a_0\left(\frac{1}{\sigma_t}\frac{1}{\sigma_c} + \frac{1}{3a_0}\right); \qquad \text{(B24)}$$

The effects of shear, compressive and tensile ice strength on the yield curve are shown in Figures B4, B5 and B6, respectively. The curve from Kierkegaard (1993) is also shown in the figures for a_0 =2.588 MPa^2, a_1=8.63 MPa and a_2=–0.163. This situation corresponds to ice strengths of $\sigma_t \approx$ –0.82 MPa, $\tau \approx$ 1.61 MPa and $\sigma_c \approx$ 9.0 MPa.

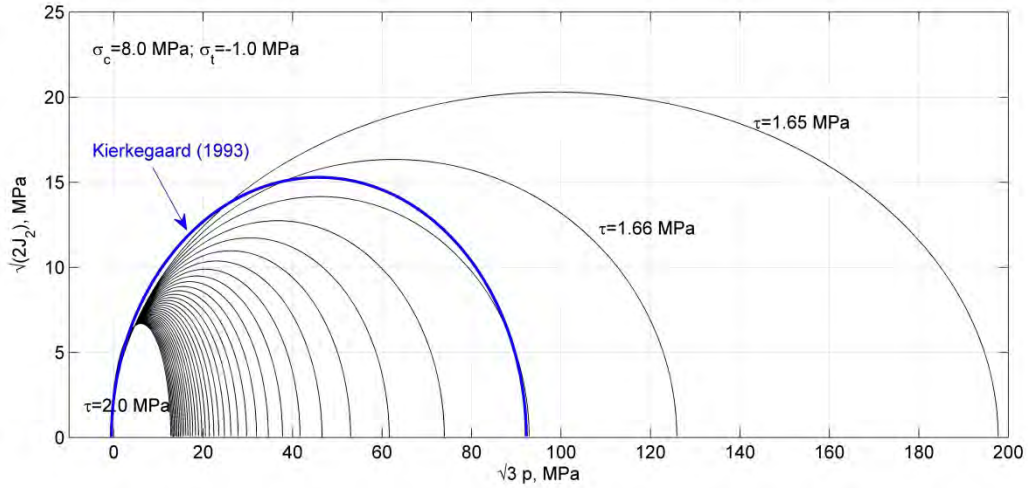

Figure B4: Effect of ice shear strength; $\Delta\tau$=0.01 MPa.

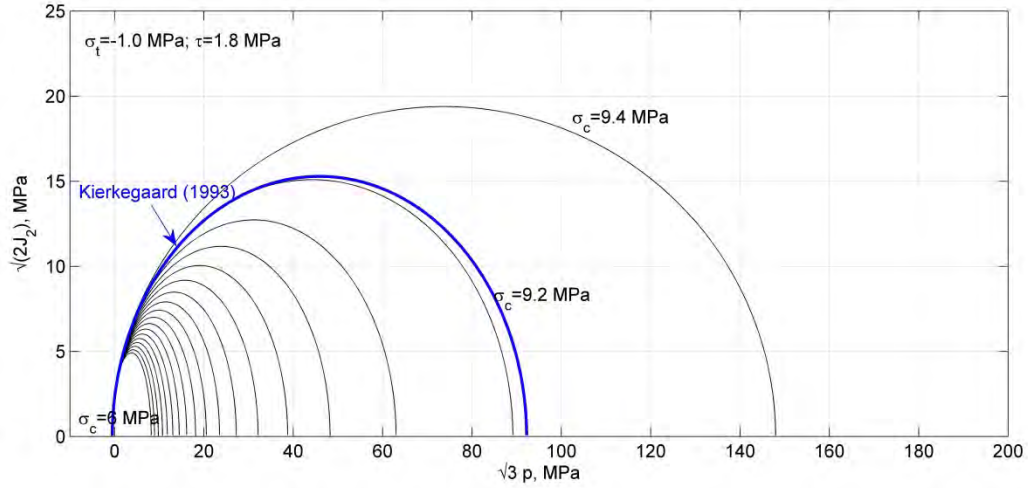

Figure B5: Effect of ice compressive strength; $\Delta\sigma_c$=0.2 MPa.

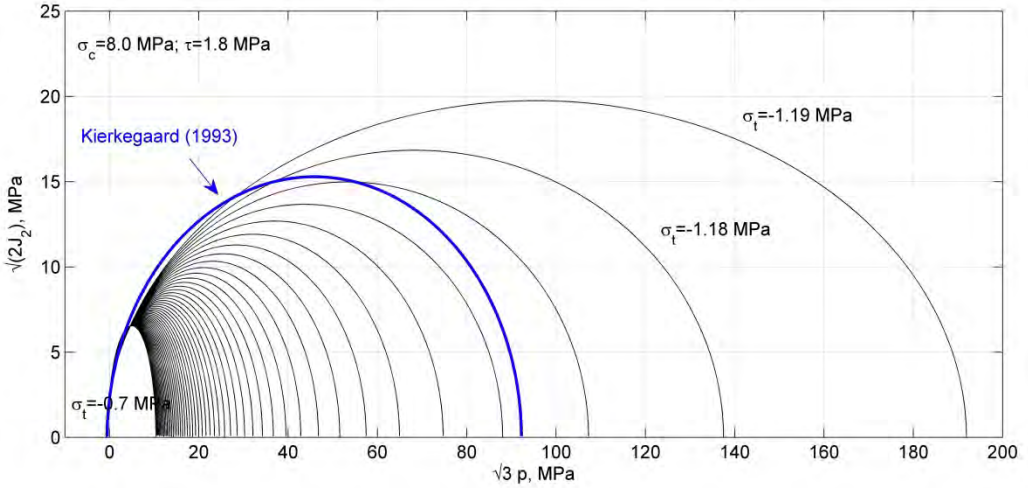

Figure B6: Effect of ice tensile strength; $\Delta\sigma_t$=0.01 MPa.

From Figures B4, B5 and B6, one may conclude that the pressure-softening component of the yield curve is affected more than the pressure-hardening component. For example, the magnitude of pressure required to bring the ice to the melting point

(i.e., the pressure at J_2 =0.0 MPa^2) will be significantly affected by a slight variation of the shear, compressive, or tensile ice strength. For ice at a temperature of T=–10°C, one can estimate the magnitude of the ice melting pressure p^*=–T/0.074=135 MPa (Schulson and Duval, 2009). However, melting itself requires heat known as the heat of fusion, and for ice, it is equal to 333.55 kJ/kg. There is insufficient evidence, i.e., experimental data (see, e.g., Fish and Zaretsky (1997)), to solidly conclude that the yield surface should narrow to a point (an equilibrium melting point) on the hydrostatic axis. For practical use of the yield function, a focus on the calibration of accurate values of ice strengths is recommended rather than on the ice-melting pressure.

C. *ESTIMATION OF ICE PRESSURE DURING IMPACT*

The use of simplified analytical methods requires knowledge of the loading patch and the pressure distribution within this area during impact. Due to high uncertainties related to ice (homogeneity, integrity of ice at the impact zone, constitutive behavior of the laboratory-grown ice), it is not possible to determine the ice pressure distribution accurately. Therefore, a uniform pressure within the contact area may be assumed (Figure C1).

Experimental data of ice indentation may be used to estimate average pressure applied to the area in Figure C1.

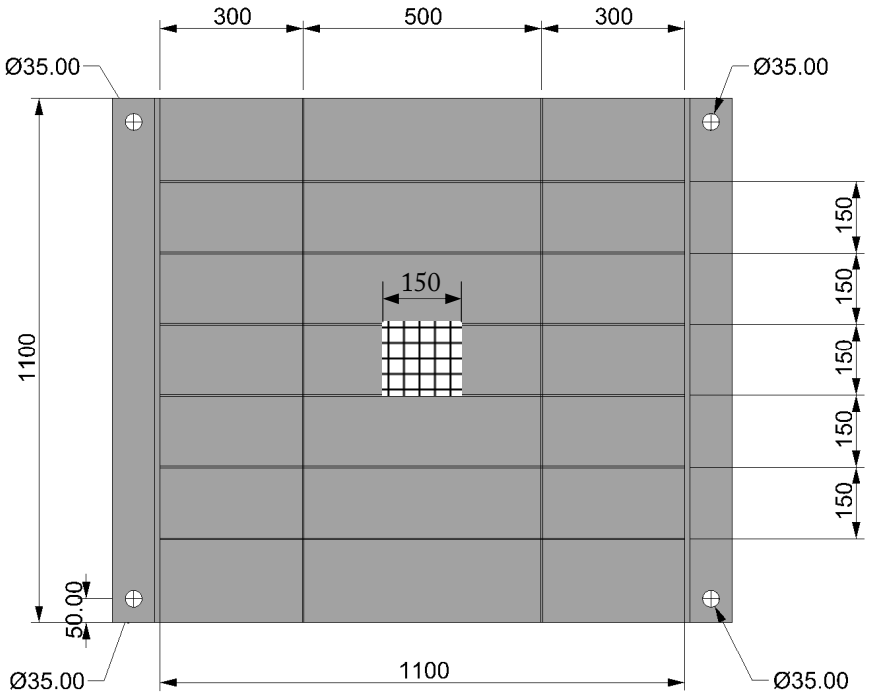

Figure C1: Schematic description of the loaded area (grid pattern).

In Figure C2, experimental data from medium-scale experiments on iceberg ice (Masterson and Frederking (1993)) and small-scale experiments on freshwater ice (Wells et al. (2007) and Section 3.1) are shown in log-log pressure-area axes. The gray-colored area in the middle of the plot indicates the scale of drop-weight tests and impact tests in water. The lower bound (the dashed line on the left) corresponds to a contact area that incorporates at least ten ice grains in each dimension (2–3 mm grains). The upper bound (the dashed line on the right) correspond to an area $A_n=\pi u(2r_i-u)$, where r_i =0.45 m is the radius of a spherically shaped ice mass, u is the crushing distance ($u=0.2r_i$ is assumed). The vertical red line in Figure C2 corresponds to the contact area shown in Figure C1 (square hatched area).

From Figure C2 one could see that the contact pressure significantly varies within the grey area. In addition, experimental data are lacking for smaller contact areas (between 0.001 and 0.02 m^2).

An upper bound pressure as a function of contact area $p=5.0A^{-0.46}$ is shown in Figure C2; $p=0.51A^{-0.46}$ is a lower bound pressure. In order to estimate the "average" ice pressure, a Matlab based fit was used on all data in the form of a power type curve $p=CA^x$ (p is the pressure, A is the contact area, C and x are empirical constants); see Figure C2.

Different fitting algorithms implemented in Matlab (i.e., Trust-Region, Levenberg-Marquardt and Gauss-Newton) give different empirical constants: C varying between 1.2 and 3.3, x varying between –0.39 and –0.26.

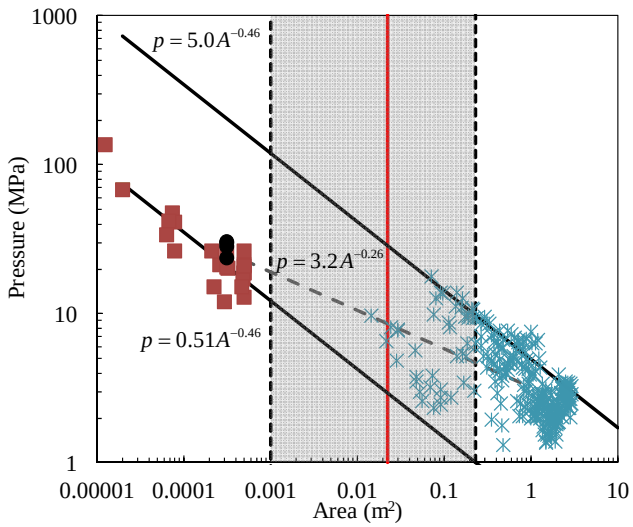

Figure C2: A pressure area log-log plot: $p=3.2A^{-0.26}$ is a power curve fit to data for a spherical rigid indenter; $p=0.51A^{-0.46}$ is a lower bound pressure estimate; $p=5.0A^{-0.46}$ is an upper bound pressure estimate.

The discussion on numerical procedures behind those algorithms is not within the scope of this study. Hence, the relationship between p and A will vary depending on the fitting algorithms used from $p=1.2A^{-0.39}$ to $p=3.3A^{-0.27}$. Further $p=3.2A^{-0.26}$ will be

used as it gives the smallest value of SSE (Sum of Squares due to Errors) and the highest value of R^2.

D. *Nonlinear-finite element analysis. Uncertainty of ice material parameters*

A sensitivity study of the nonlinear solution for the problem of the ice block vs. rigid plate collision is presented. The objectives of this sensitivity study were to determine main causes affecting the peak ice-load during a collision event and the main causes for ice failure.

Calculations were carried out in the finite element code LS-DYNA version ls971d R4.2.1. For simplicity, the ice mass was modeled as a sphere of radius R_i=0.45 m and the density of 1350 kg/m^3 (in the calculations, effect of water was included through the added mass). Ice material was modeled according to Liu et al. (2011). Initial velocity of the ice mass was set to 2 m/s. A fixed rigid plate and contact between the ice and the plate were modeled by using the LS-DYNA RIGIDWALL PLANAR FORCES command. The ice mass was discretized using the eight-node solid elements with one integration point and viscous hourglass control.

The variability of the following factors was considered: elasticity modulus of ice, size of the yield surface, cutoff pressure, initial failure strain, shape of the failure surface, finite element size (Table D1).

Table D1. Studied factors (E_i – elasticity modulus of ice; YS – yield surface; p_c – cutoff pressure; ε_0 – initial failure strain; FS –failure surface; FE – finite element).

Factor	Low level	High level
E_i, MPa	3500	9500
YS, $f(J_2, p)$=0	J_2=1.6+4.3p–0.62p^2	J_2=23+2.06p–0.023p^2
p_c, MPa	–1.0	–2.0
ε_0	0.008	0.1
FS, $f(\varepsilon_{eff}^p, p)$=0	$\varepsilon_{eff}^p = \varepsilon_0^{\left(1-\frac{p}{100}\right)}$	$\varepsilon_{eff}^p = \varepsilon_0 + \left(\frac{p}{100} - 0.5\right)^2$
FE mesh, mm	30×30	60×60

Note: Compression is considered to be positive

Input parameters to the numerical trials and the resulting peak force are given in Table D2. Results of the sensitivity study are given in Figures D1–D3.

Figure D1 shows that the numerical results (peak force) are more sensitive to the mesh size than to variations in other considered factors (i.e., size of the yield surface, elastic modulus of ice, shape of the failure surface, initial failure strain). With decreasing mesh size from 60 to 30 mm the impact force decreases from 501 kN to 206 kN. This mesh dependency may be viewed as a discretization error (i.e., error in the solution due to the choice of finite time and space resolution). Figure D2 shows an effect of mesh size on elements' stress state before element erosion took place.

Table D2. Design layout of the numerical trials and the response values (0 – input parameter at low level; 1 – input parameter at high level).

Trial #	E	$f(J_2,p)$	p_c	ε_0	$f(\varepsilon_{eff}^p, p)$	FE mesh	Peak force, kN	El. Erosion
1	1	1	1	1	1	1	548	no
2	1	1	1	0	0	1	464	yes
3	0	1	1	0	1	1	430	no
4	1	0	1	0	1	1	296	yes
5	1	1	0	0	1	1	500	yes
6	1	1	1	0	1	1	501	yes
7	1	1	1	0	1	0	206	yes

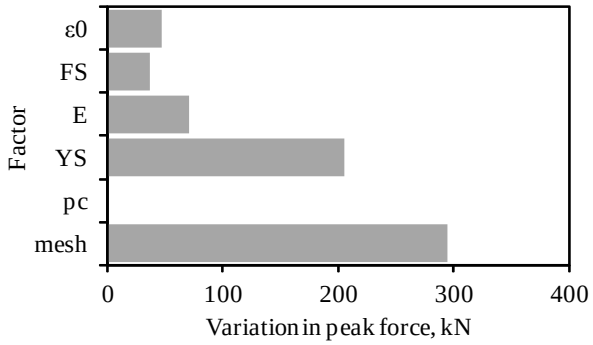

Figure D1: Sensitivity of the peak force exerted on the rigid plane during a collision event.

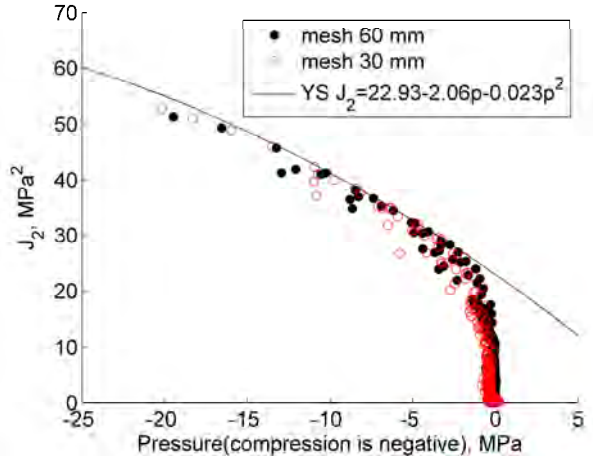

Figure D2: Sensitivity of stress state in ice to the mesh size (J_2 is the second invariant of the deviatoric stress tensor). Reported values of pressures and J_2 were interpreted from the average nodal data.

The effect of the mesh size on elements' stress state is not as noticeable as that on the impact force (see Figure D2). From Figure D3 it is observed that the shape of the failure surface controls the process of element erosion. For example, the shape of the failure surface (FS) controls the direction of the element erosion (U-shape of FS leads to erosion from inside out, power-law curve leads to erosion from the periphery to the center of the contact zone). Table D2 and Figure D1 show that the cutoff pressure does not influence the results.

N	Cross section of the ice block, element erosion and the contours of pressure are shown
2	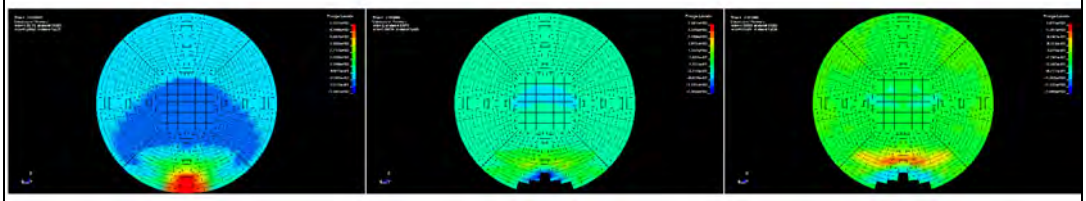
4	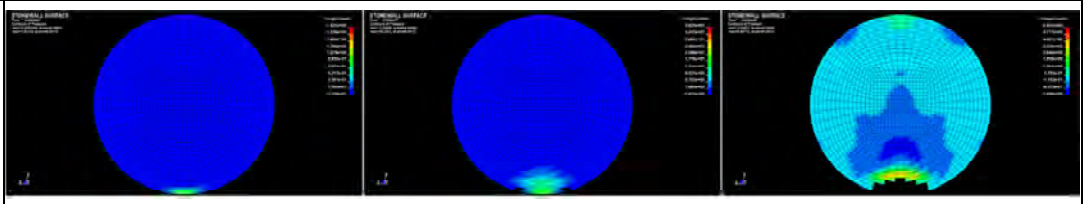
5	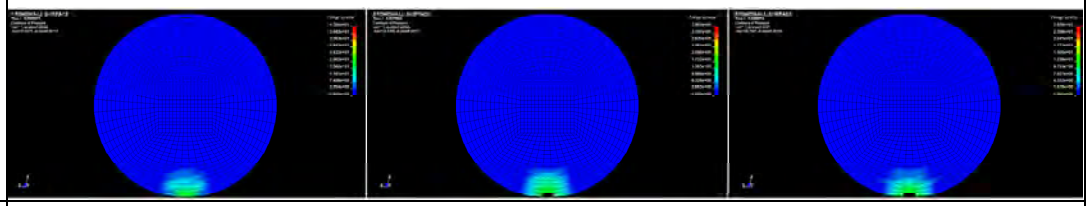
6	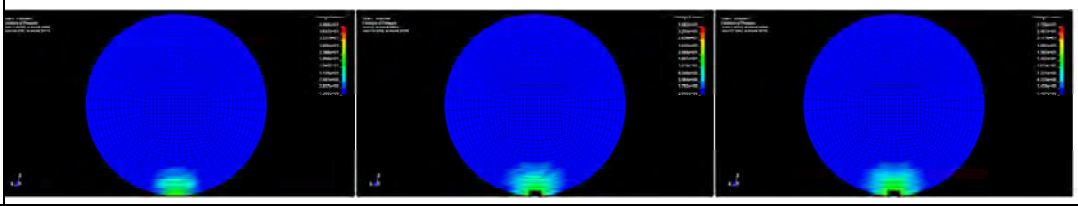
7	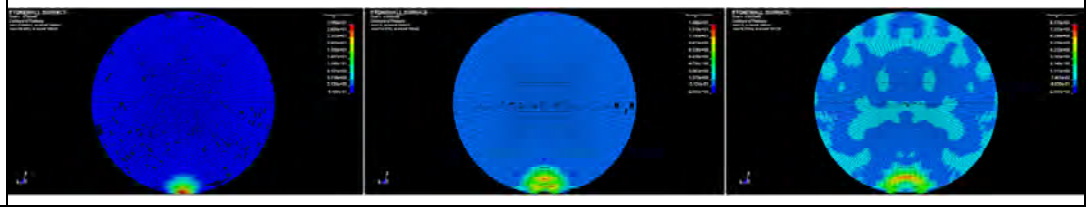

Figure D3: Sensitivity of the ice failure (element erosion) to the factors listed in Table D1. Contours of pressure are interpreted from the integration points.

A sensitivity study of the nonlinear solution for the dynamic problem of the ice-rigid plate collision showed that the impact force (exerted onto the rigid plate) is more affected by mesh size than by the variations in ice properties.

To summarize, due to the mesh dependency of the impact force, the design of panels for collision experiments should mainly be based on the simplified analytical or nonlinear methods. Integrated (coupled) nonlinear finite element analysis (including the ice model) may be used as a support tool to reduce the uncertainty of the design.

E. Crystallography of impacted ice

Figure E1 presents a vertical thin section of freshwater columnar S2 ice impacted by a free-fall projectile; see Figure 5 in Jones and Sinha (1990).

Figure E1: Vertical thin section of ice sample taken with a combination of cross polaroid and reflected light; source: Jones and Sinha (1990).

The thickness of the impacted ice was 28 cm. The ice was impacted with a spherically shaped projectile of 100 mm radius. Jones and Sinha (1990) observed a heavily damaged zone immediately below the indenter and many intra-granular microcracks, which formed throughout the ice below the indenter. The authors noted that horizontal cracks mostly stay within one grain and argued that the punched out portion at the bottom (see Figure E1) is evidence of grain boundary sliding along the columns.